Titre: Title:	Development of an MRI Template and Analysis Pipeline for the Spinal Cord and Application in Patients with Spinal Cord Injury
Auteur: Author:	Benjamin De Leener
Date:	2017
Type:	Mémoire ou thèse / Dissertation or Thesis
Référence: Citation:	De Leener, B. (2017). Development of an MRI Template and Analysis Pipeline for the Spinal Cord and Application in Patients with Spinal Cord Injury [Thèse de doctorat, École Polytechnique de Montréal]. PolyPublie. https://publications.polymtl.ca/2743/

Document en libre accès dans PolyPublie
Open Access document in PolyPublie

URL de PolyPublie: PolyPublie URL:	https://publications.polymtl.ca/2743/
Directeurs de recherche: Advisors:	Julien Cohen-Adad
Programme: Program:	Génie biomédical

UNIVERSITÉ DE MONTRÉAL

DEVELOPMENT OF AN MRI TEMPLATE AND ANALYSIS PIPELINE FOR THE SPINAL CORD AND APPLICATION IN PATIENTS WITH SPINAL CORD INJURY

BENJAMIN DE LEENER

INSTITUT DE GÉNIE BIOMÉDICAL

ÉCOLE POLYTECHNIQUE DE MONTRÉAL

THÈSE PRÉSENTÉE EN VUE DE L'OBTENTION

DU DIPLÔME DE PHILOSOPHIAE DOCTOR

(GÉNIE BIOMÉDICAL)

SEPTEMBRE 2017

UNIVERSITÉ DE MONTRÉAL

ÉCOLE POLYTECHNIQUE DE MONTRÉAL

Cette thèse intitulée:

DEVELOPMENT OF AN MRI TEMPLATE AND ANALYSIS PIPELINE FOR THE SPINAL
CORD AND APPLICATION IN PATIENTS WITH SPINAL CORD INJURY

présentée par : DE LEENER Benjamin

en vue de l'obtention du diplôme de : Philosophiae Doctor

a été dûment acceptée par le jury d'examen constitué de :

M. KADOURY Samuel, Ph. D., président

M. COHEN-ADAD Julien, Ph. D., membre et directeur de recherche

M. PETIT Yvan, Ph. D., membre

M. WEBER H. Michael, Ph. D., membre

DEDICATION

To my fiancée,
who has embraced this long journey with me

ACKNOWLEDGEMENTS

RÉSUMÉ

La moelle épinière est un organe fondamental du corps humain. Étant le lien entre le cerveau et le système nerveux périphérique, endommager la moelle épinière, que ce soit suite à un trauma ou une maladie neurodégénérative, a des conséquences graves sur la qualité de vie des patients. En effet, les maladies et traumatismes touchant la moelle épinière peuvent affecter l'intégrité des neurones et provoquer des troubles neurologiques et/ou des handicaps fonctionnels. Bien que de nombreuses voies thérapeutiques pour traiter les lésions de la moelle épinière existent, la connaissance de l'étendue des dégâts causés par ces lésions est primordiale pour améliorer l'efficacité de leur traitement et les décisions cliniques associées. L'imagerie par résonance magnétique (IRM) a démontré un grand potentiel pour le diagnostic et pronostic des maladies neurodégénératives et traumas de la moelle épinière. Plus particulièrement, l'*analyse par template* de données IRM du cerveau, couplée à des outils de traitement d'images automatisés, a permis une meilleure compréhension des mécanismes sous-jacents de maladies comme l'Alzheimer et la Sclérose en Plaques. Extraire automatiquement des informations pertinentes d'images IRM au sein de régions spécifiques de la moelle épinière présente toutefois de plus grands défis que dans le cerveau. Il n'existe en effet qu'un nombre limité de template de la moelle épinière dans la littérature, et aucun ne couvre toute la moelle épinière ou n'est lié à un template existant du cerveau. Ce manque de template et d'outils automatisés rend difficile la tenue de larges études d'analyse de la moelle épinière sur des populations variées.

L'objectif de ce projet est donc de proposer un nouveau template IRM couvrant toute la moelle épinière, recalé avec un template existant du cerveau, et intégrant des atlas de la structure interne de la moelle épinière (e.g., matière blanche et grise, tracts de la matière blanche). Ce template doit venir avec une série d'outils automatisés permettant l'extraction d'information IRM au sein de régions spécifiques de la moelle épinière. La question générale de recherche de ce projet est donc « *Comment créer un template générique de la moelle épinière, qui permettrait l'analyse non biaisée et reproductible de données IRM de la moelle épinière ?* ». Plusieurs contributions originales ont été proposées pour répondre à cette question et vont être décrites dans les prochains paragraphes.

La première contribution de ce projet est le développement du logiciel *Spinal Cord Toolbox* (SCT). SCT est un logiciel open-source de traitement d'images IRM multi-parametrique de la moelle

épinière (De Leener, Lévy, et al., 2016). Ce logiciel intègre notamment des outils pour la détection et la segmentation automatique de la moelle épinière et de sa structure interne (i.e., matière blanche et matière grise), l'identification et la labellisation des niveaux vertébraux, le recalage d'images IRM multimodales sur un template générique de la moelle épinière (précédemment le template MNI-Poly-AMU, maintenant le template PAM50, proposé içi). En se basant sur un atlas de la moelle, SCT intègre également des outils pour extraire des données IRM de régions spécifiques de la moelle épinière, comme la matière blanche et grise et les tracts de la matière blanche, ainsi que sur des niveaux vertébraux spécifiques. D'autres outils additionnels ont aussi été proposés, comme des outils de correction de mouvement et de traitement basiques d'images appliqués le long de la moelle épinière. Chaque outil intégré à SCT a été validé sur un jeu de données multimodales.

La deuxième contribution de ce projet est le développement d'une nouvelle méthode de recalage d'images IRM de la moelle épinière (De Leener, Mangeat, et al., 2017). Cette méthode a été développée pour un usage particulier : le redressement d'images IRM de la moelle épinière, mais peut également être utilisé pour recaler plusieurs images de la moelle épinière entre elles, tout en tenant compte de la distribution vertébrale de chaque sujet. La méthode proposée se base sur une approximation globale de la courbure de la moelle épinière dans l'espace et sur la résolution analytique des champs de déformation entre les deux images. La validation de cette nouvelle méthode a été réalisée sur une population de sujets sains et de patients touchés par une compression de la moelle épinière.

La contribution majeure de ce projet est le développement d'un système de création de template IRM de la moelle épinière et la proposition du template PAM50 comme template de référence pour les études d'analyse par template de données IRM de la moelle épinière. Le template PAM50 a été créé à partir d'images IRM tiré de 50 sujets sains, et a été généré en utilisant le redressement d'images présenté ci-dessus et une méthode de recalage d'images itératif non linéaire, après plusieurs étapes de prétraitement d'images. Ces étapes de prétraitement incluent la segmentation automatique de la moelle épinière, l'extraction manuelle du bord antérieur du tronc cérébral, la détection et l'identification des disques intervertébraux, et la normalisation d'intensité le long de la moelle. Suite au prétraitement, la ligne centrale moyenne de la moelle et la distribution vertébrale ont été calculées sur la population entière de sujets et une image initiale de template a été générée. Après avoir recalé toutes les images sur ce template initial, le template PAM50 a été créé en utilisant un processus itératif de recalage d'image, utilisé pour générer des templates de cerveau.

Le PAM50 couvre le tronc cérébral et la moelle épinière en entier, est disponible pour les contrastes IRM pondérés en T1, T2 et T2*, et intègre des cartes probabilistes et atlas de la structure interne de la moelle épinière. De plus, le PAM50 a été recalé sur le template ICBM152 du cerveau, permettant ainsi la tenue d'analyse par template simultanément dans le cerveau et dans la moelle épinière.

Finalement, plusieurs résultats complémentaires ont été présentés dans cette dissertation. Premièrement, une étude de validation de la répétabilité et reproductibilité de mesures de l'aire de section de la moelle épinière a été menée sur une population de patients touchés par la sclérose en plaques. Les résultats démontrent une haute fiabilité des mesures ainsi que la possibilité de détecter des changements très subtiles de l'aire de section transverse de la moelle, importants pour mesurer l'atrophie de la moelle épinière précoce due à des maladies neurodégénératives comme la sclérose en plaques. Deuxièmemement, un nouveau biomarqueur IRM des lésions de la moelle épinière a été proposé, en collaboration avec Allan Martin, de l'Université de Toronto. Ce biomarqueur, calculé à partir du ratio d'intensité entre la matière blanche et grise sur des images IRM pondérées en T2*, utilise directement les développements proposés dans ce projet, notamment en utilisant le recalage du template de la moelle épinière et les méthodes de segmentation de la moelle. La faisabilité d'extraire des mesures de données IRM multiparamétrique dans des régions spécifiques de la moelle épinière a également été démontrée, permettant d'améliorer le diagnostic et pronostic de lésions et compression de la moelle épinière. Finalement, une nouvelle méthode d'extraction de la morphométrie de la moelle épinière a été proposée et utilisée sur une population de patients touchés par une compression asymptomatique de la moelle épinière, démontrant de grandes capacités de diagnostic (> 99%).

Le développement du template PAM50 comble le manque de template de la moelle épinière dans la littérature mais présente cependant plusieurs limitations. En effet, le template proposé se base sur une population de 50 sujets sains et jeunes (âge moyen = 27 +- 6.5) et est donc biaisée vers cette population particulière. Adapter les analyses par template pour un autre type de population (âge, race ou maladie différente) peut être réalisé directement sur les méthodes d'analyse mais aussi sur le template en lui-même. Tous le code pour générer le template a en effet été mis en ligne (https://github.com/neuropoly/template) pour permettre à tout groupe de recherche de développer son propre template. Une autre limitation de ce projet est le choix d'un système de coordonnées basé sur la position des vertèbres. En effet, les vertèbres ne représentent pas complètement le

caractère fonctionnel de la moelle épinière, à cause de la différence entre les niveaux vertébraux et spinaux. Le développement d'un système de coordonnées spinal, bien que difficile à caractériser dans des images IRM, serait plus approprié pour l'analyse fonctionnelle de la moelle épinière. Finalement, il existe encore de nombreux défis pour automatiser l'ensemble des outils développés dans ce projet et les rendre robuste pour la majorité des contrastes et champs de vue utilisés en IRM conventionnel et clinique.

Ce projet a présenté plusieurs développements importants pour l'analyse de données IRM de la moelle épinière. De nombreuses améliorations du travail présenté sont cependant requises pour amener ces outils dans un contexte clinique et pour permettre d'améliorer notre compréhension des maladies affectant la moelle épinière. Les applications cliniques requièrent notamment l'amélioration de la robustesse et de l'automatisation des méthodes d'analyse d'images proposées. La caractérisation de la structure interne de la moelle épinière, incluant la matière blanche et la matière grise, présente en effet de grands défis, compte tenu de la qualité et la résolution des images IRM standard acquises en clinique. Les outils développés et validés au cours de ce projet ont un grand potentiel pour la compréhension et la caractérisation des maladies affectant la moelle épinière et aura un impact significatif sur la communauté de la neuroimagerie.

ABSTRACT

The spinal cord plays a fundamental role in the human body, as part of the central nervous system and being the vector between the brain and the peripheral nervous system. Damaging the spinal cord, through traumatic injuries or neurodegenerative diseases, can significantly affect the quality of life of patients. Indeed, spinal cord injuries and diseases can affect the integrity of neurons, and induce neurological impairments and/or functional disabilities. While various treatment procedures exist, assessing the extent of damages and understanding the underlying mechanisms of diseases would improve treatment efficiency and clinical decisions. Over the last decades, magnetic resonance imaging (MRI) has demonstrated a high potential for the diagnosis and prognosis of spinal cord injury and neurodegenerative diseases. Particularly, template-based analysis of brain MRI data has been very helpful for the understanding of neurological diseases, using automated analysis of large groups of patients. However, extracting MRI information within specific regions of the spinal cord with minimum bias and using automated tools is still a challenge. Indeed, only a limited number of MRI template of the spinal cord exists, and none covers the full spinal cord, thereby preventing large multi-centric template-based analysis of the spinal cord. Moreover, no template integrates both the spinal cord and the brain region, thereby preventing simultaneous cerebrospinal studies.

The objective of this project was to propose a new MRI template of the full spinal cord, which allows simultaneous brain and spinal cord studies, that integrates atlases of the spinal cord internal structures (e.g., white and gray matter, white matter pathways) and that comes with tools for extracting information within these subregions. More particularly, the general research question of the project was "*How to create generic MRI templates of the spinal cord that would enable unbiased and reproducible template-based analysis of spinal cord MRI data?*". Several original contributions have been made to answer this question and to enable template-based analysis of spinal cord MRI data.

The first contribution was the development of the Spinal Cord Toolbox (SCT), a comprehensive and open-source software for processing multi-parametric MRI data of the spinal cord (De Leener, Lévy, et al., 2016). SCT includes tools for the automatic segmentation of the spinal cord and its internal structure (white and gray matter), vertebral labeling, registration of multimodal MRI data (structural and non-structural) on a spinal cord MRI template (initially the MNI-Poly-AMU

template, later the PAM50 template), co-registration of spinal cord MRI images, as well as the robust extraction of MRI metric within specific regions of the spinal cord (i.e., white and gray matter, white matter tracts, gray matter subregions) and specific vertebral levels using a spinal cord atlas (Lévy et al., 2015). Additional tools include robust motion correction and image processing along the spinal cord. Each tool included in SCT has been validated on a multimodal dataset.

The second contribution of this project was the development of a novel registration method dedicated to spinal cord images, with an interest in the straightening of the spinal cord, while preserving its topology (De Leener, Mangeat et al., 2017). This method is based on the global approximation of the spinal cord and the analytical computation of deformation fields perpendicular to the centerline. Validation included calculation of distance measurements after straightening on a population of healthy subjects and patients with spinal cord compression.

The major contribution of this project was the development of a framework for generating MRI template of the spinal cord and the PAM50 template, an unbiased and symmetrical MRI template of the brainstem and full spinal cord. Based on 50 healthy subjects, the PAM50 template was generated using an iterative nonlinear registration process, after applying normalization and straightening of all images. Pre-processing included segmentation of the spinal cord, manual delineation of the brainstem anterior edge, detection and identification of intervertebral disks, and normalization of intensity along the spinal cord. Next, the average centerline and vertebral distribution was computed to create an initial straight template space. Then, all images were registered to the initial template space and an iterative nonlinear registration framework was applied to create the final symmetrical template. The PAM50 covers the brainstem and the full spinal cord, from C1 to L2, is available for T1-, T2- and T2*-weighted contrasts, and includes probabilistic maps of the white and the gray matter and atlases of the white matter pathways and gray matter subregions. Additionally, the PAM50 template has been merged with the ICBM152 brain template, thereby allowing for simultaneous cerebrospinal template-based analysis.

Finally, several complementary results, focused on clinical validation and applications, are presented. First, a reproducibility and repeatability study of cross-sectional area measurements using SCT (De Leener, Granberg, Fink, Stikov, & Cohen-Adad, 2017) was performed on a Multiple Sclerosis population (n=9). The results demonstrated the high reproducibility and repeatability of SCT and its ability to detect very subtle atrophy of the spinal cord. Second, a novel

biomarker of spinal cord injury has been proposed. Based on the T2*-weighted intensity ratio between the white and the gray matter, this new biomarker is computed by registering MRI images with the PAM50 template and extracting metrics using probabilistic atlases. Additionally, the feasibility of extracting multiparametric MRI metrics from subregions of the spinal cord has been demonstrated and the diagnostic potential of this approach has been assessed on a degenerative cervical myelopathy (DCM) population. Finally, a method for extracting shape morphometrics along the spinal cord has been proposed, including spinal cord flattening, indentation and torsion. These metrics demonstrated high capabilities for the diagnostic of asymptomatic spinal cord compression (AUC=99.8% for flattening, 99.3% for indentation, and 98.4% for torsion).

The development of the PAM50 template enables unbiased template-based analysis of the spinal cord. However, the PAM50 template has several limitations. Indeed, the proposed template has been generated with multimodal MRI images from 50 healthy and young individuals (age = 27+/- 6.5 y.o.). Therefore, the template is specific to this particular population and could not be directly usable for age- or disease-specific populations. One solution is to open-source the template-generation code so that research groups can generate and use their own spinal cord MRI template. The code is available on https://github.com/neuropoly/template. While this project introduced a generic referential coordinate system, based on vertebral levels and the pontomedullary junction as origin, one limitation is the choice of this coordinate system. Another coordinate system, based spinal segments would be more suitable for functional analysis. However, the acquisition of MRI images with high enough resolution to delineate the spinal roots is still challenging. Finally, several challenges in the automation of spinal cord MRI processing remains, including the robust detection and identification of vertebral levels, particularly in case of small fields-of-view.

This project introduced key developments for the analysis of spinal cord MRI data. Many more developments are still required to bring them into clinics and to improve our understanding of diseases affecting the spinal cord. Indeed, clinical applications require the improvement of the robustness and the automation of the proposed processing and analysis tools. Particularly, the detection and segmentation of spinal cord structures, including vertebral labeling and white/gray matter segmentation, is still challenging, given the lowest quality and resolution of standard clinical MRI acquisition. The tools developed and validated here have the potential to improve our understanding and the characterization of diseases affecting the spinal cord and will have a significant impact on the neuroimaging community.

TABLE OF CONTENTS

LIST OF TABLES

LIST OF FIGURES

Figure 4.7: Example application in T_2*-weighted data from 1.5T, 3T and 7T, different vendors and different pathologies. Here, SCT was used to segment the spinal cord, registering the MNI-Poly-AMU to the data, segmenting the gray and white matter, adjusting the warping field based on gray matter shape, and finally warping the white matter atlas to the template. The white/gray matter is shown in blue/yellow respectively, and is thresholded at 0.4 for visual purpose. The left/right corticospinal and left/right gracilis are respectively shown in yellow/blue and green/red and are thresholded at 0.4. Parameters for each subject are listed hereafter. **HC @1.5T**: GE Signa HDxt, neurovascular coil, 2D MERGE sequence, TR/TE=607/16ms, matrix=320×320, resolution=0.8×0.8×4mm^3 (interpolated to 0.4mm in-plane using zero padding), R=2 acceleration, bandwidth=244Hz/pixel. **HC @7T**: Siemens 7T whole-body scanner with SC72 gradients and 4ch-Tx/19ch-Rx coil (Zhao et al., 2014), multi-echo FLASH (all echoes were averaged), TR/TE=512/[7.8,15,22,29.4]ms, matrix=384×384, resolution=0.35×0.35×3mm^3, R=2 acceleration, bandwidth=195Hz/pixel. **Syringo @3T**: Siemens TIM Trio, 4ch neck coil, multi-echo FLASH (all echoes were averaged), TR/TE=539/[5.41,12.56,19.16]ms, matrix=320×320, resolution=0.5×0.5×5mm^3, R=2 acceleration, bandwidth=195Hz/pixel. **CSM @3T**: GE Signa HDxt, neurovascular coil, 2D MERGE sequence, TR/TE=550/13ms, matrix=320×320, resolution=0.6×0.6×4mm^3, R=1 acceleration, bandwidth=244Hz/pixel. Data courtesy of Drs. Allan Martin and Michael Fehlings from Toronto Western Hospital. **MS @7T**: Siemens 7T whole-body scanner with SC72 gradients and 4ch-Tx/19ch-Rx coil, multi-echo FLASH, TR/TE=500/[7.8,13.7,18.4]ms, matrix=480×534, resolution=0.4×0.4×3mm^3, R=2 acceleration, bandwidth=199Hz/pixel. Data courtesy of Dr. Caterina Mainero from Massachusetts General Hospital. **ALS @7T**: Siemens 7T whole-body scanner with SC72 gradients and 4ch-Tx/19ch-Rx coil, multi-echo FLASH, TR/TE=514/[7.8,15,22,29.4]ms, matrix=534×484, resolution=0.35×0.35×3mm^3, R=2 acceleration, bandwidth=195Hz/pixel. Data courtesy of Dr. Nazem Atassi from Massachusetts General Hospital. **SCI @7T**: Siemens 7T whole-body scanner with SC72 gradients and 4ch-Tx/19ch-Rx coil, multi-echo FLASH, TR/TE=514/[7.8,15,22,29.4]ms, matrix=534×480, resolution=0.37×0.37×3mm^3, R=2

LIST OF SYMBOLS AND ABBREVIATIONS

ALS	amyotrophic lateral sclerosis
APW	antero-posterior width
C3	cervical vertebral level (3rd vertebra)
CAD	computer-aided diagnosis
COV	coefficient of variation
CNS	central nervous system
CSA	cross sectional area
CSF	cerebrospinal fluid
DCM	degenerative cervical myelopathy
DTbM	double threshold based segmentation method
DTI	diffusion tensor imaging
EDSS	extended disability status scale
EPI	echo planar imaging
FAI	fuzzy anisotropy index
fMRI	functional MRI
FOV	field-of-view
FrAt	Friedreich's ataxia
FSPGR	Fast Spoiled Gradient-Recalled-Echo
GM	gray matter
GRE	gradient echo
HC	healthy control
HDE	Hausdorff distance error
ICC	intra-class correlation coefficient
LRW	left-right width
MJD	Machado-Joseph disease
mpMRI	multi-parametric MRI
MPRAGE	Magnetization Prepared Rapid Acquisition Gradient Echoes
MP2RAGE	Magnetization Prepared 2 Rapid Acquisition Gradient Echoes
MRI	Magnetic Resonance Imaging
MS	multiple sclerosis
MSDE	mean surface distance error
MT	magnetization-transfer imaging
MTR	magnetization transfer ratio

NMO	neuromyelitis optica
NURBS	non-uniform rational Bezier splines
PCA	principal component analysis
PMJ	pontomedullary junction
PNS	peripheral nervous system
PSIR	Phase Sensitive Inversion Recovery
PVE	partial volume effect
qMRI	quantitative MRI
ROI	region of interest
SCI	spinal cord injury
SMA	spinal muscular atrophy
SNR	signal-to-noise ratio
STAPLE	Simultaneous Truth and Performance Level Estimation
STIR	short inversion time inversion recovery
TBM	tensor based morphometry
UHF	ultra high field
VBM	voxel based morphometry
WM	white matter
Ø	diameter

CHAPTER 1   INTRODUCTION

The spinal cord plays a fundamental role in the human body as the transmission vector between the brain and the peripheral nervous system (PNS). The spinal cord is also responsible for key neuronal mechanisms for generating patterns for walking and reflexes. Unfortunately, the spinal cord can be affected by various diseases, including spinal cord injury (SCI), caused by trauma, or specific diseases, such as Degenerative Cervical Myelopathy (DCM), that compress the spinal cord and cause the progressive degeneration of neurons. Neurodegenerative diseases such as Multiple Sclerosis (MS) and Amyotrophic Lateral Sclerosis (ALS) can also impact the spinal cord, as these diseases affect the neurons in the central nervous system (CNS).

Spinal cord injury (SCI) affects nearly 86,000 Canadians and can induce severe functional disability (paralysis) and chronic pain (Bickenbach, 2013). The personal, social, and economic burden is tremendous, with an estimated $3.6 billion annual cost to Canada (Spinal Cord Injury Canada, 2015). Unfortunately, there is currently no cure to SCI and patients are often left without proper treatment. Novel magnetic resonance imaging (MRI) techniques (e.g., diffusion, magnetization transfer) were shown to provide efficient biomarkers for improved diagnosis/prognosis and objective assessment of new treatments (e.g., drugs, nano-medicine) (Fawcett et al., 2007; Rowland, Hawryluk, Kwon, & Fehlings, 2008). Particularly, new quantitative MRI (qMRI) techniques are now more sensitive to underlying microstructure and metabolism, therefore providing insights into the pathogenesis of neurological diseases (Cohen-Adad & Wheeler-Kingshott, 2014a). Unfortunately, few of these techniques are currently being applied to spinal cord studies, a direct consequence of the lack of image analysis software dedicated to spinal cord MRI data (Wheeler-Kingshott et al., 2014).

Recent advances of neuroimaging techniques triggered an increasing number of studies investigating the spinal cord, including atrophy assessment in multiple sclerosis (Brex et al., 2001; Horsfield et al., 2010; Ingle, Stevenson, Miller, & Thompson, 2003; Kalkers, Barkhof, Bergers, van Schijndel, & Polman, 2002; Kearney et al., 2014; Lin, Blumhardt, & Constantinescu, 2003; C. Liu, Edwards, Gong, Roberts, & Blumhardt, 1999; Losseff, Webb, O'riordan, et al., 1996; Stevenson et al., 1998; Yiannakas et al., 2012a) as well as diffusion MRI and magnetization transfer, in MS (Agosta, Laganà, et al., 2007; Agosta, Pagani, Caputo, & Filippi, 2007; Bozzali et al., 1999; Charil et al., 2006; Ciccarelli et al., 2007; Filippi et al., 2000; Freund et al., 2010; Oh et

al., 2013; Rovaris et al., 2004, 2008, 2001; Valsasina et al., 2005), ALS (Cohen-Adad, El Mendili, et al., 2013; Iwata et al., 2011; Nair et al., 2010) and Cervical Spondylotic Myelopathy (CSM) (Facon et al., 2005; Hori, Okubo, Aoki, Kumagai, & Araki, 2006; Kara et al., 2011; Mamata, Jolesz, & Maier, 2005). The common trait of all these studies is the manual intervention necessary by researchers for extracting relevant MR metrics, being the identification of spinal cord contours or regions of interest, therefore introducing a bias that decreases the reproducibility and accuracy of these studies.

Solutions for extracting information from regions of MRI images with minimum bias include automated segmentation and template-based analysis. Indeed, several volumetric parcellations of the brain have been proposed (Caviness, Meyer, Makris, & Kennedy, 1996; Collins, Evans, Holmes, & Peters, 1995; Destrieux, Fischl, Dale, & Halgren, 2010; Evans, 2007) to automatically extract MRI metrics from brain regions while minimizing the user-bias. While recent progress has been made concerning the segmentation of the spinal cord and its internal structures (De Leener, Kadoury, & Cohen-Adad, 2014; Dupont et al., 2016), only a few MRI templates of the spinal cord have been proposed, e.g., (Fonov et al., 2014; Stroman, Figley, & Cahill, 2008; Valsasina et al., 2012), and there is no template that covers the full spinal cord and that would be available for multiple MRI contrasts. Moreover, no atlas of the spinal cord has been integrated into templates, forcing studies to manually delineate the regions of interest.

The objective of my project was to propose a new MRI template of the full spinal cord, which allows simultaneous brain and spinal cord studies, that integrates atlases of the spinal cord internal structures (e.g., white and gray matter, white matter pathways) and that comes with tools for extracting information within these subregions. More particularly, the general research question of the project was "*How to create generic MRI templates of the spinal cord that would enable unbiased and reproducible template-based analysis of spinal cord MRI data?*". Chapter 2 will present a critical review of the literature on the analysis of spinal cord MRI, Chapter 3 will describe the methodology followed to answer the research question while Chapter 4Chapter 5, 0Chapter 7 present the published results related to this project, including new methods for analyzing spinal cord MRI data, the proposed MRI template of the spinal cord, and the application of the proposed developments in a clinical context.

CHAPTER 2   LITERATURE REVIEW

This chapter presents a critical review of the literature related to this project, including a non-exhaustive introduction to spinal cord anatomy/morphology and MRI. Section 2.1 presents an overview of the internal and external anatomy of the spinal cord, as well as some insights of the various functionalities it is responsible for. Section 2.2 follows on the various diseases and traumas that can affect the integrity and function of the spinal cord, and how it appears in MRI images. Section 2.3 offers a brief introduction to the fundamental principles of MRI, particularly structural MRI, and details challenges and progress in MRI acquisition specific to the spinal cord. Finally, section 2.4 presents a critical review of the literature on MRI analysis of the spinal cord, including a list of available neuroimaging software, an exhaustive review of segmentation methods developed and/or applied on spinal cord structure, a review of existing MRI template and atlases of the spinal cord and an overview of the clinical and research potential of spinal cord CSA.

2.1 Anatomy and histology of the spinal cord

2.1.1 The neuron and its support

The neuron is one of the most fundamental elements of the central nervous system (CNS). It is composed of three main parts: the soma, the dendrites and the axon. The soma is the body of the neuron and contains the nucleus of the cell, including the DNA, as well as the organelles (mitochondria, ribosomes, etc.), which are responsible for maintaining the protein and nucleic material of the cell. The dendrites are highly branched processes that project from the soma. Their main function is to receive the signal from other neurons and transmit it for processing to the cell body. At the opposite end of the dendrites is the axon, a tubular structure responsible for transmitting the processed signal to other neurons through their dendrites. The axons diameters can vary from a few micrometers to about 20 micrometers and can reach a length of one meter in humans, starting in the brain and ending in the spinal cord. Most of the axons are surrounded by myelin sheaths, which allows for faster and more efficient transmission of the electrical signal along the cell membrane.

The transmission of the signal between axons and dendrites is performed via specialized junctions (synapses) that work mainly by releasing neurotransmitters in the intercellular compartments, causing a change in the electrical state of the post-synaptic neuronal membrane, resulting in its hyper/de-polarization.

Neurons can vary in size, shape and organization, depending on their location and functions (Figure 2.1). In the spinal cord, the main types of neurons are sensory neurons, motor neurons and interneurons. Motor neurons are specialized neurons that project outside of the spinal cord through spinal roots and control directly or indirectly organs, mainly the muscles. Sensory neurons convert internal (e.g., blood pressure) or external (e.g., temperature, touch, smell) stimuli into action potentials that are transmitted to the spinal cord and to the brain. Interneurons are specialized in the relay of information between two different types of neurons.
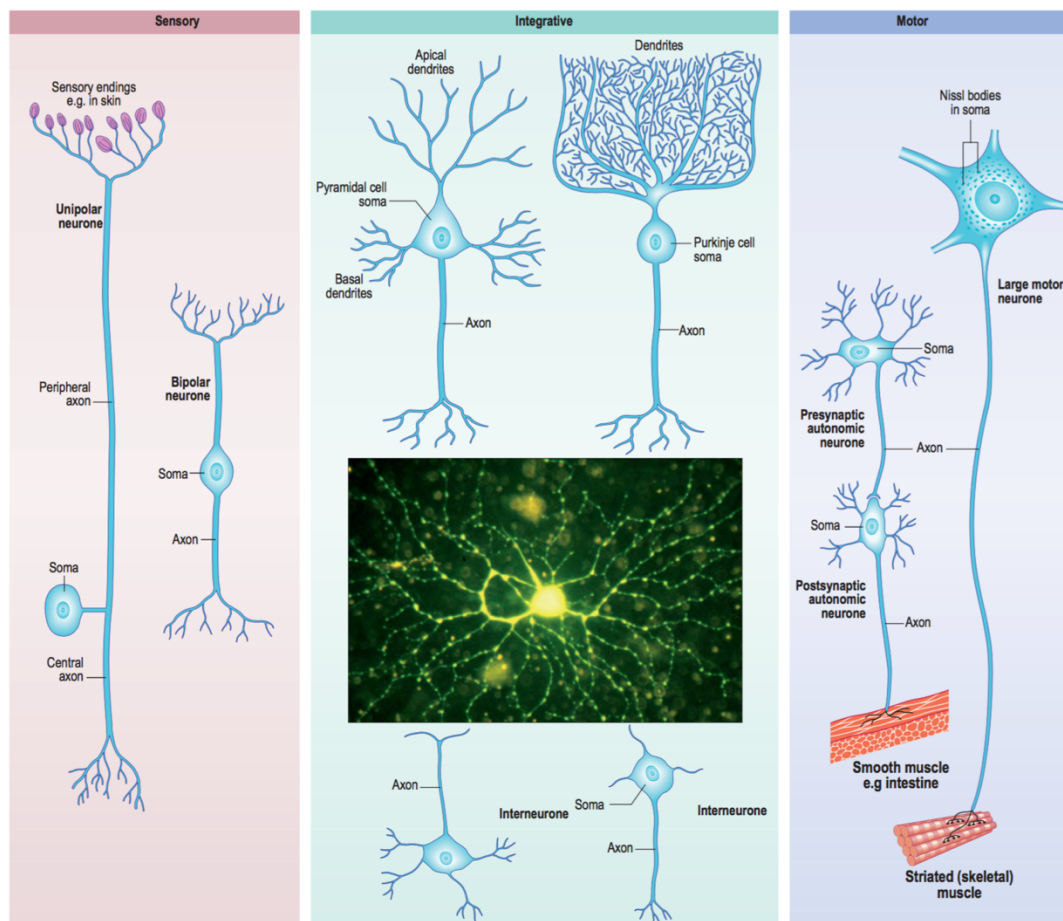
Figure 2.1: Schematic representation of the different types of neurons in the CNS. Adapted from (Standring, 2008), Fig. 3.3.

While the importance of neurons is indisputable, many other cell types, called glial cells, can be found in the CNS with as much importance on brain functions as the neurons. Glial cells represent approximately 90% of the total number of cells in the CNS and notably include astrocytes and oligodendrocytes. Astrocytes have a characteristic star shape with many ramifications and act as structural support for other cells, while oligodendrocytes produce the myelin in the CNS. The myelin is a fat-based layered structure that surrounds the axon in discontinuous sheaths, to allow faster transmission of the electrical signal along the axon. The loss of myelin integrity can induce irreparable damages to the central nervous system.

2.1.2 Global morphology

The spinal cord is a long tubular structure that is embedded into the spine and that links the brain, via the brainstem to the PNS. The spinal cord generally ends around L1-L2 vertebral levels and measures 45 cm on average for men and 42 cm for women. Its shape can be circular or elliptical and its diameter (equivalent to a circle) varies with the vertebral level and ranges from 5 to 10 mm. Two enlargements can be found along the spinal cord, in the cervical region and in the lumbar region (Figure 2.2). These structures, called cervical and lumbar enlargements, deserve mainly the superior and inferior members, respectively. The spinal cord has a natural curvature that follows the spine curvature and that depends on the positioning, age and size of the subject.

The spinal cord extends to the PNS via the spinal roots that emerge between two adjacent vertebral bodies. The spinal roots define functional regions of the spinal cord, called spinal segments, that can be subdivided per vertebral regions: 8 in the cervical region; 12 in the thoracic region; 5 in the lumbar region; 5 in the sacral region. The position of spinal segments is not completely related to the position of the associated vertebrae (Figure 2.2), as the spine and spinal cord do not have the same length and do not grow at the same speed through normal development. For example, the C4 spinal nerves are usually located around C3 vertebral level, and they emerge from the spinal cord between the C3 and C4 vertebral levels, while the C8 spinal nerves are usually located around C6-C7 intervertebral disk and emerge from the spinal cord between the C7 and T1 vertebrae (Cadotte et al., 2015). The spinal cord ends with the conus medullaris, after which spinal nerves are separated and form the *filum terminale*.
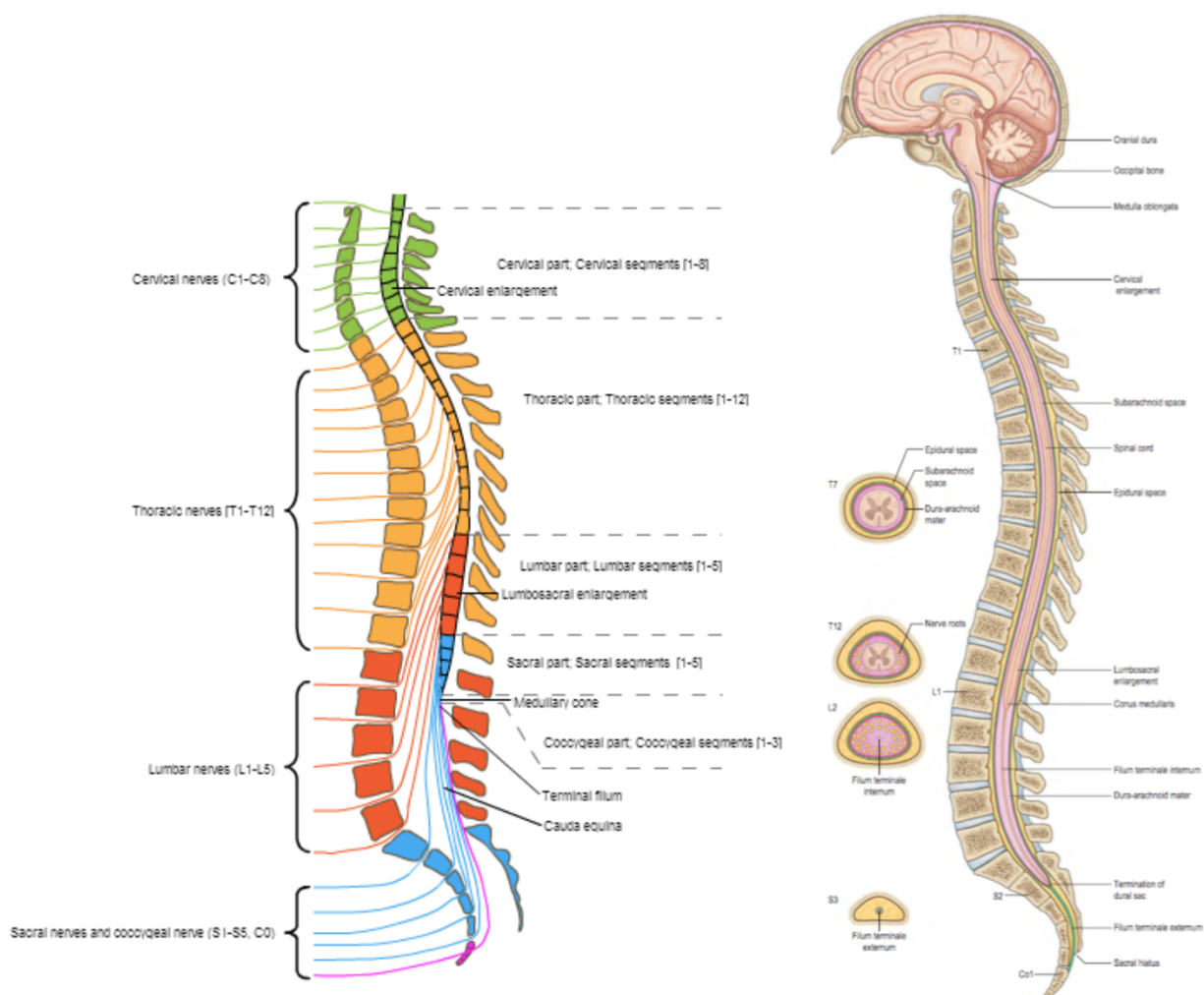
Figure 2.2: (Left) Representation of the vertebral levels and spinal segments and their misalignment. Adapted from (e-Anatomy, 2017). (Right) Representation of the spinal cord within the vertebrae, the spinal enlargements and different tissues surrounding the spinal cord. Adapted from (Standring, 2008), Fig. 43.2.

The volume of the spinal cord also depends on several anatomical and social parameters, such as the age, the sex, the weight and the size of the subject (Yanase et al., 2006). Moreover, Engl et al. have demonstrated the correlation between the spinal cord volume and the brain volume and weight (Engl et al., 2013). While many research groups have studied the relation between the spinal cord morphology and these influence parameters, no global consensus has been reached to date.

2.1.3 Internal structure

The spinal cord internal structure can be separated in two regions, the white matter (WM) and the gray matter (GM). The white matter is located at the spinal cord periphery and is mainly composed of compact bundles of myelinated axons that follow the spinal cord curvature (Figure 2.3). The white matter can be subdivided into 30 tracts, regrouped into several large funiculi: the dorsal columns, the ventral columns and the lateral columns. The dorsal columns typically contain ascending pathways that relay sensory information from the PNS to the brain, while the ventral and lateral columns generally contain descending tracts (Susan Standring, 2008).
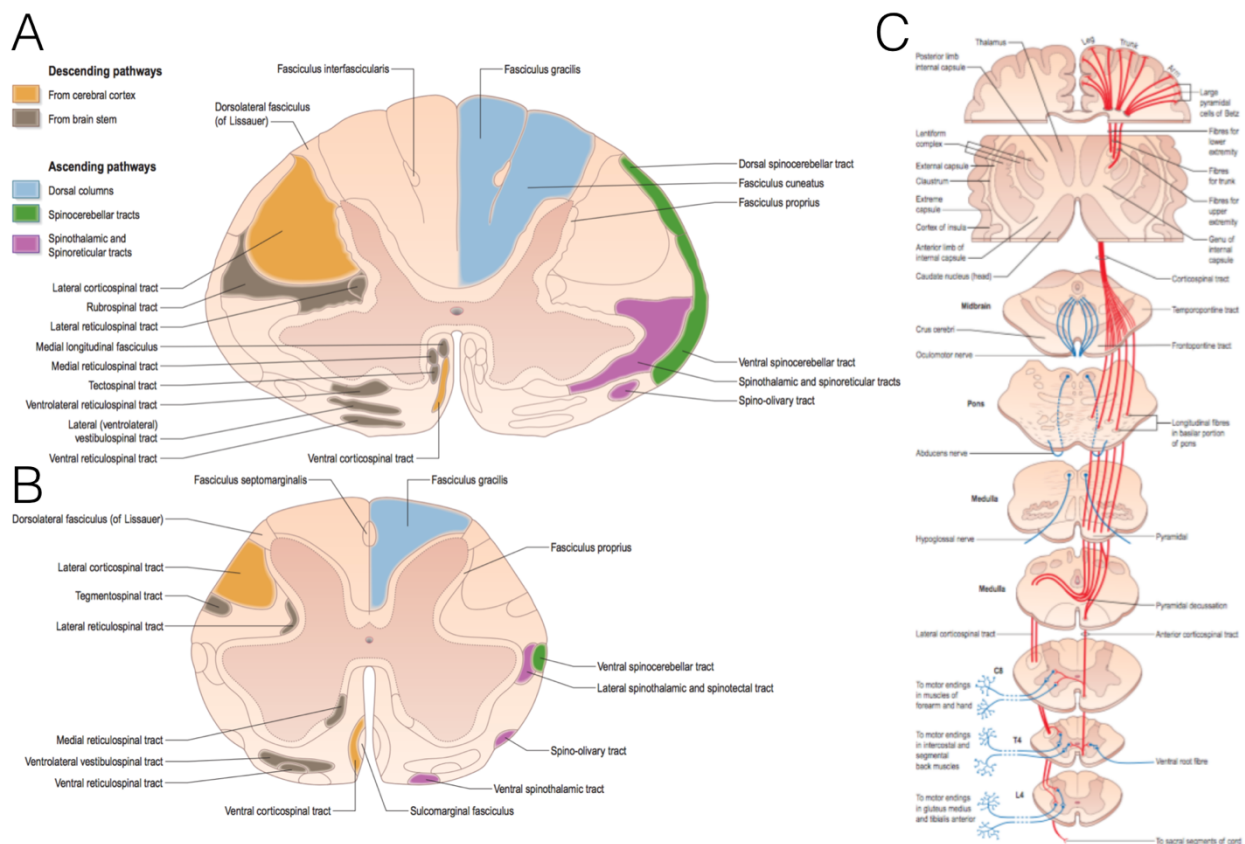
Figure 2.3: Adapted from (Standring, 2008), Fig. 18.9 & 18.17. Schematic representation of the internal structure of the spinal cord. (A) Approximate position of nerve fibre tracts at the mid-cervical level. (B) Approximate position of nerve fibre tracts at the lumbar level. (C) Location of the corticospinal tracts, one of the major descending tracts of the spinal cord, starting in the motor cortex of the brain and ending in the sacral region of the spinal cord.

The gray matter is a butterfly-shaped structure located inside the white matter and has a high content of motor neurons. The gray matter is responsible for processing information coming from afferent neurons (sensory neurons) and transmitting it to the brain. The spinal cord gray matter is also responsible for direct actions in response to certain stimuli, such as reflexes in response to intense heat. The gray matter can be decomposed into several subregions: the left and right dorsal horns that connect with terminations of afferent neurons, and the left and right ventral horns, from which emerge spinal nerves that go into the PNS via spinal roots.

2.2 Diseases / injuries affecting the spinal cord

Various diseases and injuries can affect the spinal cord integrity, including neurodegenerative diseases, traumatic and non-traumatic spinal cord injuries and myelopathies. This section aims at providing a brief overview of these diseases, their causes and how the MRI community is exploring them.

2.2.1 Neurodegenerative diseases

Neurodegenerative diseases encompass all pathologies that affect the integrity of the CNS by touching the neurons and/or glial cells. The present section will focus on a subsample of these diseases, particularly on those affecting the spinal cord and that have been explored through this project, including Multiple Sclerosis (MS) and Amyotrophic Lateral Sclerosis (ALS).

MS is a chronic, inflammatory and demyelinating disorder of the central nervous system that can induce important disabilities in patients. MS affected an estimate of 2.3 million patients in 2013, making it the most common neurological disorder worldwide (Thompson & Baneke, 2014). While MS processes are not fully understood, it has been demonstrated that MS inflammation affects the sheaths of myelin that surrounds axons in the brain and spinal cord. However, the inflammation and demyelination can sometimes disappear as the CNS repairs itself and recover to a steady nervous condition. If the inflammation and demyelination mechanisms are faster than remyelination mechanisms, non-reversible damages can appear. The various phenotypes of MS can be separated into different groups, for example the Relapsing Remitting MS (RRMS) patients that show relapses of the diseases that appear and disappear over time, and Secondary Progressive MS (SPMS) that present a constant and non-reversible progression of disability (Compston & Coles, 2008). While MS diagnosis is usually performed on structural MR imaging of the brain,

several research groups have demonstrated the potential of measuring the spinal cord atrophy as a biomarker for MS progression (Losseff, Webb, O'Riordan, et al., 1996; Lundell et al., 2011; Mann, Constantinescu, & Tench, 2007). Moreover, analysis of MS lesions in the spinal cord (Figure 2.4) has been increasingly studied over the last few years (Evangelou, DeLuca, Owens, & Esiri, 2005; Filippi et al., 2000).

The Amyotrophic Lateral Sclerosis (ALS) disease is a neurodegenerative disease that affects the motor neurons in the brain and spinal cord, inducing a loss in the control of voluntary muscles. While one possible cause of ALS is genetic, the cause of most ALS cases is not known to date and its cure has not yet been found. However, several studies have explored the potential of MRI for the diagnosis and prognosis of ALS, particularly when looking at the spinal cord atrophy and features extracted from multiparametric MRI (Branco et al., 2014; Cohen-Adad, El Mendili, et al., 2011a).

2.2.2 Traumatic injury

Traumatic spinal cord injury (SCI) is a traumatic condition that affects primarily young adults usually after a traumatic accident. The most common mechanisms associated with SCI are compression, contusion, laceration, transection and traction of the spinal cord (Poon, Gupta, Shoichet, & Tator, 2007). Secondary mechanisms of the injury, such as edema, hemorrhage, ischemia and inflammation, can cause non-reversible damage to spinal cord nerves and induce import disabilities. Early diagnosis and surgery of SCI is usually recommended to minimize the impact of secondary SCI mechanisms on patients. Structural and multiparametric MRI have been largely used for the diagnosis and prognosis of SCI patients (Wheeler-Kingshott et al., 2014), as well as providing better understanding of internal mechanisms following the injury (Cohen-Adad, El Mendili, et al., 2011a).

2.2.3 Myelopathy

Degenerative Cervical Myelopathy (DCM) is a common degenerative disease that affects predominantly the elderly population and that causes the degeneration of intervertebral disks. As disk degeneration happens, mechanical stresses are induced on the ventral aspect of the spinal cord, resulting in the compression of spinal nerves and their degeneration (Figure 2.4). Conventional structural MRI is commonly used in clinical practice to diagnose DCM and recent advances in

multiparametric MRI (e.g., diffusion MRI, magnetization transfer, spectroscopy) have demonstrated a high potential for both diagnosis and prognosis of the disease (Martin et al., 2016).

Healthy Subject   Degenerative Cervical Myelopathy   Multiple Sclerosis
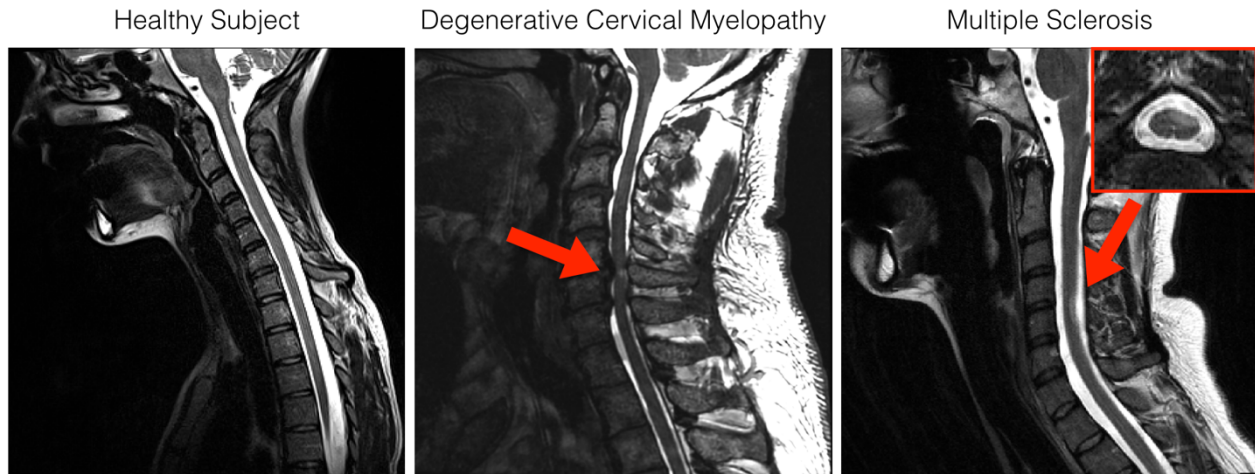
Figure 2.4: Example of T2-weighted images a healthy subject (left), a patient with Degenerative Cervical Myelopathy (middle) and a patient with Multiple Sclerosis (right). The right arrows highlight the spinal cord lesions.

2.3 Magnetic Resonance Imaging

Magnetic Resonance Imaging (MRI) is a non-invasive imaging modality widely used in both clinical and research practices. MRI principles are based on the nuclear magnetic resonance (NMR) phenomenon, which affects nuclei with an odd number of neutrons when placed in a strong constant magnetic field in one direction, and produces a magnetic precession around this direction (Z). In biological tissues, the most abundant atoms that are affected by the magnetic resonance phenomenon used in MRI are Hydrogen (^{1}H), as basic elements of water molecules. Inside a large static magnetic field (B_0), the Hydrogen spins precess around their nuclei at a rotational frequency called Larmor frequency, which depends on the strength of the magnetic field (ranging from 1.5 Tesla to 7 Tesla for human clinical scanners).

Tissue sampling is performed by exciting the Hydrogen atoms with a radiofrequency magnetic field B_1, applied perpendicularly to the constant magnetic field B_0. As the frequency of the B_1 field correspond to their resonance frequency, the Hydrogen spins will rotate towards the X-Y plane and make all the spins precess with the same phase. Once the B_1 field is turned off, the spins will relax in their stable state (aligned with Z) via two independent relaxation mechanisms that will dephase

the spins: the longitudinal (T1) and transverse (T2) relaxations. Both spins relaxations emit signals that can be acquired orthogonally to the B_0 and B_1 fields. These signals characteristics depend on tissue properties and evolve as exponentials with T1 and T2 time constants. Adjusting the MRI parameters (e.g., time of excitation, time between excitation and acquisition, time between two repetitions of MRI sequences) allows to obtain intensity contrasts between tissues. Spatial encoding of MR imaging is obtained by applying magnetic gradients along the three spatial directions, in order to excite only a small portion of the tissue sample (e.g., a voxel or a slice).

An important note on MRI acquisition is that the signal that is received by MR antennae after excitation depends on the MRI parameters of each MRI sequence. Therefore, the intensity in MRI images is *relative* and is not a direct (*absolute*) measure of tissue properties. Structural MRI (e.g., T1-, T2-, T2*-weighted images) aims at providing structural context in images by optimizing the contrast between tissues. Quantitative MRI (qMRI) proposes MRI acquisition protocols that would provide direct measures of tissue properties (e.g., T1- and T2-mapping). More broadly, multiparametric MRI (mpMRI) offers different types of MRI mechanisms to highlight specific properties of biological tissues. For example, diffusion MRI (dMRI) measures the diffusion properties of the tissue, while magnetization transfer (MT) focus on magnetization exchanges between tissue molecules. qMRI and mpMRI have demonstrated a great potential for the characterization of neurological damages, as many of the MRI acquisition protocols (dMRI, MT, T2*) has proven to be correlated with myelin content and are sensitive to neuron damage. Many of these MRI features have been explored for the assessment of spinal cord integrity (Martin et al., 2016).

2.4 Analysis of spinal cord MRI data

This section will critically review the literature of methods and algorithms for spinal cord MRI analysis, including a non-exhaustive listing of neuroimaging software, and a list of methods for detecting, segmenting and extracting information from the spinal cord in MRI images, including template-based analysis and morphometry analysis. At this point, the distinction between a *template* and an *atlas* should be made. As described in section 2.4.4, a *template* is defined as a normalized average image of multiple subjects or patients and is usually built using nonlinear registration/transformation. An *atlas* is also an image (or a series of images) that represent binary or probabilistic maps of tissue subregions, here the brain and the spinal cord.

2.4.1 Neuroimaging software

Over the last 20 years, numerous neuroimaging software have been developed, particularly for MR imaging. However, all these software were initially dedicated to brain imaging, hence were not adapted for spinal cord images. The following paragraphs provide a non-exhaustive list of neuroimaging software that were developed and can be used for MRI, with an interest in software that are used in spinal cord studies. I will specifically discuss the limitations of these software for spinal cord MRI, as well as their availability and usability for users, being either researcher or clinician. Most of these software are free to use and can be found on the Neuroimaging Informatics Tools and Resources Clearinghouse (NITRC).

FSL is a comprehensive library of analysis tools for functional, structural and diffusion MRI (Jenkinson, Beckmann, Behrens, Woolrich, & Smith, 2012a; Smith et al., 2004; Woolrich et al., 2009). FSL is dedicated for brain imaging and integrates tools for fMRI data analysis (FEAT, MELODIC, FABBER, BASIL, VERBENA), brain extraction (BET), brain segmentation/registration (FAST, FIRST), quantitative volume measurements (SIENA/X), linear intra- and inter-modal brain image registration (FLIRT), brain template registration (FNIRT), structural voxel-based analysis (FSLVBM), brain diffusion/tractography analysis (FDT, TBSS). FSL also integrates many algorithms for motion, eddy current and susceptibility artifacts correction (SUSAN, EDDY, TOPUP, FUGUE, MCFLIRT) and lots of basic image processing, utilitary and visualization tools (fsl_anat, FSLUtils, FSLView). FSL is available for any operating system as a command-line software and is easily installable. Some methods are provided with a graphical user interface (GUI) for easy use.

The Insight Segmentation and Registration Toolkit (ITK) is an open-source C++ library that provides an extensive suite of algorithms for segmentation and registration of digital images (McCormick, Liu, Jomier, Marion, & Ibanez, 2014). Among all ITK's algorithm, we can note advanced image processing methods, such as denoising, fast marching and image fusion, image segmentation algorithms, such as level sets, deformable models, watershed and classifiers, and various image registration methods. ITK follows a developer-based approach and is cross-platform, meaning it can be compiled, installed and used on any operating system. While ITK is developed in C++, it provides wrappers to many languages such as Python and Java. As an object-oriented C++ library, ITK can be difficult to use and is not suited for direct use by non-experienced users.

A simpler version of ITK has been released recently, SimpleITK (Lowekamp, Chen, Ibáñez, & Blezek, 2013). SimpleITK was designed to provide an easy to use interface to ITK's algorithms. Many applications/software were developed based on ITK, such as ITK-SNAP, a free software dedicated to semi-automated medical image segmentation (Yushkevich et al., 2006).

The Medical Imaging Interaction Toolkit (MITK) is a free open-source software for the development of interactive medical image processing methods. MITK is a C++ library based on ITK and the Visualization Toolkit (VTK) (Schroeder, Martin, & Lorensen, 2006) and integrates many image processing algorithms dedicated to medical images, including structural and diffusion MRI. MITK also provides a powerful GUI, called MITK Workbench, that has complimentary features with FSLview.

MeVisLab (http://www.mevislab.de/) is a free, modular and object-oriented framework for image processing with a special focus on medical images (Ritter et al., 2011). This software integrates segmentation, registration, volumetry, as well as quantitative morphological and functional analysis.

FreeSurfer is an open-source and automatic software for processing and analyzing MRI data of the human brain (Fischl, 2012). FreeSurfer includes skullstripping, registration, subcortical and cortical segmentation, cortical surface reconstruction, cortical thickness estimation, fMRI analysis tools, tractography, and visualization GUI.

The Advanced Normalization Tools (ANTs) are another example of software based on the ITK library (Avants et al., 2014; Avants, Tustison, & Song, 2009). ANTs is a C++ command-line software that provides methods for medical image segmentation and registration, including a vast variety of image transformation (diffeomorphic, elastic, etc.), as well as many tools for multidimensional medical image processing. Particularly, the symmetric diffeomorphic registration model, SyN (Avants, Epstein, Grossman, & Gee, 2008), and its regularized equivalent, BSplineSyN (Tustison & Avants, 2013), are two registration models that have proven good results for small and large-scale deformation (Klein et al., 2009), both important for spinal cord registration.

The MINC tools (http://www.bic.mni.mcgill.ca/ServicesSoftware/MINC) provide a proprietary file format adapted for medical images and various image processing applications, including geometric distortion correction, intensity normalization, image registration algorithms and

segmentation tools for brain images. MINC also contains methods for statistical analysis, classification and visualization (MincView). The MINC package can be compiled on any operating system as a C++ binaries.

Unfortunately, none of the software described above integrate neither image processing methods dedicated to spinal cord MRI or spinal cord MRI template. However, many of them include tools and methods that are relevant for processing and analyzing spinal cord MRI data, especially the image registration methods from ANTs, image segmentation methods from ITK and visualization capabilities of FSL. Other software exist that implement methods dedicated for spinal cord MRI.

The Java Image Science Toolkit (JIST) is a free Java-based image processing environment (Lucas et al., 2010) similar to ITK/VTK frameworks and provides many tools for medical image processing and analysis. Particularly, JIST integrates a multi-atlas segmentation method dedicated to the segmentation of spinal cord internal structure (Asman, Bryan, Smith, Reich, & Landman, 2014) as well as a template-based automatic spinal cord segmentation method (Chen et al., 2013). By its Java's nature, JIST is directly compatible for any operating system and is easily installable.

Jim is also a Java-based software that provides a semi-automatic spinal cord segmentation and atrophy assessment (Horsfield et al., 2010), along with many medical image processing tools (http://www.xinapse.com/features/). However, Jim is not free-to-use and therefore not affordable to all users.

SpineSeg is a free software providing a semi-automatic method for segmenting the spinal cord (Bergo, França, Chevis, & Cendes, 2012). SpineSeg is available for Unix systems. Spinalfmri8 is a free software for processing and analysis of functional MRI data of the cervical spinal cord and brainstem (http://post.queensu.ca/~stromanp/software.html). This software includes a structural template of the human spinal cord and semi-automatic method to register new subjects on this template. It works for sagittal MR images.

Nifty Tools (http://cmictig.cs.ucl.ac.uk/research/software/software-nifty) are a suite of open-source software package for segmentation (NiftySeg) and registration (NiftyReg) of brain and spinal cord MRI data, including recent algorithms for segmenting the spinal cord gray matter (Prados et al., 2016).

2.4.2 Article 1: Segmentation of the human spinal cord

This article presents a critical review of the literature on method dedicated to the segmentation of the human spinal cord structure as well as the spinal cord white and gray matter sub-structures from MRI images. The manuscript also presents applications of such algorithms on patients' populations. My contribution (60%) included the design of the literature review, research and critical review of spinal cord segmentation methods and the redaction of the paper.

This manuscript has been published in Magnetic Resonance Materials in Physics, Biology and Medicine (MAGMA) on April 2016, Volume 29, Issue 2, pp 125–153.

Title: Segmentation of the human spinal cord

Authors:

Benjamin De Leener [1,2], Manuel Taso [3-5], Julien Cohen-Adad [1,2], Virginie Callot [4,5]

Affiliations:

[1] Neuroimaging Research Laboratory (NeuroPoly), Institute of Biomedical Engineering, Polytechnique Montreal, Montréal, QC, Canada

[2] Functional Neuroimaging Unit, CRIUGM, Université de Montréal, Montreal, QC, Canada

[3] Aix-Marseille Université, IFSTTAR, LBA UMR T 24, Marseille, France

[4] Centre de Résonance Magnétique Biologique et Médicale (CRMBM), UMR 7339, Aix-Marseille Université, CNRS, Marseille, France

[5] Centre d'Exploration Métabolique par Résonance Magnétique (CEMEREM), AP-HM, Hôpital de la Timone, Pôle d'imagerie médicale, Marseille, France

2.4.2.1 Abstract

Segmenting the spinal cord contour is a necessary step for quantifying spinal cord atrophy in various diseases. Delineating gray matter (GM) and white matter (WM) is also useful for quantifying GM atrophy or for extracting multi-parametric MRI metrics into specific WM tracts.

Spinal cord segmentation in clinical research is not as developed as brain segmentation, however with the substantial improvement of MR sequences adapted to spinal cord MR investigations, the field of spinal cord MR segmentation has advanced greatly within the last decade. Segmentation techniques with variable accuracy and degree of complexity have been developed and reported in the literature. In this paper we review some of the existing methods for cord and WM/GM segmentation, including intensity-based, surface-based and image-based methods. We also provide recommendations for validating spinal cord segmentation techniques, as it is important to understand the intrinsic characteristics of the methods and to evaluate their performance and limitations. Lastly, we illustrate some applications in the healthy and pathological spinal cord.

One conclusion of this review is that robust and automatic segmentation is clinically relevant as it would allow for longitudinal and group studies free from user bias, as well as reproducible multi-centric studies in large populations, thereby helping to further our understanding of the spinal cord pathophysiology and to develop new criteria for early detection of subclinical evolution for prognosis prediction and for patient management.

An other conclusion is that at the present time, no single method adequately segments the cord and its substructure in all the cases encountered (abnormal intensities, loss of contrast, deformation of the cord, etc.). A combination of different approaches is thus advised for future developments, along with the introduction of probabilistic shape models. Maturation of standardized frameworks, multiplatform availability, inclusion in large suite and data sharing would also ultimately benefit to the community.

Key-words: spinal cord, segmentation, white matter, gray matter, MRI

2.4.2.2 Introduction

The human spinal cord (Figure 2.5 and Figure 2.6) is a highly organized and complex part of the central nervous system whose function is to ensure the conduction of the neural signals from the brain to the peripheral nervous system (motor information) and from the peripheral nervous system to the brain (sensory information). Schematically, this information transits through myelinated motor and sensory axons contained in white matter (WM), and is relayed and controlled by spinal interneurons mostly located in gray matter (GM) (Figure 2.5c-e). The spinal cord GM also contains intrinsic neuronal circuits that are responsible for maintaining specialized functions such as the locomotion.

Damage to these spinal cord components through motor neuron degeneration such as encountered in amyotrophic lateral sclerosis (ALS) or WM bundle demyelination and degeneration induced by neurodegenerative diseases (multiple sclerosis (MS), neuromyelitis optica (NMO), etc.) or spinal cord trauma, may severely impact spinal cord function and lead to different symptoms, including loss of coordination, loss of sensation, pain, and/or paralysis. Clinical disability has been shown to correlate with cord atrophy caused by axon or neuron degeneration. Moreover, both the severity of the symptoms and the prognosis for functional recovery are highly dependent on the localization and the extent of the tissue impairment. Our ability to assess and characterize such microstructural damage is therefore clinically relevant and MRI is among the recommended methods for this purpose due to its non-invasiveness and sensitivity to parenchymal tissue.

Spinal cord MRI has long been technically challenging by the small dimensions of the cord (cf. Figure 2.6e), susceptibility artifacts from surrounding vertebral structures and cerebrospinal fluid (CSF) pulsatility. However, improvements in hardware and pulse sequences (e.g., highly parallelized coils, reduced field of view with outer volume suppression, parallel imaging, 2D radiofrequency excitation, localized shimming, cardiac gating, etc.) (Stroman et al., 2014) during the last decade have meant progress in tackling these issues and opened new horizons for spinal cord anatomy, structure and function analyses (Wheeler-Kingshott et al., 2014).
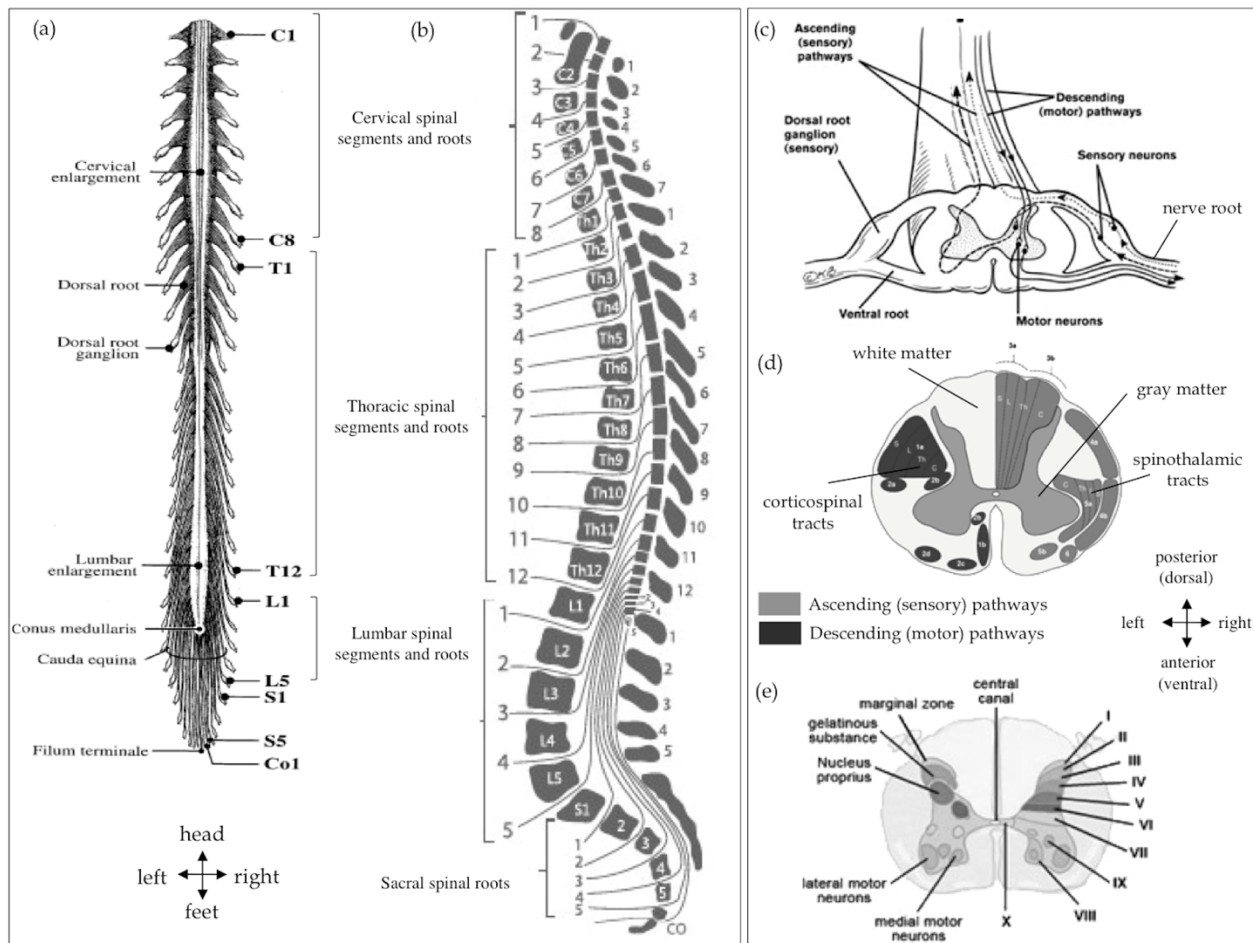
Figure 2.5: (a) Schematic coronal representation of the cord, with spinal cord segment labeling (C1 to C8, T1 to T12, etc.) and representation of the cross sectional area variation (cervical and lumbar enlargements are associated with nerves for the upper and lower limbs). (b) Schematic view of the vertebral (C1-C7, T1-T12, etc.) and spinal cord levels (C1-C8, T1-T12, etc.) in the sagittal plane. The discrepancy of the levels, more pronounced in the lower spinal cord, is due to different duration of growth. This difference requires specific attention when correlating advanced imaging data and neuroanatomic origin, e.g. in fMRI studies. In such cases, the nerve rootlet and vertebral body distributions should be accounted for (Cadotte et al., 2015). (c-e) Schematic cross-sectional representations of the cord and its WM/GM substructures: (c) Neural signals transit through ascending and descending pathways and are then carried to or from the body through the nerve roots. (d) The WM consists of myelinated motor (e.g. corticospinal) and sensory (e.g. spinothalamic) axons grouped into tracts. WM is conventionally divided into dorsal, lateral and ventral funiculi. (e) The GM can be divided into dorsal, intermediate and ventral horns. GM is composed of 10 laminae and is made up dendrites, axons, glial cells and neuronal cell bodies

organized into functional clusters called nuclei. The cord is protected by three membranes called the spinal meninges (pia, arachnoid and dura matters from inner to outer), not represented here and usually not visible on MR images. Modified from (Altman & Bayer, 2001), (Wikipedia, the free encyclopedia, 2017), and (Dubuc, 2015).

2.4.2.2.1 Spinal cord segmentation

Data processing, and more particularly spinal cord segmentation, have consequently become a necessary step towards robust and automated interpretation of morphometric and multi-parametric MR images (mp-MRI). Historically, the main motivation for spinal cord segmentation has been to obtain cross-sectional area (CSA) measurement for quantitative assessment of disease progression and therapeutic monitoring in MS (Losseff, Webb, O'Riordan, et al., 1996).

Segmentation can also be used for co-registration and spatial normalization to a common coordinate space (i.e., template), which can be used to quantify morphometric changes or to perform atlas-based quantitative multi-parametric analyses (DTI, MT, fMRI, etc.) in order to investigate the structural and functional integrity of the spinal cord. More generally, automatic or semi-automatic spinal cord and WM/GM segmentation has great potential for longitudinal and group studies because manual delineation is time consuming and prone to inter- or intra-operator variability.

Compared to brain segmentation, which is widely used for analyzing different brain structures, for delineating lesions or for surgical planning (Despotović, Goossens, & Philips, 2015), the use of spinal cord segmentation in clinical research is however lagging behind.

2.4.2.2.2 Spinal cord segmentation challenges

Despite the apparently simplistic shape of the spinal cord, its segmentation can be complicated by inconsistent surrounding tissue intensities, image artifacts and pathology-induced changes in the image contrast.

The cord can be defined as an ellipsoid in the cross sectional plane with its first axis aligned with the left-right direction. This shape is not consistent however, as the ratio of the first and second radii can change along the rostro-caudal direction and can differ between subjects. The spinal cord generally presents a substantial intensity gradient with the surrounding CSF (cf. Figure 2.6d) in multiple contrasts (T_1, T_2, T_2^*) (Figure 2), which facilitates cord/CSF delineation. However, the

cord has a natural curvature from head to feet and can sometimes touch the wall of the spinal canal (cf. Figure 2.6c), thus leading to confounding contrast between the cord and its surroundings. Similarly, spinal canal narrowing, induced for example by the presence of osteophytes (cf. Figure 2.7a), may alter CSF circulation, erasing the usual cord/CSF/vertebra intensity gradients.

MR images not degraded by subject motion may also be corrupted by CSF flow artifacts (resulting in areas of hyperintensity or signal voids), Gibbs artifacts (ringing lines parallel to large intensity gradients in the image), static noise, signal loss due to B_1^- inhomogeneities, or contrast alterations due to B_1^+ inhomogeneities. Partial volume effects (PVE) may also be prominent due to the large fraction of voxels in the cord cross-section that have signal contributions from the surrounding CSF and dura mater. PVE is exacerbated when the image slice is not orthogonal to the spinal cord axis, especially when the voxels have non-isotropic resolution. The appearance of cord boundaries may also be affected by the signal attenuation induced by the short T_2 relaxation time of the dura matter (Fujimoto et al., 2014) as compared to the cord.

Regarding WM/GM segmentation, difficulties arise from the need for sub-millimetric resolution and from the poor contrast between WM and GM. Relaxation times are indeed relatively similar: about 870/970 ms for T_1 and 73/76 ms for T_2 at 3T, in the spinal cord WM and GM respectively (Smith, Edden, Farrell, Barker, & Van Zijl, 2008). No known study reported T_2* values in the spinal cord WM and GM specifically, however values in the brain at 3T are 53 and 66 ms in the WM and GM respectively (Peters et al., 2007).

Segmentation techniques adapted to the contrast arising from manifestation of the above properties in MR images may however perform sub-optimally in the presence of pathological hyperintense signal or cord deformation, such as encountered in MS, ALS, myelopathy or trauma (fig. 3).
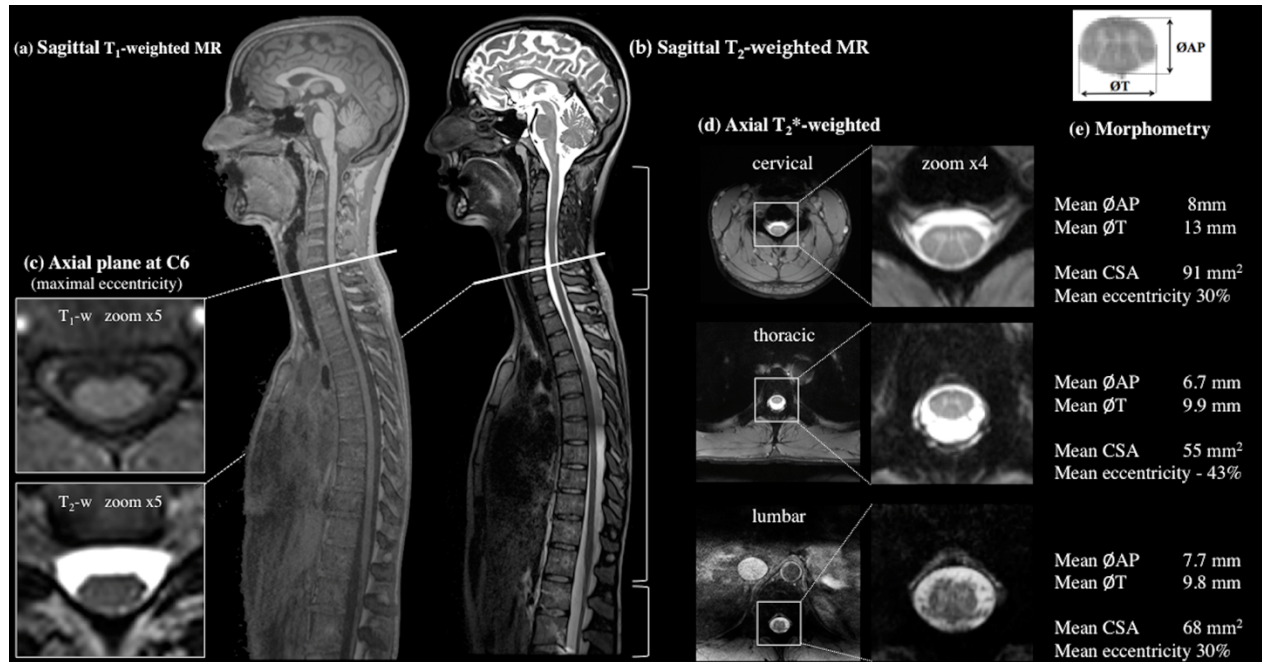
Figure 2.6: Sagittal and transverse MR images of the spinal cord acquired with T_1 (a), T_2 (b) and T_2*-weightings (d). (a, b) The spinal cord presents as a long, thin and cylindrical structure that extends from the medulla oblongata to the first or second lumbar vertebrae. The cord is surrounded by CSF (cerebrospinal fluid) presenting lower (resp. higher) signal intensity than the cord in T_1-w (resp. T_2-w) images. The global curvature of the spine (lordosis or convex anterior in the cervical region and kyphosis or concave anterior in the thoracic region) leads to eccentricity of the spinal cord within the spinal canal. (c) T_1 and T_2-weighted cross sectional images of the cord at the C6 vertebral level – (i) Eccentricity of the cord within the canal may limit CSF circulation around the cord. (ii) Absence of contrast on both T_1 and T_2-w images preclude delineation of the WM/GM structures. (d) Transverse T_2*-weighted images with characteristic GM butterfly-shape, at cervical, thoracic and lumbar levels, along with (e) mean morphometric measurements (transverse and antero-posterior diameters, CSA, and eccentricity of the cord within the spinal canal (Fradet, Arnoux, Ranjeva, Petit, & Callot, 2014)).
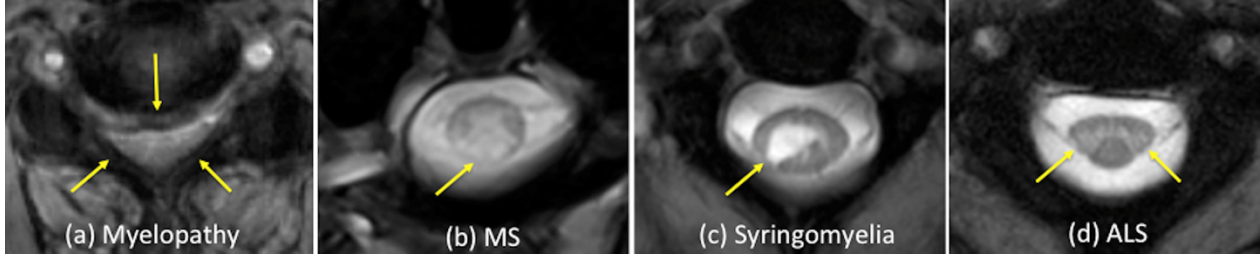
Figure 2.7: Typical cord deformation and hypersignal encountered in pathological spinal cord (yellow arrows indicate abnormal areas).

2.4.2.2.3 Objectives of the paper

The goal of this review is to provide an overview of segmentation methods for the human spinal cord that have been published or presented in scientific meetings. First, we present some general considerations about MRI acquisition and validation of segmentation algorithms. Then, we classify techniques for spinal cord and WM/GM segmentation according to their segmentation mechanisms (intensity-based, energy minimization, etc.), and we describe their level of automaticity, accuracy, regularization and availability/implementation in software. Finally, we illustrate applications of spinal cord segmentation methods in pathologies and discuss perspectives for developing new algorithms.

2.4.2.3   General considerations

2.4.2.3.1 MRI Acquisition

The most fundamental requirement for spinal cord segmentation is good cord/CSF contrast. People typically use a 3D T_1-weighted MPRAGE sequence with inversion recovery to suppress CSF signal (bright cord, dark CSF), or a 3D T_2-weighted fast spin echo sequence (dark cord, bright CSF). Others have shown that the Phase Sensitive Inversion Recovery (PSIR) sequence also provides good segmentation results (Kearney et al., 2014; Papinutto et al., 2015). Recently, the MP2RAGE sequence has been shown to yield good results in brain cortical segmentation thanks to the inherent homogeneous tissue contrast due to the normalization (Marques et al., 2010) and should therefore be a good candidate for spinal cord segmentation as well. A typical resolution is 1mm isotropic to minimize the potential for bias caused by PVE when the cord is not perfectly orthogonal to the slice.

For WM/GM segmentation, it is recommended to acquire 2D GRE T_2* data as it provides good WM/GM contrast, and high in-plane resolution (0.5x0.5 mm^2) with large slice thickness (3-5 mm) for good delineation of internal structure while keeping sufficient signal-to-noise ratio (SNR). The use of multiple averaged echoes (multi echo data image combination, MEDIC (Held, Dorenbeck, Seitz, Fründ, & Albrich, 2003)) can improve SNR (with early echoes, ~5ms) while increasing WM/GM contrast at higher echoes (>20ms at 3T).

2.4.2.3.2 Preprocessing steps

Some preprocessing steps may be performed before segmentation. Among them:

- Bias field correction, which corrects for the smooth signal intensity variation induced by the B_1^+ (excitation) and B_1^- (reception) inhomogeneities. N3/N4 algorithms (Sled, Zijdenbos, & Evans, 1998) can be used to improve the performance of intensity-based segmentation methods,

- Denoising, using a Gaussian or non-local mean filter (Buades, Coll, & Morel, 2005), which helps reduce noise and enhance image clarity,

- Field-of-view (FOV) cropping, which is required by some algorithms to ensure that the spinal cord is centered in the image, or

- Preliminary image registration (e.g. rigid transformation to align center of mass of a target image to a model space), which may be used for initializing spinal cord segmentation algorithms.

2.4.2.3.3 Evaluation of segmentation techniques / validation methods

Every time a segmentation technique is introduced its performance should be evaluated against gold standard techniques (e.g., manual segmentation or state-of-the-art methods) using metrics that quantify global and/or local errors (see below, *overlap-based and distance-based metrics*). Cross-sectional area or cord volume is often considered for the validation. The computational performance can also be reported.

2.4.2.3.3.1 Overlap-based metrics

The false positive (FP), false negative (FN), true positive (TP) and true negative (TN) counts can be generated, along with sensitivity (TP/(TP+TN), the fraction of cord voxels that are correctly segmented and specificity (TN/(TN+FP), the fraction of non-cord voxels that are correctly detected.

In practice, the agreement between two segmentations is evaluated using the Dice (D) similarity index, which is defined as:

$$D = \frac{2N(A \cap B)}{N(A) + N(B)}$$

with *N(A)* being the number of pixels in the structure obtained with the reference segmentation (A), *N(B)* the number of pixels in the structure obtained with the technique (B) being evaluated, and (**A** ∩ **B**) the intersection between the structures. Dice index ranges from 0 (no overlap between the two segmentations) to 1 (both segmentations are identical). Alternatively, some authors report the Jaccard index, which is a measure of overlap and is defined as:

$$J = \frac{N(A \cap B)}{N(A \cup B)}$$

with N(A ∪ B) the union between both structures. These global metrics give useful summary measure of spatial overlap (misclassified or correctly classified), however they depend on the size of the object and they do not account for the distance errors to the ideal segmentation.

2.4.2.3.3.2 Distance-based metrics

To account for global and local distance errors (Aspert, Santa Cruz, & Ebrahimi, 2002) one can calculate the mean surface distance error (MSDE) between the surface S given by the segmentation method to evaluate, and the reference surface (S_{ref}). MSDE is defined as:

$$MSDE = \frac{1}{2} \left[\bar{d}(S, Sref) + \bar{d}(Sref, S) \right]$$

with $\bar{d}(S, Sref)$ being the mean of distances between every surface voxel in S and the closest surface voxel in S_{ref}, while $\bar{d}(Sref, S)$ is computed in a similar way.

The bi-directional Hausdorff distance error (HDE) can also be calculated, and measures the local maximum distance between the two surfaces S and S_{ref}:

$$HDE = max(max(d(S,S_{ref}), max(d(S_{ref}, S))$$

2.4.2.3.3.3   Recommendations

An accurate validation should be performed by comparing the segmentation outcome of the proposed method to manual or state-of-the-art segmentation methods, through DICE, MSDE, and HDE measurements so as to reflect both global and local errors. Validation should be performed both in 3D and slice by slice, on a sufficiently large number of dataset.

Validation data should of course be different than that used for creating segmentation algorithms (in case of dictionary-based methods).

It is worth noting that validations based on manual segmentation should be critically considered since they are subjective and prone to errors. The manual segmentation should therefore first be evaluated to estimate (i) intra-observer (repeated manual segmentation of the same dataset by the same rater), (ii) inter-observer (segmentation of the same dataset by different raters) and (iii) scan-rescan reproducibilities (segmentation of data acquired on the same subjects on separate occasions), which can be assessed by calculating the coefficients of variation (COV) and/or the intra-class correlation coefficients (ICC).

Note that when a set of expert segmentations is available for the reference segmentation, a voting rule can be used to select the voxels where the majority of experts agree on the structure. More representative, classifiers that compute a probabilistic estimate of the true segmentation and a measure of the performance level represented by each segmentation are now largely used (e.g. STAPLE, Simultaneous Truth and Performance Level Estimation [15]).

2.4.2.4   Segmentation methods

Segmentation methods provide either a set of contours/surfaces that describe the region boundaries of the object of interest (e.g. the edges of the spinal cord) or an image of labels identifying homogeneous regions (e.g. white matter and gray matter). Image segmentation can be performed on 2D or 3D images and can be done entirely manually, semi-automatically (requiring only a few manual interventions) or fully automatically. Segmentation performance will depend on the characteristics of the object to be segmented: shape, edge contrast, noise, and signal homogeneity, and can be improved by incorporating probabilistic prior shape models.

Segmentation methods can be categorized into fives classes: (i) threshold-based methods, (ii) edge-detection-based methods, (iii) region-based methods (e.g., region growing, split&merge), (iv) watershed methods, and (v) energy minimization methods. The long and flexible tubular shape of the spinal cord and its close proximity to multiple anatomical structures make accurate and automatic segmentation of the spinal cord challenging. Most of the existing segmentation methods for the spinal cord can therefore be considered as "high-level" and categorized as follows (also see Figure 2.8):

1. Intensity-based segmentation methods, including threshold-based, edge detection and region-based algorithms;

2. Surface-based segmentation methods, including energy minimization-based algorithms such as active contours/surfaces, deformable models, active shape/appearance model and level-set methods;

3. Image-based segmentation methods, including graph-cut and watershed methods as well as template/atlas deformation methods.

In the following section, cord segmentation methods will first be presented, followed by methods dedicated to WM/GM segmentation. Table 2.1 summarizes the main publications related to cord/CSF and WM/GM segmentation along with their principal characteristics (algorithm, automatic/semi-automatic, 2D/3D, etc.).
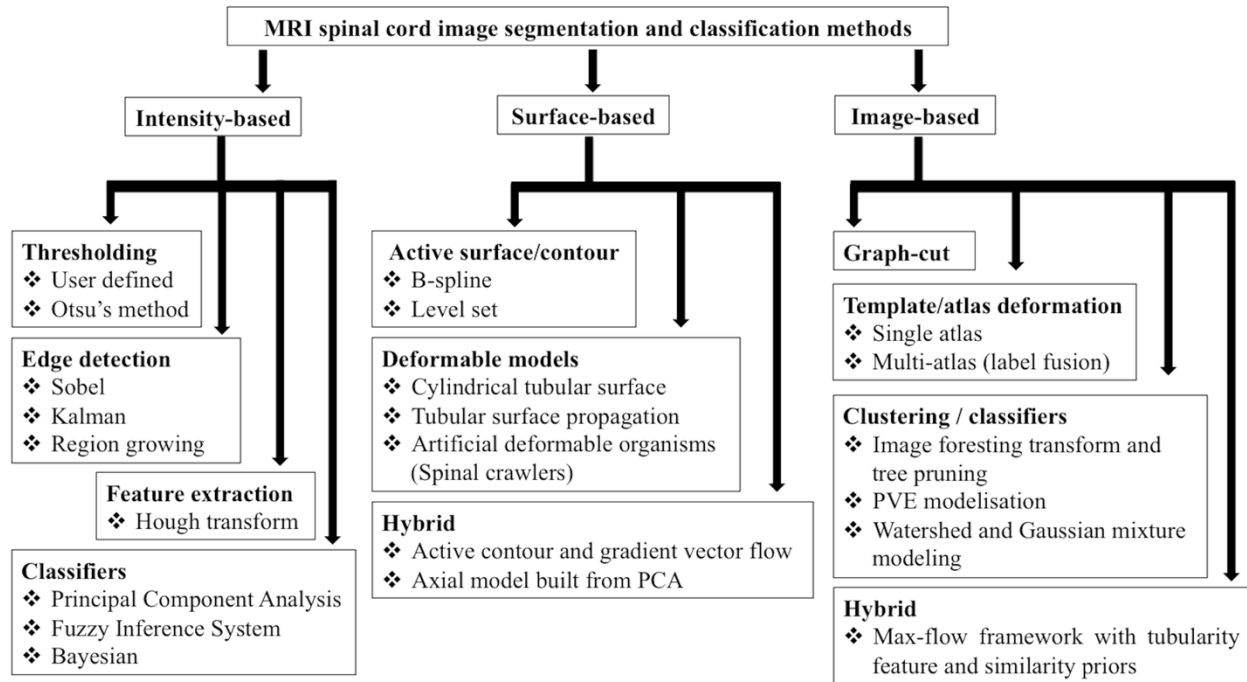
Figure 2.8: Classification of MRI spinal cord segmentation methods

Table 2.1: Human spinal cord segmentation methods. (*) Segmentation done on 2D slices and propagated to 3D...

Authors	Auto / semi-auto	Initialization	Methods / Mathematics	2D / 3D	Images / contrast	Population
CORD SEGMENTATION						
Methods based on mathematical morphology, edge detection and region growing						
Losseff et al. (1996)	Semi-auto	ROI + seed point	Intensity-based thresholding and region-growing segmentation	2D	T1-like (FSPGR)	HC, MS
Behrens et al. (2003)	Semi-auto	Multiple points	Hough transform + Kalman filter	3D	T1w	HC
Tench et al. (2005)	Semi-auto	ROI + seed point	Edge detection + PV correction	2D	T1w	HC
Zivadinov et al. (2008)	Semi-auto	Identification of edges	Edge detection	2D	T1w, T2w	HC, MS
El Mendili et al. (2015)	Semi-auto	ROI	Double-thresholding	2D→3D (*)	T2w	HC, ALS, SMA, SCI
Methods based on energy minimization: active contours / surfaces						
Coulon et al. (2002)	Semi-auto	Points along spinal cord	B-splines active surface	3D	T1-like (IR-FSPGR)	HC, MS
McIntosh et al. (2006)	Semi-auto	Two points	Spinal crawlers (artificial organisms)	3D	T1w	HC, MS
Van Uitert et al. (2006)	Semi-auto	Points along spinal cord	Level-set + morphological filtering	2D	T1-like (FIESTA)	HC
Sonkova et al. (2008)	Semi-auto	ROI	Level-set	2D→3D	T1-like (IR-FSPGR)	HC, MS
Horsfield et al. (2010)	Semi-auto	Points along spinal cord	Active Surface (rays refinement)	3D	T1w, T2w	HC, MS
Koh et al. (2010)	Auto	Assumed ROI	Active contour	2D	T2w	CAD
Koh et al. (2011)	Auto	Assumed ROI	Saliency map + level-set segmentation	2D	T2w	CAD
Kawahara et al. (2013-ISBI)	Semi-auto	Two points	Minimal path and ACP of axial slices	3D	T1w	HC, MS
Kawahara et al. (2013-MLMI)	Semi-auto	Two points	Same + auto-contextualization	3D	T1w	HC, MS
Law et al. (2013)	Semi-auto	Two points	Gradient competition descriptor with orientation coherence + intensity classification	3D	T1w, T2w	HC

De Leener et al. (2014)	Auto		Propagation of a deformable model	3D	T1w, T2w, T2*w	HC
Methods based on energy minimization: image-based methods (atlas, template, graph-cut, watershed)						
Carbonell-Caballero et al. (2006)	Auto	Template	PVE modelisation	2D	T2w	HC, MS
Stroman et al. (2008)	Semi-auto	Template	Spatial normalization	3D	T2w	HC
Bergo et al. (2012)	Semi-auto	Points along spinal cord	Tree pruning on morphological gradients	2D→3D	T1w	HC, FrAt, MJD
Kayal et al. (2013)	Semi-auto	Several points	Graph cut	2D	T1w, T2w, FA (DTI)	HC, SCI
Chen et al. (2013)	Auto		Atlas registration with topology constraint		T1w, T2*w	HC, MS
Pezold et al. (2013)	Semi-auto	Mask and several points	Graph cut	3D	T1w	HC, MS
Yen et al. (2013)	Semi-auto	Set of points	3D random walker	3D	STIR	
Fonov et al. (2014)	Semi-auto	Points along spinal cord	Graph-cut	2D	T2w	HC
Weiler et al. (2015)	Semi-auto	Two points	Watershed + tissue classification based on intensity-distribution Gaussian mixture modelling	3D	T1w	HC, MS
Pezold et al. (2015)	Auto		Continuous max-flow with cross-sectional similarity prior	3D	T1w	HC, MS
WM/GM SEGMENTATION						
Methods based on mathematical morphology (classification)						
Ellingson et al. (2007)	Semi-auto	Histological template	Fuzzy classification	2D	DTI	HC
Yiannakas et al. (2012)	Semi-auto	Manual seed	Fuzzy connector	2D	T2*	HC
Tang et al. (2013)	Auto		Multi-channel feature extraction + Bayesian classifier	2D	DTI	HC, MS, NMO
Methods based on energy minimization: image-based methods (atlas, template, graph-cut, watershed)						
Asman et al. (2014)	Auto		Multi-atlas label fusion	2D	T2*	HC
De Leener et al. (2015)	Auto	Pre-segmentation	Single-atlas deformation	2D	T2 + T2*w	HC
Taso et al. (2015)	Auto	SC segmentation	Template deformation	2D	T2*	HC

2.4.2.4.1 Cord segmentation

2.4.2.4.1.1   Intensity-based segmentation methods

To the best of our knowledge, the first robust and semi-automatic spinal cord segmentation method was introduced by (Losseff, Webb, O'Riordan, et al., 1996). The authors suggested an intensity-based segmentation approach based on a semi-automatic mean intensity estimation of the cord tissue and its surrounding CSF. Two ROIs are manually drawn in an axial slice of the spinal cord: the first within the cord ('inner') and the second outside the cord but within the spinal canal ('outer'). The mean cord signal intensity (SI) is directly calculated as the mean intensity in the 'inner' ROI. The mean CSF SI is computed as the following:

$$mean\ CSF\ intensity\ = \frac{(mean\ SI\ outer \times area\ outer) - (mean\ SI\ inner \times area\ inner)}{(area\ outer - area\ inner)}$$

Then, the mean of the cord and CSF SIs defines the intensity of their interface. Based on a seed point provided by the user, a region-growing method robustly segments the spinal cord. The authors have extensively validated their method on healthy controls (n=30) and patients with MS (n=60) by computing the average CSA on FSPGR MR images. Since its publication, this segmentation algorithm has been used by many groups for diverse clinical applications and is still considered as the state-of-the-art technique for spinal cord segmentation.

Later, Tench *et al.* (Tench, Morgan, & Constantinescu, 2005) demonstrated the necessity of correcting measurements of CSAs for partial volume effect. They have proposed a semi-automatic segmentation method based on Sobel edge detection on 2D axial slices. CSA is then corrected by taking into account the orientation of the spinal cord and PVE with the CSF. Losseff *et al.* and Tench *et al.* have validated their algorithms on synthetic phantoms (cylindrical acrylic resin plastic rods of known dimensions); such validation does not appear to have been performed by other groups.

Recently, El Mendili *et al.* (2015) (El Mendili, Chen, Tiret, Villard, et al., 2015) have developed a semi-automated double threshold-based segmentation method (DTbM) (cf. Figure 2.9). First, DTbM extracts rough segmentations of spinal cord and CSF regions on 2D axial slices using Otsu's thresholding (first threshold), morphological mathematics and flood-fill algorithms. Then, these segmentations are used as input for the threshold-based method proposed by Losseff *et al.* (second

threshold) in order to obtain an accurate segmentation of the spinal cord. The authors have validated their algorithm against manual segmentations on 82 healthy subjects and 30 patients with various SC disease/injury (ALS, SMA and SCI) and compared the results with the *Active Shape Model* (ASM) method from Horsfield *et al.* (2010) (see surface-based segmentation methods section). Results have demonstrated higher accuracy compared to the existing methods on both healthy controls and patients.
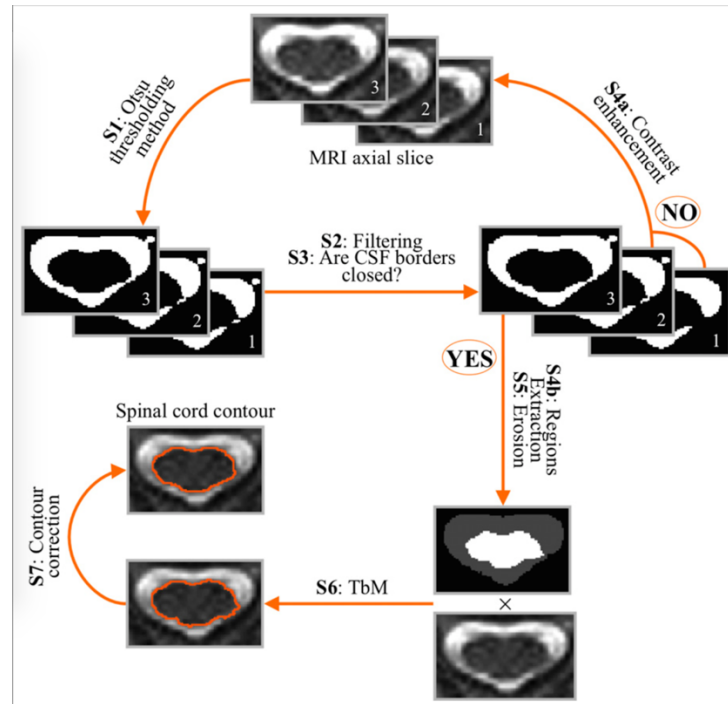
Figure 2.9: Overview of DTbM algorithm, from (El Mendili, Chen, Tiret, Villard, et al., 2015).

Meanwhile, Behrens *et al.* (2003) (Behrens, Rohr, & Stiehl, 2003) have developed a generalized algorithm that can segment tubular structures in MRI volumes by using randomized Hough transform coupled with Kalman filtering. Despite a successful application on synthetic and real data of spinal cord MRI, this method has an important computational cost due to repeated calculation of Hough transform.

Zivadinov *et al.* (2008) (Zivadinov et al., 2008) developed a semi-automated segmentation method in order to compare three different measurements of atrophy on a MS population: cervical cord absolute volume (CCAV), cervical cord fraction (CCF) = CCAV/thecal sac absolute volume, and cervical cord to intracranial volume (ICV) fraction (CCAV/ICV). First, an edge-detection technique extracts spinal cord boundaries from a cervical MRI volume and Gaussian smoothing

followed by Sobel filtering are applied to generate gradient magnitude and direction maps. Second, noise and non-maximal image intensity suppression is used to trace and automatically connect edges in the image. Finally, the user selects the set of edges that correspond to the spinal cord. The authors have validated their method on 66 MS patients and 19 healthy controls and have demonstrated high reproducibility of atrophy measures (scan-rescan, intra-rater and inter-raters). To our knowledge, Zivadinov *et al.* were the first to validate a spinal cord segmentation method on different MRI contrasts (T_1- and T_2-weighted).

2.4.2.4.1.2   Surface-based segmentation methods

Coulon *et al.* (2002) (Coulon et al., 2002) appear to have been the first to develop a spinal cord segmentation method for MR images based on an active surface. Based on several points located along the centerline of the spinal cord and selected by the user, a B-spline cylindrical surface is generated around the spinal cord. The surface is then deformed to fit the cord edges by minimizing a gradient and Laplacien-based energy equation, along with regularization to avoid aberrant segmentation in presence of noise or the lack of CSF. This method can measure CSA and cord volume while directly taking into account the spinal cord orientation and PVE.

Several years later, Horsfield *et al.* (2010) (Horsfield et al., 2010) developed a similar approach, deforming a cylindrical tubular surface built from manually-identified points distributed along the spinal cord (cf. Figure 2.10). The segmentation is computed by iteratively refining individual radii from the tubular surface towards high image gradients while constraining deformation with a smoothness regularization. The convergence is reached when no radius change anymore. Because the surface definition is computationally lighter than the B-spline model, this approach for spinal cord segmentation is faster. Horsfield *et al.* have assessed the accuracy and reproducibility of their segmentation method on T_1- and T_2-weighted volumes from 20 healthy subjects and 40 MS patients.
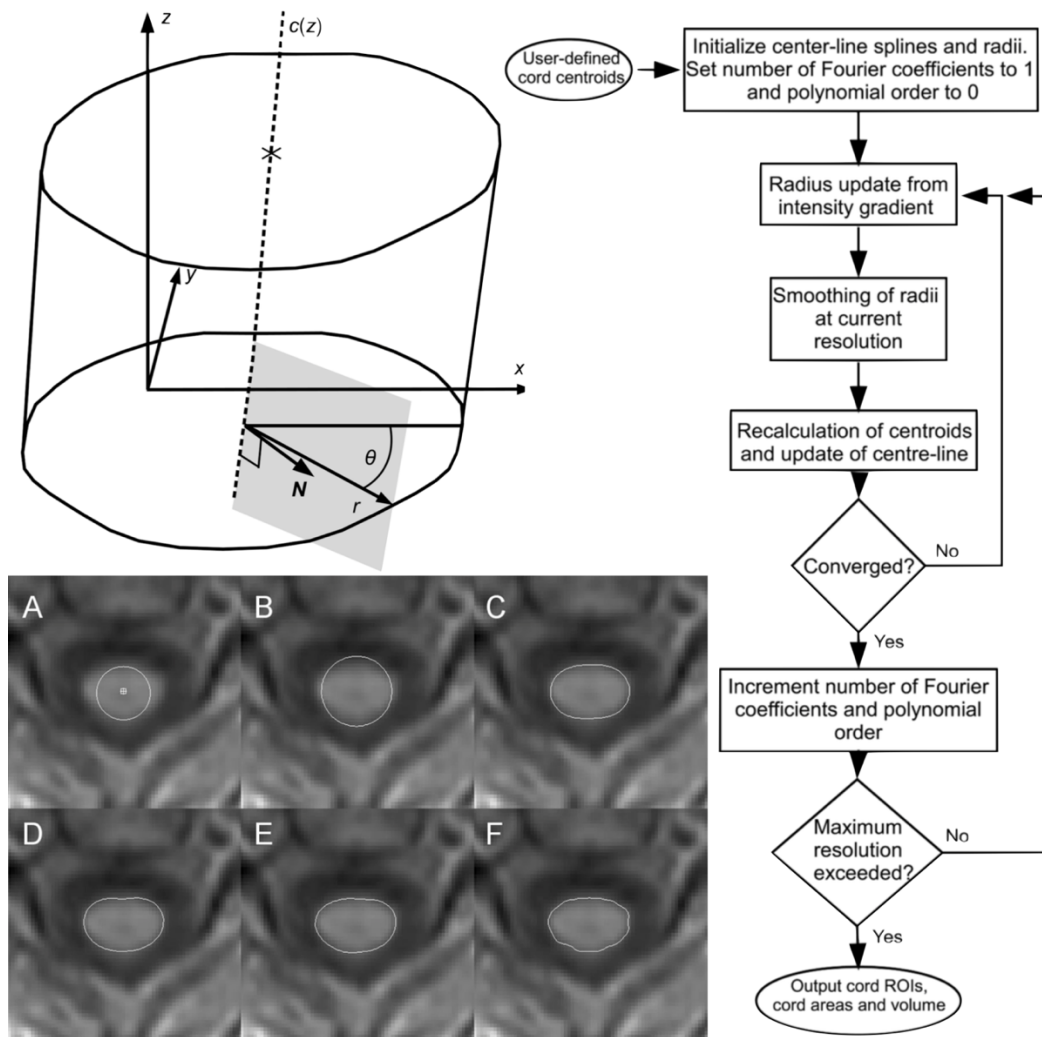
Figure 2.10: Overview of the active surface algorithm, from Horsfield *et al.* (2010) (Horsfield et al., 2010), with permission from Elsevier. The upper left panel shows the parametrization of the active surface. The centerline c(z) is represented by a cubic spline approximator and each radius r of the surface is parameterized in z and theta, the angle between the radius vector and the x-axis. The flow diagram of the algorithm is shown in the right panel and an example of its application is shown on the left lower panel.

Meanwhile, McIntosh *et al.* (2006) (McIntosh & Hamarneh, 2006) have proposed a semi-automatic segmentation algorithm based on deformable organisms, called *Spinal Crawlers*. After initializing a tubular surface around two points provided by the user, the spinal cord is segmented by deforming the surface on image gradients using several layers of rules. The authors have validated their method on four healthy subjects against manual segmentation. Later, McIntosh *et al.* (2011) (McIntosh, Hamarneh, Toom, & Tam, 2011) extended and successfully applied *Spinal Crawlers*

to clinical images with various resolution and challenging anatomy, such as that encountered in MS patients due to the presence of lesions. They have validated their method on T_1-weighted images from 10 healthy controls at 3 T and from 10 MS patients at 1.5 T, demonstrating high accuracy despite high variability in image quality.

De Leener *et al.* (2014) (De Leener, Kadoury, & Cohen-Adad, 2014) have developed a fully automatic segmentation method, called *PropSeg*, based on the iterative propagation of a multi-resolution deformable model (cf. Figure 2.11). Firstly, the method finds an approximation of the position and direction of the spinal cord. Secondly, an initial tubular surface with low resolution is built around the point calculated in the detection step and is registered on spinal cord edges using a deformable model framework based on image gradients. Then, the surface is iteratively propagated in both rostral and caudal directions of the spinal cord by duplicating, orienting and deforming small parts of the surface. Finally, the resolution of the surface is increased by a factor 4 and finely deformed to produce an accurate segmentation of the spinal cord. The algorithm has shown high accuracy on T_1- and T_2-weighted images from 15 healthy subjects and two SCI patients. The authors have also demonstrated the applicability of their method on T_2*-weighted images, despite high variability in image intensity due to the internal structures of the spinal cord. They have subsequently proposed an improved method for automatically detecting the spinal cord by refining the Hough transform detection with vesselness filtering (De Leener, Cohen-Adad, & Kadoury, 2015). Further, they have combined spinal cord segmentation with automatic vertebral labeling technique (Ullmann, Pelletier Paquette, Thong, & Cohen-Adad, 2014), defining a generic coordinate system based on vertebral levels. The segmentation tool is freely available online (see Annex 1).
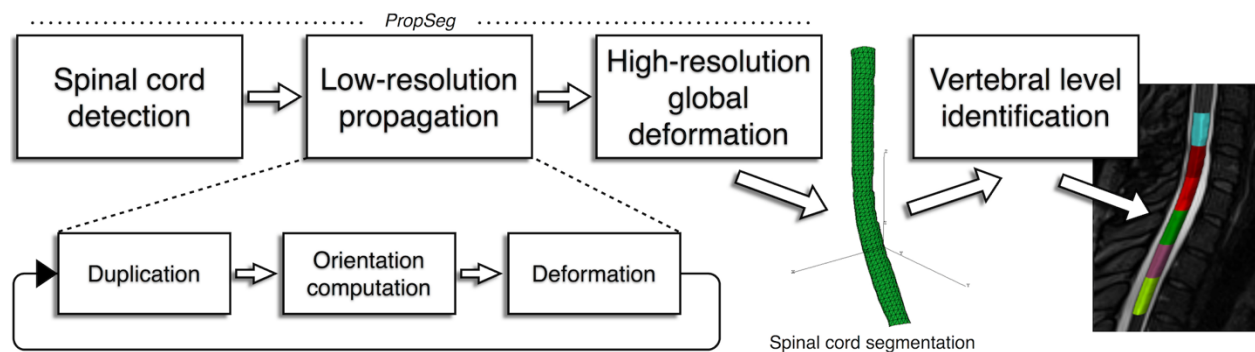
Figure 2.11: Overview of *PropSeg*, an automatic spinal cord segmentation algorithm, based on the iterative propagation of deformable models, from De Leener *et al*. (2015) (De Leener et al., 2015),

with permission from Elsevier. The algorithm is coupled with a vertebrae identification method, in order to extract CSAs at specific vertebral levels.

Over the years, several groups have developed segmentation methods for 2D images of the spinal cord. Koh *et al.* (2010) (Koh, Kim, Chaudhary, & Dhillon, 2010) first proposed an automatic active contour-based method using gradient vector flow for segmenting the lumbar canal and spinal cord on 2D sagittal slices. Later, taking inspiration from the human visual system, they used an attention model (Gabor filter detecting orientation and specific spatial frequencies in the image) along with a level-set technique for improving segmentation of the spinal canal (Koh, Scott, Chaudhary, & Dhillon, 2011). In both publications, they have validated their method against manual segmentations from large populations of subjects (N=52) and patients (N=60), although the results have shown less accuracy of their methods compared to inter-rater variability in the manual segmentation. Earlier, Van Uitert *et al.* (2005) (Van Uitert, Bitter, & Butman, 2005) introduced a segmentation method for sagittal images that combined several basic image processing filters (anisotropic smoothing, edge detection, image inversion, morphological mathematics) along with level-set segmentation, however the method was only validated on one subject.

Sonkova *et al.* (2008) (Sonkova et al., 2008) have used a similar level-set approach to segment the spinal cord semi-automatically on multiple 2D sagittal slices. The only user intervention is the definition of a region of interest around the spinal cord. Then, the algorithm automatically finds the mid-sagittal plane and segments the spinal cord using level-sets. The 2D segmentations are then stacked to form a 3D volume. Validation was based on 12 MS patients and 12 age- and gender-matched healthy controls.

Recently, Kawahara *et al.* (2013) (Kawahara, McIntosh, Tam, & Hamarneh, 2013) have developed a semi-automatic spinal cord segmentation method for T_2-weighted 3D volumes requiring only two points from the user. The algorithm is based on an axial model of the spinal cord, built using principal component analysis on axial slices from healthy subjects. The segmentation is performed by combining the model parameters for a given axial slice, while accounting for smoothing constraints for regularization. Later, they improved their algorithm by including image classification and auto-contextualization with global geometric features in the segmentation process (Kawahara, McIntosh, Tam, & Hamarneh, 2013). Auto-context is an iterative framework that learn appearance and regularization features and can improve the robustness of segmentation.

The authors have validated this method on T_1-weighted images from 10 healthy subjects and 10 patients with MS.

Law *et al.* (2013) (Law et al., 2013) proposed a semi-automatic algorithm that first finds the centerline of the spinal cord by extracting a gradient competition descriptor from the image while ensuring coherence of gradient orientation. The algorithm then segments the spinal cord by partitioning the neighborhood of the centerline into two regions (i.e., the spinal cord and the surrounding structures) based on intensity differences. This method has proven to be robust towards noise and lack of cord/CSF contrast, when validated against manual segmentations on numerical simulations, 10 T_1-weighted images and 15 T_2-weightd images from 25 healthy subjects.

2.4.2.4.1.3   Image-based segmentation methods

Improvements in computational power over the last few years have enabled the development of advanced image segmentation techniques such as active surface, deformable models, template-based registration and level-sets, as presented in the previous section. The high computational cost of such techniques is mainly due to the inherent optimization processes. A newer variety of segmentation methods that takes advantage of computational improvements of computers are the image-based minimization methods such as template/atlas-based segmentation and graph cut algorithms.

Carbonell-Caballero *et al.* (2006) (Carbonell-Caballero et al., 2006) developed the first two fully automatic spinal cord segmentation methods for 2D T_2-w axial slices of the cervical spine. Firstly, the spinal cord location is automatically found by registering a cord pattern to the subjects' scan using cross-correlation. Secondly, the spinal cord is segmented using two possible approaches: (i) finding spinal cord boundary as in Losseff *et al.* (Losseff, Webb, O'Riordan, et al., 1996) or (ii) histogram-based classification of the spinal cord and surrounding structures using Gaussian approximation of signal distributions. PVE is taken into account when calculating spinal cord CSAs. The authors validated their segmentation algorithms with a longitudinal study of MS patients, demonstrating high accuracy and reproducibility of the measurements.

Bergo *et al.* (2012) (Bergo, França, et al., 2012) have developed a semi-automatic method for segmenting the spinal cord in 2D slices perpendicular to the SC extracted from a T_1-weighted volume. The image analysis tool is freely available online (see Annex 1). First, the user manually identifies several points along the spinal cord and a linear interpolation (or cubic Hermite spline)

is used to represent the spinal cord position along the body. Then, the spinal cord is segmented using image foresting transform and tree pruning on a gradient-like image. If the semi-automated method fails to segment the cord, the authors provided an interactive ellipse-fitting method where the user selects several border points of the cord. The method has been validated on 10 healthy controls and 20 patients with diseases inducing spinal cord atrophy (Friedreich's Ataxia and Machado-Joseph disease), demonstrating high reproducibility of CSA measures across experts.

Several groups have used semi-automated graph cut algorithms (Boykov, Veksler, & Zabih, 2001) to segment the spinal cord and spinal canal on MR images. Kayal *et al.* (2013) (Kayal, 2013) developed such a method to classify CSF and spinal cord regions on T_2-weighted and DTI 2D images from several healthy controls and SCI patients. Manual identification of several points around the cord and CSF was necessary to accurately segment the structures. Later, Fonov *et al.* (2014) (Fonov et al., 2014) proposed a similar method that segments a 2D axial slice of the spinal cord, requiring only one seed manually placed at the center of the spinal cord. Then, graph cut segmentation on adjacent slices is initiated by linear registration. The authors have used spinal cord and CSF segmentations to generate the MNI-Poly-AMU generic template of the spinal cord. Meanwhile, Pezold *et al.* (2014) (Pezold et al., 2014) have proposed a graph cut algorithm to segment the spinal cord in 3D T_1-weighted volumes that requires multiple points in regions to perform the segmentation. The authors have validated their method on healthy controls and MS patients, by computing CSAs at different cervical levels and correlating these measurements with clinical scores (EDSS).

Stroman *et al.* (2008) (Stroman et al., 2008) have developed the first cervical spinal cord and brainstem template (spinalfmri8) for fMRI, based on 24 3D fMRI images from 8 healthy subjects. Registering a new anatomical image on this template is performed in two steps: (i) the user manually identify points along the spinal cord, (ii) a spatial normalization using 3D alignment, based on spinal cord curvature provided by the user in step (i), and linear transformation. Once registered, the inverse transformation can be applied to the template to provide the segmentation of the targeted spinal cord image. The validation of the normalization process was performed by determining the distance error between corresponding anatomical landmarks, demonstrating high accuracy of registration (< 2mm in 93% of landmarks). The template and the software for image registration and template-based analysis are freely available online (see Annex 1).

Yen *et al.* (2013) (Yen, Su, Lai, Liu, & Lee, 2013) have developed a method for segmenting the cord and nerves root on T_2-weighted STIR images based on 3D random walker algorithm (Grady, 2006). First, the user manually identifies two sets of points, in the background and in the foreground (spinal cord and nerves). Then, a slab-wise algorithm based on random walker provides the probability of each voxel to belong to a category (spinal cord and nerves vs background). Finally, a classification based on highest probabilities provides spinal cord and nerves segmentation. Despite promising qualitative results, the authors did not quantitatively validate the method on MRI data.

To the best of our knowledge, Chen *et al.* (2013) (Chen et al., 2013) were the first to propose a fully automated method for segmenting the spinal cord in 3D MRI images, while making no assumptions on image resolution or FOV. The algorithm computes a nonlinear transformation between the image subject and an intensity atlas of the spinal cord. The nonlinear registration is coupled with topology constraints (classification atlas of the spinal cord, CSF and background) and statistical maps of the presence of the spinal cord and CSF, in order to ensure the integrity of the segmented spinal cord (cf. Figure 2.12). The intensity template, topology and statistical atlases are computed prior to the segmentation on manually segmented spinal cords from many subjects but can also be generated from one single subject. Chen *et al.* have validated their algorithm against manual segmentations on T_1-weighted images from 7 healthy subjects and on MT images from 18 healthy subjects and 2 patients with MS. Moreover, more than 200 other MT volumes were segmented and results were qualitatively validated (visual assessment).

Intensity Atlas — **Topology Atlas** — **Statistical Atlas (Spinal Cord)** — **Statistical Atlas (CSF)** — **Statistical Atlas (Wrapper)**
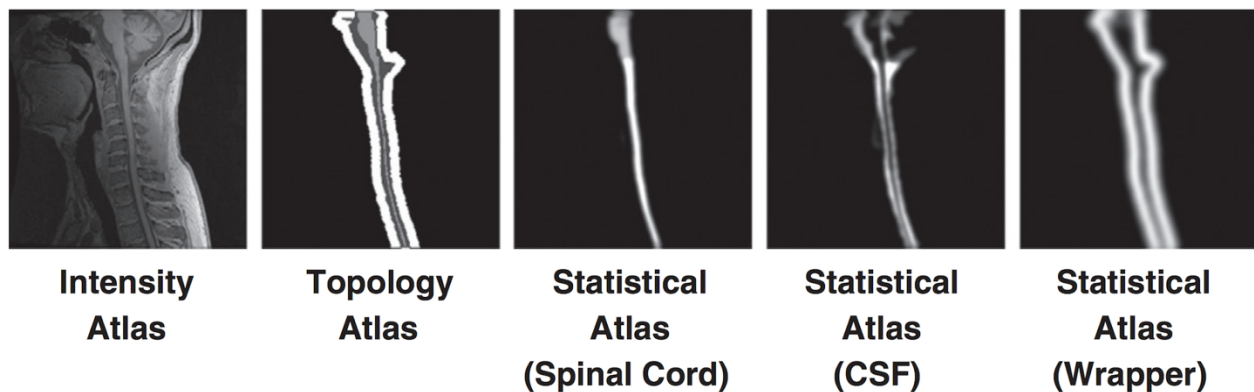
Figure 2.12: Example of the intensity, topology and statistical atlases constructed from a single T_1-weighted MR image, from Chen *et al.* (2013) (Chen et al., 2013), with permission from Elsevier.

Recently, Weiler *et al.* (2015) (Weiler, Daams, Lukas, Barkhof, & Hahn, 2015) have developed a segmentation method based on a manually-initiated watershed technique followed by tissue classification using an intensity-distribution Gaussian mixture modelling. The user manually identifies two points in the spinal cord separated by several vertebral levels. These points serve as seeds for watershed pre-segmentation. An accurate volumetric segmentation of the spinal cord is then computed using a tissue classifier, based on a Gaussian mixture model fitting of the intensity distribution of the pre-segmentation (cf. Figure 2.13). The authors have demonstrated the high reproducibility of CSA measurements extracted using their algorithm on T_1-weighted images from five healthy subjects.
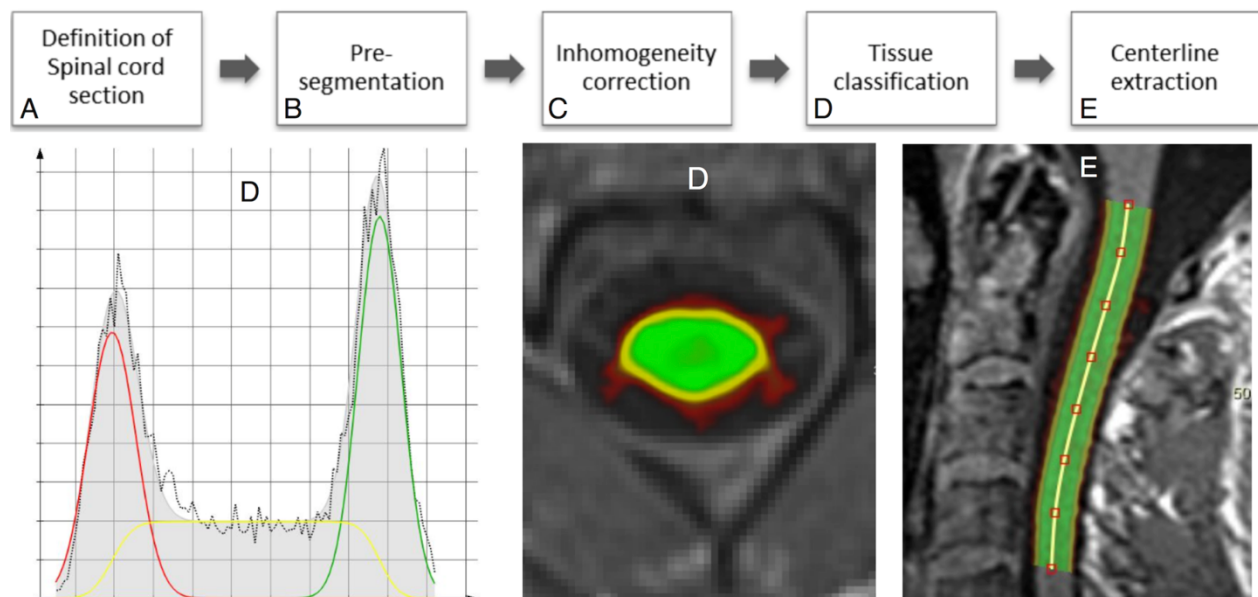
Figure 2.13: Overview of the segmentation algorithm, from Weiler *et al*. (2015) (Weiler et al., 2015), with permission from the authors. The segmentation of the spinal cord is completed by using a Gaussian mixture model classification (D) on a watershed-based pre-segmentation (B).

Pezold *et al.* (2015) (Pezold et al., 2015) have also recently proposed an automatic segmentation method for the spinal cord, based on a continuous max-flow framework, coupled with cross-sectional similarity priors as well as tubularity and CSF features (cf. Figure 2.14). Tubularity features (known as vesselness features) are computed based on the Hessian matrix of the image. The authors also provided features to help the segmentation in difficult cases. The accuracy and reproducibility of the algorithm was assessed on T_1-weighted volumes from 11 healthy controls and 32 MS patients.
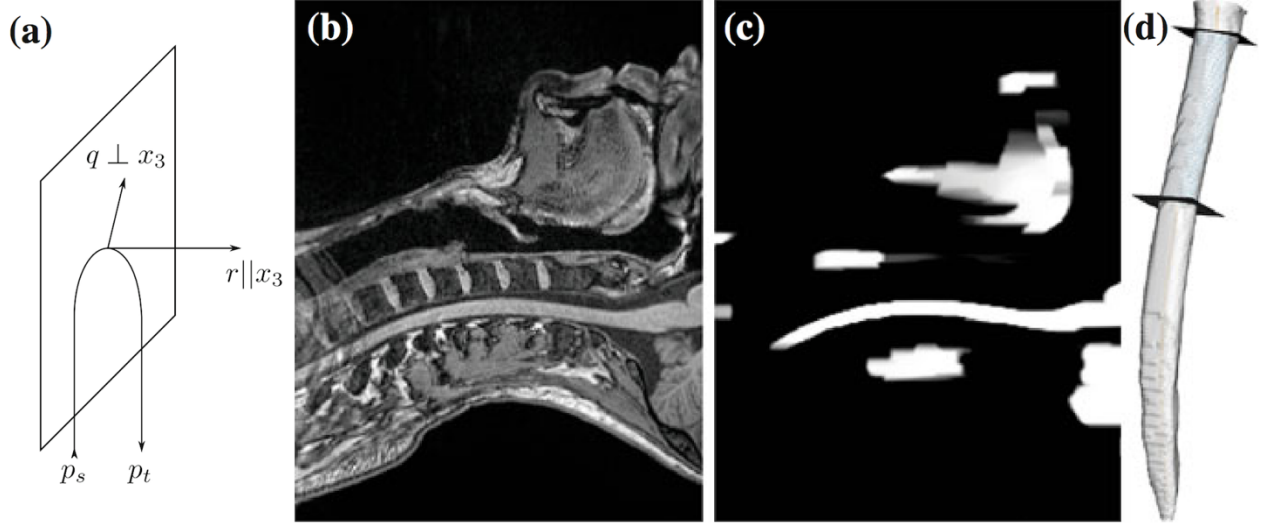
Figure 2.14: Overview of the method proposed by Pezold *et al*. (2015) (Pezold et al., 2015), with permission from Springer. (a) Proposed flow configuration: the spatial flow is split into an in-slice component q, perpendicular to the axis along which the tubular structure is oriented, and a through-slice component r, parallel to the axis. (b) Sample sagittal slice of one of the images used for evaluation. (c) Segmentation result. (d) Surface reconstruction.

2.4.2.4.2 WM/GM segmentation

Delineating the spinal cord's white and gray matter is of tremendous interest for both morphological and multi-parametric analysis of spinal cord MR images collected in healthy and pathological conditions (cf. Applications section).

As stated in the introduction, prerequisites for accurate WM/GM delineation are high MR contrast and high spatial resolution (the GM area represents just 15 and 20% of the spinal cord CSA (Fradet et al., 2014)). In the few reports addressing WM/GM segmentation so far, two main MR modalities have been used:

- High-resolution T_2*-w MRI, as it provides higher contrast than conventional T_1/T_2-w images (Held et al., 2001) due to greater differences in T_2* relaxation times between WM and GM (Samson, Ciccarelli, & others, 2013), and

- Diffusion Tensor Imaging (DTI), providing high GM/WM contrast thanks to different tissue content and organization (isotropic GM vs. anisotropic WM).

Among those reports of WM/GM segmentation, two main methods have been identified and will be detailed in the current section:

1. Intensity-based classification method (clustering, PCA …),

2. Energy minimization based on image registration (single or multi-atlas)

2.4.2.4.2.1   Intensity-based method

The first report of WM/GM delineation based on classification was made by Ellingson *et al.* in 2007 (Ellingson, Ulmer, & Schmit, 2007). A template was first constructed from histological slices to generalize the morphology of the upper cervical spinal cord (Figure 2.15, top). The template was then used for training a fuzzy inference system to identify the GM, the WM and PVE regions based upon three orthogonal anisotropy indices derived from the DTI data (defined as the deviation of the eigenvalues with respect to the mean diffusivity). The degree of membership of a specific voxel as a particular tissue type was then mapped to the new variable space termed the *fuzzy anisotropy index* (FAI), which was then used to classify GM regions and intact WM tracts. In their study, ten slices from the total 25 slices collected on 5 subjects were used as a training dataset and the remaining 15 slices served as test data for quantitative comparison. The labeling resulting from this classification was compared to those provided by conventional DTI. The validation included receiver operator characteristics (ROC) analysis. The authors concluded that the fuzzy inference system improved the accuracy of WM and GM delineation compared to conventional DTI indices such as FA or axial diffusivity. They applied this method in a study addressing morphological and structural changes in SCI patients (Ellingson, Ulmer, & Schmit, 2008).
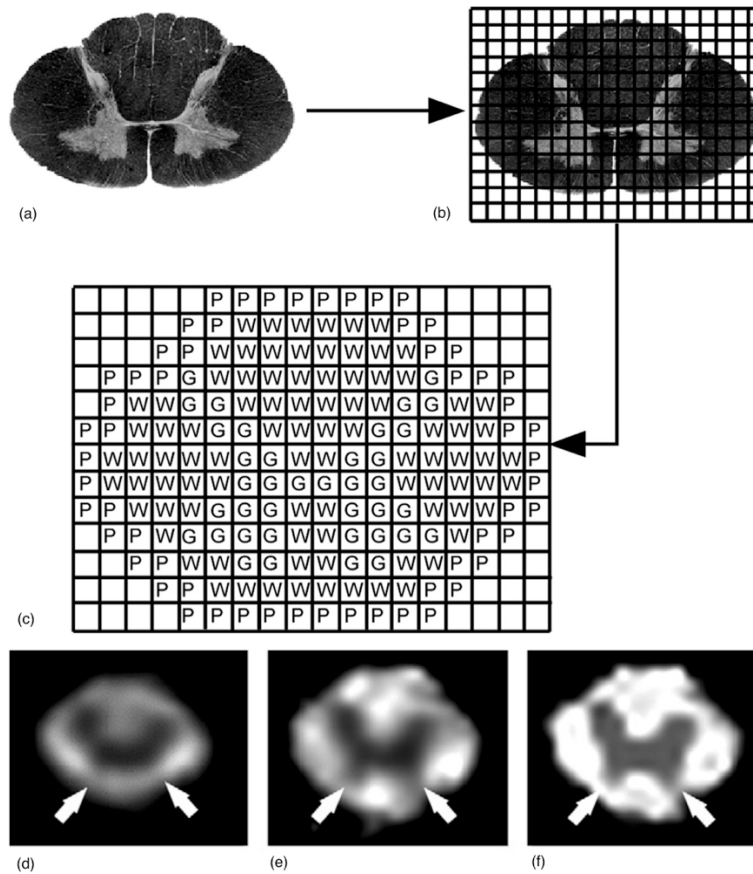
Figure 2.15: Top: Creation (b) of a template (c) from a histological slice of cervical spinal cord (a). G = gray matter; W = white matter; P = partial volume between white matter and cerebrospinal fluid, counted as both white matter and cerebrospinal fluid. Bottom: Comparison between fractional anisotropy (FA) (d), DTI 1st eigenvalue (e) and fuzzy anisotropy index (FAI) (f) for WM/GM delineation. The FAI image appeared to represent the GM morphology more accurately than the FA, especially in the regions of the ventral horns (white arrows). From Ellingson et al. (2007) (Ellingson et al., 2007), with permission from Elsevier.

Another implementation of fuzzy logic has been used by Yiannakas *et al.* (2012) (Yiannakas et al., 2012a) to semi-automatically segment the WM/GM based on high-resolution (0.5x0.5 mm^2 in-plane) 3D gradient echo images. The user manually defines seeds in the GM of specific axial slices, then the spinal cord is segmented using an active surface method (Horsfield et al., 2010) followed by a fuzzy connector method implemented in the Jim software (Udupa & Samarasekera, 1996). They demonstrated the reproducibility of the segmentation method (with low inter /intra observer and inter-scan COV and high ICC) on 5 healthy subjects. They also showed proof-of-concept

application for magnetization transfer ratio (MTR) measurements on 10 subjects. However, as seen on Figure 2.16, this method may require manual intervention to correct the segmentation in the posterior horns of the GM due to the poorer WM/GM CNR.
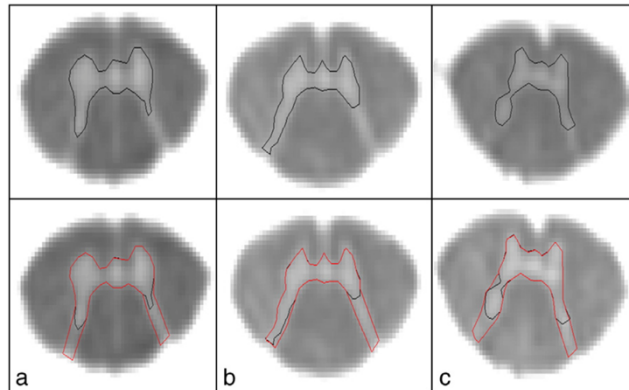
Figure 2.16: Semi-automated segmentation from the fuzzy connector (black - top) with manual edition to complete missing voxels in the posterior GM (red), from Yiannakas *et al*. (2012) (Yiannakas et al., 2012a), with permission from Elsevier.

Finally, Tang *et al.* (2013) (Tang et al., 2013) also proposed a fully automated WM/GM segmentation pipeline based on DTI images (cf. Figure 2.17). After estimation of the diffusion tensors, the authors performed a PCA on 14 parametric maps derived from the diffusion tensors before application of a Bayesian classifier for a three-classes classification. To assess the accuracy of the proposed method, they computed volume overlap with manual segmentations in 10 subjects including 2 patients presenting MS and NMO lesions in the cervical spinal cord. While the overall overlap was good, the presence of lesions induced segmentation errors. However and as rightly pointed out by the authors, this method (as does the one proposed by Ellingson *et al*.) suffers from inherent drawbacks due to the use of DTI images. While presenting high WM/GM contrast, DTI images also come with a lower spatial resolution than anatomical imaging leading to pronounced PVE especially in the dorsal horns of the GM, leading to potentially wrong segmentation. Also, geometrical distortions due to the EPI readout (commonly used for diffusion imaging) also limited the segmentation accuracy.
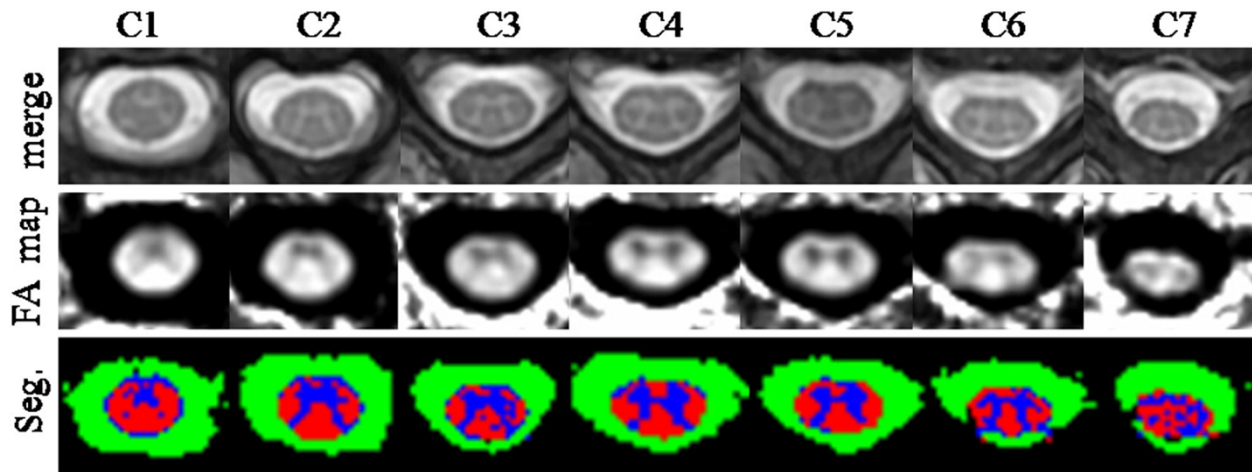
Figure 2.17: Comparison between high-resolution T_2*-w images (Multiple Echo Recombined Gradient Echo (**MERGE**), FA map and resulting automated segmentation, from Tang *et al*. (2013) (Tang et al., 2013), with permission from Elsevier.

Generally speaking, although intensity-based methods do not require prior information, they are very sensitive to the CNR between the WM and the GM and to the potential signal alterations caused by artifacts or pathology. These limitations are illustrated in the work of Yiannakas *et al.* in which systematic manual edition was required to compensate for the poorer contrast between WM and GM in the posterior regions. Similarly, Tang *et al.* demonstrated segmentation failures in pathological cases where signal alterations are found in the WM and/or in the GM, in diseases such as MS or NMO. Finally, all these reports were limited to the segmentation of the cervical spinal cord with few or no investigations in the thoracic and lumbar spinal cord.

2.4.2.4.2.2   Image-based energy minimization methods

In contrast to the previously-described methods, the following methods rely on priors provided by an atlas (be it a single or multi-atlas) (Asman et al., 2014; De Leener, Roux, Taso, Callot, & Cohen-Adad, 2015) or template with a specific MR weighting (Taso et al., 2015) combined with an atlas/subject registration for deriving WM and GM binary masks.

Asman *et al.* (2014) (Asman et al., 2014) introduced a method based on slice-based group-wise registration. They first manually segmented T_2*-w data from 67 healthy subjects. These segmentations were used to build multiple slice-based atlases and to build a model of spinal cord variability (using PCA). Any new subject is then automatically segmented by comparing each slice to the model (group-wise registration) and then labeling each voxel with the structure to which it

belongs. They tested different algorithms for label fusion[1], including majority vote, STAPLE and non-local STAPLE (cf. Figure 2.18) and performed a leave-one-out validation to test the accuracy of the resulting segmentation using DICE coefficients, HDE and MSDE. The authors concluded that the non-local STAPLE approach provides the more robust label fusion method yielding higher similarity measurements between manual and multi-atlas based segmentations. As pointed out by the authors, inclusion of more atlases in the model and improvement of the pre-registration (based on rigid 2D registration) would potentially increase the accuracy of the method. The codes needed to run the image analysis are freely available online (see Annex 1).
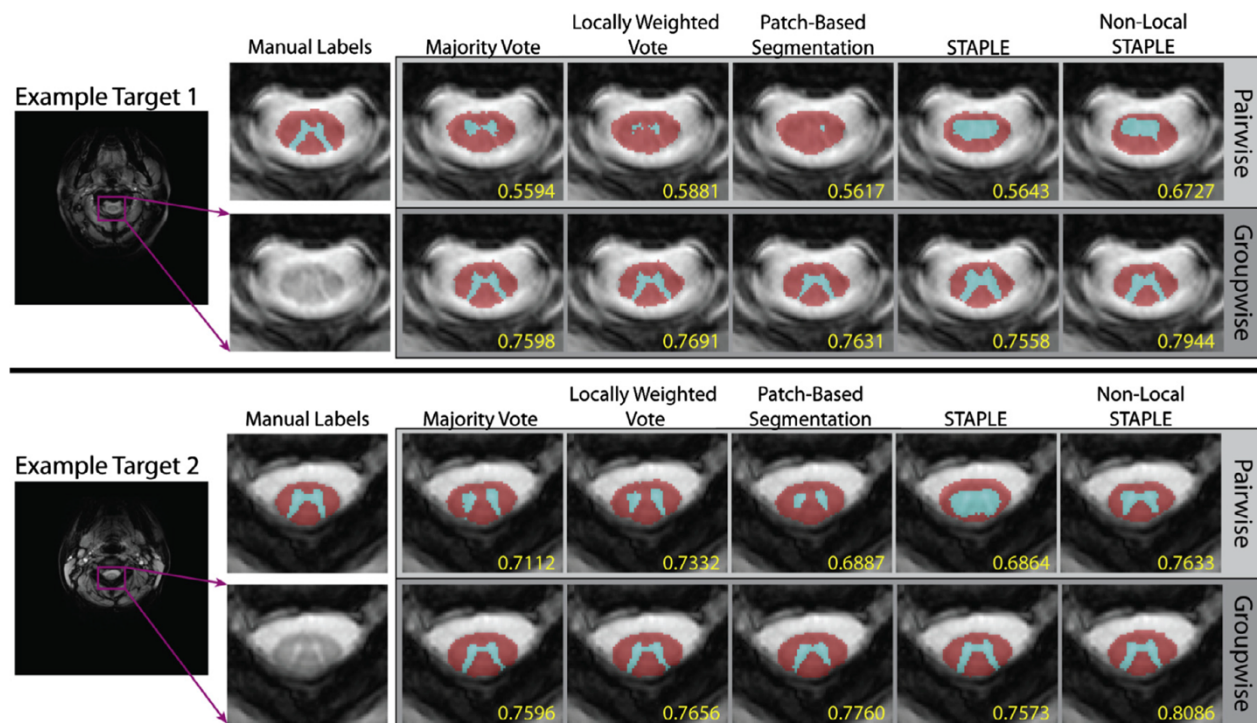
Figure 2.18: Examples of comparison manual/automated segmentation with different label fusion methods, from Asman *et al*. (2014) (Asman et al., 2014), with permission from Elsevier.

Meanwhile, the development of WM and GM probabilistic atlases (i.e., maps indicating the location of anatomical structure, such as the AMU atlases) (Taso et al., 2014) and spinal cord templates (i.e., average anatomical image used as a common reference for analysis, such as the

---

[1] Label fusion is a method used for resolving pixel conflicts when deforming multiple atlases into a single target

MNI-Poly-AMU template) (Fonov et al., 2014) have opened new perspectives for automated WM/GM segmentation.

In the report detailing the construction of the MNI-Poly-AMU template, Fonov *et al.* presented preliminary results of template-based analysis of multi-parametric MR data using an integrated version of the WM and GM probabilistic atlases (freely available online, see Annex 1). Based upon these developments, De Leener *et al.* (2015) (De Leener et al., 2015) proposed a framework for automated WM/GM segmentation relying on single GM atlas deformation. The method relies on T_2-w and high-resolution T_2*-w images. Firstly, the T_2-w volume is registered to the MNI-Poly-AMU T_2-w template. Secondly, T_2- and T_2*-w images are co-registered using non-rigid algorithms. Thirdly, the GM probabilistic atlas included in the MNI-Poly-AMU template is warped to the subjects' T_2*-w scan (obtained at step #1), then registered to the GM visible in the T_2*-w image using nonlinear smooth deformations provided by the Advanced Normalization Tools (ANTs) software package with optimized regularization parameters. The authors compared this automated segmentation to manual segmentation using DICE coefficients and reported mean DICE of 0.79 for GM segmentation on 5 healthy subjects.

Taso *et al.* (2015) (Taso et al., 2015) recently proposed an automated WM/GM segmentation pipeline relying on nonlinear deformation of high-resolution multi-echo GRE T_2*-w acquisitions to a T_2*-w template made of 40 subjects (AMU_{40}). This approach nonetheless requires a cord segmentation for initialization of the nonlinear deformation. As seen before, robust automated spinal cord segmentation methods are now available, which may lead to a fully automated WM/GM segmentation pipeline. The authors validated their approach by performing a leave-one-out validation (N=40 subjects) between manual and automated segmentation using the DICE similarity coefficient and considered their results satisfactory (mean GM DICE > 0.8). Similar DICE indices (mean GM DICE > 0.83, N=25) were observed when using this automated pipeline to segment T_2*-w MR images of elderly volunteers (Figure 2.19). This pipeline was used to perform TBM analysis and to investigate morphological changes occurring with age (see Application section). As pointed out by the authors, the method could face difficulties in case of strong signal alteration within the SC (e.g., in SCI) or artifacts (e.g., susceptibility-related signal dropout).
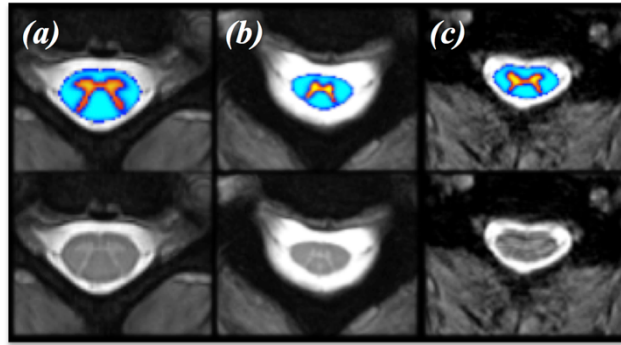
Figure 2.19: Automated WM/GM segmentation on T_2*-w images of (a) a young healthy volunteer at C4 (b) an elderly volunteer at C2, and (c) an elderly volunteer with poor contrast at C5, modified from Taso *et al*. (2015) (Taso et al., 2015) with permission from Elsevier.

In the future, we can anticipate that GM/WM segmentation methods will benefit from ultra-high field (UHF) MRI data (7T and beyond) thanks to the increased spatial resolution (as low as 0.18x0.18 mm2 in-plane resolution reported so far) and WM/GM contrast (Cohen-Adad, Zhao, et al., 2013; Sigmund et al., 2012).

2.4.2.5 Applications

Spinal cord segmentation can be used for multiple purposes. Firstly, cord segmentation can provide measures of CSA for assessing SC atrophy. CSA can be obtained by computing the circumference of the segmentation at a particular slice (Losseff, Webb, O'Riordan, et al., 1996) or across a group of adjacent slices after being reformatted in the plane orthogonal to the SC centerline (Lundell et al., 2011). Once CSA is extracted, several methods exist to normalize it with morphological features, such as SC length, intracranial volume (Klein et al., 2011) or C3 CSA (Fradet et al., 2014; Kameyama, Hashizume, & Sobue, 1996). By computing CSA across several levels one can also compute the SC volume, which is another marker of cord atrophy as shown in MS patients (Hickman, Hadjiprocopis, Coulon, Miller, & Barker, 2004).

Secondly, internal segmentation of the GM can be used to compute the ratio between WM and GM CSA, which can provide additional specificity to tissue atrophy. For example, this ratio could help differentiate pure motor neuron diseases (e.g., ALS) from diseases affecting both the white and the gray matter. Moreover, with the development of automatic WM and GM segmentation methods (Taso et al., 2015), measuring WM/GM ratio robustly in diseases seems feasible and relevant, as illustrated in Figure 2.20.
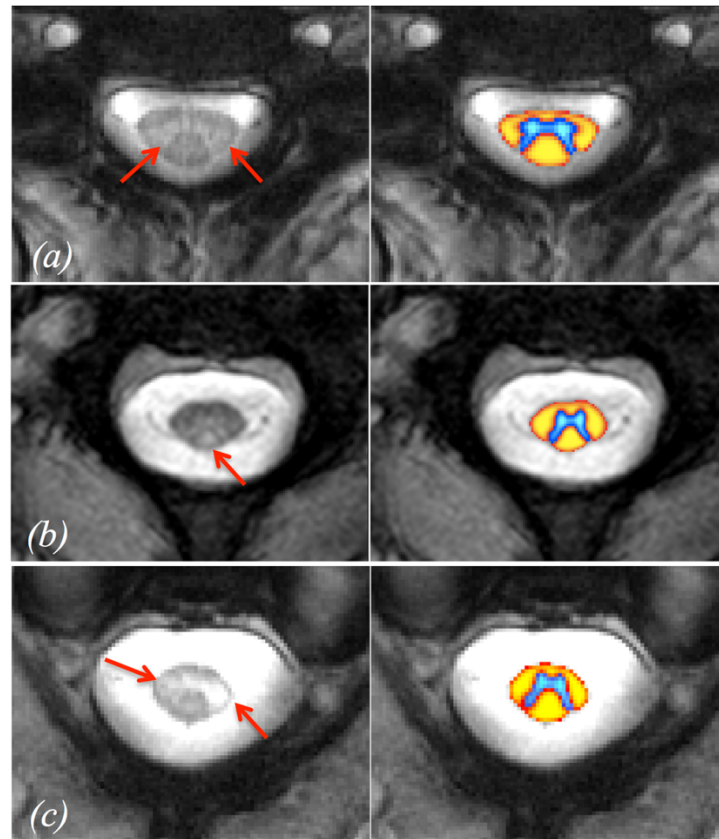
Figure 2.20: Examples of automated WM/GM segmentation on (a) an ALS patient with signal hyperintensity in the corticospinal tracts, (b) a patient with zinc-induced copper deficiency and hyperintensity in the dorsal column, and (c) a MS patient with large hyperintensity signal lesions in GM and WM, using (Taso et al., 2015). Note that even though the presence of hyperintensity within the cord renders automatic WM/GM segmentation difficult, segmentation was nevertheless successful in these cases.

Thirdly, regions of interest (ROI) derived from SC segmentation can be used for extracting mp-MRI metrics, such as DTI-based fractional anisotropy or magnetization transfer ratio. For example, Hickman et al. computed MTR within the SC of MS patients using ROI based on SC segmentation obtained using an active contour method (Hickman et al., 2004). Segmenting the SC internal structure (e.g., spinal pathways) also has great interest for correlating specific tract degeneration with motor and sensory deficits. Until recently, the state-of-the-art method for quantifying mp-MRI metrics in the SC was to manually draw an ROI in "what appears to be" the tract of interest, over several slices, based on the knowledge of spinal cord anatomy (Ciccarelli et al., 2007; Cohen-Adad et al., 2008; Gullapalli, Krejza, & Schwartz, 2006; Klawiter et al., 2011; Lindberg, Feydy, &

Maier, 2010; Narayana, Grill, Chacko, & Vang, 2004; Onu et al., 2010; Qian et al., 2011; Smith et al., 2010; Xu et al., 2013). This approach has major flaws: (i) the identification of the tract location is biased by the user experience and knowledge of the anatomy, (ii) the manual delineation of ROIs is long and tedious, especially if several slices, tracts and subjects are involved and (iii) ROIs consist of binary masks and hence do not account for PVE. To address these issues, an MRI atlas of WM tracts was recently created (Lévy et al., 2015) and is illustrated in Figure 2.21. This atlas is composed of 30 tracts and it is merged with the MNI-Poly-AMU template, enabling multimodal registration followed by automatic ROI-based quantification of mpMRI metrics. It was notably used to show differences in young and aged population (Taso et al., 2015).
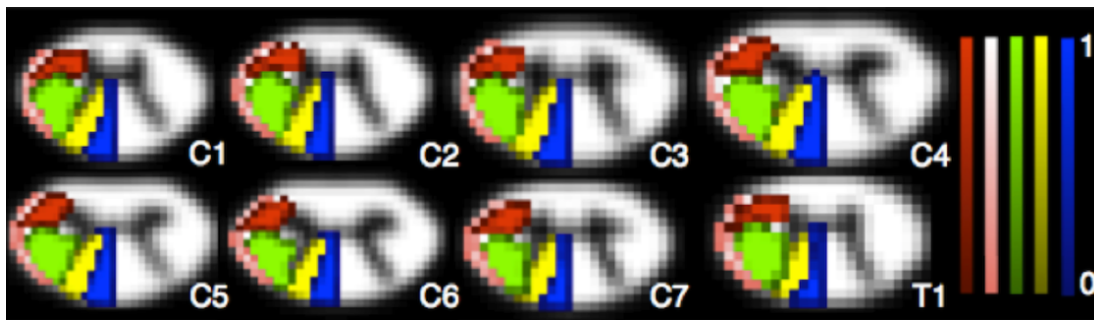
Figure 2.21: WM atlas overlaid on the MNI-Poly-AMU WM template. Among 30 tracts, the following tracts are shown here: Left spinal lemniscus tract (red), spinocerebellar tract (pink), lateral corticospinal tract (green), cuneatus (yellow) and fasciculus gracilis (blue). Modified from (Lévy et al., 2015), with permission from Elsevier.

Beside the WM, segmentation of the spinal cord GM can have useful application for fMRI investigations, where researchers are interested in quantifying the presence of BOLD responses within the spinal neurons (e.g., ventral vs. dorsal horns for motor vs. painful stimuli) (Stroman, 2009; Stroman, Tomanek, Krause, Frankenstein, & Malisza, 2002). The following paragraphs describe applications of SC segmentation in some major diseases and normal aging.

2.4.2.5.1 *Multiple sclerosis (MS)*

MS is an inflammatory disorder of the CNS. It is characterized by inflammation, demyelination, axonal loss, and gliosis. Clinical symptoms manifest as motor and cognitive (Hickman et al., 2004) impairment as a result of impaired saltatory conduction at affected sites. Diagnostic criteria include the number and size of white matter lesion in the brain and spinal cord detected with MRI

(typically, PD- and T_2-weighting) (McDonald et al., 2001). However, lesion frequency and volumes do not always explain the degree of clinical disability in patients (Kidd et al., 1993).

Atrophy has been outlined as the most robust method to monitor the neurodegenerative process in MS patients (Bakshi, Dandamudi, Neema, De, & Bermel, 2005). SC atrophy represents whole tissue loss, including axonal destruction, demyelination and other tissue degeneration. In MS, spinal cord atrophy may be focal at the site of the lesions or involve an extended portion of the cord as a consequence of axon degeneration (Bastianello et al., 2000). Atrophy has been shown to correlate strongly with disability in cross-sectional and in longitudinal studies (Liu et al., 1999; Losseff, Webb, O'Riordan, et al., 1996; Stevenson et al., 1998). Spinal cord atrophy is most marked in progressive forms of MS and greatest in secondary progressive MS (SPMS) (Losseff, Webb, O'Riordan, et al., 1996). Interestingly, in primary progressive MS (PPMS), the rates of atrophy in the brain and in the spinal cord are different, suggesting that the underlying pathological processes differ in these two regions (Ingle et al., 2003). Two clinical trials have included an atrophy measure to monitor the evolution of MS under treatment (Kalkers et al., 2002; Lin et al., 2003). Kidd *et al*. were the first to report quantitative analysis of spinal cord atrophy in MS (Kidd et al., 1993). They calculated mean cord areas across four vertebral levels (C5, T2, T7 and T11). The mean cord areas in MS patients were significantly smaller than that in control subjects, and those patients with atrophy had higher disability evaluated by EDSS (Kurtzke, 1983). Beyond measuring the entire SC cross-section, GM was also manually segmented in MS patients to retrieve measures of atrophy (Schlaeger et al., 2014).

The standard protocol for measuring atrophy in MS was first introduced by Losseff *et al*. and was based on a semi-automated edge detection method (Losseff, Webb, O'Riordan, et al., 1996). Later on, more advanced methods were introduced and tested in patients (Zivadinov et al., 2008), including active contour (Horsfield et al., 2010), active surface and propagation of mesh (McIntosh et al., 2011; Yiannakas et al., 2016). In a comparison of imaging sequences on which to base segmentation, 3D phase sensitive inversion recovery (PSIR) demonstrated higher performance than other commonly used sequences, including MPRAGE (Kearney et al., 2014).

ROI-based quantification of mpMRI is another popular application of SC segmentation. This technique was notably applied to measure DTI (Ciccarelli et al., 2007; Freund et al., 2010) and MT (Zackowski et al., 2009) metrics in MS patients.

2.4.2.5.2 Neuromyelitis Optica (NMO)

NMO is an inflammatory and demyelinating disease of the CNS, with particular involvement of the optic nerve and spinal cord. Disability and loss of function is thought to be mediated by axonal damage that accumulates incrementally with clinical relapses. Although NMO is clinically and immunologically distinct from MS (Wingerchuk, Hogancamp, O'Brien, & Weinshenker, 1999), it is sometimes misdiagnosed as MS, which can be harmful for the patient because the treatments for these distinct conditions can be very different (Society NMS, 2015).

SC segmentation could potentially help to differentiate NMO from other demyelinating diseases. For example, a study found that the severity of SC atrophy might be predictive of the more severe neurologic dysfunction and worse prognosis in NMO spectrum disorders (Wang et al., 2014). In another study, NMO showed SC atrophy with mild brain atrophy, while MS demonstrated more brain atrophy, especially in the gray matter (Liu et al., 2015). GM segmentation could also be useful for studying the preferential spinal central GM involvement in NMO (Nakamura et al., 2008).

2.4.2.5.3 Amyotrophic Lateral Sclerosis (ALS)

ALS is characterized by the degeneration of the lower and upper motor neurons, leading to progressive muscle atrophy, weakness, spasticity, and eventually respiratory failure and death within about 5 years of symptom onset (Brooks, 1996). The diagnosis is based on the presence of signs of upper and lower motor neuron dysfunction within the same body segments (Brooks, 1994). Lower motor neuron dysfunction can be quantified using electrophysiological techniques such as motor unit number estimation (MUNE), but accurate quantification of upper motor neuron dysfunction has been challenging (Shefner et al., 2011). Post-mortem microscopy findings in ALS show a loss of Betz cells in the motor cortex and the anterior horns in the spinal cord. Degeneration of the CST is evidenced by the presence of myelin loss, macrophages, and astrocytosis (Brownell, Oppenheimer, & Hughes, 1970). In addition to CST impairment, the degeneration of lower motor neurons, associated with symptoms such as weakness, atrophy, cramps and fasciculations, occurs at various spinal levels. Detecting local spinal atrophy in metameres corresponding to specifically altered muscles might be useful for the future non-invasive and objective quantification of lower motor neuron degeneration. Indeed, a neuroimaging study showed that local spinal cord atrophy was associated with weakness in the corresponding muscle territory (measured with evoked potentials), i.e. C4 level for deltoid and C7 level for hand muscles (Cohen-Adad, El Mendili, et al.,

2013). Although atrophy may partly be explained by degeneration of white matter pathways (via degeneration of upper motor neurons), the specific association between C8 atrophy and the amplitude of motor-evoked potentials of the adductor digiti minimi provides strong evidence for gray matter atrophy, given that these measures reflect impairment of lower motor neurons, not of the CST. This demonstrates an association between muscle deficits and local spinal cord atrophy, suggesting that atrophy is a sensitive biomarker of anterior horn cell degeneration of lower motor neurons in ALS.

Regarding the quantification of ventral horn atrophy in ALS, UHF MRI (7T) has shown great potential thanks to the high-resolution and higher sensitivity to visualize demyelinating lesions (Cohen-Adad, Zhao, et al., 2013) and should hence increase the sensitivity of GM atrophy monitoring.

2.4.2.5.4 *Spinal cord injury (SCI)*

In pathologies that affect spinal cord morphology, such as cervical spondylotic myelopathy (CSM) and traumatic SCI, we distinguish atrophy that results from a degenerative process (e.g., Wallerian degeneration) (Tator & Fehlings, 1991) from compression of the cord. In both cases, it can be useful to report spinal cord CSA. In cases where atrophy is mediated by secondary degenerative processes, CSA is useful because it can provide the clinician an indication of how much irreversible impact the lesion has had on white matter tracts, which has consequences on the potential for recovery of the patient. CSA may also provide objective assessment of regeneration/remyelination in testing trials. Atrophy caused by secondary degenerative processes can be assessed by measuring CSA above and below the lesion, under the assumption that ascending tracts would degenerate above the lesion while descending tracts would degenerate below the lesion, as demonstrated using diffusion MRI in animal models (Cohen-Adad, Leblond, et al., 2011) and humans (Cohen-Adad, El Mendili, et al., 2011b; El Mendili, Chen, Tiret, Pélégrini-Issac, et al., 2015). This method also proves to be useful in patients with metallic implants where the loss of image quality due to susceptibility artifacts at the level of injury often renders the images useless for analysis.

In cases where atrophy is caused by actual compression of the cord, animal (Rossignol et al., 2015) and human (Cadotte & Fehlings, 2014) studies have shown that the amplitude and shape of the compression can bring useful prognosis values. In particular, Fehlings *et al.* showed that measures

of spinal cord compression and spinal canal compromise predicted the baseline ASIA motor score and neurologic recovery (Miyanji, Furlan, Aarabi, Arnold, & Fehlings, 2007).

Although global CSA was shown to be clinically relevant, this measure lacks information about the type of tracts that goes under degeneration. To address this issue, Lundell *et al*. introduced a systematic method for assessing regional CSA by reporting the antero-posterior width (APW) and the left-right width (LRW) (Lundell et al., 2011). The application of these measures in 19 chronic incomplete SCI patients showed that the clinical motor score (muscle strength testing) was correlated to LRW, consistent with the degeneration of the CST, and that the sensory score (light touch and pinprick) was correlated to APW, consistent with degeneration of the dorsal column (gracilis and cuneatus). These results suggest that APW and LRW can be used to assess sensory and motor function independently, with potential applications in other diseases such as MS and ALS. It should be noted however that this approach is limited because LRW may also be influenced by the degeneration of sensory tracts (e.g., spinothalamic and spinocerebellar) and similarly, APW can be influenced by motor tracts (e.g., ventral CST). Further work is needed to assess atrophy in specific tracts with higher specificity, and more generally to characterize and quantify impairment in specific tracts, e.g., using mp-MRI.

2.4.2.5.5 Aging

Normal aging is associated with morphological and structural changes in CNS structures. More than a decade ago, brain imaging studies yielded evidence of diffuse and progressive GM and WM atrophy in healthy elderly volunteers using VBM (Good et al., 2001). In the spinal cord, histological analysis of post-mortem tissues showed evidence of neuro-degeneration, characterized by neuronal loss in the anterior horns of the GM (motor neurons) (Cruz-Sánchez, Moral, Tolosa, de Belleroche, & Rossi, 1998). Age-related atrophy of spinal cord GM was also detected in vivo using high resolution MRI (Fradet et al., 2014; Papinutto et al., 2015). Recently, a cross-sectional study of 90 healthy volunteers (Valsasina et al., 2012), making use of spinal cord segmentation by the active-surface method (Horsfield et al., 2010) and VBM has provided a statistical mapping of age-related alterations in the spinal cord, highlighting an anteroposterior SC atrophy occurring in the aging cervical cord. Similarly, a recent study reported diffuse GM atrophy associated with aging using TBM based on T_2*-w scans (Taso et al., 2015). Finally, from a microstructural point of view, quantitative or semi-quantitative MR techniques showed age-related changes in the spinal cord

WM using DTI (Agosta, Laganà, et al., 2007), myelin water fraction (MacMillan et al., 2011) and ^{1}H-MRS (Abdel-Aziz et al., 2014). These studies however did not consider separate regions of interest and used manual ROI definition, which is prone to user bias. A more recent study took advantage of automatic GM and WM segmentation (including distinction between motor and sensory tracts) to assess regional variations of DTI, MT and inhomogeneous MT metrics (Varma, Duhamel, de Bazelaire, & Alsop, 2015) in the aging cervical spinal cord (Taso et al., 2015).

2.4.2.6   Discussion and conclusions

The purpose of this review was to describe the existing methods for segmenting the human spinal cord from MRI data and to illustrate some of their applications. Note that several studies have also introduced interesting algorithms for segmenting the spinal cord in animals (two of them are briefly detailed in Annex 2), however a full coverage was beyond the scope of this review.

In addition to the methodological description of the segmentation algorithms, the review covered different aspects related to segmentation, including recommended acquisition parameters, image preprocessing and validation methods.

The following discussion synthesizes the segmentation methods, discusses their validation and concludes on potential perspectives.

The pros/cons of existing spinal cord segmentation algorithms can be summarized as follows. Intensity-based methods (Losseff, Webb, O'Riordan, et al., 1996; Tench et al., 2005; Weiler et al., 2015) are efficient and fast, but the presence of pathology, artifacts or poor cord/CSF contrast can yield errors, necessitating user intervention or strategies for regularization. On the other hand surface-based algorithms and methods based on spinal cord edges are more reliable in the face of such problems because only the image gradients are used for segmentation. Surface-based and energy equation-based methods include regularization terms, allowing more robustness against variations in cord/CSF contrast. Multi-atlas methods (Asman et al., 2014) are an interesting avenue for segmenting the cord and/or internal structure. However, a large database with various image contrast, cord shape and pathology is necessary for these algorithms to perform well. This emphasizes the need for the community to have a shared database that could serve this purpose.

In conclusion, there is currently no single method that can adequately segment the cord and its substructure with 100% robustness. A combination of different approaches is recommended, along

with the introduction of probabilistic shape models. Co-registration to dedicated template along with vertebral or spinal cord level identification should also facilitate the segmentation.

The choice of segmentation techniques to use will be dictated by the type of images available and the parameters to be quantified (cord atrophy, regional investigation, etc.). Techniques that have been adequately validated and reported to be robust are recommended. As a 100%-success rate in segmentation does not exist so far, inspection of the segmented data and manual editing should have to be considered.

Regarding the availability of the methods, some have been implemented in software suites (see Annex 1). Further efforts are needed to make the spinal cord community fully benefits from the techniques and to make their use easier (standardization of the processing, multiplatform availability, user-friendly integration (automatic and/or customizable workflows, step by step guidance), algorithm documentation, etc.). Such inclusion in large suite would ultimately benefit to clinical research studies, pathophysiological description and treatment evaluation.

Concerning spinal cord segmentation development, one should keep in mind that algorithms should come with accurate validation. Such validation is typically done by computing overlap indices and distance errors (local and global) between the proposed method and manual segmentations. Validation should ideally include different contrasts, slice orientation, coverage and if possible multi-site data. Since inherently subjected to user bias, manual segmentation should be performed by several raters, and intra- and inter-rater coefficients should be reported. The use of classifiers that compute a probabilistic estimate of the true segmentation based on several expert segmentations and a measure of the performance level represented by each segmentation should also be used if possible (e.g. STAPLE, Simultaneous Truth and Performance Level Estimation (Warfield, Zou, & Wells, 2004)). In fine, the community would strongly benefit from a shared database that would include multi-contrast data and their manual segmentation. We also encourage researchers to share the implementation of their methods so that they can be compared against others. Standardization of validation also includes the development of digital spinal cord phantoms, similar to the digital brain phantom images of normal and MS subjects (BrainWeb, 2015), and although they do not represent realistic image characteristics (e.g., partial volume artifacts, intensity heterogeneity, structured noise, normal and pathologic anatomic variability).

Altogether, the emergence of common templates (Fonov et al., 2014; Taso et al., 2015), atlases (Lévy et al., 2015; Taso et al., 2014) and software (Asman et al., 2014; Bergo, França, et al., 2012; Chen et al., 2013; De Leener et al., 2015, 2014; Horsfield et al., 2010) for quantifying mp-MRI data in the spinal cord now overcomes the biases associated with manual delineation and offers a common processing framework that is expected to be reproducible across centers and longitudinal studies. These new automatic methods can be applied to study demyelination and degeneration in various spinal cord diseases such as MS or cervical myelopathy. Measurement of the CSA, which has been demonstrated to be a marker of atrophy, and investigation within specific regions of interest (GM, WM tracts) are of particular importance. By facilitating longitudinal and multi-center studies, these methods should greatly help in further understanding the spinal cord pathophysiology, and to develop new criteria for early detection of subclinical evolution, for prognosis prediction and or patient management.

2.4.2.7 References

Abdel-Aziz, K., Solanky, B. S., Yiannakas, M. C., Altmann, D. R., Wheeler-Kingshott, C. A. M., Thompson, A. J., & Ciccarelli, O. (2014). Age related changes in metabolite concentrations in the normalspinal cord. *PLoS One*, *9*(10), e105774.

Agosta, F., Laganà, M., Valsasina, P., Sala, S., Dall'Occhio, L., Sormani, M. P., … Filippi, M. (2007). Evidence for cervical cord tissue disorganisation with agingby diffusion tensor MRI. *Neuroimage*, *36*(3), 728–735.

Altman, J., & Bayer, S. A. (2001). An overview of spinal cord organization. In *Development of the Human Spinal Cord: An Interpretation Based onExperimental Studies in Animals* (pp. 1–87). New York: Oxford University Press.

Archip, N., Erard, P.-J., Egmont-Petersen, M., Haefliger, J.-M., & Germond, J.-F. (2002). A Knowledge-Based Approach to Automatic Detection of the Spinal Cord in CT Images. *IEEE Transactions on Medical Imaging*, *21*(12), 1504–16. https://doi.org/10.1109/TMI.2002.806578

Asman, A. J., Bryan, F. W., Smith, S. A., Reich, D. S., & Landman, B. A. (2014). Groupwise multi-atlas segmentation of the spinal cord's internal structure. *Med. Image Anal.*, *18*(3), 460–471.

Aspert, N., Santa Cruz, D., & Ebrahimi, T. (2002). MESH: measuring errors between surfaces using the Hausdorffdistance. In *ICME (1)* (pp. 705–708). stage.nitrc.org.

Bakshi, R., Dandamudi, V. S. R., Neema, M., De, C., & Bermel, R. A. (2005). Measurement of brain and spinal cord atrophy by magneticresonance imaging as a tool to monitor multiple sclerosis. *J. Neuroimaging*, *15*(4 Suppl), 30S–45S.

Bastianello, S., Paolillo, A., Giugni, E., Giuliani, S., Evangelisti, G., Luccichenti, G., … Fieschi, C. (2000). MRI of spinal cord in MS. *J. Neurovirol.*, *6 Suppl 2*, S130–3.

Behrens, T., Rohr, K., & Stiehl, H. S. (2003). Robust segmentation of tubular structures in 3D medicalimages by parametric object detection and tracking. *IEEE Trans. Syst. Man Cybern. B Cybern.*, *33*(4), 554–561.

Bergo, F. P. G., Franca, M. C., Chevis, C. F., & Cendes, F. (2012). {SpineSeg}: A segmentation and measurement tool for evaluation of spinal cord atrophy. In *Proceedings of the 7th Iberian Conference on Information Systems and Technologies, {CISTI}* (pp. 1–4). Madrid.

Bergo, F. P. G., França, M. C., Chevis, C. F., & Cendes, F. (2012). {SpineSeg}: A segmentation and measurement tool for evaluation of spinal cord atrophy. In *7th Iberian Conference on Information Systems and Technologies ({CISTI} 2012)* (pp. 1–4).

Boykov, Y., Veksler, O., & Zabih, R. (2001). Fast approximate energy minimization via graph cuts. *IEEE Trans. Pattern Anal. Mach. Intell.*, *23*(11), 1222–1239.

Brooks, B. R. (1994). El Escorial World Federation of Neurology criteria for thediagnosis of amyotrophic lateral sclerosis. Subcommittee onMotor Neuron Diseases/Amyotrophic Lateral Sclerosis of theWorld Federation of Neurology Research Group on NeuromuscularDiseases and the El Escorial ``Clinical limits of amyotrophiclateral sclerosis'' workshop contributors. *J. Neurol. Sci.*, *124 Suppl*, 96–107.

Brooks, B. R. (1996). Natural history of ALS: symptoms, strength, pulmonaryfunction, and disability. *Neurology*, *47*(4 Suppl 2), S71–81–2.

Brownell, B., Oppenheimer, D. R., & Hughes, J. T. (1970). The central nervous system in motor neurone disease. *J. Neurol. Neurosurg. Psychiatry*, *33*(3), 338–357.

Buades, A., Coll, B., & Morel, J. (2005). A Review of Image Denoising Algorithms, with a New One. *Multiscale Model. Simul.*, *4*(2), 490–530.

Cadotte, D. W., Cadotte, A., Cohen-Adad, J., Fleet, D., Livne, M., Wilson, J. R., … Fehlings, M. G. (2015). Characterizing the location of spinal and vertebral levels in the human cervical spinal cord. *AJNR Am. J. Neuroradiol.*, *36*(4), 803–810.

Cadotte, D. W., & Fehlings, M. G. (2014). Traumatic Spinal Cord Injury: Acute Spinal Cord Injury andPrognosis. In J. Cohen-Adad & C. Wheeler-Kingshott (Eds.), *Quantitative MRI of the Spinal Cord* (pp. 39–48). Elsevier.

Carbonell-Caballero, J., Manjón, J. V, Mart'\i-Bonmat'\i, L., Olalla, J. R., Casanova, B., la Iglesia-Vayá, M., … Robles, M. (2006). Accurate quantification methods to evaluate cervical cordatrophy in multiple sclerosis patients. *MAGMA*, *19*(5), 237–246.

Chen, M., Carass, A., Oh, J., Nair, G., Pham, D. L., Reich, D. S., & Prince, J. L. (2013). Automatic magnetic resonance spinal cord segmentation with topology constraints for variable fields of view. *Neuroimage*, *83*, 1051–1062.

Ciccarelli, O., Wheeler-Kingshott, C. A., McLean, M. A., Cercignani, M., Wimpey, K., Miller, D. H., & Thompson, A. J. (2007). Spinal cord spectroscopy and diffusion-based tractography toassess acute disability in multiple sclerosis. *Brain*, *130*(Pt 8), 2220–2231.

Cohen-Adad, J., Descoteaux, M., Rossignol, S., Hoge, R. D., Deriche, R., & Benali, H. (2008). Detection of multiple pathways in the spinal cord using q-ballimaging. *Neuroimage*, *42*(2), 739–749.

Cohen-Adad, J., El Mendili, M.-M., Lehéricy, S., Pradat, P.-F., Blancho, S., Rossignol, S., & Benali, H. (2011). Demyelination and degeneration in the injured human spinal cord detected with diffusion and magnetization transfer MRI. *NeuroImage*, *55*(3), 1024–33. https://doi.org/10.1016/j.neuroimage.2010.11.089

Cohen-Adad, J., El Mendili, M.-M., Morizot-Koutlidis, R., Lehéricy, S., Meininger, V., Blancho, S., … Pradat, P.-F. (2013). Involvement of spinal sensory pathway in ALS andspecificity of cord atrophy to lower motor neurondegeneration. *Amyotroph. Lateral Scler. Frontotemporal Degener.*, *14*(1), 30–38.

Cohen-Adad, J., Leblond, H., Delivet-Mongrain, H., Martinez, M., Benali, H., & Rossignol, S. (2011). Wallerian degeneration after spinal cord lesions in catsdetected with diffusion tensor imaging. *Neuroimage*, *57*(3), 1068–1076.

Cohen-Adad, J., Zhao, W., Keil, B., Ratai, E.-M., Triantafyllou, C., Lawson, R., … Atassi, N. (2013). {7-T} {MRI} of the spinal cord can detect lateral corticospinal tract abnormality in amyotrophic lateral sclerosis. *Muscle Nerve*, *47*(5), 760–762.

Coulon, O., Hickman, S. J., Parker, G. J., Barker, G. J., Miller, D. H., & Arridge, S. R. (2002). Quantification of spinal cord atrophy from magnetic resonance images via a B-spline active surface model. *Magnetic Resonance in Medicine : Official Journal of the Society of Magnetic Resonance in Medicine / Society of Magnetic Resonance in Medicine*, *47*(6), 1176–85. https://doi.org/10.1002/mrm.10162

Cruz-Sánchez, F. F., Moral, A., Tolosa, E., de Belleroche, J., & Rossi, M. L. (1998). Evaluation of neuronal loss, astrocytosis and abnormalities of cytoskeletal components of large motor neurons in the human anterior horn in aging. *J. Neural Transm.*, *105*(6–7), 689–701.

De Leener, B., Cohen-Adad, J., & Kadoury, S. (2015). Automatic Segmentation of the Spinal Cord and Spinal Canal Coupled with Vertebral Labeling. *IEEE Transactions on Medical Imaging*, *34*(8). https://doi.org/10.1109/TMI.2015.2437192

De Leener, B., Kadoury, S., & Cohen-Adad, J. (2014). Robust, accurate and fast automatic segmentation of the spinal cord. *NeuroImage*, *98*. https://doi.org/10.1016/j.neuroimage.2014.04.051

De Leener, B., Roux, A., Taso, M., Callot, V., & Cohen-Adad, J. (2015). Spinal cord gray and white matter segmentation using atlasdeformation. In *Proceedings of the 23th Annual Meeting of ISMRM, Toronto,Canada, Toronto* (Vol. 4424, p. 4424). Toronto.

Despotović, I., Goossens, B., & Philips, W. (2015). MRI segmentation of the human brain: challenges, methods,and applications. *Comput. Math. Methods Med.*, *2015*, 450341.

Dubuc, B. (2015). The brain from top to bottom.

El Mendili, M.-M., Chen, R., Tiret, B., Pélégrini-Issac, M., Cohen-Adad, J., Lehéricy, S., … Benali, H. (2015). Validation of a semi-automated spinal cord segmentationmethod. *J. Magn. Reson. Imaging*, *41*(2), 454–459.

El Mendili, M.-M., Chen, R., Tiret, B., Villard, N., Trunet, S., Pélégrini-Issac, M., … Benali, H. (2015). Fast and accurate semi-automated segmentation method of spinal cord {MR} images at {3T} applied to the construction of a cervical spinal cord template. *PLoS One*, *10*(3), e0122224.

Ellingson, B. M., Ulmer, J. L., & Schmit, B. D. (2007). Gray and white matter delineation in the human spinal cordusing diffusion tensor imaging and fuzzy logic. *Acad. Radiol.*, *14*(7), 847–858.

Ellingson, B. M., Ulmer, J. L., & Schmit, B. D. (2008). Morphology and morphometry of human chronic spinal cord injuryusing diffusion tensor imaging and fuzzy logic. *Ann. Biomed. Eng.*, *36*(2), 224–236.

Fonov, V. S., Le Troter, A., Taso, M., De Leener, B., Lévêque, G., Benhamou, M., … Cohen-Adad, J. (2014). Framework for integrated MRI average of the spinal cordwhite and gray matter: the MNI-Poly-AMU template. *Neuroimage*, *102 Pt 2*, 817–827.

Fradet, L., Arnoux, P.-J., Ranjeva, J.-P., Petit, Y., & Callot, V. (2014). Morphometrics of the entire human spinal cord and spinalcanal measured from in vivo high-resolution anatomicalmagnetic resonance imaging. *Spine*, *39*(4), E262–9.

Freund, P., Wheeler-Kingshott, C., Jackson, J., Miller, D., Thompson, A., & Ciccarelli, O. (2010). Recovery after spinal cord relapse in multiple sclerosis is predicted by radial diffusivity. *Mult. Scler.*, *16*(10), 1193–1202.

Fujimoto, K., Polimeni, J. R., van der Kouwe, A. J. W., Reuter, M., Kober, T., Benner, T., … Wald, L. L. (2014). Quantitative comparison of cortical surface reconstructionsfrom MP2RAGE and multi-echo MPRAGE data at 3 and 7 T. *Neuroimage*, *90*, 60–73.

Good, C. D., Johnsrude, I. S., Ashburner, J., Henson, R. N., Friston, K. J., & Frackowiak, R. S. (2001). A voxel-based morphometric study of aging in 465 normal adulthuman brains. *Neuroimage*, *14*(1 Pt 1), 21–36.

Grady, L. (2006). Random walks for image segmentation. *IEEE Trans. Pattern Anal. Mach. Intell.*, *28*(11), 1768–1783.

Gullapalli, J., Krejza, J., & Schwartz, E. D. (2006). In vivo DTI evaluation of white matter tracts in rat spinalcord. *J. Magn. Reson. Imaging*, *24*(1), 231–234.

Held, P., Dorenbeck, U., Seitz, J., Fründ, R., & Albrich, H. (2003). MRI of the abnormal cervical spinal cord using 2D spoiledgradient echo multiecho sequence (MEDIC) with magnetizationtransfer saturation pulse. A T2* weighted feasibility study. *J. Neuroradiol.*, *30*(2), 83–90.

Held, P., Seitz, J., Fründ, R., Nitz, W., Lenhart, M., & Geissler, A. (2001). Comparison of two-dimensional gradient echo, turbo spin echoand two-dimensional turbo gradient spin echo sequences inMRI of the cervical spinal cord anatomy. *Eur. J. Radiol.*, *38*(1), 64–71.

Hickman, S. J., Hadjiprocopis, A., Coulon, O., Miller, D. H., & Barker, G. J. (2004). Cervical spinal cord {MTR} histogram analysis in multiple sclerosis using a {3D} acquisition and a B-spline active surface segmentation technique. *Magn. Reson. Imaging*, *22*(6), 891–895.

Horsfield, M. A., Sala, S., Neema, M., Absinta, M., Bakshi, A., Sormani, M. P., … Filippi, M. (2010). Rapid semi-automatic segmentation of the spinal cord frommagnetic resonance images: application in multiple sclerosis. *Neuroimage*, *50*(2), 446–455.

Ingle, G. T., Stevenson, V. L., Miller, D. H., & Thompson, A. J. (2003). Primary progressive multiple sclerosis: a 5-year clinical andMR study. *Brain*, *126*(Pt 11), 2528–2536.

Kalkers, N. F., Barkhof, F., Bergers, E., van Schijndel, R., & Polman, C. H. (2002). The effect of the neuroprotective agent riluzole on {MRI} parameters in primary progressive multiple sclerosis: a pilot study. *Mult. Scler.*, *8*(6), 532–533.

Kameyama, T., Hashizume, Y., & Sobue, G. (1996). Morphologic features of the normal human cadaveric spinalcord. *Spine*, *21*(11), 1285–1290.

Kawahara, J., McIntosh, C., Tam, R., & Hamarneh, G. (2013). Augmenting Auto-context with Global Geometric Features forSpinal Cord Segmentation. In *Machine Learning in Medical Imaging* (pp. 211–218). Nagoya, Japan: Springer, Cham.

Kawahara, J., McIntosh, C., Tam, R., & Hamarneh, G. (2013). Globally optimal spinal cord segmentation using a minimal path in high dimensions. In *2013 {IEEE} 10th International Symposium on Biomedical Imaging* (pp. 848–851). IEEE Computer Society.

Kayal, N. (2013). *An investigation of grow cut algorithm for segmentation of MRIspinal cord images in normals and patients with SCI*. Temple University Graduate School, Ann Arbor.

Kearney, H., Yiannakas, M. C., Abdel-Aziz, K., Wheeler-Kingshott, C. A. M., Altmann, D. R., Ciccarelli, O., & Miller, D. H. (2014). Improved MRI quantification of spinal cord atrophy inmultiple sclerosis. *J. Magn. Reson. Imaging*, *39*(3), 617–623.

Kidd, D., Thorpe, J. W., Thompson, A. J., Kendall, B. E., Moseley, I. F., MacManus, D. G., … Miller, D. H. (1993). Spinal cord MRI using multi-array coils and fast spin echo.II. Findings in multiple sclerosis. *Neurology*, *43*(12), 2632–2637.

Klawiter, E. C., Schmidt, R. E., Trinkaus, K., Liang, H.-F., Budde, M. D., Naismith, R. T., … Benzinger, T. L. (2011). Radial diffusivity predicts demyelination in ex vivo multiple sclerosis spinal cords. *Neuroimage*, *55*(4), 1454–1460.

Klein, J. P., Arora, A., Neema, M., Healy, B. C., Tauhid, S., Goldberg-Zimring, D., … Bakshi, R. (2011). A {3T} {MR} imaging investigation of the topography of whole spinal cord atrophy in multiple sclerosis. *AJNR Am. J. Neuroradiol.*, *32*(6), 1138–1142.

Koh, J., Kim, T., Chaudhary, V., & Dhillon, G. (2010). Automatic segmentation of the spinal cord and the dural sac in lumbar {MR} images using gradient vector flow field. In *2010 Annual International Conference of the {IEEE} Engineering in Medicine and Biology* (pp. 3117–3120). Buenos Aires: IEEE.

Koh, J., Scott, P. D., Chaudhary, V., & Dhillon, G. (2011). An automatic segmentation method of the spinal canal from clinical {MR} images based on an attention model and an active contour model. In *2011 {IEEE} International Symposium on Biomedical Imaging: From Nano to Macro* (pp. 1467–1471). ieeexplore.ieee.org.

Kurtzke, J. F. (1983). Rating neurologic impairment in multiple sclerosis: an expandeddisability status scale (EDSS). *Neurology*, *33*(11), 1444–1452.

Law, M. W. K., Garvin, G. J., Tummala, S., Tay, K., Leung, A. E., & Li, S. (2013). Gradient competition anisotropy for centerline extraction andsegmentation of spinal cords. *Inf. Process. Med. Imaging*, *23*, 49–61.

Lévy, S., Benhamou, M., Naaman, C., Rainville, P., Callot, V., & Cohen-Adad, J. (2015). White matter atlas of the human spinal cord with estimation ofpartial volume effect. *Neuroimage*, *119*(0), 262–271.

Lin, X., Blumhardt, L. D., & Constantinescu, C. S. (2003). The relationship of brain and cervical cord volume todisability in clinical subtypes of multiple sclerosis: athree-dimensional MRI study. *Acta Neurol. Scand.*, *108*(6), 401–406.

Lindberg, P. G., Feydy, A., & Maier, M. A. (2010). White matter organization in cervical spinal cord relates differently to age and control of grip force in healthy subjects. *J. Neurosci.*, *30*(11), 4102–4109.

Liu, C., Edwards, S., Gong, Q., Roberts, N., & Blumhardt, L. D. (1999). Three dimensional MRI estimates of brain and spinal cordatrophy in multiple sclerosis. *J. Neurol. Neurosurg. Psychiatry*, *66*(3), 323–330.

Liu, Y., Wang, J., Daams, M., Weiler, F., Hahn, H. K., Duan, Y., … Barkhof, F. (2015). Differential patterns of spinal cord and brain atrophy inNMO and MS. *Neurology*, *84*(14), 1465–1472.

Losseff, N. A., Webb, S. L., O'Riordan, J. I., Page, R., Wang, L., Barker, G. J., … Thompson, A. J. (1996). Spinal cord atrophy and disability in multiple sclerosis. Anew reproducible and sensitive MRI method with potential tomonitor disease progression. *Brain*, *119 (Pt 3)*(3), 701–708.

Lucas, B. C., Bogovic, J. A., Carass, A., Bazin, P.-L., Prince, J. L., Pham, D. L., & Landman, B. A. (2010). The Java Image Science Toolkit ({JIST}) for rapid prototyping and publishing of neuroimaging software. *Neuroinformatics*, *8*(1), 5–17.

Lundell, H., Barthelemy, D., Skimminge, A., Dyrby, T. B., Biering-Sørensen, F., & Nielsen, J. B. (2011). Independent spinal cord atrophy measures correlate to motorand sensory deficits in individuals with spinal cord injury. *Spinal Cord*, *49*(1), 70–75.

MacMillan, E. L., Mädler, B., Fichtner, N., Dvorak, M. F., Li, D. K. B., Curt, A., & MacKay, A. L. (2011). Myelin water and T(2) relaxation measurements in the healthycervical spinal cord at 3.0T: repeatability and changes withage. *Neuroimage*, *54*(2), 1083–1090.

Marques, J. P., Kober, T., Krueger, G., der Zwaag, W., de Moortele, P.-F. cois, & Gruetter, R. (2010). MP2RAGE, a self bias-field corrected sequence for improvedsegmentation and T1-mapping at high field. *Neuroimage*, *49*(2), 1271–1281.

McDonald, W. I., Compston, A., Edan, G., Goodkin, D., Hartung, H. P., Lublin, F. D., … Wolinsky, J. S. (2001). Recommended diagnostic criteria for multiple sclerosis:guidelines from the International Panel on the diagnosis ofmultiple sclerosis. *Ann. Neurol.*, *50*(1), 121–127.

McIntosh, C., & Hamarneh, G. (2006). Spinal crawlers: deformable organisms for spinal cord segmentation and analysis. *Medical Image Computing and Computer-Assisted Intervention : MICCAI … International Conference on Medical Image Computing and Computer-Assisted Intervention*, *9*(Pt 1), 808–15. Retrieved from http://www.ncbi.nlm.nih.gov/pubmed/17354965

McIntosh, C., Hamarneh, G., Toom, M., & Tam, R. C. (2011). Spinal Cord Segmentation for Volume Estimation in Healthy and Multiple Sclerosis Subjects Using Crawlers and Minimal Paths. In *2011 {IEEE} First International Conference on Healthcare Informatics, Imaging and Systems Biology* (pp. 25–31). ieeexplore.ieee.org.

Miyanji, F., Furlan, J. C., Aarabi, B., Arnold, P. M., & Fehlings, M. G. (2007). Acute cervical traumatic spinal cord injury: MR imagingfindings correlated with neurologic outcome–prospective studywith 100 consecutive patients. *Radiology*, *243*(3), 820–827.

Mukherjee, D. P., Cheng, I., Ray, N., Mushahwar, V., Lebel, M., & Basu, A. (2010). Automatic segmentation of spinal cord MRI using symmetricboundary tracing. *IEEE Trans. Inf. Technol. Biomed.*, *14*(5), 1275–1278.

Nakamura, M., Miyazawa, I., Fujihara, K., Nakashima, I., Misu, T., Watanabe, S., … Itoyama, Y. (2008). Preferential spinal central gray matter involvement inneuromyelitis optica. An MRI study. *J. Neurol.*, *255*(2), 163–170.

Narayana, P. A., Grill, R. J., Chacko, T., & Vang, R. (2004). Endogenous recovery of injured spinal cord: longitudinal in vivo magnetic resonance imaging. *J. Neurosci. Res.*, *78*(5), 749–759.

Onu, M., Gervai, P., Cohen-Adad, J., Lawrence, J., Kornelsen, J., Tomanek, B., & Sboto-Frankenstein, U. N. (2010). Human cervical spinal cord funiculi: investigation withmagnetic resonance diffusion tensor imaging. *J. Magn. Reson. Imaging*, *31*(4), 829–837.

Papinutto, N., Schlaeger, R., Panara, V., Zhu, A. H., Caverzasi, E., Stern, W. A., … G. (2015). Age, gender and normalization covariates for spinal cord graymatter and total cross-sectional areas at cervical andthoracic levels: A 2D phase sensitive inversion recoveryimaging study. *PLoS One*, *10*(3), e0118576.

Peters, A. M., Brookes, M. J., Hoogenraad, F. G., Gowland, P. A., Francis, S. T., Morris, P. G., & Bowtell, R. (2007). T2* measurements in human brain at 1.5, 3 and 7 T. *Magn. Reson. Imaging*, *25*(6), 748–753.

Pezold, S., Amann, M., Weier, K., Fundana, K., Radue, E. W., Sprenger, T., & Cattin, P. C. (2014). A semi-automatic method for the quantification of spinal cordatrophy. In *Computational Methods and Clinical Applications for SpineImaging* (pp. 143–155). Springer International Publishing.

Pezold, S., Fundana, K., Amann, M., Andelova, M., Pfister, A., Sprenger, T., & Cattin, P. C. (2015). Automatic Segmentation of the Spinal Cord Using Continuous MaxFlow with Cross-sectional Similarity Prior and TubularityFeatures. In J. Yao, B. Glocker, T. Klinder, & S. Li (Eds.), *Recent Advances in Computational Methods and ClinicalApplications for Spine Imaging* (Vol. 20, pp. 107–118). Springer International Publishing.

Qian, W., Chan, Q., Mak, H., Zhang, Z., Anthony, M.-P., Yau, K. K.-W., … Kim, M. (2011). Quantitative assessment of the cervical spinal cord damage inneuromyelitis optica using diffusion tensor imaging at 3 Tesla. *J. Magn. Reson. Imaging*, *33*(6), 1312–1320.

Rossignol, S., Martinez, M., Escalona, M., Kundu, A., Delivet-Mongrain, H., Alluin, O., & Gossard, J.-P. (2015). The ``beneficial'' effects of locomotor training after varioustypes of spinal lesions in cats and rats. *Prog. Brain Res.*, *218*, 173–198.

Samson, R. S., Ciccarelli, O., & others. (2013). Tissue-and column-specific measurements from multi-parameter mapping of the human cervical spinal cord at 3 {T}. *NMR Biomed.*, *26*, 1823–1830.

Schlaeger, R., Papinutto, N., Panara, V., Bevan, C., Lobach, I. V, Bucci, M., … Henry, R. G. (2014). Spinal cord gray matter atrophy correlates with multiple sclerosis disability. *Ann. Neurol.*, *76*(4), 568–580.

Sdika, M., Callot, V., Hebert, M., Duhamel, G., & Cozzone, P. J. (2010). Segmentation of the structure of the mouse spinal cord on DTIimages. In *Proceedings of the 19th scientific meeting, internationalsociety for magnetic resonance in medicine, ISMRM, Stockholm* (Vol. 5092, p. 5092). Stockholm.

Shefner, J. M., Watson, M. L., Simionescu, L., Caress, J. B., Burns, T. M., Maragakis, N. J., … Rutkove, S. B. (2011). Multipoint incremental motor unit number estimation as an outcome measure in {ALS}. *Neurology*, *77*(3), 235–241.

Sigmund, E. E., Suero, G. A., Hu, C., McGorty, K., Sodickson, D. K., Wiggins, G. C., & Helpern, J. A. (2012). High-resolution human cervical spinal cord imaging at 7 {T}. *NMR Biomed.*, *25*(7), 891–899.

Sled, J. G., Zijdenbos, A. P., & Evans, A. C. (1998). A nonparametric method for automatic correction of intensitynonuniformity in MRI data. *IEEE Trans. Med. Imaging*, *17*(1), 87–97.

Smith, S. A., Edden, R. A. E., Farrell, J. A. D., Barker, P. B., & Van Zijl, P. C. M. (2008). Measurement of {T1} and {T2} in the cervical spinal cord at 3 tesla. *Magn. Reson. Med.*, *60*(1), 213–219.

Smith, S. A., Jones, C. K., Gifford, A., Belegu, V., Chodkowski, B., Farrell, J. A. D., … van Zijl, P. C. M. (2010). Reproducibility of tract-specific magnetization transfer and diffusion tensor imaging in the cervical spinal cord at 3 tesla. *NMR Biomed.*, *23*(2), 207–217.

Sonkova, P., Evangelou, I. E., Gallo, A., Cantor, F. K., Ohayon, J., McFarland, H. F., & Bagnato, F. (2008). Semi-automatic segmentation and modelling of the cervical spinalcord for volume

quantification in multiple sclerosis patientsfrom magnetic resonance images. In J. M. Reinhardt & J. P. W. Pluim (Eds.), *Medical Imaging* (Vol. 6914, p. 69144I–69144I–10). International Society for Optics and Photonics.

Stevenson, V. L., Leary, S. M., Losseff, N. A., Parker, G. J., Barker, G. J., Husmani, Y., … Thompson, A. J. (1998). Spinal cord atrophy and disability in {MS}: a longitudinal study. *Neurology*, *51*(1), 234–238.

Stroman, P. W. (2009). Spinal fMRI investigation of human spinal cord function overa range of innocuous thermal sensory stimuli and study-relatedemotional influences. *Magn. Reson. Imaging*, *27*(10), 1333–1346.

Stroman, P. W., Figley, C. R., & Cahill, C. M. (2008). Spatial normalization, bulk motion correction andcoregistration for functional magnetic resonance imaging ofthe human cervical spinal cord and brainstem. *Magn. Reson. Imaging*, *26*(6), 809–814.

Stroman, P. W., Tomanek, B., Krause, V., Frankenstein, U. N., & Malisza, K. L. (2002). Mapping of neuronal function in the healthy and injured humanspinal cord with spinal fMRI. *Neuroimage*, *17*(4), 1854–1860.

Stroman, P. W., Wheeler-Kingshott, C., Bacon, M., Schwab, J. M., Bosma, R., Brooks, J., … Tracey, I. (2014). The current state-of-the-art of spinal cord imaging: methods. *Neuroimage*, *84*, 1070–1081.

Tang, L., Wen, Y., Zhou, Z., von Deneen, K. M., Huang, D., & Ma, L. (2013). Reduced field-of-view DTI segmentation of cervical spinetissue. *Magn. Reson. Imaging*, *31*(9), 1507–1514.

Taso, M., Girard, O., Duhamel, G., Le Troter, A., Feiweier, T., Guye, M., … Callot, V. (2015). Regional and age-related variations of the healthy spinal cordstructure assessed by multimodal MRI. In *Proceedings of the 23th annual meeting of ISMRM, Toronto,Canada* (Vol. 681, p. 681). Toronto, Canada.

Taso, M., Le Troter, A., Sdika, M., Cohen-Adad, J., Arnoux, P.-J., Guye, M., … Callot, V. (2015). A reliable spatially normalized template of the human spinal cord--Applications to automated white matter/gray matter segmentation and tensor-based morphometry ({TBM}) mapping of gray matter alterations occurring with age. *Neuroimage*, *117*, 20–28.

Taso, M., Le Troter, A., Sdika, M., Ranjeva, J.-P., Guye, M., Bernard, M., & Callot, V. (2014). Construction of an in vivo human spinal cord atlas based onhigh-resolution MR images at cervical and thoracic levels:preliminary results. *MAGMA*, *27*(3), 257–267.

Tator, C. H., & Fehlings, M. G. (1991). Review of the secondary injury theory of acute spinal cordtrauma with emphasis on vascular mechanisms. *J. Neurosurg.*, *75*(1), 15–26.

Tench, C. R., Morgan, P. S., & Constantinescu, C. S. (2005). Measurement of cervical spinal cord cross-sectional area byMRI using edge detection and partial volume correction. *J. Magn. Reson. Imaging*, *21*(3), 197–203.

Udupa, J. K., & Samarasekera, S. (1996). Fuzzy Connectedness and Object Definition: Theory, Algorithms,and Applications in Image Segmentation. *Graphical Models and Image Processing*, *58*(3), 246–261.

Ullmann, E., Pelletier Paquette, J. F., Thong, W. E., & Cohen-Adad, J. (2014). Automatic labeling of vertebral levels using a robust template-based approach. *Int. J. Biomed. Imaging*, *2014*, 719520.

Valsasina, P., Horsfield, M. A., Rocca, M. A., Absinta, M., Comi, G., & Filippi, M. (2012). Spatial normalization and regional assessment of cordatrophy: voxel-based analysis of cervical cord 3DT1-weighted images. *AJNR Am. J. Neuroradiol.*, *33*(11), 2195–2200.

Van Uitert, R., Bitter, I., & Butman, J. A. (2005). Semi-automatic spinal cord segmentation and quantification. *Int. Congr. Ser.*, *1281*(0), 224–229.

Varma, G., Duhamel, G., de Bazelaire, C., & Alsop, D. C. (2015). Magnetization transfer from inhomogeneously broadened lines: Apotential marker for myelin. *Magn. Reson. Med.*, *73*(2), 614–622.

Wang, Y., Wu, A., Chen, X., Zhang, L., Lin, Y., Sun, S., … Lu, Z. (2014). Comparison of clinical characteristics between neuromyelitisoptica spectrum disorders with and without spinal cord atrophy. *BMC Neurol.*, *14*, 246.

Warfield, S. K., Zou, K. H., & Wells, W. M. (2004). Simultaneous truth and performance level estimation ({STAPLE)}: an algorithm for the validation of image segmentation. *IEEE Trans. Med. Imaging*, *23*(7), 903–921.

Weiler, F., Daams, M., Lukas, C., Barkhof, F., & Hahn, H. K. (2015). Highly accurate volumetry of the spinal cord. In *SPIE Medical Imaging* (Vol. 9413, pp. 941302–941302–6). Orlando, Florida: International Society for Optics and Photonics.

Wheeler-Kingshott, C. A., Stroman, P. W., Schwab, J. M., Bacon, M., Bosma, R., Brooks, J., … Tracey, I. (2014). The current state-of-the-art of spinal cord imaging: applications. *Neuroimage*, *84*, 1082–1093.

Wingerchuk, D. M., Hogancamp, W. F., O'Brien, P. C., & Weinshenker, B. G. (1999). The clinical course of neuromyelitis optica (Devic's syndrome). *Neurology*, *53*(5), 1107–1114.

Xu, J., Shimony, J. S., Klawiter, E. C., Snyder, A. Z., Trinkaus, K., Naismith, R. T., … Song, S.-K. (2013). Improved in vivo diffusion tensor imaging of human cervicalspinal cord. *Neuroimage*, *67*, 64–76.

Yen, C., Su, H.-R., Lai, S.-H., Liu, K.-C., & Lee, R.-R. (2013). 3D Spinal Cord and Nerves Segmentation from STIR-MRI. In *Proceedings of the International Computer Symposium ICS 2012* (pp. 383–392). Hualien, Taiwan.

Yiannakas, M. C., Kearney, H., Samson, R. S., Chard, D. T., Ciccarelli, O., Miller, D. H., & Wheeler-Kingshott, C. A. M. (2012). Feasibility of gray matter and white matter segmentation ofthe upper cervical cord in vivo: a pilot study withapplication to magnetization transfer measurements. *Neuroimage*, *63*(3), 1054–1059.

Yiannakas, M. C., Mustafa, A. M., De Leener, B., Kearney, H., Tur, C., Altmann, D. R., … Gandini Wheeler-Kingshott, C. A. M. (2016). Fully automated segmentation of the cervical cord from T1-weighted MRI using PropSeg: Application to multiple sclerosis. *NeuroImage: Clinical*, *10*. https://doi.org/10.1016/j.nicl.2015.11.001

Zackowski, K. M., Smith, S. A., Reich, D. S., Gordon-Lipkin, E., Chodkowski, B. A., Sambandan, D. R., … Calabresi, P. A. (2009). Sensorimotor dysfunction in multiple sclerosis and column-specific magnetization transfer-imaging abnormalities in the spinal cord. *Brain*, *132*(Pt 5), 1200–1209.

Zhang, Y., Brady, M., & Smith, S. (2001). Segmentation of brain MR images through a hidden Markovrandom field model and the expectation-maximization algorithm. *IEEE Trans. Med. Imaging*, *20*(1), 45–57.

Zivadinov, R., Banas, A. C., Yella, V., Abdelrahman, N., Weinstock-Guttman, B., & Dwyer, M. G. (2008). Comparison of three different methods for measurement ofcervical cord atrophy in multiple sclerosis. *AJNR Am. J. Neuroradiol.*, *29*(2), 319–325.

2.4.2.8   Annex 1 – Software for SC segmentation

Table 2.2: Available software suites

	OS/platform	Free	Method	References
JIM	Multi (Java)	no	2D surface contour	(Horsfield et al., 2010)
	http://www.xinapse.com/Manual/index.html			
SCT (sct_propseg)	Linux / OSX (Windows on virtual machine)	yes	3D surface propagation	(De Leener et al., 2015, 2014; De Leener et al., 2015)
	http://sourceforge.net/projects/spinalcordtoolbox/			
JIST	Multi (Java)	yes	Groupwise Multi-Atlas segmentation	(Asman et al., 2014; Chen et al., 2013; Lucas et al., 2010)
	http://www.nitrc.org/projects/jist			
SpineSeg	Unix	yes	Image Foresting transform	(Bergo, Franca, Chevis, & Cendes, 2012)
	http://www.lni.hc.unicamp.br/app/spineseg/			
Spinalfmri8	Multi (Matlab)	yes	Spatial normalization	(Stroman et al., 2008)
	http://post.queensu.ca/~stromanp/software.html			

2.4.2.9   Annex 2 – Animal spinal cord segmentation methods

The review focused on segmentation methods for human, however several studies also introduced interesting algorithms for segmenting the spinal cord in animals. Two of them are briefly detailed below.

2.4.2.9.1   *Automatic segmentation into WM/GM substructures (lateral, dorsal, ventral)*

Diffusion Tensor Imaging (DTI) is now largely used in spinal cord rodent models either to describe the potential alteration/regeneration consequent to the disease or to test the effects of different therapeutic strategies. In these rodent studies, as for human studies, fully automated segmentation into WM/GM subregions (lateral, anterior, posterior) is thus of great importance as it removes a tedious operation during the analysis of the data. In the method developed by Sdika *et al.* (Sdika,

Callot, Hebert, Duhamel, & Cozzone, 2010), the segmentation process consisted in four steps: (i) a small patch containing the spinal cord was first detected using a machine learning procedure (SVM); (ii) the mask of the spinal cord was then computed on a Mean Diffusivity Weighted Image (MDWI) using FAST (Y. Zhang, Brady, & Smith, 2001); (iii) the WM/GM segmentation (cf. Figure 2.22b) was then performed on a diffusion sensitized image along the spinal cord axis, using FAST as well; (iv) the spinal cord was finally divided into its left and right side by finding the best symmetry axis on the input WM/GM segmentation image (cf. Figure 2.22c), and into ventral and dorsal GM by a line orthogonal to the left/right (L/R) axis (cf. Figure 2.22d). To discriminate sub-structures of WM (cf. Figure 2.22e), the first point on the L/R axis after the spinal cord mask was determined (P2) and the Ur point (resp Ul), which was the furthest from P2 in the right (resp. left) part of the spinal cord, was used to discriminate right (resp. left) lateral WM from ventral WM. The Dr point (resp Dl), defined as the point of the WM/GM border the furthest from Ur (resp Ul) was used to discriminate right (resp. left) lateral from dorsal WM. Five mice were used as a training group for SVM and the method was tested on the 13 remaining mice. Future works should now include adaptation of the process to pathological mice or to human data.

2.4.2.9.2 *Automatic segmentation using body symmetry*

Mukherjee *et al.* (2010) (Mukherjee et al., 2010) have developed the first method that uses the body symmetry to segment the spinal cord automatically, in order to assist rehabilitation surgery planning. The algorithm is based on an image-gradient-based open-ended active contour and has been applied on T2*-weighted images of cat's spinal cord. It can be described by the following steps: (i) the axis of symmetry of the body is detected based on the Bhattacharya coefficient, (ii) the boundaries of muscle tissues around the spinal cord on one initial slice are located by actively tracing and connecting neighboring pixels of contours and by constraining the detection with the body symmetry, and (iii) the contours are deformed on neighboring slices using a dynamic-programming-based edge energy minimization technique (Archip, Erard, Egmont-Petersen, Haefliger, & Germond, 2002). Despite its application and validation on cat's spinal cord, the authors have designed the algorithm for human spinal cord as well, based on the similarity in size and shape between cats and humans spinal cords.
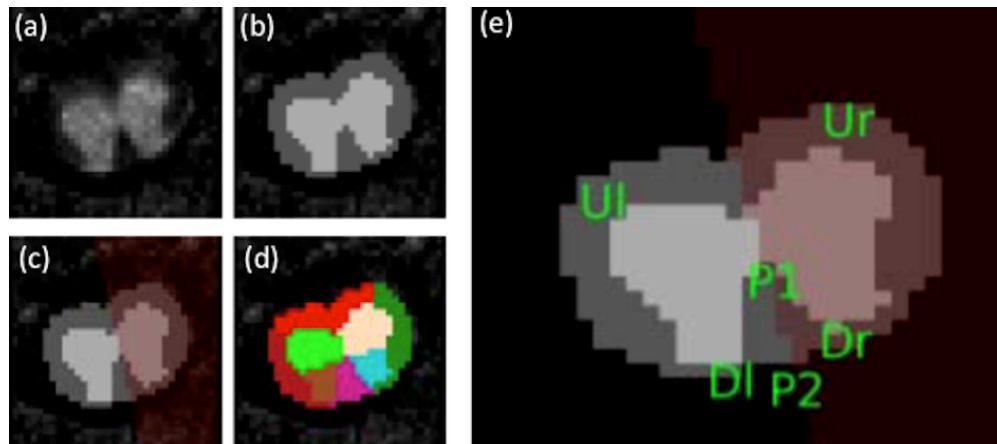
Figure 2.22: (a) DWI, (b) WM/GM segmentation, (c) Left/Right axis, (d) final segmentation into dorsal, lateral and ventral WM, as well as ventral and dorsal GM. (e) Points used to define the substructure of the WM and GM tissues. From (Sdika et al., 2010), with permission from the authors.

2.4.3 Recent progress in spinal cord segmentation

Several methods for spinal cord segmentation have been proposed recently, including spinal cord gray matter segmentation as part of the first "*spinal cord gray matter segmentation challenge*" (Prados et al., 2017). The following paragraphs will present these recent advanced techniques for spinal cord segmentation.

Prados et al. combined two existing segmentation methods based on label fusion to develop a spinal cord gray matter segmentation algorithm (Prados et al., 2016). First, an Optimized PatchMatch Label Fusion algorithm (OPAL) was used for detecting the spinal cord in T2*w MR images (Figure 2.23). Then, a Similarity and Truth Estimation for Propagated Segmentations (STEPS), based on a 2D slice-wise multi-atlas segmentation propagation strategy, was applied on small 2D patches covering the spinal cord to accurately segment the spinal cord gray matter. The authors made their algorithms freely available as part of the open-source package NiftySeg.
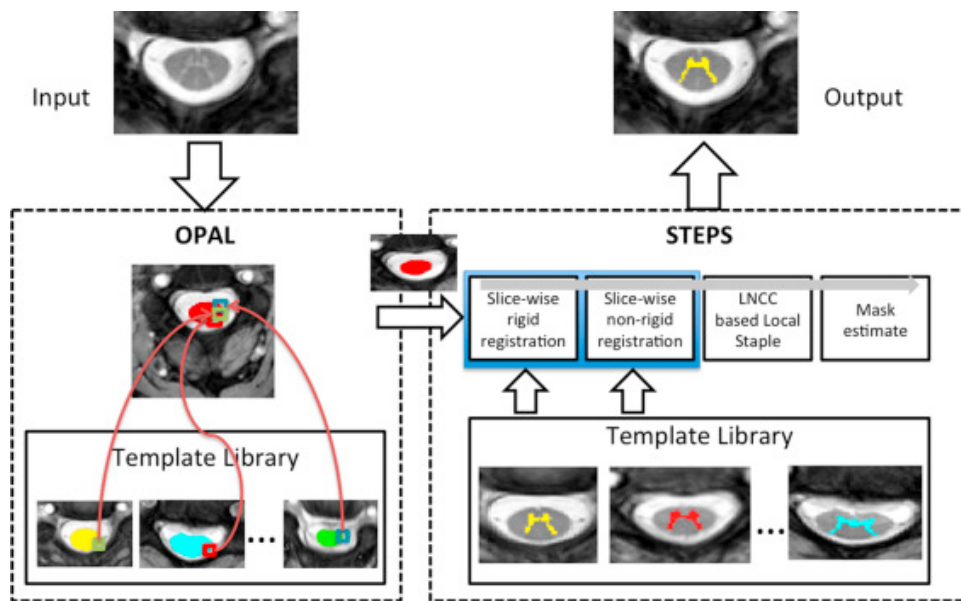
Figure 2.23: Schematic representation of the GM segmentation method proposed by (Prados et al., 2016). Adapted from (Prados et al., 2017).

Ljungberg et al. have proposed a 3D convolutional encoder network with shortcut connections, initially developed for MS lesion segmentation in the brain (Brosch et al., 2016), and further improved for spinal cord gray matter segmentation. The proposed network structure (Figure 2.24) was based on U-net architecture (Ronneberger, Fischer, & Brox, 2015) and contained 11 layers, alternating convolutional and pooling layers on the descending side and deconvolutional and

pooling layers on the ascending side of the network. Shortcut connections between the descending and ascending half of the network were used to allow the integration of high- and low-level features with variable sizes. Such network architecture has proven to improve the segmentation of structure with a wide range of size and resolution.
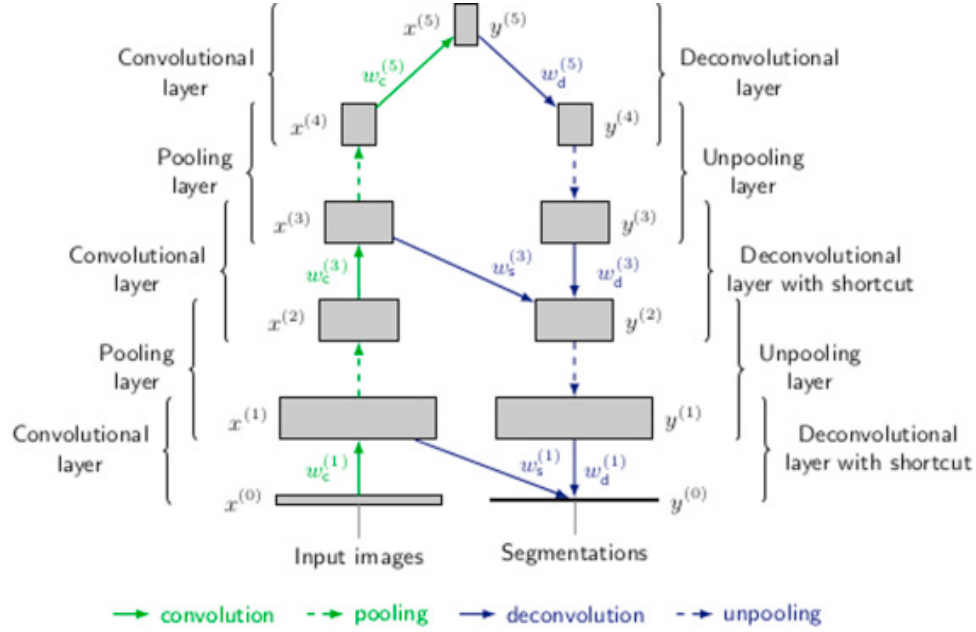
Figure 2.24: Diagram presenting the architecture of the 11-layer convolutional network proposed by (Brosch et al., 2016) for GM segmentation. Adapted from (Prados et al., 2017).

Datta et al. used a shape template registration method coupled with Morphological Geodesic Active Contour (MGAC) models to develop a semi-automated GM segmentation algorithm (Datta et al., 2017). First, the spinal cord is segmented using JIM (Horsfield et al., 2010) and images were cropped around the spinal cord and resampled to high resolution (0.05×0.05 mm^2). Second, level-specific contour templates of the GM and the whole spinal cord were created using a training dataset of 40 healthy subjects, based on registration of distance maps. Then, an initial guess of the GM segmentation was performed using nonlinear registration of the templates. Finally, a MGAC approach was to robustly register a model on the GM and provide an accurate segmentation (Figure 2.25).
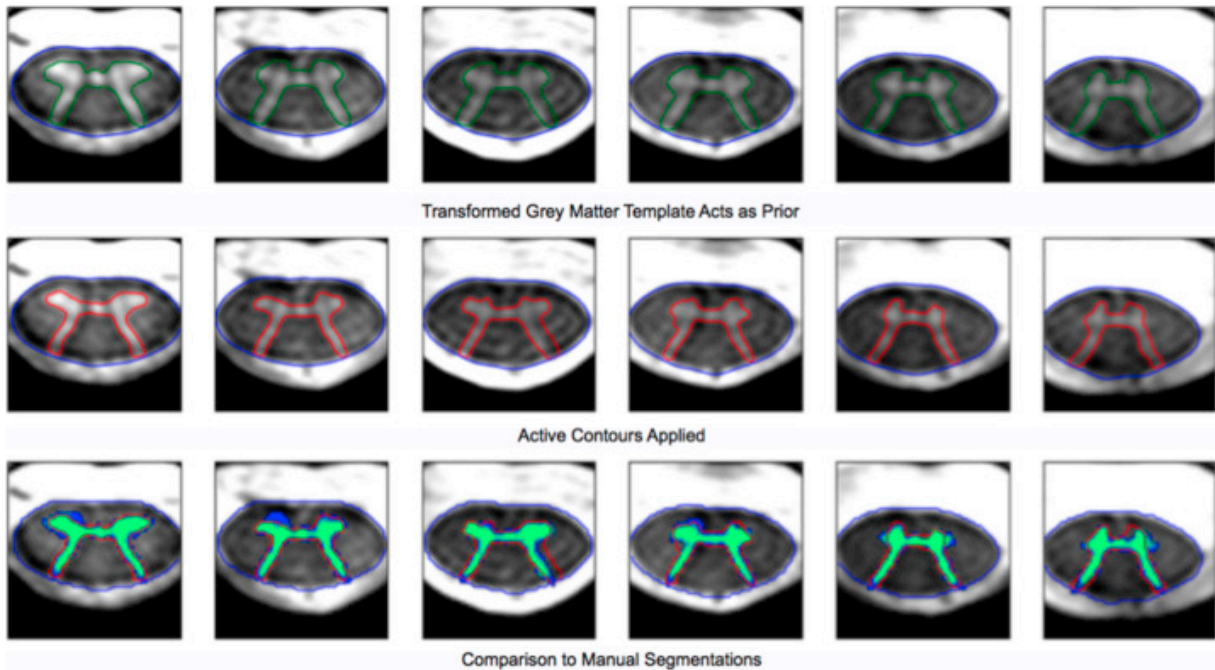
Figure 2.25: Example of segmentation performed by the MGAC method proposed by (Datta et al., 2017) and compared against manual segmentation. Adapted from (Prados et al., 2017).

Saporito et al. proposed a three-stage semi-automated supervised algorithm based on maximum entropy for GM segmentation. First, the spinal cord was semi-automatically detected using SCT (De Leener et al., 2014), and the images were denoised and intensity-normalized on a slice-by-slice basis. Then, an automatic thresholding algorithm, based on entropy maximization and sliding-windowing, was performed to extract a rough estimation of the GM segmentation. Finally, an outlier detection algorithm based on morphological characteristics was used to refine the GM segmentation.

Dupont et al. introduced a multi-atlas supervised approach to compute accurate segmentations of both the white matter and the gray matter of the spinal cord (Dupont et al., 2017) into multiple MRI contrasts (T2*w, diffusion MRI) and on both healthy and SCI populations. First, a model of the spinal cord intensity was built using manual segmentation from 40 healthy subjects. The model creation was performed by automatically extracting the spinal cord contour using PropSeg (De Leener et al., 2014), resampling the image to 0.3x0.3 mm^2, applying non-local means adaptive denoising and cropping the image around the spinal cord, while masking it to only keep the spinal cord in the image. Then, a slice-based PCA model of the spinal cord WM and GM intensities was created and manual segmentation of the WM and GM was linked to each image in the model.

Segmenting the WM and GM in a new image was performed by applying the same pre-processing steps and projecting each slice into the model, after the nonlinear registration of the images on the average image of the model. Then a similarity procedure is applied to find the closest images in the dictionary and used label fusion on the respective segmentations to provide the final segmentation of the spinal cord GM and WM (Figure 2.26).
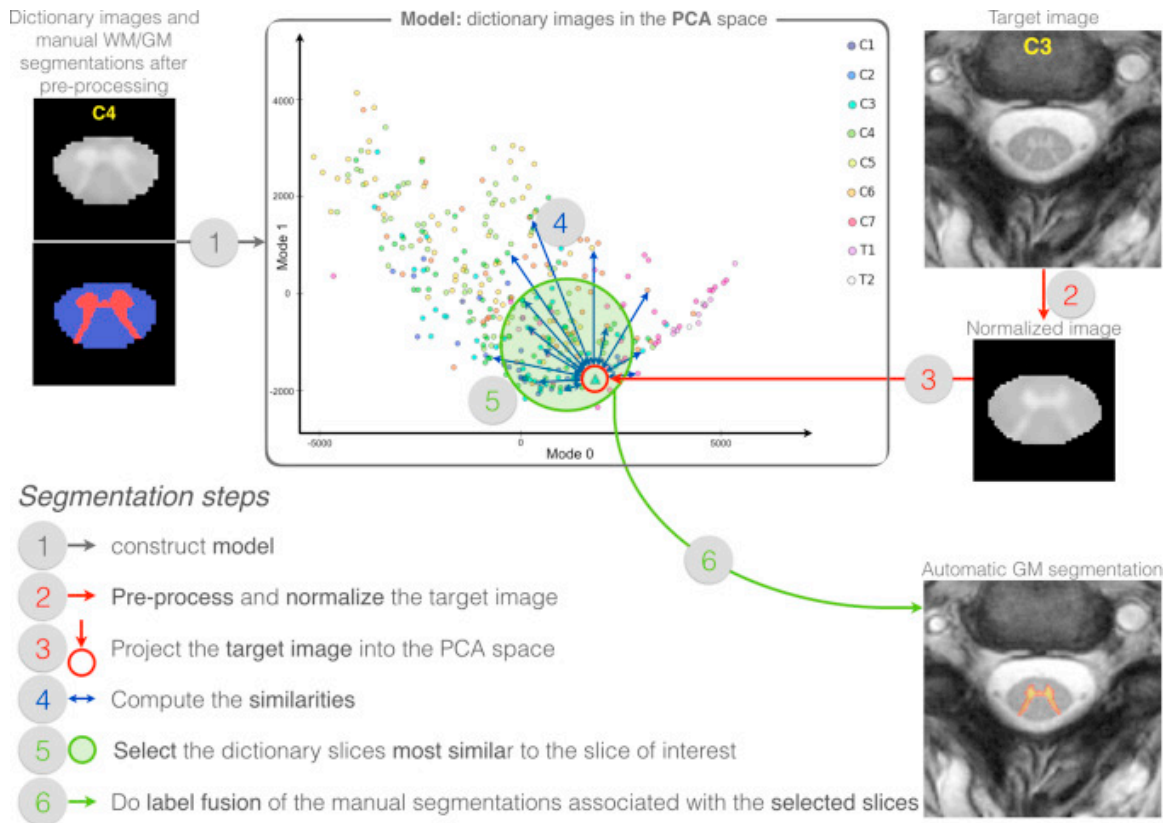
Figure 2.26: Schematic representation of the multi-atlas based method proposed by (Dupont et al., 2017) for GM segmentation. Adapted from (Prados et al., 2017).

Blaiotta et al. proposed a framework to capture both shape and intensity of spinal cord MRI using semisupervised Variational Bayes Expectation Maximization (VBEM) algorithm (Blaiotta, Jorge Cardoso, & Ashburner, 2016). First, an average shaped reference anatomy model, in the form of tissue probability maps, is constructed from 40 healthy subjects. Then, each new image is segmented by fitting this model using nonlinear registration and Gaussian mixture modelling with expectation maximization. The proposed algorithm has the potential to be successfully applied in an unsupervised fashion.

The validation of the 6 algorithms described above has been performed on a dataset of 40 healthy subjects, for which each image was manually segmented by 4 different experts. All performance results can be found in (Prados et al., 2017).

Additionally, Horvath et al. have proposed a robust variational approach for the segmentation of the spinal cord gray matter on 2D slices at C3 vertebral level (Horváth et al., 2016). Using priors on CSF, SC and GM shape, the proposed algorithm segments the gray matter by relaxing a convex variational formulation of continuous contours. The mathematical implementation of the method allows for a robust and simple algorithmic resolution of the segmentation.

Several methods have been recently proposed for the segmentation of the whole spinal cord. Liao et al. introduced an atlas-free method for segmentation of the cervical spinal cord on mid-sagittal T2w MR images (Liao, Ting, & Xiao, 2017). The proposed method uses median filtering, expectation maximization and dynamic programming for detecting the anterior and posterior edges of the spinal cord, reaching very high accuracy (Jaccard indices = 0.98 +/- 0.014). Recently, Gupta et al. proposed a semi-automated surface-based approach for segmenting the spinal cord and aorta on MRI images (Gupta, Schmitter, Uhlmann, & Unser, 2017). While the proposed method requires manual initialization, it allows an easy and robust way to manually correct the surface, in case of failure or image artifacts (Figure 2.27).
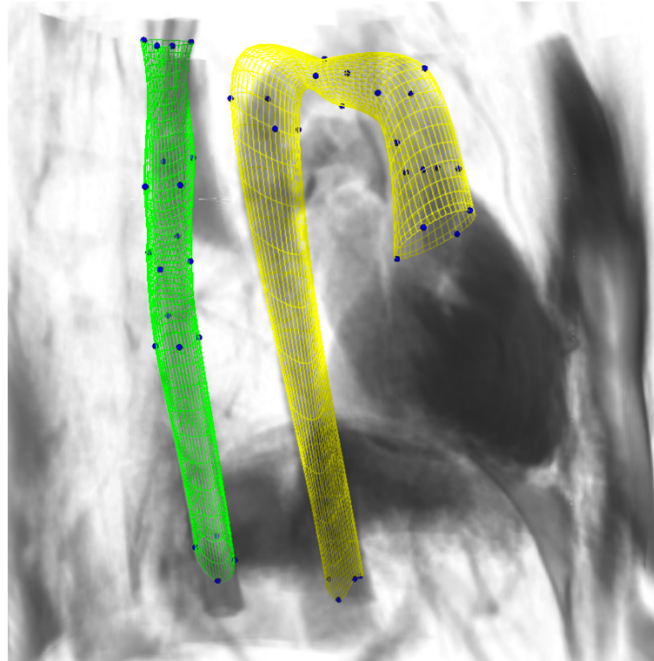
Figure 2.27: Segmentation of the spinal cord (green) and aorta (yellow) on MRI data from (Gupta et al., 2017). Adapted from (Gupta et al., 2017).

2.4.4 Spinal cord MRI template and atlases

This section aims at providing an overview of the existing MRI template and atlases of the spinal cord. Unfortunately, there are only a few templates available in the literature, due to the challenges in the acquisition of spinal cord MRI data and to the lack of comprehensive software for processing these data. Moreover, the proposed templates are usually specific to the related experiments.

Stroman et al. (Stroman et al., 2008) proposed a straight MRI template based on 1x1x2 mm^3 T2-weighted (T2w) fast-spin echo from eight healthy subjects, dedicated to functional MRI (fMRI) studies. Later, the authors proposed an extended version of the template (Stroman et al., 2012), including 2 additional subjects (Figure 2.28) and introducing a normalization approach based on the distance from the pontomedullary junction (PMJ). This normalization procedure offered an improved representation of the averaged spinal levels and the authors recently extended this template to 356 healthy subjects, covering the brainstem and the cervical spinal cord (Bosma & Stroman, 2014), and have successfully applied in pain studies (Khan & Stroman, 2015; Stroman et al., 2016).
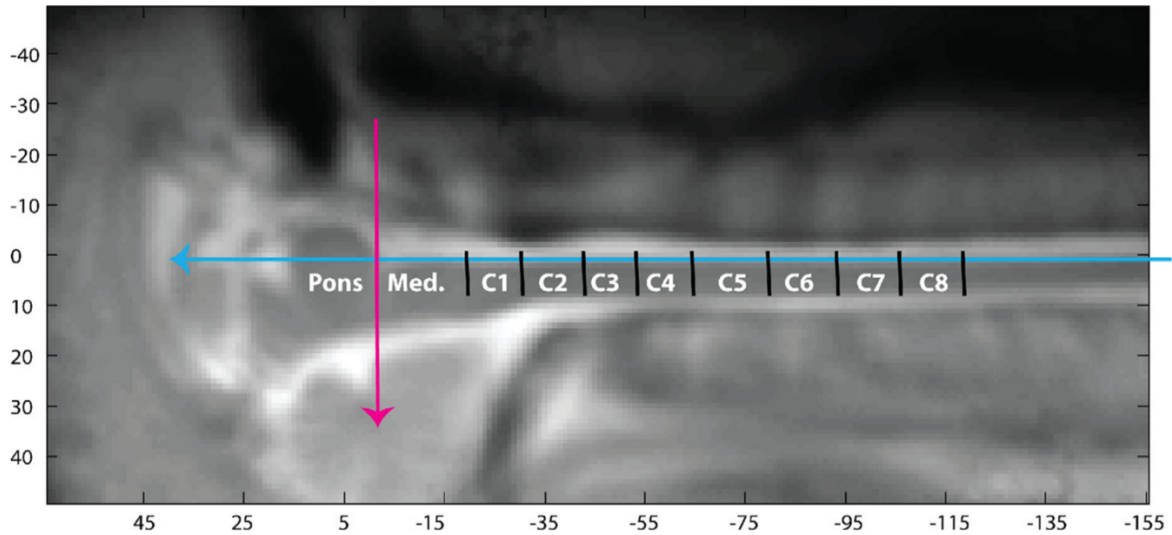
Figure 2.28: Spinal cord template and definition of the proposed normalized coordinate system. Adapted from (Stroman, Bosma, & Tsyben, 2012).
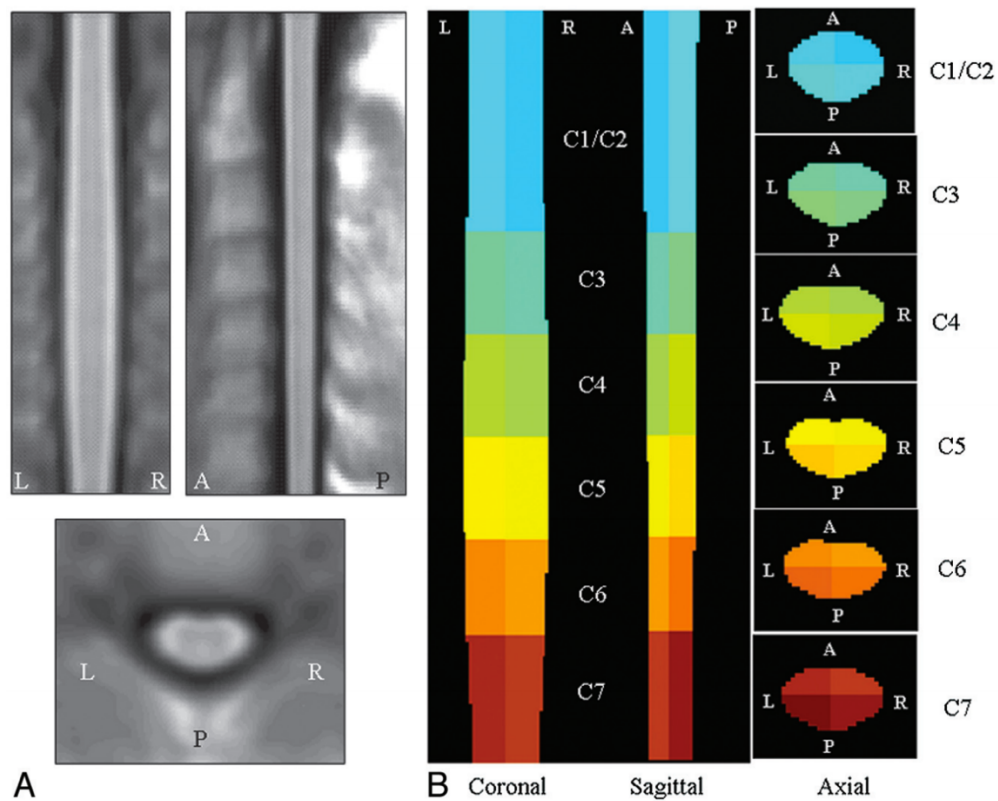
Figure 2.29: Cervical spinal cord template (A) based on the normalization of 83 healthy subjects along with masks vertebral levels and 24 reference anatomic regions (B). Adapted from (Valsasina et al., 2012).

Meanwhile, Valsasina et al. introduced a template generation procedure based on the normalization of semi-automated segmentation of the spinal cord, and applied it on T1-weighted images (Valsasina et al., 2012). The authors applied this template on a healthy population (n=83) to perform a voxel-based analysis in the context of spinal cord atrophy (Figure 2.29). Another group built a T1-weighted template of the spinal cord based on cervical MRI from 15 healthy subjects (Eippert, Finsterbusch, Bingel, & Büchel, 2009), although the main limitation was the arbitrary selection of a specific subject to which register all the others. Later, Fonov et al. (2014) have proposed the MNI-Poly-AMU (Fonov et al., 2014), a MRI template based on T2w data from 16 healthy subjects, covering C1 to T6 vertebral levels (Figure 2.30). Based on an iterative nonlinear registration procedure developed for brain templates (Fonov, Evans, et al., 2011), the MNI-Poly-AMU was the first spinal cord template to be unbiased towards a single subject. The MNI-Poly-AMU template is available for T1w, T2w and T2*w contrasts and is free and open-source. Moreover, the proposed template is merged with probabilistic maps of white and gray matter as well as an atlas of the white matter pathways and the gray matter subregions (Lévy et al., 2015). More recently, El Mendili et al. (2015) have proposed an approach similar to (Valsasina et al., 2012), to semi-automatically segment the spinal cord, based on double-thresholding, and to generate a template of the cervical spinal cord. The proposed template is normalized using the spinal cord length instead of vertebral levels (El Mendili, Chen, Tiret, Villard, et al., 2015).

Figure 2.30: T2-weighted MNI-Poly-AMU template of the spinal cord, covering C1 to T6 vertebral level. Adapted from (Fonov et al., 2014).

Finally, Taso et al. have developed an axial MRI template of the spinal cord (AMU15), along with probabilistic atlases of the white and gray matter, based on T2*-weighted images from 15 young healthy subjects (Taso et al., 2014). The template was constructed using affine co-registration of all images, based on manual segmentation, by alternatively selecting one subject as a reference. The 15 templates were then registered on a virtual elliptical external reference built from anatomical measurements to provide an unbiased template. The developed template provides one slice per vertebral level, from C1 to T12. Later, the authors (Taso et al., 2015) extended their

template and atlases to 40 young healthy subjects (age below 40 y.o.) of the cervical spinal cord (C1 to C7 vertebral levels). While this new template only covers part of the spinal cord, the delineation of the white and gray matter was more pronounced (Figure 2.31) and allowed accurate segmentation of the spinal cord internal structures.
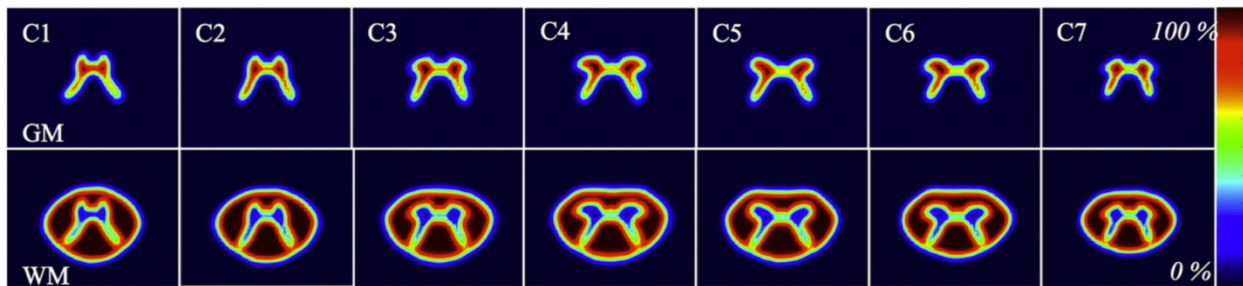
Figure 2.31: AMU40 probabilistic atlas of the cervical spinal cord gray matter and white matter. Adapted from (Taso et al., 2015).

2.4.5 Analysis of spinal cord morphology

As demonstrated in the previous sections, the morphology of the spinal cord, particularly the CSA, varies within a single subject but also within groups of healthy subjects. Variations can also be found between healthy subjects and patients, mainly related to spinal cord atrophy, caused by degenerative diseases such as MS or ALS. Over the last two decades, spinal cord CSA has proven to be a powerful biomarker for the diagnosis and prognosis of neurodegenerative diseases and their progression through time, such as MS (Brex et al., 2001; Kearney et al., 2014; Losseff, Webb, O'Riordan, et al., 1996; Lundell et al., 2011; Miller, Barkhof, Frank, Parker, & Thompson, 2002; Stevenson et al., 1998; Tartaglino et al., 1996; Thielen & Miller, 1996) , ALS (Cohen-Adad, El Mendili, et al., 2011a) and Huntington disease (Mühlau et al., 2014). For example, the spinal cord volume and CSA have been correlated with clinical scores such as the Expanded Disability Status Scale (EDSS) used in MS clinical protocols.

With the progress of spinal cord MR image acquisition, it has become feasible to image the spinal cord internal structure (Yiannakas et al., 2012b), the WM and the GM, and to accurately extract its shape, as presented in Section 2.4.2.4.2. Such advances in image processing methods enable the integration of CSA of the WM/GM into spinal cord atrophy analysis. Indeed, the location of atrophy in the spinal cord may differ depending on the disease. MS may affect the WM of the spinal cord more than its GM, as the disease induces the degeneration of the myelin around axons,

that are dominant in the WM. Oppositely, ALS is a disease that affects the motor neurons, so the spinal cord atrophy caused by ALS may be dominated by GM atrophy rather than WM atrophy. For example, (Taso et al., 2015) used the AMU40 template to perform a tensor-based morphometry mapping of age-specific populations, showing anterior gray matter atrophy in elderly volunteers (> 50 y.o.), when compared to a young population (< 40 y.o.), and thereby demonstrating the feasibility of studying local alterations of spinal cord internal structures.

However, the accurate computation of the spinal cord CSA is still a challenge, as many bias can affect the measurements. For example, Papinutto et al. have demonstrated the impact of patients' positioning in the scanner on the CSA measurement error, due to the nonlinearities of the scanner gradients (Papinutto, Bakshi, Bischof, & others, 2017). Moreover, taking into account the variability of the spinal cord in analysis studies of its morphology is still a challenge, as no consensus on CSA normalization has been made in the literature (as explained in Section 2.1.2). This absence of consensus may be caused by the lack of referential system dedicated to the spinal cord, which would take into account both vertebral levels and spinal segments in the analysis of spinal cord MRI data. Such a referential system has the potential to improve the reproducibility and repeatability of spinal cord MRI studies, as suggested by the meta-analysis performed by (Frostell, Hakim, Thelin, Mattsson, & Svensson, 2016) (Figure 2.32).
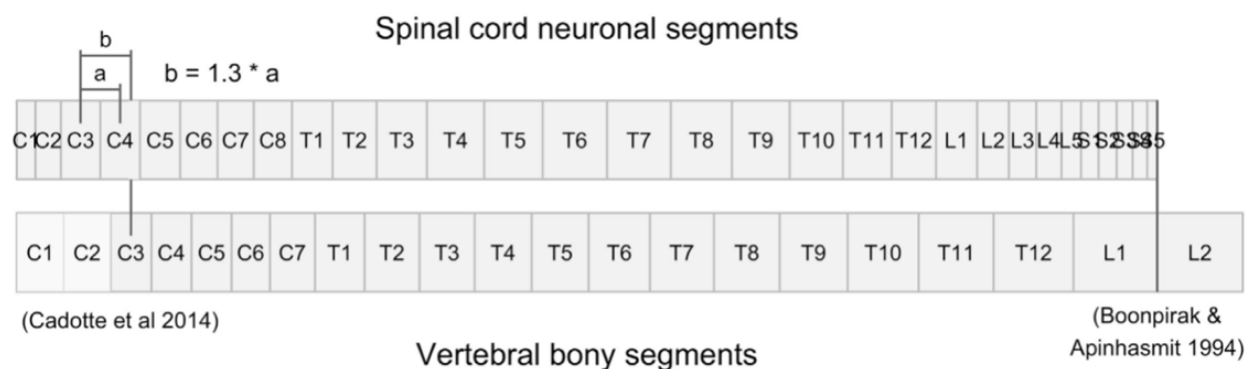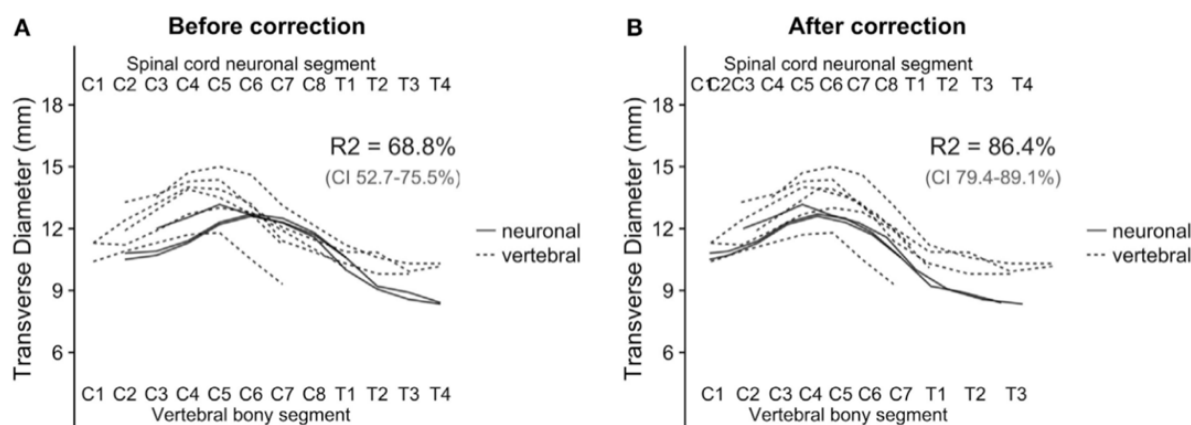
Figure 2.32: The top panel shows the relative position of the spinal segments and the vertebral levels. The bottom left panel show the transverse diameter of the spinal cord depending on the relative position of vertebral levels and spinal segments, and bottom right panel show the same information after correction of the relative position of each subject based on the position of spinal segments, showing improved correspondence of spinal cord morphology between subjects. Adapted from (Frostell et al., 2016).

Although many studies have explored the volume and area of the spinal cord, the spinal cord can also be described by its shape. Indeed, the spinal cord has a specific shape (elliptical over the cervical region, and circular over the thoracic and lumbar region), which can be affected by spinal cord diseases. For example, the degeneration of intervertebral disks can produce a compression on the frontal side of the spinal cord, which induces an indentation in the spinal cord shape, and which can be quantified by shape features.

2.4.6 Multiparametric MRI of the spinal cord

The application of conventional MRI (i.e., T1w, T2w, and proton-density MRI) to spinal cord diseases has matured progressively over the last three decades but provides only little information about the integrity of the spinal cord tissue itself, as the signal intensity is non-specific to physiological changes. Many studies have explored the application of multiparametric MRI (Figure 2.33) to the understanding of underlying mechanisms of spinal cord diseases. For example, diffusion tensor imaging (DTI) has largely been applied in the study of neurodegenerative diseases affecting the spinal cord, as it has been demonstrated that the diffusion of water molecules (e.g., fractional anisotropy, mean and radial diffusivity) change due to axons myelin loss.
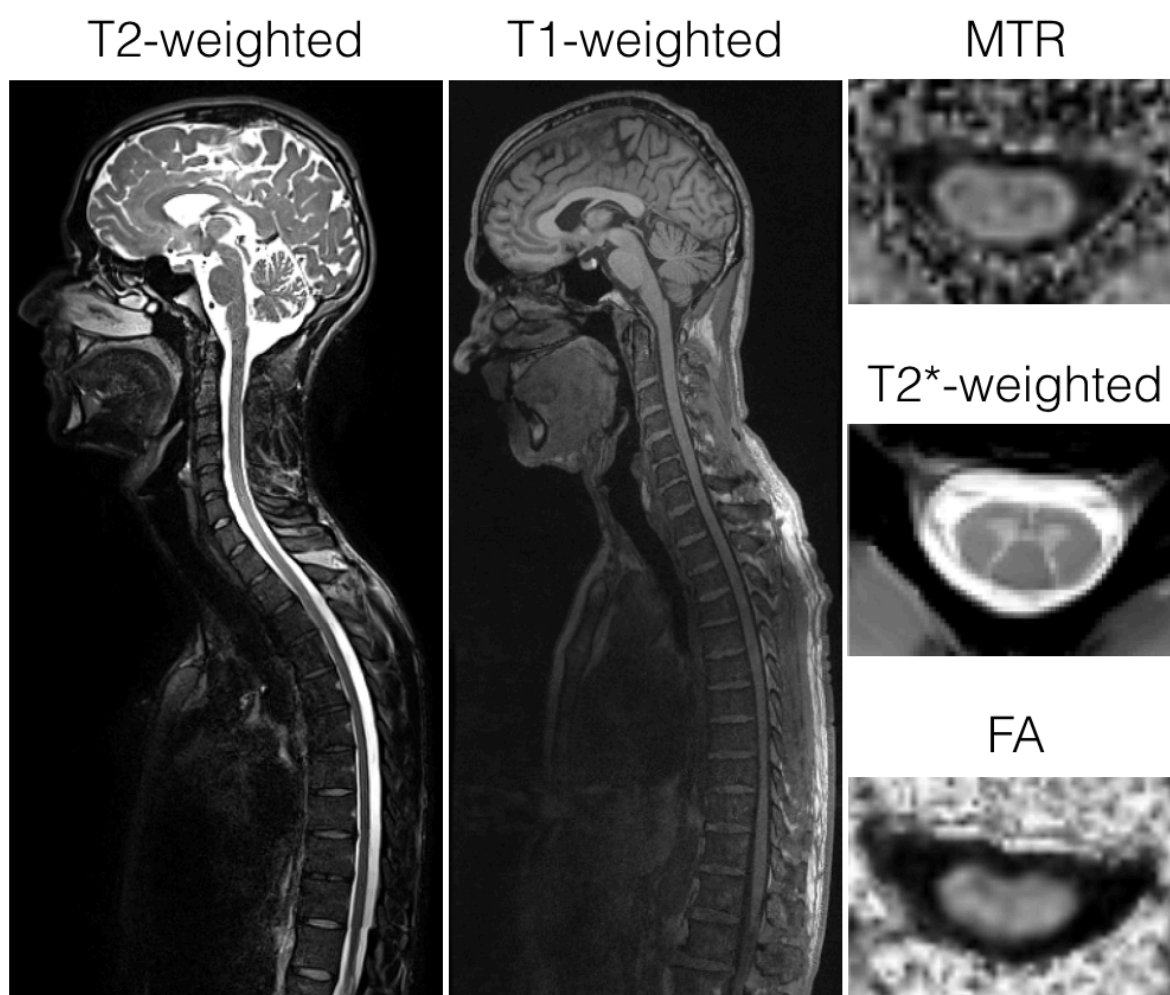
Figure 2.33: Example of MRI contrasts from multi-parametric MRI, including T1-, T2- and T2*-weighted images and magnetization transfer ratio (MTR) and fractional anisotropy (FA).

A most comprehensive review of multiparametric MRI techniques applied (DTI, MT, MWF, MRS and fMRI) to the spinal cord can be found in (Martin et al., 2016). By exploring the content of 104 studies, Martin et al. have demonstrated the low level of evidence and the high risk of bias in the spinal cord multiparametric MRI literature, applied to clinical setup. Indeed, most of these studies have used manual methods of ROI selection to extract quantitative features from MRI data. Manual extraction of MRI metrics within small regions of the spinal cord is a slow process, subject to expert bias and introduces a large variability in studies results. The use of semi- or fully-automatic and robust analysis tools dedicated to the spinal cord, including template-based analysis tools, is a mandatory requirement for the translation of quantitative MRI into clinics (Martin et al., 2016) as well as for reproducible analyses of large populations.

CHAPTER 3   METHODOLOGY

Based on the extensive literature review presented in Chapter 2, the following conclusions can be made concerning methods and algorithms dedicated to the spinal cord MRI data:

1. Template-based analysis of spinal cord MRI data would enable reproducible and comparable analyses of large groups of patients, and has the potential to improve our understanding of spinal cord diseases; Moreover, robust and automated analysis tools dedicated to the spinal cord would help to improve the diagnosis and prognosis of spinal cord diseases;

2. Only a few templates of the spinal cord exist in the literature, and no template covers the full spinal cord nor provide a referential system that would enable simultaneous brain and spinal cord studies in a reproducible way;

3. Over the last few years, several semi- and fully-automatic methods have been proposed for segmenting the spinal cord overall structure and its internal subregions (i.e., white and gray matter). However, there is no comprehensive software in the literature that provides all the necessary methods to perform complete analysis of spinal cord MRI data (e.g., segmentation, image registration, metric extraction).

Based on these statements, the following research question has been raised:

"How to create generic MRI templates of the spinal cord that would enable unbiased and reproducible template-based analysis of spinal cord MRI data?"

The **main objective** of my Ph. D. project is to answer this question by developing an MRI template that covers the full spinal cord, that is available for multiple MRI contrasts, that includes atlases of the spinal cord internal structure, and that shares a common referential with brain templates, as well as all processing tools required to automatize template-based analysis.

The **specific objectives** of my project are:

O1. Develop a framework for creating multimodal MRI templates of the full spinal cord and brainstem, which would be compatible with state-of-the-art brain templates and apply it on a population of 50 healthy subjects;

O2. Develop new image processing and registration methods dedicated to spinal cord MRI data, and provide a comprehensive and open-source software for spinal cord MRI analysis;

O3. Translate the proposed developments in a clinical setup, with a focus on diseases that modify the morphology of the spinal cord, such as atrophy caused by MS and compression caused by DCM.

3.1 Structure of the dissertation

As illustrated in Figure 3.1, Chapter 4 presents my developments on new image processing tools dedicated to the spinal cord (objective 2), as part of the article titled "*SCT: Spinal Cord Toolbox, an open-source software for processing spinal cord MRI data*", published in Neuroimage (IF=6.943) (De Leener, Lévy, et al., 2017). These tools are combined into SCT, a comprehensive and open-source software for the analysis of spinal cord MRI data, and include algorithms for:

-   automatic segmentation of the spinal cord as well as its internal structure (WM and GM);

-   registration of multimodal MRI data (structural and non-structural) on a spinal cord MRI template (initially the MNI-Poly-AMU template, later the PAM50 template) and co-registering spinal cord MRI images;

-   robust extraction of MRI metric within specific regions of the spinal cord (WM, GM, white matter tracts, gray matter subregions) and specific vertebral levels using a spinal cord atlas.

Chapter 5 introduces the article "*Topologically-preserving straightening of spinal cord MRI*", published in Journal of Magnetic Resonance Imaging (IF=3.083) (De Leener, Mangeat, et al., 2017), which presents a novel technique for straightening MRI images of the spinal cord, with no constraints on the field of view and while preserving the spinal cord topology (parts of objective 1 and 2). Based on curve approximation using Non-Uniform Rational Bezier Splines (NURBS) and on the analytical computation of deformation fields adapted to the spinal cord curvature, this method offers a robust and accurate registration tool for spinal cord MRI images. The proposed method is particularly important as there is currently no registration/straightening algorithms that preserve the topology of the spinal cord in MRI images that work on any field of view and any MRI contrast.

0 presents the main contribution of my project: the PAM50, an unbiased and symmetrical multimodal MRI template of the full spinal cord and brainstem, aligned with ICBM/MNI152 brain template (objective 1), as part of the article titled "*Unbiased multimodal template of the brainstem and spinal cord aligned with the ICBM152 space*", submitted to Neuroimage (IF=6.943). The proposed framework extends the straightening algorithm described in Chapter 5 with a robust alignment of vertebral levels and allows the creation of spinal cord MRI template of different populations.

Chapter 7 extends the results of the three articles presented in Chapters 4, 5 and 6, by translating the proposed developments to clinical applications. Particularly, spinal cord CSA extracted using SCT has been validated on a MS population, and novel MRI biomarkers of spinal cord white matter injury and DCM are presented, as part of a collaboration with Allan R. Martin and Michael G. Fehlings from University of Toronto.
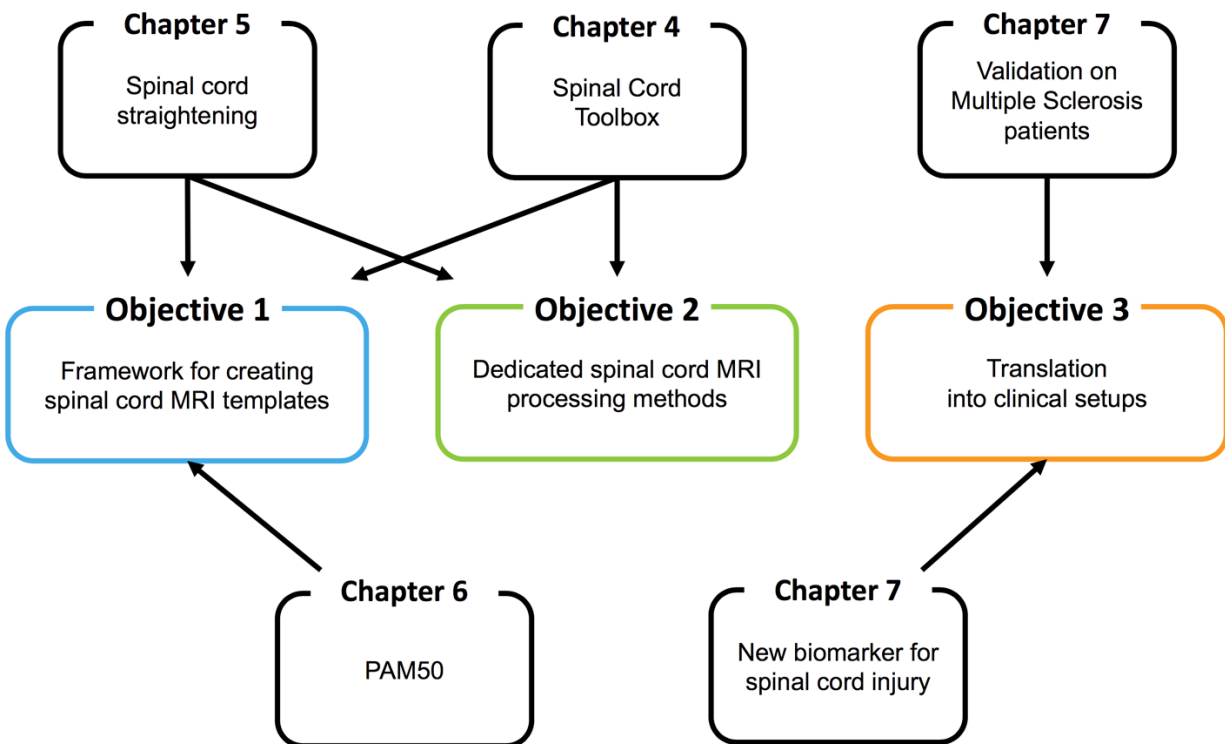
Figure 3.1: Illustration of the contributions presented in this thesis and their relations to the specific objectives of the project.

3.2 Additional publications

The present dissertation introduces one review article and three original articles that have been published/submitted during my Ph.D. project. Several additional publications have resulted from this project, as part of collaborations, or presented at local/international conferences and are listed in chronological order in the two following sections.

3.2.1 Peer-reviewed articles

1. Fonov VS, Le Troter A, Taso M, **De Leener B**, Lévêque G, Benhamou M, et al. Framework for integrated MRI average of the spinal cord white and gray matter: the MNI-Poly-AMU template. Neuroimage. 2014;102 Pt 2: 817–827. doi:10.1016/j.neuroimage.2014.08.057

2. Cameron Craddock R, S Margulies D, Bellec P, Nolan Nichols B, Alcauter S, A Barrios F, et al. Brainhack: a collaborative workshop for the open neuroscience community. Gigascience. 2016;5: 16. doi:10.1186/s13742-016-0121-x

3. Yiannakas MC, Mustafa AM, **De Leener B**, Kearney H, Tur C, Altmann DR, et al. Fully automated segmentation of the cervical cord from T1-weighted MRI using PropSeg: Application to multiple sclerosis. Neuroimage Clin. 2016;10: 71–77. doi:10.1016/j.nicl.2015.11.001

4. Dupont SM, **De Leener B**, Taso M, Le Troter A, Nadeau S, Stikov N, et al. Fully-integrated framework for the segmentation and registration of the spinal cord white and gray matter. Neuroimage. Elsevier; 2017;150: 358–372. doi:10.1016/j.neuroimage.2016.09.026

5. Martin AR, **De Leener B**, Cohen-Adad J, Cadotte DW, Kalsi-Ryan S, Lange SF, et al. A Novel MRI Biomarker of Spinal Cord White Matter Injury: T2*-Weighted White Matter to Gray Matter Signal Intensity Ratio. AJNR Am J Neuroradiol. 2017;38: 1266–1273. doi:10.3174/ajnr.A5162

6. Martin AR, **De Leener B**, Cohen-Adad J, Cadotte DW, Kalsi-Ryan S, Lange SF, et al. Clinically Feasible Microstructural MRI to Quantify Cervical Spinal Cord Tissue Injury Using DTI, MT, and T2*-Weighted Imaging: Assessment of Normative Data and Reliability. AJNR Am J Neuroradiol. 2017;38: 1257–1265. doi:10.3174/ajnr.A5163

7. Prados F, Ashburner J, Blaiotta C, Brosch T, Carballido-Gamio J, Cardoso MJ, et al. Spinal cord gray matter segmentation challenge. Neuroimage. 2017;152: 312–329. doi:10.1016/j.neuroimage.2017.03.010

3.2.2 Conferences abstracts

1. **De Leener B**, Levy S, Touati J, Roux A, Benhamou M, Cadotte D, et al. Spinal Cord Toolbox: Open-source framework for multi-parametric MRI of the spinal cord. Imagining Imaging Symposium. 2014.

2. **De Leener B**, Roux A, Touati J, Levy S, Taso S, Fonov VS, et al. Template-based analysis of multi-parametric MRI data with the Spinal Cord Toolbox. 7th Scientific Day of QBIN. 2015.

3. **De Leener B**, Roux A, Levy S, Duval T, Cohen-Adad J. Spinal Cord Toolbox: Automated Software For Processing Quantitative MRI Data Of The Spinal Cord. 4th ISCoS And Asia Joint Scientific Meeting. 2015.

4. **De Leener B**, Roux A, Taso M, Callot V, Cohen-Adad J. Spinal cord gray and white matter segmentation using atlas deformation. Proceedings of the 23th Annual Meeting of ISMRM, Toronto, Canada, Toronto. Toronto; 2015. p. 4424.

5. Yiannakas MC, Mustafa A, **De Leener B**, Cohen-Adad J, Kearney H, Miller DH, et al. Fully automated segmentation of the cervical spinal cord using PropSeg: application to multiple sclerosis. Proceedings of the 23th Annual Meeting of ISMRM, Toronto, Canada. 2015. p. 4354.

6. Touati J, Taso M, Fonov V, Le Troter A, **De Leener B**, Collins DL, et al. T1 and T2 template of the human brainstem and spinal cord. Proceedings of the 23th Annual Meeting of ISMRM, Toronto, Canada. Toronto; 2015. p. 5712.

7. **De Leener B**, Taso M, Fonov VS, Le Troter A, Stikov N, Collins DL, et al. PAM50: Fully integrated T1, T2 and T2* atlas of the brainstem and spinal cord. 8th Scientific Day of QBIN. 2016.

8. Dupont SM, **De Leener B**, Taso M, Stikov N, Callot V, Cohen-Adad J. Fully-integrated framework for registration of spinal cord white and gray matter. Proceedings of the 24th Annual Meeting of ISMRM, Singapore, Singapore. 2016.

9. **De Leener B**, Taso M, Fonov VS, Le Troter A, Stikov N, Collins DL, et al. Fully integrated T1, T2, T2*, white and gray matter atlases of the spinal cord. Proceedings of the 24th Annual Meeting of ISMRM, Singapore, Singapore. Singapore; 2016. p. 1129.

10. **De Leener B**, Taso M, Fonov VS, Le Troter A, Stikov N, Collins DL, et al. PAM50: Fully integrated T1, T2 and T2* MRI atlas of the brainstem and spinal cord. NeuroSymposium 2016. 2016.

11. Martin AR, **De Leener B**, Cohen-Adad J, Aleksanderek I, Cadotte DW, Kalsi-Ryan S, et al. Microstructural MRI Quantifies Tract-Specific Injury and Correlates With Global Disability and Focal

Neurological Deficits in Degenerative Cervical Myelopathy. Neurosurgery. 2016. p. 165. doi:10.1227/01.neu.0000489732.76982.7f

12. **De Leener B**, Taso M, Fonov V, Le Troter A, Stikov N, Collins L, et al. Fully-integrated T1, T2, T2*, white and gray matter atlases of the spinal cord. Proceedings of the 24th Annual Meeting of International Society for Magnetic Resonance in Medicine, Suntec City, Singapore. 2016.

13. Martin AR, **De Leener B**, Cohen-Adad J, Aleksanderek I, Cadotte D, Crawley A, et al. Clinically feasible microstructural MRI to assess cervical spinal cord tissue injury: methods, normative data and reliability. Journal of neurotrauma. 2016. pp. A49–A49.

14. Martin AR, De Leener B, Cohen-Adad J, Aleksanderek I, Cadotte D, Kalsi-Ryan S, et al. Microstructural cervical spinal cord MRI quantifies tract-specific injury and correlates with global and focal deficits. Journal of Neurotrauma. 2016. p. A–1–A–139. doi:10.1089/neu.2016.29008.abstracts

15. Martin AR, De Leener B, Cohen-Adad J, Aleksanderek I, Cadotte D, Crawley A, et al. Clinically feasible microstructural MRI to assess cervical spinal cord tissue injury: methods, normative data and reliability. Journal of neurotrauma. 2016. pp. A49–A49.

16. **De Leener B**, Taso M, Fonov V, Le Troter A, Stikov N, Collins L, et al. Fully-integrated T1, T2, T2*, white and gray matter atlases of the spinal cord. Proceedings of the 24th Annual Meeting of International Society for Magnetic Resonance in Medicine, Suntec City, Singapore. 2016.

17. **De Leener B**, Fonov V, Collins DL, Callot V, Stikov N, Cohen-Adad J. PAM50: Multimodal MRI template and atlases of the brainstem and spinal cord. Proceedings of Québec Engineering Competition 2017. 2017.

18. Martin AR, **De Leener B**, Cohen-Adad J, Cadotte DW, Wilson JR, Tetreault L, et al. Multi-Parametric Spinal Cord MRI Detects Subclinical Tissue Injury in Asymptomatic Cervical Spinal Cord Compression. Proceedings of the 25th Annual Meeting of ISMRM, Honolulu, USA. 2017.

19. Martin AR, **De Leener B**, Cohen-Adad J, Cadotte DW, Wilson JR, Tetreault L, et al. Multi-Parametric Cervical Spinal Cord MRI Provides An Accurate Diagnostic Tool for Detecting Clinical Myelopathy. Proceedings of the 25th Annual Meeting of ISMRM, Honolulu, USA. 2017.

20. Martin AR, **De Leener B**, Cohen-Adad J, Cadotte DW, Wilson JR, Tetreault L, et al. Towards Clinical Translation of Quantitative Spinal Cord MRI: Serial Monitoring to Identify Disease Progression in Patients with Degenerative Cervical Myelopathy. Proceedings of the 25th Annual Meeting of ISMRM, Honolulu, USA. 2017.

21. **De Leener B**, Granberg T, Fink K, Stikov N, Cohen-Adad J. Repeatability and reproducibility of spinal cord atrophy measurements in a multiple sclerosis population using the Spinal Cord Toolbox. Proceedings of the 25th Annual Meeting of ISMRM, Honolulu, USA. 2017.

22. Van Assel C, Mangeat G, **De Leener B**, Stikov N, Mainero C, Cohen-Adad J. Partial volume effect correction for surface-based cortical mapping. Proceedings of the 25th Annual Meeting of ISMRM, Honolulu, USA. 2017.

23. Mangeat G, **De Leener B**, Karrenbauer VD, Warntjes M, Stikov N, Mainero C, et al. Fast multivariate relaxometry can differentiate neurodegenerative disease processes and phenotypes. Proceedings of the 25th Annual Meeting of ISMRM, Honolulu, USA. 2017.

24. Gros C, **De Leener B**, Martin AR, Fehlings MG, Callot V, Stikov N, et al. Robust and automatic spinal cord detection on multiple MRI contrasts using machine learning. Proceedings of the 25th Annual Meeting of ISMRM, Honolulu, USA. 2017.

25. **De Leener B**, Fonov V, Collins DL, Callot V, Stikov N, Cohen-Adad J. PAM50: Multimodal template of the brainstem and spinal cord compatible with the ICBM152 space. Proceedings of the 25th Annual Meeting of ISMRM, Honolulu, USA. 2017.

26. Ouellette RA, Granberg T, Treaba CA, Herranz E, **De Leener B**, Sloane J, et al. In vivo characterization of gray and white matter spinal cord pathology in multiple sclerosis using ultra high field MRI. Proceedings of the 69th Annual Meeting of the American Academy of Neurology. 2017.

27. Gros C, **De Leener B**, Dupont SM, Martin AR, Fehlings MG, Bakshi R, et al. OptiC: Robust and automatic spinal cord localization on a large variety of MRI data using a distance transform based global optimization. Proceedings of the 20th International Conference on Medical Image Computing and Computer-Assisted Interventions. 2017.

CHAPTER 4   ARTICLE 2: SCT: SPINAL CORD TOOLBOX, AN OPEN-SOURCE SOFTWARE FOR PROCESSING SPINAL CORD MRI DATA

This manuscript presents the development and validation of the Spinal Cord Toolbox (SCT), a comprehensive and open-source software for processing spinal cord MRI data. SCT includes tools for the automatic segmentation of the spinal cord and its internal structure (WM and GM), vertebral labeling, registration of multimodal MRI data (structural and non-structural) on a spinal cord MRI template (initially the MNI-Poly-AMU template, later the PAM50 template) and co-registering spinal cord MRI images, as well as the robust extraction of MRI metric within specific regions of the spinal cord (WM, GM, white matter tracts, gray matter subregions) and specific vertebral levels using a spinal cord atlas. Additional tools include robust motion correction and image processing along the spinal cord. Each tool included in SCT has been validated on a large multimodal dataset. Coupled with Chapter 4, this manuscript is an essential contribution to this project as it proposes answers to its second objective.

My contribution (80%) on the Spinal Cord Toolbox included the full development of the method for segmenting the spinal cord (100%), the design and development of the MNI-Poly-AMU template (70%) and later the PAM50 template (100%), the development of various registration methods dedicated to the spinal cord (80%), the development of the gray matter segmentation tools (40%), the design and development of the white matter atlas and metric extraction methods (40%) and the development of the testing procedure (90%). My contribution to the article includes the design of the paper, as well as its redaction.

This manuscript has been published in Neuroimage in January 2017, Volume 145, pp 24–43.

Title: SCT: Spinal Cord Toolbox, an open-source software for processing spinal cord MRI data

Authors:

Benjamin De Leener[1], Simon Lévy[1,2], Sara M. Dupont[1], Vladimir S. Fonov[3], Nikola Stikov[1,4], D. Louis Collins[3], Virginie Callot[5,6], Julien Cohen-Adad[1,2]

Affiliations:

[1] NeuroPoly Lab, Institute of Biomedical Engineering, Polytechnique Montreal, Montreal, QC, Canada

[2] Functional Neuroimaging Unit, CRIUGM, Université de Montréal, Montreal, QC, Canada

[3] Montreal Neurological Institute, McGill University, Montreal, QC, Canada

[4] Montreal Heart Institute, Montreal, QC, Canada

[5] Aix-Marseille Université, CNRS, CRMBM UMR 7339, Marseille, France

[6] AP-HM, Hopital de la Timone, Pôle d'imagerie médicale, CEMEREM, Marseille, France

4.1 Abstract

For the past 25 years, the field of neuroimaging has witnessed the development of several software packages for processing multi-parametric magnetic resonance imaging (mpMRI) to study the brain. These software packages are now routinely used by researchers and clinicians, and have contributed to important breakthroughs for the understanding of brain anatomy and function. However, no software package exists to process mpMRI data of the spinal cord. Despite the numerous clinical needs for such advanced mpMRI protocols (multiple sclerosis, spinal cord injury, cervical spondylotic myelopathy, etc.), researchers have been developing specific tools that, while necessary, do not provide an integrative framework that is compatible with most usages and that is capable of reaching the community at large. This hinders cross-validation and the possibility to perform multi-center studies. In this study we introduce the *Spinal Cord Toolbox* (SCT), a comprehensive software dedicated to the processing of spinal cord MRI data. SCT builds on previously-validated methods and includes state-of-the-art MRI templates and atlases of the spinal cord, algorithms to segment and register new data to the templates, and motion correction methods for diffusion and functional time series. SCT is tailored towards standardization and automation of the processing pipeline, versatility, modularity, and it follows guidelines of software development and distribution. Preliminary applications of SCT cover a variety of studies, from cross-sectional area measures in large databases of patients, to the precise quantification of mpMRI metrics in specific spinal pathways. We anticipate that SCT will bring together the spinal cord neuroimaging community by establishing standard templates and analysis procedures.

Keywords: Spinal cord, MRI, software, template, atlas, open-source

4.2 Introduction

Pathologies of the spinal cord can result from neurodegenerative and vascular diseases, disc degeneration, trauma and cancer, all of which can induce severe functional disabilities and neuropathic pain (Adams & Salam-Adams, 1991; Rowland et al., 2008). Precise assessment of the structural (e.g., extent of the lesion) and functional damage to the spinal cord is critical for informing on the prognosis and for guiding the intervention therapy program (Bozzo, Marcoux, Radhakrishna, Pelletier, & Goulet, 2011; van Middendorp et al., 2011). Moreover, the development of novel therapeutic approaches require objective biomarkers that can help assessing the efficiency and specific effect of these treatments, e.g., regeneration and axonal growth in spinal cord injury (Bradbury & McMahon, 2006) or remyelination in multiple sclerosis (Harlow, Honce, & Miravalle, 2015; Luessi, Kuhlmann, & Zipp, 2014). While conventional Magnetic Resonance Imaging (MRI) based on relaxation parameters and proton density provides useful structural information that complement clinical and neurophysiological exams (Cadotte et al., 2011; Kearney, Miller, & Ciccarelli, 2015), it can sometimes miss subtle pathological events such as Wallerian degeneration (Mac Donald, Dikranian, Bayly, Holtzman, & Brody, 2007; J. Zhang et al., 2009) or diffusely abnormal white matter in multiple sclerosis (Laule et al., 2011; West et al., 2014). The ongoing development of multi-parametric MRI (mpMRI), e.g., diffusion tensor imaging (DTI), magnetization transfer ratio (MTR) and functional MRI (fMRI) (Cohen-Adad & Wheeler-Kingshott, 2014b; Tofts, 2003) provides a closer look at white matter microstructure and neuronal function and thus can more precisely characterize the pathological spinal cord (Martin et al., 2016).

While mpMRI has been used in the brain for several decades now, spinal cord imaging in research and clinics is still largely underutilized (Stroman et al., 2014; Wheeler-Kingshott et al., 2014). One reason is the difficulty in acquiring good quality data due to the numerous artifacts and the small cross-sectional size of the spinal cord. For the past few years though, researchers have developed methods to overcome these challenges, such as advanced coil designs (Cohen-Adad, Mareyam, Keil, Polimeni, & Wald, 2011) and pulse sequences (Dowell, Jenkins, Ciccarelli, Miller, & Wheeler-Kingshott, 2009; Finsterbusch, 2009; Wilm et al., 2007). A second reason is that, in contrast to the brain, fewer tools exist that are dedicated to processing of spinal cord images (Stroman et al., 2014). Unlike popular software packages for brain neuroimaging (e.g., FSL, SPM, BrainVoyager, FreeSurfer, AFNI, MINC Toolkit), spinal cord researchers have only been

developing specific tools, e.g., for spinal cord segmentation (De Leener, Taso, Cohen-Adad, & Callot, 2016). Moreover, these single tools don't provide an integrative framework that is compatible with most usages (i.e., adapted to a large variety of mpMRI protocols) and that can reach the community at large (i.e., open source, license-free scripting environment, extensive documentation, support forum, continuous integration service for integrity testing). At the same time, brain software packages are not optimized for spinal cord images because (i) the spine is an articulated structure, therefore standard motion-correction algorithms assuming rigid or affine transformation are inadequate, (ii) brain extraction and segmentation tools are not adapted to the spinal cord because of different shape, contrast-to-noise ratio, etc., (iii) common brain MRI templates (Evans et al., 1992; V. Fonov, Evans, et al., 2011) and atlases (Brodmann, 1909) are *de facto* not usable for spinal cord imaging, (iv) useful features are *de facto* missing, such as spinal cord cross-sectional area (CSA) measurement. The lack of a standard processing platform has had negative impacts on the spinal cord neuroimaging community as it has limited the ability of researchers to compare and reproduce published results, as well at to conduct collaborative and multi-center studies.

In this paper we introduce the Spinal Cord Toolbox (SCT), a software package specifically designed to process spinal cord mpMRI data and to perform atlas-based analysis. SCT includes state-of-the-art tools, which have been validated in this manuscript (see Appendix) and/or are already published (see list of publications in the next section). SCT is compatible with any scanner brand as it uses NIfTI format and is designed to accept a variety of sequences, modalities and contrasts. Being based on Python language, SCT ensures cross-platform compatibility, is free and open source. The article is organized as follows. First, an overview of the software is presented, along with a description of the main features. Then, technical details are presented (e.g., coding language, installation) followed by an example application and a discussion.

4.3 Main features

SCT is a comprehensive and open-source library of analysis tools for multi-parametric MRI of the spinal cord. The primary objective of SCT is to provide a common pre-processing platform, which supplements what is missing from the common brain software package. Hence, the goal of SCT is not to replace entirely what other software already offers (e.g., first- and second-level analysis of fMRI data), but to provide the necessary tools to pre-process mpMRI data, to perform group

analysis within standard space, and/or to perform cord-specific quantification such as quantification of cross-sectional area across vertebral levels. A typical user-case example consists of registering the spinal cord of several patients to a common template, then quantifying DTI metrics along vertebral levels C2 to C5 within the corticospinal tract. This can be done automatically with SCT, thanks to some of the following features:

- Automatic segmentation of the spinal cord (De Leener et al., 2014)

- Automatic segmentation of the spinal canal (which includes the cord and CSF) (De Leener, Cohen-Adad, & Kadoury, 2015a)

- Automatic segmentation of the white and gray matter using multi-atlas algorithm (Dupont et al., 2017)

- Automatic vertebral labeling (Ullmann et al., 2014)

- MRI template of the human spinal cord (Fonov et al., 2014)

- Probabilistic template of white and gray matter (Taso et al., 2014)

- Atlas of white matter tracts (Lévy et al., 2015)

- Probabilistic map of spinal levels (Cadotte et al., 2015)

- Pipeline for registering data with the template (Fonov et al., 2014)

- Robust motion correction methods for diffusion and functional MRI time series (Cohen-Adad, Lévy, & Avants, 2015).

A complete list of tools is available at: https://sourceforge.net/p/spinalcordtoolbox/wiki/tools/. The following section will detail some of the main features.

4.3.1 Segmentation

4.3.1.1 Spinal cord

The delineation of the spinal cord contour is a common procedure for quantifying CSA or spinal cord volume (De Leener, Taso, et al., 2016). As described in section "Template and atlases", segmentation can also be used to improve the quality of registration. Here we have implemented a fast, robust and accurate automatic segmentation algorithm for spinal cord MRI called *PropSeg*

(De Leener et al., 2015a, 2014). The algorithm consists of (i) detecting the center of the spinal cord using ellipse detection and information from the body symmetry, then (ii) propagating a tubular surface along the spinal cord edge using deformable models. The outputs include a binary mask of the spinal cord, a 3D parametric surface and CSA measure for each axial slice along the spinal cord. *PropSeg* has been validated against multiple contrasts (T_1-, T_2- and T_2*-weighted) (De Leener et al., 2014) and was shown to be robust in pathological cases, including in patients with multiple sclerosis (MS) (Yiannakas et al., 2015).

While *PropSeg* is fully automatic, it can sometimes fail if contrast between the CSF and the cord is low, if strong artifacts are present (e.g., caused by metallic implants or large cord compression in trauma) or if the FOV only includes a small portion of the spinal cord (e.g., brain scan, with only small portion of the cord visible). In such cases it is possible to adjust the parameters to better fit the type of data (e.g., specifying that the spinal cord is only visible in the inferior portion of the FOV) or to add manual initialization (e.g., three points in the spinal cord, or several points along the spinal cord centerline, or "attraction points" which will force the 3D mesh to be attracted to these points), similar to the method proposed by (Horsfield et al., 2010). Manual initialization is handled by a window which pops up and shows axial slices of the cord: the user can then quickly add labels on this window.

4.3.1.2 Gray matter

Gray matter segmentation in SCT builds upon the groupwise multi-atlas segmentation method from Asman *et al.* (Asman et al., 2014) and includes additional improvements (Dupont et al., 2017) (see Appendix). Firstly, prior knowledge of vertebral level (obtained from automatic vertebral labeling) helps to select better candidates from the dictionary of gray matter shapes, resulting in more accurate segmentation. Secondly, while the original method requires the input image to have similar contrast to images from the dictionary, gray matter segmentation in SCT includes a tissue-specific robust linear intensity normalization (obtained from the pre-registration of the gray matter atlas) which makes it possible to input any image contrast, such as T_2*-weighted, magnetization transfer or fractional anisotropy map from DTI. In addition to providing clinically relevant information, gray matter segmentation also proves to be useful for improving the accuracy of atlas-based registration, as will be described in the next section.

4.3.2 Template and atlases

SCT includes the MNI-Poly-AMU[2] template, which is a collection of MRI volumes that forms a common anatomical space reference, covering C1 to T6 vertebral levels sampled at 0.5 mm isotropic. This template includes an averaged T_2-weighted volume (Fonov et al., 2014), a binary mask of the spinal cord and surrounding cerebrospinal fluid, a labeling of vertebral levels, probabilistic labeling of spinal levels (Cadotte et al., 2015), a probabilistic atlas of the white and gray matter (Taso et al., 2015) and an atlas of spinal white matter tracts with partial volume information (Lévy et al., 2015). The template was constructed from straightened spinal cord for facilitating registration and visualization of results. Note that the T_2w template and the atlas of white and gray matter resulted from the fusion of 15 T_2-w and 16 T_2*-w images from different subjects and different scanners. Figure 4.1 illustrates the MNI-Poly-AMU template. The next sections describe how to register a new subject with the template.
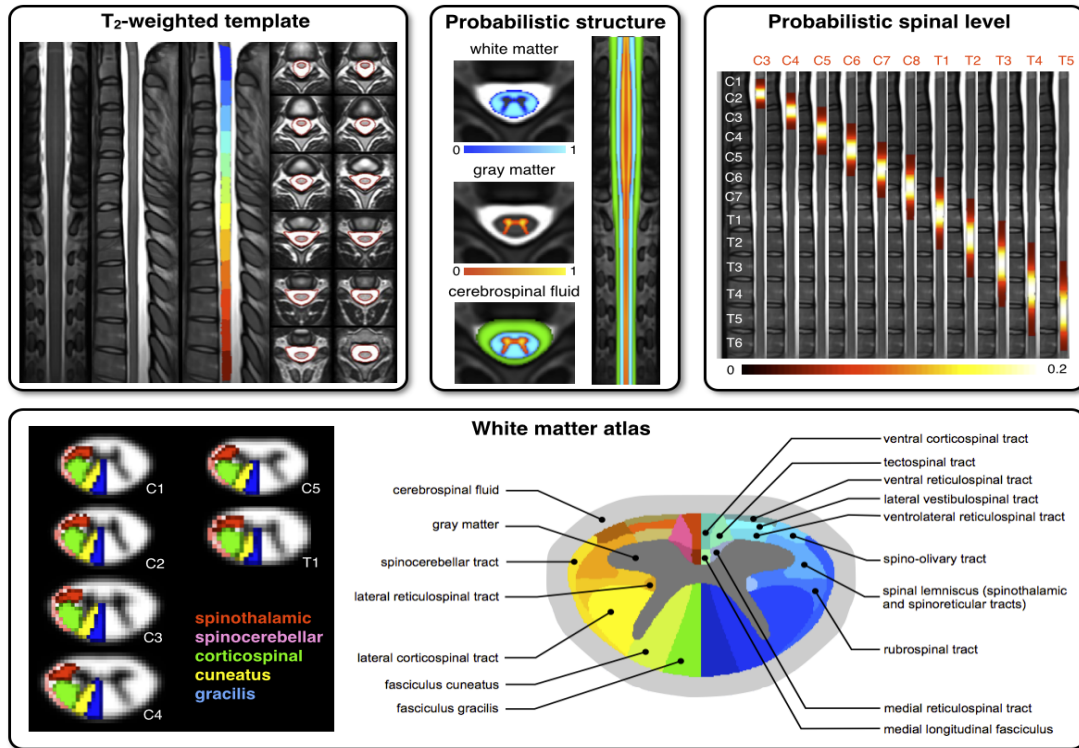
Figure 4.1: Template and atlases included in SCT: straight T_2-weighted template with vertebral levels and spinal cord/CSF segmentation (top left), probabilistic atlases of white and gray matter

---

[2] The acronym stands for the Montreal Neurological Institute (MNI), Polytechnique Montreal (Poly) and Aix-Marseille Université (AMU).

(top center), probabilistic map of spinal levels according to vertebral levels (top right) and white matter atlas (bottom).

4.3.2.1 Registering new data with the template

One motivation for registering new data with the template is to perform atlas-based analysis of mpMRI data. Registration is best done using an anatomical dataset (e.g., T_1- or T_2-weighted) with isotropic resolution (e.g., $1mm^3$). The main steps are:

1. **Spinal cord segmentation** (e.g., using *PropSeg*)

2. **Identification of two vertebral levels**. Each of these two landmarks consists of one voxel located in the middle of the spinal cord, at the level of the corresponding mid-vertebral body. The value of each voxel corresponds to the vertebral level, e.g., value=2 for C2 and value=10 for T3. Note that this vertebral labeling can be done automatically (Ullmann et al., 2014) using function `sct_label_vertebrae`, assuming the data are acquired in a consistent manner (e.g., FOV centered at the C3/C4 disc).

3. **Registration to the template**. Firstly, the spinal cord image is straightened to match the shape of the template. Straightening is achieved by automatically generating a series of labels (cross-shape) along the spinal cord centerline, and then registering these labels to a straight centerline using landmark-based affine and nonlinear transformations as implemented in ITK (McCormick et al., 2014). Secondly, local deformations are performed using multi-step nonlinear registration constrained in the axial plane and regularized in the inferior-superior direction (for more details, see section "Multi-modal registration").

4. **Warping the template** back into the native space of the subject by applying the transformation to each template object (e.g., spinal cord mask, vertebral and spinal labeling, white matter atlas, etc.).

The registration procedure outputs forward (*warp_anat2template.nii.gz*) and backward (*warp_template2anat.nii.gz*) transformations in ITK format, which can be concatenated to subsequent transformations if needed. For example, if other mpMRI data (e.g., DTI) from the same subject need to be registered to the template, these data are first registered to the anatomical data, then warping fields are concatenated to yield a single direct transformation between the template and these additional data. This approach ensures minimum interpolations and hence preserves the

effective spatial resolution of the data. If these mpMRI data also present enough gray/white contrast, gray matter segmentation can be performed to further improve the registration of the white matter atlas. Figure 4.2 illustrates the procedure. The next section describes how registration is performed in SCT.
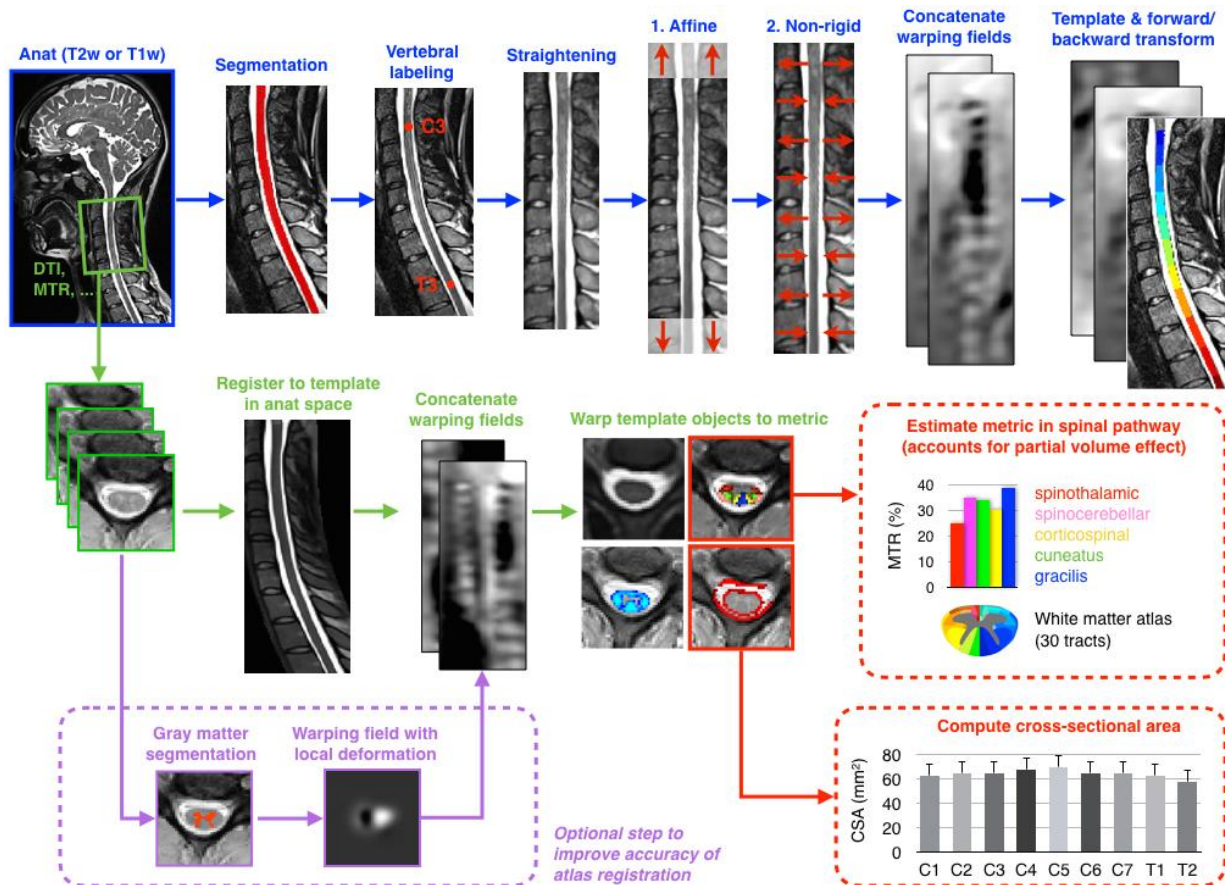
Figure 4.2: Overview of the template-based analysis pipeline. Firstly, anatomical data are registered to the template (blue arrows). Additional multi-parametric data acquired during the same scan session (e.g., DTI, MTR, fMRI) are registered to the anatomical data, then template objects are warped to the multi-parametric data (green arrows). To improve accuracy of template registration, it is possible to add a step where gray matter is segmented (manually or automatically) and then warped to the gray matter template in order to update the warping fields (purple arrows). Subsequently, mpMRI metrics can be quantified within the spinal cord or within specific tracts of the white matter at specific vertebral levels (red arrows). Cord and gray matter CSA and cord volume can also be computed from the mpMRI data, or from the anatomical data in the first place.

4.3.3 Multi-modal registration

4.3.3.1 Slice-by-slice regularized registration (SliceReg)

In typical mpMRI protocols, there is a need to co-register multiple data from one subject together, e.g., T_1-, T_2-, T_2*-, diffusion, MT-weighted images and fMRI time series. While common registration methods for the brain employ unconstrained affine or non-rigid registrations (Klein et al., 2009), multimodal registration in spinal cord MRI data is often performed using affine transformations constrained in the axial plane (Figure 4.3, left panel), assuming that subject motion in the inferior-superior direction is negligible because subjects are usually lying in supine position. Although fairly robust, affine transformations often lack accuracy because of the articulated nature of the spine, which can produce non-rigid deformations. To overcome this problem, planar translations and/or rotations can be estimated for each slice in the axial plane ("Slice-by-slice" in Figure 4.3). While this method has become popular in the spinal cord imaging community (Summers, Brooks, & Cohen-Adad, 2014), correcting each slice independently is sub-optimal because it does not consider the smooth nature of the deformation along z, hence reducing robustness compared to volume-based registration. SCT offers a new registration method that estimates slice-by-slice translations while ensuring regularization constraints along z (*SliceReg* in Figure 4.3). Regularization is achieved using a polynomial function (order to be specified by the user) and is part of the convergence algorithm of the cost function (i.e., it is not applied after the estimation but during). *SliceReg* was shown to be more accurate than rigid-body transformations and offers more robustness than non-regularized slice-by-slice registration (Cohen-Adad et al., 2015). This algorithm is part of the generalized procedure for multi-modal registration, as described in the next section.
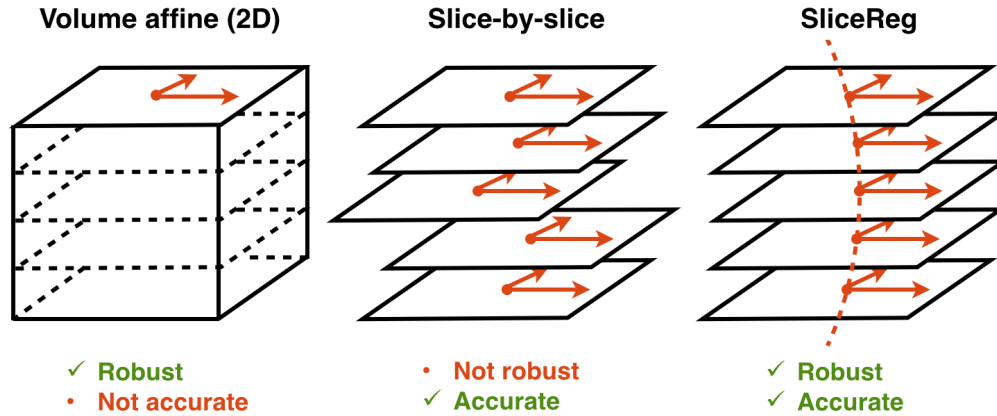
Figure 4.3: Illustration of methods for registration of spinal cord MRI.

4.3.3.2 Multi-step registration

4.3.3.2.1 Purpose

The purpose of `sct_register_multimodal` is to register one image (source) to another image (target), such as for instance, an MT_off to an MT_on, or a T2 anatomical to a mean b=0. As suggested by these examples, the source and target images do not need to be in the same space. The function features several methods for affine and non-rigid registration, as listed in Table 4.1. All these methods are constrained in the axial plane (with or without regularizations along *z*), hence the target volume is assumed to be in the radiological orientation[3].

An important feature of `sct_register_multimodal` is that several registration steps can be prescribed in a single command line. This allows to perform multi-scale registration while using different algorithms at each step. Typically, the first step would consist in addressing large deformations while latter steps would deal with cord shape and fine anatomical adjustments. Multiple registration steps are specified by the flag "-param" as shown in the following example

```
sct_register_multimodal  -i  image.nii.gz  -d  dest.nii.gz  -iseg  image_seg.nii.gz  -dseg
dest_seg.nii.gz                                                                        -param
step=1,type=seg,algo=slicereg,metric=MeanSquares,smooth=5,poly=5:step=2,type=seg,algo=
bsplinesyn,metric=MeanSquares,smooth=1,iter=5:step=3,type=im,algo=syn,metric=CC,iter=5
```

---

[3] Radiological orientation refers to the order of data storage for a volume, with *x*, *y* and *z* coordinates corresponding to Right→Left, Posterior→Anterior and Inferior→Superior, respectively.

A list of parameters available for each step is given in Table 4.1, along with explanations and suggestions for best usage. The accuracy and robustness of registration has been addressed in (Fonov et al., 2014). An example of mpMRI registration with the template is illustrated in Figure 4.4.

Table 4.1: Parameters available for multi-step registration.

Parameter	Value	Description
step	*int*	Step identification number (starts with 1).
type	*im*: image *seg*: cord segmentation	Type of information used for registration. If cord segmentation is available, it could be used for robust gross alignment (first step). In some cases (e.g., if images are corrupted by artifacts), cord segmentation can also be used at later steps as a more reliable definition of cord contour.
algo	*translation*: Tx, Ty (2 dof) *rigid*: Tx, Ty, Rz (3 dof) *affine*: Tx, Ty, Rz, Sx, Sy (5 dof) *syn*: (Avants et al., 2008) *bsplinesyn*: (Tustison & Avants, 2013) *slicereg*: slice-wise regularized rigid (Cohen-Adad et al., 2015)	Type of transformation. For large-scale deformations (e.g., gross realignment of cord centerlines between source and target image), rigid/affine transformations based on cord segmentations are prefered. For small-scale deformations, the algorithm SyN based on the image is prefered. To maintain the consistency of the internal structure (e.g., gray matter and surrounding white matter tracts), users can prefer the B-spline-regularized version of SyN (Tustison & Avants, 2013).
slicewise	*int*	0: volume-based registration 1: slice-by-slice registration. Only for algo={*translation*, *rigid*, *affine*}.
metric	*CC*: cross-correlation (slow, recommended for type=*im*) *MI*: mutual information *MeanSquares*: mean square (fast, recommended for type=*seg*)	Similarity metric used for registration. In general, for type=*im* we recommend *CC* (performs well on multi-modal images but slow), while for type=*seg* we recommend *MeanSquares* (fast). The metric *MI* (mutual information) can be used for both images and segmentations, but requires enough image overlap and voxel count to compute histogram (otherwise it fails).

iter	*positive int*	Number of iterations in current registration step.
shrink	*strictly positive int (>0)*	Shrink factor, which specifies sub-sampling factor of the destination volume for faster computation. Default=1. Only for algo={*syn, bsplinesyn*}
smooth	*positive int*	Smooth factor, which specifies in mm the sigma of the Gaussian smoothing kernel applied to the source and destination volumes before registration. Recommended for type=seg. Default=0. Only for algo={*syn, bsplinesyn*}
gradstep	*strictly positive float*	Gradient descent optimization. The higher the more deformation. Default=0.5. Only for algo={*syn, bsplinesyn*}
poly	*positive int*	Polynomial degree. Only for algo=*slicereg*.
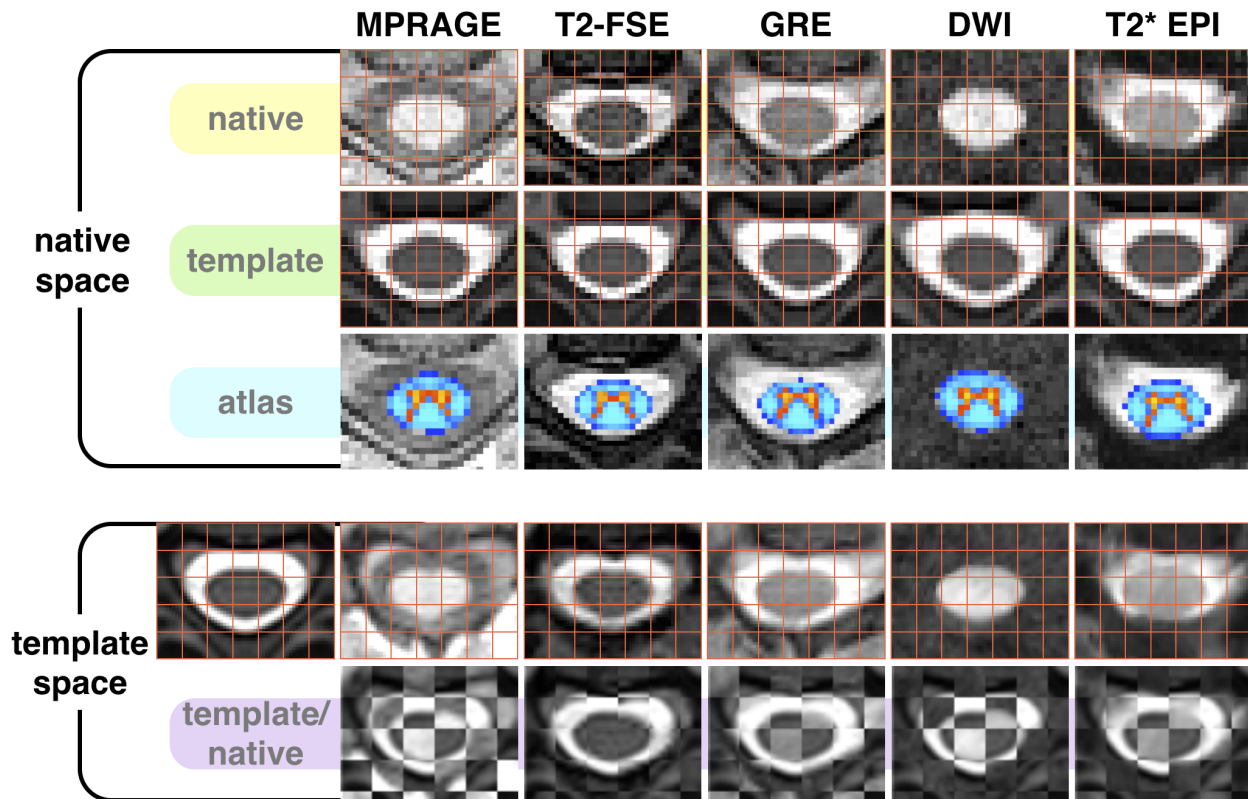
Figure 4.4: Example of co-registration between T_1-weighted MPRAGE, T_2-weighted fast spin echo, T_2*-weighted gradient echo, diffusion-weighted image, T_2*-weighted EPI and the MNI-Poly-AMU template. Note that in the "native space" box, the category "template" refers to the

warped template, and the category "atlas" refers to the warped atlas. Despite the different contrasts and levels of distortions across sequences, all images were successfully registered to the template, as assessed qualitatively. The red grid overlaid on images and the checkerboard images enable to appreciate the spatial correspondence within each sequence (between native and template), and the slight deformation/motion inherent to each sequence. Reproduced with permission from (Fonov et al., 2014).

4.3.4 Atlas-based analysis of mpMRI metrics

Once mpMRI data are registered with the template it is possible to extract relevant metrics (e.g., DTI fractional anisotropy) using pre-existing atlases, without the need to manually draw ROIs. This analysis can either be performed on the template space (after warping the mpMRI data to the template using the function `sct_apply_transfo`) or on the mpMRI space (after warping the template objects to the mpMRI data using the function `sct_warp_template`). The former approach is preferred for obtaining group maps of mpMRI results, while the latter approach is preferred for minimizing interpolation errors during metric extractions.

Metrics can be quantified automatically using the function `sct_extract_metric` and an atlas. The default atlas (Lévy et al., 2015) is the perfect candidate as it includes *Ntracts*=30 different tracts of the white matter as well as the gray matter and the surrounding CSF.

A notable feature of metric quantification in SCT is the possibility to account for partial volume effect using Gaussian mixture modelling, which provides a more accurate estimate of mpMRI metrics within the spinal cord regions in comparison to the traditional average within binary mask (Lévy et al., 2015). In brief, the signal in each voxel is assumed to be a linear combination of signals from adjacent regions (e.g., gray matter, CSF) and weighted by the partial volume information of each region. The simplest form of estimation is the maximum likelihood (*ml*). Let's call *n* the total number of voxels in the template, *y* the metric data rearranged in vector form ($n\times1$), *X* the atlas containing partial volume values ($n\times Ntracts$) and β the 'true' metric within each tract ($Ntracts\times1$). The least-square solution of β is:

$$\beta = (X^t \cdot X)^{-1} \cdot X^t \cdot y$$

A limitation of the maximum likelihood method however is its poor robustness to noise, hence values estimated within small tracts can be aberrant. To mitigate this poor robustness, constraints

can be added to 'force' the estimated β needs to be close to a prior β_0. This can be done using the maximum a posteriori (*map*) approach. The equation now reads:

$$\beta = \beta_0 + (X^t \cdot X + I)^{-1} \cdot X^t \cdot (y - X \cdot \beta_0)$$

with *I* being the identity matrix. Here, a pragmatic approach was chosen to estimate β_0 a priori, by considering that tracts within the white matter have similar values, therefore the white matter can be considered as a single class with a global mean. In order to robustly and accurately estimate β_0 in the white matter, maximum likelihood estimation was employed, by considering the following three classes that represent adjacent regions: white matter, gray matter and CSF. Following estimation of β_0, the *map* method can be applied.

More traditional quantification methods are also available in SCT, including the binary average (*bin*) and the weighted average (*wa*). The accuracy and precision of each method was assessed using simulations (Lévy et al., 2015), and suggest highest performance for the *map* method. Further simulations on the effect of spatial resolution are available in Annex 9.8. Note that metrics can be estimated in single tracts, in a group of tracts (e.g., right and left fasciculus gracilis and cuneatus) or in the entire white matter. It is also possible to specify the range of slices or the vertebral levels to extract the metrics from (e.g., C2 to C5). Also note that extraction of metric in the gray matter is possible with correction for partial volume effect (using maximum likelihood). However, the current version of the gray matter template does not include sub-structure (e.g., motor neurons, dorsal nucleus, etc.), therefore the extracted value will correspond to the total gray matter at a given slice (or group of slices).

4.3.5 Miscellaneous tools

4.3.5.1 Motion correction for diffusion and functional MRI time series

Diffusion and functional MRI datasets consist of a collection of multiple volumes whose number can range from 10-20 to several hundreds. These data usually take several minutes to acquire. If the subject moves between volumes, this can compromise the analysis done on the whole dataset (e.g., tensor estimation or statistical analysis in fMRI). It is thus common procedure to perform motion correction, which consists in registering all volumes to a target volume (e.g., the first one). However, as mentioned previously in section "4.3.3. Multi-modal registration", spinal cord movement can be non-affine (e.g., if subject tilts the head) therefore in contrast to the brain, affine

transformations cannot be employed (or at the risk of poor accuracy). It is commonly accepted to perform motion correction using slice-wise translations in axial plane (Cohen-Adad et al., 2010; Duval et al., 2015; El Mendili et al., 2014; Grussu, Schneider, Zhang, Alexander, & Wheeler-Kingshott, 2015; Iglesias et al., 2015; Kong, Jenkinson, Andersson, Tracey, & Brooks, 2012; Mohammadi, Freund, Feiweier, Curt, & Weiskopf, 2013; Smith et al., 2010), which in SCT can be performed using regularization along the *z* direction (*SliceReg* algorithm).

In addition to this feature, motion correction in SCT includes the methods of Xu *et al*. for grouping successive volumes, thereby improving the robustness of registration in high b-value diffusion MRI data (Xu et al., 2013). For example, if one volume is acquired with diffusion-weighted gradients along the spinal cord, signal might be too low to estimate a meaningful transformation. In such cases it can be preferred to rely on volumes adjacent in time and estimate the transformation from groups of *n* successive volumes (typically 3 to 5) averaged together. This approach is particularly successful for correcting slow drifts in long acquisitions, but fails in presence of strong Eddy-current distortions, which affect each diffusion-weighted volume independently from its next predecessor and successor. In that case, *n*=1 would be preferable. Note that the target volume is iteratively updated by averaging the registered volumes with the target volume.

Another feature that improves motion correction is the possibility to mask out undesired regions. It is known in spinal cord times series that other structures can move independently from the spinal cord, such as the muscles or the chest (in thoracic imaging). Given that these structures usually contain more voxels than the spinal cord, estimating a global transformation on the entire volume can lead to spurious displacement of the spinal cord (because the metric of the cost function will be weighted towards larger structures). Hence, a mask of the spinal cord can be input for motion correction to overcome this problem. This mask can be obtained automatically from the spinal cord segmentation using the function `sct_create_mask`.

4.3.5.2   Smoothing along spinal cord centerline

Denoising an MRI image of the spinal cord with a classical isotropic Gaussian smoothing kernel leads to undesired partial volume effect with CSF, therefore decreasing the accuracy of spinal cord measurements. Even a unidirectional kernel (e.g., in the inferior-superior direction) can lead to CSF contamination in some parts of the spinal cord due to its variable curvature. To circumvent this issue, SCT features an algorithm that can smooth a dataset along the spinal cord centerline, as

illustrated in Figure 4.5. This approach is analogous to the 2D surface smoothing that is popular for brain cortical analysis (Hagler Jr, Saygin, & Sereno, 2006; Kiebel, Poline, Friston, Holmes, & Worsley, 1999). Our algorithm works by straightening the cord, applying a 1-D Gaussian smoothing kernel (size can be adjusted by the user) and then un-straightening the cord back into the original space. Centerline smoothing can be useful for improving the sensitivity for spinal cord fMRI experiments or for structural assessment of degenerative pathology occurring along the superior-inferior direction. Further demonstration about the usefulness of this algorithm is required.
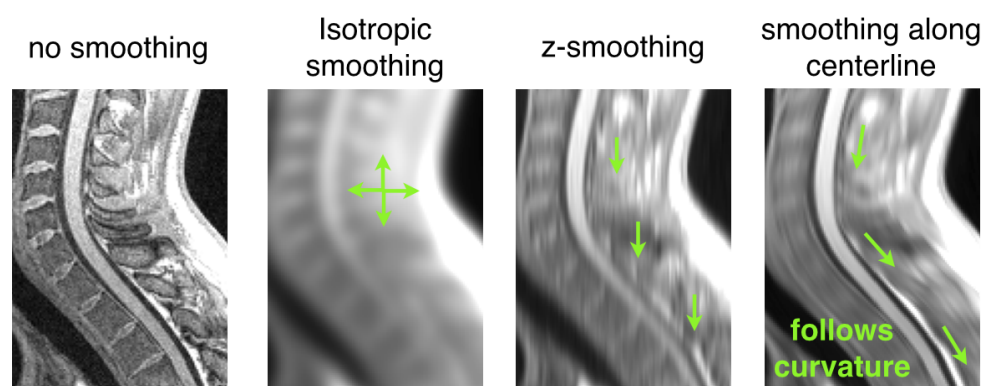
Figure 4.5: Methods to smooth the spinal cord. From left to right: no smoothing; smoothing using isotropic Gaussian kernel (classical approach); smoothing using anisotropic Gaussian kernel; smoothing using an adaptive Gaussian kernel oriented along the spinal cord centerline.

4.4 Technical considerations

4.4.1 License, language and dependences

SCT is an open-source project that falls under the MIT license[4]. SCT is written in Python and has been designed in an object-oriented programming fashion in order to improve modularity and extensibility. SCT tools are available via two interfaces: (i) a command-line software, meaning that tools can be called within a Unix terminal, and (ii) a Python library called within Python code.

---

[4] https://opensource.org/licenses/MIT

Dependent Python libraries include: nibabel[5] for reading/writing NIFTI files, numpy[6] and scipy[7] for scientific computation and dipy[8] for processing diffusion-weighted imaging. The only external dependent software is ANTs (Avants et al., 2009), however the required binaries are already included in SCT packages therefore users don't need to install it. The image format that is currently supported by SCT is NIfTI[9]. In order to ensure stability and reproducibility towards Python dependences, SCT comes with an integrated light distribution of Python, called Miniconda[10]. When called via command-line, each script calls a Python launcher that sets a virtual environment for the correct Python distribution and then runs the script. This prevents SCT from interfering with the user's default Python distribution.

4.4.2 Download and installation

The main project is hosted on Sourceforge[11] and NITRC[12] while source code is available on GitHub[13]. SCT is currently available for Mac OSX (10.7 and higher) and Linux users (Debian/Ubuntu, Fedora and RedHat families). For Windows users, a Virtual Machine based on NeuroDebian[14] with SCT installed is provided, however future versions of SCT will be compatible with Windows. SCT installation can be done by downloading a package[15] and running the script `./install_sct` that copies the necessary files, downloads the binaries associated with the running OS, downloads data, installs Python requirements, installs the latest patch and updates environment variables. Version numbering follows software standard: X.Y.Z., with X corresponding to major changes in the software, Y corresponding to new versions and Z corresponding to patches (backward compatibility ensured). Each patch release comes with an installer. To test if SCT and dependencies are properly installed, the user can run: `sct_check_dependencies`.

---

[5] http://nipy.org/nibabel/
[6] http://www.numpy.org/
[7] http://www.scipy.org/
[8] http://nipy.org/dipy/
[9] http://nifti.nimh.nih.gov/
[10] http://conda.pydata.org/miniconda.html
[11] https://sourceforge.net/projects/spinalcordtoolbox/
[12] https://www.nitrc.org/projects/sct/
[13] https://github.com/neuropoly/spinalcordtoolbox
[14] http://neuro.debian.net/
[15] https://sourceforge.net/projects/spinalcordtoolbox/files/

4.4.3 Getting started

After installing SCT, the user is redirected to a shell script (`batch_processing.sh`) that includes a list of command lines illustrating a typical processing of mpMRI data. An example mpMRI dataset is also provided to the user. Table 4.2 presents a portion of the batch script for processing T$_2$-weighted data. Because SCT is in constant evolution, this script is subject to modifications in future versions of SCT.

Table 4.2: Example of code for processing T2-weighted data, including segmentation of the spinal cord, labeling of vertebrae, registration to the MNI-Poly-AMU template and extraction of T2-weighted in the white matter over several vertebral levels. Tested on version dev-e4e9c242674eaa515efe4ad89faa67a09cd12604.

```
# download example data
sct_download_data -d sct_example_data
# go to folder
cd sct_example_data/t2
# spinal cord segmentation
sct_propseg -i t2.nii.gz -c t2
# vertebral labeling. Here we use the fact that the FOV is centered at C7.
sct_label_vertebrae -i t2.nii.gz -s t2_seg.nii.gz -initcenter 7
# create labels at C2 and T2 vertebral levels
sct_label_utils -i t2_seg_labeled.nii.gz -label-vert 2,9
# register to template
sct_register_to_template -i t2.nii.gz -s t2_seg.nii.gz -l labels.nii.gz
# warp template and white matter atlas
sct_warp_template -d t2.nii.gz -w warp_template2anat.nii.gz
# compute average cross-sectional area between C3 and C4 levels and output result in EXCEL
file
sct_process_segmentation -i t2_seg.nii.gz -p csa -vert 3:4
# --> Mean CSA: 77.299559 +/- 2.015639 mm^2
```

4.4.4 Testing

Being open-source, SCT benefits from the popular testing platform Travis [16]. Each time the code is pushed on GitHub, the entire project is tested on both Linux and OSX environments. Each

---

[16] https://travis-ci.org/neuropoly/spinalcordtoolbox/builds

function of the toolbox has its own testing procedure which assesses crash and integrity (i.e., verifies if the output of the function is the same as the provided ground-truth). The user can also run tests on its own machine using the function: `sct_testing`. This function downloads a small testing dataset and performs crash and integrity tests on each SCT script.

In addition to the single-dataset testing, the function `isct_test_function` can test a specific function on a large dataset (e.g., 200 subjects). This function uses multi-threading (one core per subject) and outputs useful metrics in the Python *panda* format, which facilitates the generation of statistics and figures. This function is used internally on multi-center and multi-modal datasets in order to quantify the robustness, accuracy and reproducibility of every SCT functions, as well as to ensure the stability of the code and various releases across time. For each function, specific metrics can be computed (e.g., Dice coefficient between automatic segmentation and manual cord segmentation, with appropriate pass/fail threshold). The Appendix shows results of `isct_test_function` on the following functions: `sct_propseg`, `sct_straighten_spinalcord`, `sct_register_to_template` and `sct_label_vertebrae`.

4.4.5 Quality control (QC)

SCT provides convenient means of performing QC. While a function is running, the Terminal prints out a description of all sub-processes that are ongoing in real time, allowing the user to re-run any step for debugging purpose or for playing with processing parameters. To this end, most functions feature a flag "-r" that enables/disables removal of temporary folder that contains all temporary files created by SCT. Warning message (displayed in yellow) is sent if something abnormal is detected, but the process continues to run. Error message (displayed in red) stops the process and displays the error. At the end of most functions, a command line is displayed that can be copied/pasted by the user via the Terminal. This command line opens *fslview* (Smith et al., 2004) and displays input/output images with appropriate colormaps and overlay opacity depending on the function. Moreover, some functions output *png* images that show one slice or a matrix of slices in the appropriate orientation, in order to assess the quality of each process (e.g., segmentation, registration). QC information specific to each function is listed hereafter and examples of application for testing are included in the Appendix.

The function `sct_propseg` displays the radius of the initial circle (to verify initialization) and the final length of the propagation (to verify cord segmentation). If the propagation length is too low (e.g., 2cm whereas the input image shows a cord that is >10cm) then the user knows that some parameters might need to be adjusted. The function can also output the 3D mesh of the segmentation for visual inspection (flag "-mesh"). Other QC outputs are available and can be listed with flag "-h".

The function `sct_straighten_spinalcord` calculates the maximum distance and the root mean square error to a straight line. These QC numbers are used by `sct_testing` (also see Appendix 4.10.2).

The function `sct_extract_metric` indicates the voxel fraction for each estimation. If the voxel fraction is too low (as discussed in section 5.1), then estimation results need to be interpreted with caution and extraction parameter might need to be adjusted (e.g., group several tracts and/or increase the rostro-caudal length).

The function `sct_label_vertebrae` displays a message indicating that the probabilistic disc-to-disc distance (based on the template) will be used instead of the image when the correlation is lower than the default threshold (which is set empirically but can be adjusted if needed).

The functions `sct_register_multimodal`, `sct_register_to_template` and `sct_register_graymatter` can display quantitative results of the optimization from the ANTs framework if verbose mode "v=2" is set (default is "v=1"). From these numbers, the user can evaluate if the convergence of the registration algorithm is sound, or if he/she needs to adjust parameters (as discussed in Section 4.3.3.2.).

The function `sct_segment_graymatter` outputs *png* images for quick visual assessment of the segmentation.

4.5 Example applications

4.5.1 Analysis of mpMRI data

An adult subject was scanned at 3T (TIM Trio, Siemens Healthcare) using the following sequences: (i) 3D T_2-weighted fast spin echo, (ii) gradient echo FLASH with and without magnetization transfer and (iii) diffusion-weighted EPI (b-value = 800 s/mm^2). For details on sequence parameters

see (Fonov et al., 2014). Processing included spinal cord segmentation, vertebral labeling, gray matter segmentation, cross-sectional measurement, registration to template, motion correction using *SliceReg* and metrics extraction using maximum a posteriori. Figure 4.6a shows vertebral labeling, CSA overlaid on the anatomical data and the corresponding CSA plot from C1 to T6. Figure 4.6b shows the gray (red) and white matter (blue) segmentation with the corresponding CSA plot between C1 and C7. Figure 4.6c shows magnetization transfer ratio (MTR), fractional anisotropy (FA), radial diffusivity (RD) and mean diffusivity (MD) images with overlay of four spinal tracts: left and right lateral corticospinal tracts and cuneatus. The table shows the maximum a posteriori estimations within each tract.

	MTR [%]	FA [0-1]	RD [µm2/s]	MD [µm2/s]
CST_R	31	0.77	410	901
CST_L	35	0.78	349	849
cuneatus_R	35	0.83	193	762
cuneatus_L	32	0.78	288	832
gray matter	25	0.64	452	776
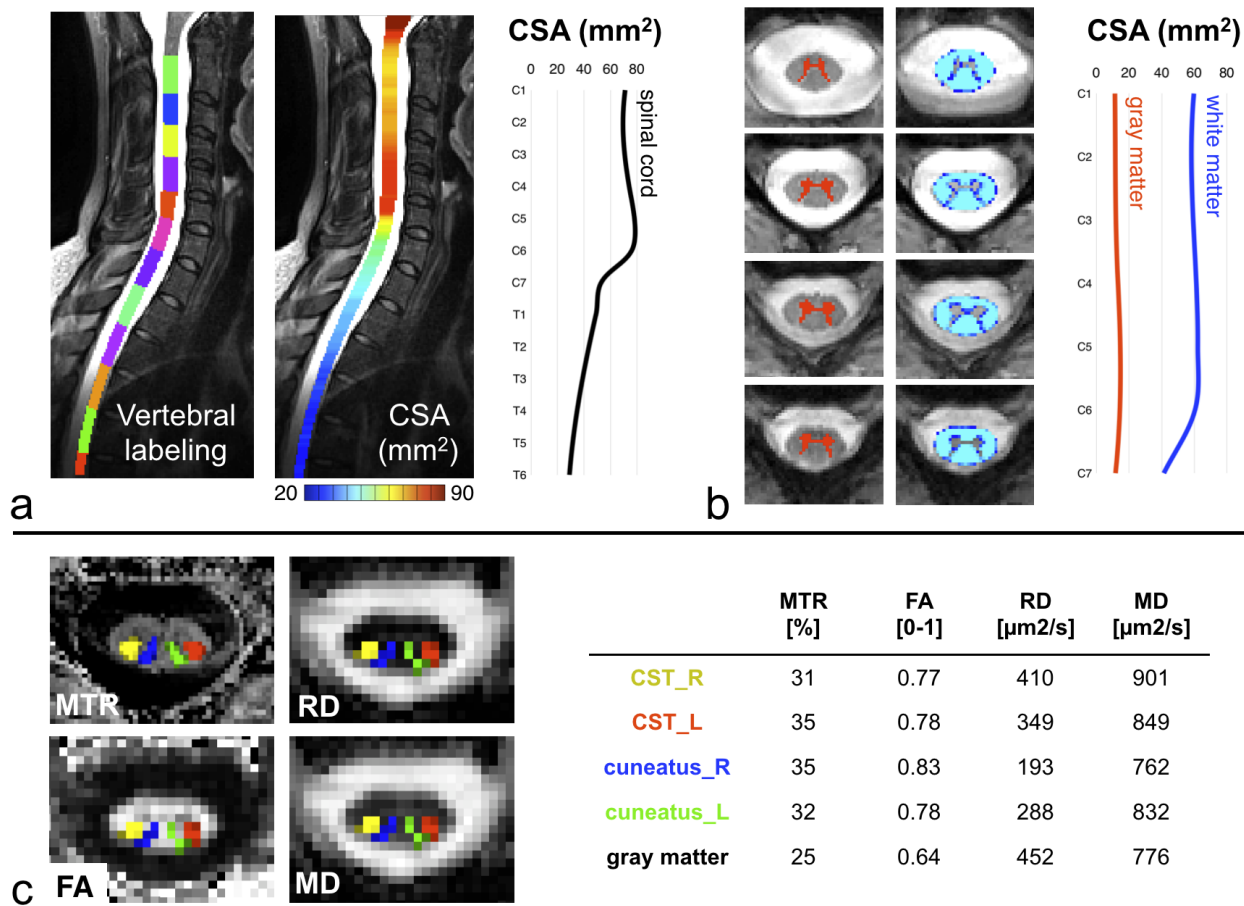
Figure 4.6: a: Following spinal cord segmentation and vertebral labeling, cross-sectional area (CSA) is overlaid on the anatomical data and values can be extracted at specific vertebral levels (here, between C1 and T6). b: Following gray and white matter segmentation on the T_2*-weighted data, CSA values can be computed. Note that output segmentations include partial volume information, therefore CSA estimation is more precise than when using binary masks. Here also,

vertebral labeling can be used to extract CSA at specific vertebral levels (here, between C1 and C7). c: Following registration of FLASH and diffusion data to the template, magnetization transfer ratio (MTR), radial diffusivity (RD), fractional anisotropy (FA) and mean diffusivity (MD) were computed within the gray matter (not displayed for clarity purpose) and four white matter tracts: corticospinal tracts left (red) and right (yellow), cuneatus left (green) and right (blue). Values were extracted between C1 and C4 levels. Note that there is an apparent overlap between the cuneatus ROIs and the dorsal horns of the gray matter, which is related to the partial volume encoding of the ROIs (thresholded at 0.3 for visual purpose).

4.5.2 Applications at other field strengths and in pathologies

While SCT has mostly been validated and used in healthy data from 3T scanners, it can also be applied to lower/higher field strength as well as in patients, providing data quality is sufficient. Figure 4.7 shows example applications at 1.5T, 3T and 7T, in a variety of spinal cord pathologies (multiple sclerosis, cervical spondylotic myelopathy, amyotrophic lateral sclerosis, syringomyelia, ischemia). Here, T_2*-weighted data were acquired, then processing consisted in segmenting the spinal cord and gray matter, then registering the data to the MNI-Poly-AMU template and warping back four white matter tracts on the data (left/right corticospinal tracts and gracilis).

	T$_2$*-w	Cord seg	WM/GM seg	WM atlas
HC @1.5T		CSA=72.6 mm²	CSA=63.7/12.0	
HC @7T		CSA=83.5 mm²	CSA=68.1/13.4	
Syringo. @3T		CSA=77.4 mm²	CSA=60.4/16.0	
CSM @3T		CSA=77.9 mm²	CSA=61.9/15.4	
CSM @3T		CSA=65.3 mm²	CSA=54.2/12.9	
MS @7T		CSA=70.6 mm²	CSA=58.9/11.7	
ALS @7T		CSA=73.9 mm²	CSA=61.3/12.2	
SCI @7T		CSA=71.5 mm²	CSA=61.0/11.8	

Figure 4.7: Example application in T_2*-weighted data from 1.5T, 3T and 7T, different vendors and different pathologies. Here, SCT was used to segment the spinal cord, registering the MNI-Poly-AMU to the data, segmenting the gray and white matter, adjusting the warping field based on gray matter shape, and finally warping the white matter atlas to the template. The white/gray matter is shown in blue/yellow respectively, and is thresholded at 0.4 for visual purpose. The left/right corticospinal and left/right gracilis are respectively shown in yellow/blue and green/red and are thresholded at 0.4. Parameters for each subject are listed hereafter. **HC @1.5T**: GE Signa HDxt, neurovascular coil, 2D MERGE sequence, TR/TE=607/16ms, matrix=320×320, resolution=0.8×0.8×4mm^3 (interpolated to 0.4mm in-plane using zero padding), R=2 acceleration, bandwidth=244Hz/pixel. **HC @7T**: Siemens 7T whole-body scanner with SC72 gradients and 4ch-Tx/19ch-Rx coil (Zhao et al., 2014), multi-echo FLASH (all echoes were averaged), TR/TE=512/[7.8,15,22,29.4]ms, matrix=384×384, resolution=0.35×0.35×3mm^3, R=2 acceleration, bandwidth=195Hz/pixel. **Syringo @3T**: Siemens TIM Trio, 4ch neck coil, multi-echo FLASH (all echoes were averaged), TR/TE=539/[5.41,12.56,19.16]ms, matrix=320×320, resolution=0.5×0.5×5mm^3, R=2 acceleration, bandwidth=195Hz/pixel. **CSM @3T**: GE Signa HDxt, neurovascular coil, 2D MERGE sequence, TR/TE=550/13ms, matrix=320×320, resolution=0.6×0.6×4mm^3, R=1 acceleration, bandwidth=244Hz/pixel. Data courtesy of Drs. Allan Martin and Michael Fehlings from Toronto Western Hospital. **MS @7T**: Siemens 7T whole-body scanner with SC72 gradients and 4ch-Tx/19ch-Rx coil, multi-echo FLASH, TR/TE=500/[7.8,13.7,18.4]ms, matrix=480×534, resolution=0.4×0.4×3mm^3, R=2 acceleration, bandwidth=199Hz/pixel. Data courtesy of Dr. Caterina Mainero from Massachusetts General Hospital. **ALS @7T**: Siemens 7T whole-body scanner with SC72 gradients and 4ch-Tx/19ch-Rx coil, multi-echo FLASH, TR/TE=514/[7.8,15,22,29.4]ms, matrix=534×484, resolution=0.35×0.35×3mm^3, R=2 acceleration, bandwidth=195Hz/pixel. Data courtesy of Dr. Nazem Atassi from Massachusetts General Hospital. **SCI @7T**: Siemens 7T whole-body scanner with SC72 gradients and 4ch-Tx/19ch-Rx coil, multi-echo FLASH, TR/TE=514/[7.8,15,22,29.4]ms, matrix=534×480, resolution=0.37×0.37×3mm^3, R=2 acceleration, bandwidth=195Hz/pixel. Data courtesy of Dr. Anne-Louise Oaklander from Massachusetts General Hospital.

4.6 Discussion

SCT is an open-source image processing software dedicated to spinal cord mpMRI data. SCT includes state-of-the-art MRI templates and atlases of the spinal cord internal structure, robust methods to register new data to the template and motion correction methods for diffusion and functional time series.

4.6.1 Atlas-based analysis

An important feature of SCT is the MNI-Poly-AMU template, which provides a spatial reference for quantifying mpMRI data within the spinal cord and/or in specific white matter tracts (e.g, the left corticospinal tract). One limitation of the current white matter atlas is that it is built from a single drawing showing the C4 mid cervical level (Standring, 2008), which is then extrapolated to superior and inferior levels using nonlinear warping (Lévy et al., 2015). While the warping is regularized using BSplineSyN function (Tustison & Avants, 2013) and takes into account the gray matter shape, the exact location of tracts might change across levels and across subjects, especially in diseased patients where only specific tracts degenerate (e.g., amyotrophic lateral sclerosis) thereby altering the overall distribution of tracts in the cross-sectional plane. While we believe these discrepancies might induce inaccuracies when quantifying metrics within certain tracts (or group of tracts), there is currently no known solution as to how find the exact location of spinal tracts *in vivo*. Brain researchers face similar issues when warping subject's brain onto a common template based on MRI-visible anatomical features (gyri/sulci, ventricles, etc.), without knowing the exact internal structure of white matter tracts or functional clusters (Frost & Goebel, 2012; Mori, Oishi, & Faria, 2009). We thus believe that although it has flaws, the proposed approach for quantifying tracts in the cord is still the least biased in comparison with the current state-of-the-art, which consists in manually drawing an ROI in "what appears to be" the tract of interest based on the user's knowledge of spinal cord anatomy (Ciccarelli et al., 2007; Cohen-Adad et al., 2008; Gullapalli et al., 2006; Klawiter et al., 2011; Lindberg et al., 2010; Narayana et al., 2004; Onu et al., 2010; Qian et al., 2011; Smith et al., 2010; Xu et al., 2013). This approach has major flaws: (i) the identification of the tract is biased by the user experience and knowledge of the anatomy, (ii) the manual delineation of ROIs is long and tedious, especially if several slices, tracts and subjects are involved and (iii) ROIs consist of binary masks and hence do not account for partial volume effect. The approach offered in SCT solves all these issues. Firstly, since the atlas is aligned with

the MNI-Poly-AMU T_2-weighted template, registration of any mpMRI data with the template ensures that the atlas is also aligned with the subject's spinal cord. Moreover, this procedure is done automatically allowing processing of a large database without user bias. Secondly, each voxel of the atlas represents the fractional volume of a specific tract, normalized by the probability to be in the white matter (Taso et al., 2014). Hence, partial volume effect can be accounted for during metric extraction using Gaussian mixture modelling (maximum likelihood, maximum a posteriori).

While quantifying metrics within large tracts (e.g., lateral corticospinal) was shown to be fairly robust using typical sequences and resolutions (Lévy et al., 2015), quantifying metrics in small tracts that sometimes only cover a fraction of a voxel in the cross-sectional plane is more prone to noise and thus requires caution and further consideration. However, when considering the superior-inferior dimension, the cumulative volume fraction can be higher than a voxel. An important aspect of metric quantification in the cord is to take advantage of the elongated nature of the tract, while assuming homogeneous metric value across a certain rostro-caudal distance (which of course might not always be true, as discussed later). As an example, let's take the left lateral reticulospinal tract across C3 level. The volume of the tract[17] at this level is about 4.6 mm^3. With a typical resolution of $0.8{\times}0.8{\times}4$ mm^3 ($= 2.56$ mm^3), the voxel fraction would be approximately 1.8 (4.6/2.56), which might be sufficient for quantifying a metric, depending on the underlying noise and extraction method. To further investigate the effect of resolution on metric extraction, simulations have been conducted and are presented in Annex 4.10.8. Despite the encouraging results of this simulation, suggesting that metrics can be quantified within small tracts with minimum error ($<2\%$) if sufficient SNR (>10) and voxel fraction (>30) are available, we would like to stress that metric extraction from real data also suffers from image artifacts (e.g., chemical shift, distortions, dropout, motion), mis-registration and subject-to-subject differences in the underlying white matter anatomy. To summarize, the important aspects to consider for robust metric estimation are: the number of voxels covering the tract (in voxel fraction) and the level of noise. There is no universal approach as to what minimum tract size people can quantify, as it not only depends on the robustness of estimation (which, as mentioned before, depends on tract voxel fraction and noise level), but also on the scientific question that is being addressed. For example, if the goal is to detect a metric difference

---

[17] To calculate this volume the command is:
```
source sct_env; sct_process_segmentation -i $SCT_DIR/data/atlas/WMtract__05.nii.gz -p
csa -vert 3 -vertfile $SCT_DIR/data/template/MNI-Poly-AMU_level.nii.gz
```

between two populations, then the anticipated effect size should be part of the statistical power calculation. We therefore encourage people to choose the metric extraction method in light of the scientific hypotheses. For instance, if the goal is to detect subtle Wallerian degeneration above a compressed cord, then there is likely a diffuse abnormality that spans several vertebral levels above, and therefore estimation should encompass all levels above in order to increase the robustness of the estimation. Grouping tracts together (e.g., right and left fasciculus gracilis and cuneatus to form the dorsal column) is another trick to gain robustness, which again should comply with the underlying hypotheses.

Another aspect of the MNI-Poly-AMU template that warrants caution is the probabilistic spinal level location based on (Cadotte et al., 2015). We would like to stress that this location is based on 20 adult subjects and that further validation (e.g., from fMRI studies) is needed.

4.6.2 Modularity and cross-compatibility with other software

SCT was designed to be modular, i.e., to facilitate the addition of new functionalities, template or atlases. For example, if researchers want to use an external template (e.g., for pediatric population), they can specify the location of this external template when calling the function for template registration. Another aspect of the modularity is the possibility to reuse part of SCT into other spinal cord imaging packages. Like most brain software packages, SCT is composed of callable functions with explicit input/output and proper documentation, therefore some of them can easily be wrapped into other software packages.

A notable aspect that facilitates cross-compatibility is that the generated transformations (affine or warping fields) are compatible with ITK and ANTs protocols, but can also be used with other software such as FSL and SPM. A typical example of fMRI analysis would be to preprocess the fMRI time series with SCT (e.g., motion correction, registration to the template) and then use the estimated transformations to perform the first and second level analysis of the general linear models implemented in FSL, as was shown in a recent publication (Kong et al., 2014).

4.6.3 Applications

Since its first release (June 2014), SCT has been used in several studies such as resting-state fMRI of the spinal cord (Eippert et al., 2017; Kong et al., 2014), fMRI study of cord activity during an isometric upper extremity motor task (Weber 2nd, Chen, Wang, Kahnt, & Parrish, 2016b) and

thermal stimulation (Weber 2nd, Chen, Wang, Kahnt, & Parrish, 2016a), investigation of microstructure in aging (Taso, Girard, Duhamel, Le Troter, & others, 2016), adrenomyeloneuropathy (Castellano et al., 2016) and infectious myelitis (Talbott, Narvid, Chazen, Chin, & Shah, 2016), automated white matter/gray matter segmentation and tensor-based morphometry (Taso et al., 2015), mapping of fiber orientation in *ex vivo* human (Foxley et al., 2015), mapping of axonal diameter (Duval et al., 2015) and myelin g-ratio (Duval et al., 2017) *in vivo* in humans, correlation of cord atrophy with ambulation (Ljungberg et al., 2015), assessment of cord atrophy in multiple sclerosis (Yiannakas et al., 2016), quantification of axon degeneration in cervical spondylotic myelopathy (Grabher et al., 2016; Martin et al., 2016), multi-site DTI study of the cervical spinal cord (Samson et al., 2016), mapping of T_1, T_2 and T_2* relaxation times and diffusion tensor metrics from 7T data (Massire et al., 2016).

With the emergence of international initiatives for testing new drugs for the spinal cord, the standardization of mpMRI acquisition and processing methods for the spinal cord, combined with common templates and atlases, will facilitate collaborative work and will provide guidelines for future multi-center studies and clinical trials. For example, having a standard frame of reference will make it possible to share results of unthresholded statistical maps of fMRI experiments. Public repositories already exist for such initiatives[18].

SCT is primarily developed and tested on human data, although some of its functions can also be useful for non-human MRI data of the spinal cord. For example, the segmentation and the cord straightening modules have already been successfully applied to animal data (unpublished material).

4.6.4 Perspectives

Development of SCT is strongly tailored to researchers needs. As such, the MNI-Poly-AMU template is being expanded to the brainstem and full spinal cord and now includes multiple MRI contrasts: T_1-, T_2- and T_2*-weighted. The spinal cord detection module (part of *PropSeg*) is in constant evolution to be more robust and compatible with other MR contrast (e.g., diffusion- and T_2*-weighted). The two-landmark based registration to the template will be expended to higher

---

[18] http://neurovault.org/

number of landmarks to allow more accurate correspondence with vertebral levels. These improvements would lead to faster and more robust analysis of large databases.

Regarding white/gray matter segmentation, further tests are required in different pathological cases (e.g., MS, spinal cord injury). The research community would greatly benefit from a shared repository of pathological cases in order to make such validations.

The function-specific integrative testing implemented in SCT was designed to be modular, so that researchers developing methods for spinal cord can easily reuse the proposed framework. For example, if someone is developing another gray matter segmentation method, the same testing framework can be applied as that already used for the gray matter segmentation method implemented in SCT. In the long run, we hope this approach will facilitate cross-validation of other methods by comparing the same metrics with the same database and gold standards.

Finally, we would like to stress that image processing is only half of the story, and that the acquisition of good quality data and the standardization of protocols across vendors remains a challenging task, which contributes to the difficulty to perform multi-center studies (Stroman et al., 2014). The standardization of both acquisition and processing protocols for multi-parametric MRI of the spinal cord is being tackled at the international level (Samson et al., 2016), and will likely open promising avenues for cross-validating research outputs and for testing new therapeutic strategies (Wheeler-Kingshott et al., 2014).

4.7 Conclusion

SCT is a comprehensive software package dedicated to the processing of mpMRI data of the spinal cord. SCT is tailored towards standardization and automation of processing pipeline (intuitive batch scripts), versatility (user-oriented development of new features) modularity (possibility to reuse some SCT functions or to contribute to new features) and wide distribution (open-source, extensive testing framework, active support via forum). Preliminary applications of SCT cover a variety of studies, from cross-sectional area measures in a large database of patients to the precise quantification of mpMRI metrics in specific spinal pathways. It is hoped that SCT will contribute to bringing together the spinal cord neuroimaging community by establishing standard templates and analysis procedures, similarly to when MRI brain software were first introduced in the early 90'.

4.8 Acknowledgements

4.9 References

Adams, R. D., & Salam-Adams, M. (1991). Chronic nontraumatic diseases of the spinal cord. *Neurol. Clin.*, *9*(3), 605–623.

Asman, A. J., Bryan, F. W., Smith, S. A., Reich, D. S., & Landman, B. A. (2014). Groupwise multi-atlas segmentation of the spinal cord's internal structure. *Med. Image Anal.*, *18*(3), 460–471.

Avants, B. B., Epstein, C. L., Grossman, M., & Gee, J. C. (2008). Symmetric diffeomorphic image registration withcross-correlation: evaluating automated labeling of elderlyand neurodegenerative brain. *Med. Image Anal.*, *12*(1), 26–41.

Avants, B. B., Tustison, N. J., Song, G., Cook, P. A., Klein, A., & Gee, J. C. (2011). A reproducible evaluation of {ANTs} similarity metric performance in brain image registration. *Neuroimage*, *54*(3), 2033–2044.

Avants, B. B., Tustison, N., & Song, G. (2009). Advanced normalization tools (ANTS). *Insight J.*, *2*, 1–35.

Bozzo, A., Marcoux, J., Radhakrishna, M., Pelletier, J., & Goulet, B. (2011). The role of magnetic resonance imaging in the management of acute spinal cord injury. *J. Neurotrauma*, *28*(8), 1401–1411.

Bradbury, E. J., & McMahon, S. B. (2006). Spinal cord repair strategies: why do they work? *Nat. Rev. Neurosci.*, *7*(8), 644–653.

Brodmann, K. (1909). Vergleichende Lokalisationslehre der Groshirnrinde. *Leipzig: Barth*.

Cadotte, D. W., Cadotte, A., Cohen-Adad, J., Fleet, D., Livne, M., Wilson, J. R., … Fehlings, M. G. (2015). Characterizing the location of spinal and vertebral levels in the human cervical spinal cord. *AJNR Am. J. Neuroradiol.*, *36*(4), 803–810.

Cadotte, D. W., Wilson, J. R., Mikulis, D., Stroman, P. W., Brady, S., & Fehlings, M. G. (2011). Conventional MRI as a diagnostic and prognostic tool inspinal cord injury: a systemic review of its application todate and an overview on emerging MRI methods. *Expert Opin. Med. Diagn.*, *5*(2), 121–133.

Castellano, A., Papinutto, N., Cadioli, M., Brugnara, G., Iadanza, A., Scigliuolo, G., … Salsano, E. (2016). Quantitative MRI of the spinal cord and brain inadrenomyeloneuropathy: in vivo assessment of structuralchanges. *Brain*, *139*(Pt 6), 1735–1746.

Chang, H.-H., Zhuang, A. H., Valentino, D. J., & Chu, W.-C. (2009). Performance measure characterization for evaluating neuroimagesegmentation algorithms. *Neuroimage*, *47*(1), 122–135.

Ciccarelli, O., Wheeler-Kingshott, C. A., McLean, M. A., Cercignani, M., Wimpey, K., Miller, D. H., & Thompson, A. J. (2007). Spinal cord spectroscopy and diffusion-based tractography toassess acute disability in multiple sclerosis. *Brain*, *130*(Pt 8), 2220–2231.

Cohen-Adad, J., Descoteaux, M., Rossignol, S., Hoge, R. D., Deriche, R., & Benali, H. (2008). Detection of multiple pathways in the spinal cord using q-ballimaging. *Neuroimage*, *42*(2), 739–749.

Cohen-Adad, J., Gauthier, C. J., Brooks, J. C. W., Slessarev, M., Han, J., Fisher, J. A., … Hoge, R. D. (2010). {BOLD signal responses to controlled hypercapnia in humanspinal cord. *Neuroimage*, *50*(3), 1074–1084.

Cohen-Adad, J., Lévy, S., & Avants, B. (2015). Slice-by-slice regularized registration for spinal cord MRI:SliceReg. In *Proceedings of the 23th Annual Meeting of ISMRM, Toronto,Canada* (Vol. (in press), p. 5553). Toronto.

Cohen-Adad, J., Mareyam, A., Keil, B., Polimeni, J. R., & Wald, L. L. (2011). 32-channel RF coil optimized for brain and cervical spinalcord at 3 T. *Magn. Reson. Med.*, *66*(4), 1198–1208.

Cohen-Adad, J., & Wheeler-Kingshott, C. (2014). *Quantitative MRI of the Spinal Cord*. Academic Press.

De Leener, B., Cohen-Adad, J., & Kadoury, S. (2015). Automatic Segmentation of the Spinal Cord and Spinal CanalCoupled With Vertebral Labeling. *IEEE Trans. Med. Imaging*, *34*(8), 1705–1718.

De Leener, B., Kadoury, S., & Cohen-Adad, J. (2014). Robust, accurate and fast automatic segmentation of thespinal cord. *Neuroimage*, *98*, 528–536.

De Leener, B., Taso, M., Cohen-Adad, J., & Callot, V. (2016). Segmentation of the human spinal cord. *Magnetic Resonance Materials in Physics, Biology and Medicine*, *29*(2). https://doi.org/10.1007/s10334-015-0507-2

Dowell, N. G., Jenkins, T. M., Ciccarelli, O., Miller, D. H., & Wheeler-Kingshott, C. A. M. (2009). Contiguous-slice zonally oblique multislice (CO-ZOOM)diffusion tensor imaging: examples of in vivo spinal cord andoptic nerve applications. *J. Magn. Reson. Imaging*, *29*(2), 454–460.

Dupont, S. M., De Leener, B., Taso, M., LeTroter, A., Nadeau, S., Stikov, N., … Cohen-Adad, J. (2017). Fully-integrated framework for the segmentation andregistration of the spinal cord white and gray matter. *Neuroimage*, *150*, 358–372.

Duval, T., Le Vy, S., Stikov, N., Campbell, J., Mezer, A., Witzel, T., … Cohen-Adad, J. (2017). g-Ratio weighted imaging of the human spinal cord in vivo. *Neuroimage*, *145*(Pt A), 11–23.

Duval, T., McNab, J. A., Setsompop, K., Witzel, T., Schneider, T., Huang, S. Y., … Cohen-Adad, J. (2015). In vivo mapping of human spinal cord microstructure at 300mT/m. *Neuroimage*, *118*(0), 494–507.

Eippert, F., Kong, Y., Winkler, A. M., Andersson, J. L., Finsterbusch, J., Büchel, C., … Tracey, I. (2017). Investigating resting-state functional connectivity in thecervical spinal cord at 3 T. *Neuroimage*, *147*, 589–601.

El Mendili, M.-M., Cohen-Adad, J., Pelegrini-Issac, M., Rossignol, S., Morizot-Koutlidis, R., Marchand-Pauvert, V., … Pradat, P.-F. (2014). Multi-parametric spinal cord MRI as potential progressionmarker in amyotrophic lateral sclerosis. *PLoS One*, *9*(4), e95516.

Evans, A. C., Marrett, S., Neelin, P., Collins, L., Worsley, K., Dai, W., … Bub, D. (1992). Anatomical mapping of functional activation in stereotacticcoordinate space. *Neuroimage*, *1*(1), 43–53.

Finsterbusch, J. (2009). High-resolution diffusion tensor imaging with innerfield-of-view EPI. *J. Magn. Reson. Imaging*, *29*(4), 987–993.

Fonov, V., Evans, A. C., Botteron, K., Almli, C. R., McKinstry, R. C., Collins, D. L., & Brain Development Cooperative Group. (2011). Unbiased average age-appropriate atlases for pediatric studies. *Neuroimage*, *54*(1), 313–327.

Fonov, V. S., Le Troter, A., Taso, M., De Leener, B., Lévêque, G., Benhamou, M., … Cohen-Adad, J. (2014). Framework for integrated MRI average of the spinal cord white and gray matter: The MNI-Poly-AMU template. *NeuroImage*, *102*(P2). https://doi.org/10.1016/j.neuroimage.2014.08.057

Foxley, S., Mollink, J., Ansorge, O., Scott, C., Jbabdi, S., Yates, R., … Miller, K. (2015). Whole post-mortem spinal cord imaging with diffusion-weighted steady state free precession at {7T}. *Proceedings of the 23th Annual Meeting of ISMRM, Toronto, Canada*, 4429.

Frost, M. A., & Goebel, R. (2012). Measuring structural-functional correspondence: spatial variability of specialized brain regions after macro-anatomical alignment. *Neuroimage*, *59*(2), 1369–1381.

Grabher, P., Mohammadi, S., Trachsler, A., Friedl, S., David, G., Sutter, R., … Freund, P. (2016). Voxel-based analysis of gray and white matter degeneration incervical spondylotic myelopathy. *Sci. Rep.*, *6*, 24636.

Grussu, F., Schneider, T., Zhang, H., Alexander, D. C., & Wheeler-Kingshott, C. A. M. (2015). Neurite orientation dispersion and density imaging of the healthy cervical spinal cord in vivo. *Neuroimage*, *111*, 590–601.

Gullapalli, J., Krejza, J., & Schwartz, E. D. (2006). In vivo DTI evaluation of white matter tracts in rat spinalcord. *J. Magn. Reson. Imaging*, *24*(1), 231–234.

Hagler Jr, D. J., Saygin, A. P., & Sereno, M. I. (2006). Smoothing and cluster thresholding for cortical surface-basedgroup analysis of fMRI data. *Neuroimage*, *33*(4), 1093–1103.

Harlow, D. E., Honce, J. M., & Miravalle, A. A. (2015). Remyelination Therapy in Multiple Sclerosis. *Front. Neurol.*, *6*, 257.

Horsfield, M. A., Sala, S., Neema, M., Absinta, M., Bakshi, A., Sormani, M. P., … Filippi, M. (2010). Rapid semi-automatic segmentation of the spinal cord frommagnetic resonance images: application in multiple sclerosis. *Neuroimage*, *50*(2), 446–455.

Iglesias, C., Sangari, S., El Mendili, M.-M., Benali, H., Marchand-Pauvert, V., & Pradat, P.-F. (2015). Electrophysiological and spinal imaging evidences for sensory dysfunction in amyotrophic lateral sclerosis. *BMJ Open*, *5*(2), e007659.

Jenkinson, M., Bannister, P., Brady, M., & Smith, S. (2002). Improved optimization for the robust and accurate linear registration and motion correction of brain images. *Neuroimage*, *17*(2), 825–841.

Kearney, H., Miller, D. H., & Ciccarelli, O. (2015). Spinal cord MRI in multiple sclerosis [mdash] diagnostic,prognostic and clinical value. *Nat. Rev. Neurol.*, *11*(6), 327–338.

Kiebel, S. J., Poline, J. B., Friston, K. J., Holmes, A. P., & Worsley, K. J. (1999). Robust smoothness estimation in statistical parametric mapsusing standardized residuals from the general linear model. *Neuroimage*, *10*(6), 756–766.

Klawiter, E. C., Schmidt, R. E., Trinkaus, K., Liang, H.-F., Budde, M. D., Naismith, R. T., … Benzinger, T. L. (2011). Radial diffusivity predicts demyelination in ex vivo multiple sclerosis spinal cords. *Neuroimage*, *55*(4), 1454–1460.

Klein, A., Andersson, J., Ardekani, B. A., Ashburner, J., Avants, B., Chiang, M.-C., … Parsey, R. V. (2009). Evaluation of 14 nonlinear deformation algorithms applied tohuman brain MRI registration. *Neuroimage*, *46*(3), 786–802.

Kong, Y., Eippert, F., Beckmann, C. F., Andersson, J., Finsterbusch, J., Büchel, C., … Brooks, J. C. W. (2014). Intrinsically organized resting state networks in the humanspinal cord. *Proc. Natl. Acad. Sci. U. S. A.*, *111*(50), 18067–18072.

Kong, Y., Jenkinson, M., Andersson, J., Tracey, I., & Brooks, J. C. W. (2012). Assessment of physiological noise modelling methods for functional imaging of the spinal cord. *Neuroimage*, *60*(2), 1538–1549.

Laule, C., Vavasour, I. M., Leung, E., Li, D. K. B., Kozlowski, P., Traboulsee, A. L., … Moore, G. R. W. (2011). Pathological basis of diffusely abnormal white matter: insights from magnetic resonance imaging and histology. *Mult. Scler.*, *17*(2), 144–150.

Lévy, S., Benhamou, M., Naaman, C., Rainville, P., Callot, V., & Cohen-Adad, J. (2015). White matter atlas of the human spinal cord with estimation ofpartial volume effect. *Neuroimage*, *119*(0), 262–271.

Lindberg, P. G., Feydy, A., & Maier, M. A. (2010). White matter organization in cervical spinal cord relates differently to age and control of grip force in healthy subjects. *J. Neurosci.*, *30*(11), 4102–4109.

Ljungberg, E. A., Kolind, S. H., Tam, R., Freedman, M. S., Li, D. K., & Traboulsee, A. L. (2015). Correcting Cervical Spinal Cord Area for Cord LengthStrengthens Correlation Between Atrophy and Ambulation. In *MULTIPLE SCLEROSIS JOURNAL* (Vol. 21, pp. 789–790). researchgate.net.

Luessi, F., Kuhlmann, T., & Zipp, F. (2014). Remyelinating strategies in multiple sclerosis. *Expert Rev. Neurother.*, *14*(11), 1315–1334.

Mac Donald, C. L., Dikranian, K., Bayly, P., Holtzman, D., & Brody, D. (2007). Diffusion tensor imaging reliably detects experimental traumatic axonal injury and indicates approximate time of injury. *J. Neurosci.*, *27*(44), 11869–11876.

Martin, A. R., Aleksanderek, I., Cohen-Adad, J., Tarmohamed, Z., Tetreault, L., Smith, N., … Fehlings, M. G. (2016). Translating state-of-the-art spinal cord MRI techniques toclinical use: A systematic review of clinical studiesutilizing DTI, MT, MWF, MRS, and fMRI. *Neuroimage Clin*, *10*, 192–238.

Martin, A. R., De Leener, B., Aleksanderek, I., Cohen-Adad, J., Cadotte, D. W., Kalsi-Ryan, S., … Others. (2016). A prospective longitudinal study in degenerative cervical myelopathy using quantitative microstructural {MRI} with tract-specific metrics. In *Proceedings of the 24th Annual Meeting of International Society for Magnetic Resonance in Medicine, Suntec City, Singapore*.

Massire, A., Taso, M., Besson, P., Guye, M., Ranjeva, J.-P., & Callot, V. (2016). High-resolution multi-parametric quantitative magneticresonance imaging of the human cervical spinal cord at 7T. *Neuroimage*, *143*, 58–69.

McCormick, M., Liu, X., Jomier, J., Marion, C., & Ibanez, L. (2014). ITK: enabling reproducible research and open science. *Front. Neuroinform.*, *8*, 13.

Mohammadi, S., Freund, P., Feiweier, T., Curt, A., & Weiskopf, N. (2013). The impact of post-processing on spinal cord diffusion tensor imaging. *Neuroimage*, *70*, 377–385.

Mohammadi, S., Möller, H. E., Kugel, H., Müller, D. K., & Deppe, M. (2010). Correcting eddy current and motion effects by affine whole-brain registrations: evaluation of three-dimensional distortions and comparison with slicewise correction. *Magn. Reson. Med.*, *64*(4), 1047–1056.

Mori, S., Oishi, K., & Faria, A. V. (2009). White matter atlases based on diffusion tensor imaging. *Curr. Opin. Neurol.*, *22*(4), 362–369.

Narayana, P. A., Grill, R. J., Chacko, T., & Vang, R. (2004). Endogenous recovery of injured spinal cord: longitudinal in vivo magnetic resonance imaging. *J. Neurosci. Res.*, *78*(5), 749–759.

Onu, M., Gervai, P., Cohen-Adad, J., Lawrence, J., Kornelsen, J., Tomanek, B., & Sboto-Frankenstein, U. N. (2010). Human cervical spinal cord funiculi: investigation withmagnetic resonance diffusion tensor imaging. *J. Magn. Reson. Imaging*, *31*(4), 829–837.

Qian, W., Chan, Q., Mak, H., Zhang, Z., Anthony, M.-P., Yau, K. K.-W., … Kim, M. (2011). Quantitative assessment of the cervical spinal cord damage inneuromyelitis optica using diffusion tensor imaging at 3 Tesla. *J. Magn. Reson. Imaging*, *33*(6), 1312–1320.

Rowland, J. W., Hawryluk, G. W. J., Kwon, B., & Fehlings, M. G. (2008). Current status of acute spinal cord injury pathophysiology and emerging therapies: promise on the horizon. *Neurosurg. Focus*, *25*(5), E2.

Samson, R. S., Lévy, S., Schneider, T., Smith, A. K., Smith, S. A., Cohen-Adad, J., & Gandini Wheeler-Kingshott, C. A. M. (2016). ZOOM or Non-ZOOM? Assessing Spinal Cord Diffusion TensorImaging Protocols for Multi-Centre Studies. *PLoS One*, *11*(5), e0155557.

Smith, S. A., Jones, C. K., Gifford, A., Belegu, V., Chodkowski, B., Farrell, J. A. D., … van Zijl, P. C. M. (2010). Reproducibility of tract-specific magnetization transfer and diffusion tensor imaging in the cervical spinal cord at 3 tesla. *NMR Biomed.*, *23*(2), 207–217.

Smith, S. M., Jenkinson, M., Woolrich, M. W., Beckmann, C. F., Behrens, T. E. J., Johansen-Berg, H., … Matthews, P. M. (2004). Advances in functional and structural MR image analysis andimplementation as FSL. *Neuroimage, 23 Suppl 1*, S208–19.

Standring, S. (2008). Spinal cord: internal organization. *Gray's Anatomy, 40th Edition*, 257–274.

Stroman, P. W., Wheeler-Kingshott, C., Bacon, M., Schwab, J. M., Bosma, R., Brooks, J., … Tracey, I. (2014). The current state-of-the-art of spinal cord imaging: methods. *Neuroimage*, *84*, 1070–1081.

Summers, P. E., Brooks, J. C. W., & Cohen-Adad, J. (2014). Spinal cord {fMRI}. In *Quantitative {MRI} of the spinal cord*. Elsevier Inc.

Talbott, J. F., Narvid, J., Chazen, J. L., Chin, C. T., & Shah, V. (2016). An Imaging-Based Approach to Spinal Cord Infection. *Semin. Ultrasound CT MR*, *37*(5), 411–430.

Taso, M., Girard, O. M., Duhamel, G., Le Troter, A., & others. (2016). Tract-specific and age-related variations of the spinal cordmicrostructure: a multi-parametric MRI study using diffusiontensor imaging (DTI) and inhomogeneous …. *NMR Biomed.*

Taso, M., Le Troter, A., Sdika, M., Cohen-Adad, J., Arnoux, P.-J., Guye, M., … Callot, V. (2015). A reliable spatially normalized template of the human spinal cord--Applications to automated white matter/gray matter segmentation and tensor-based morphometry ({TBM}) mapping of gray matter alterations occurring with age. *Neuroimage*, *117*, 20–28.

Taso, M., Le Troter, A., Sdika, M., Ranjeva, J.-P., Guye, M., Bernard, M., & Callot, V. (2014). Construction of an in vivo human spinal cord atlas based onhigh-resolution MR images at cervical and thoracic levels:preliminary results. *MAGMA*, *27*(3), 257–267.

Tofts, P. (2003). *Quantitative {MRI} of the Brain: Measuring Changes Caused by Disease*. (Wiley, Ed.).

Tustison, N. J., & Avants, B. B. (2013). Explicit B-spline regularization in diffeomorphic imageregistration. *Front. Neuroinform.*, *7*, 39.

Ullmann, E., Pelletier Paquette, J. F., Thong, W. E., & Cohen-Adad, J. (2014). Automatic labeling of vertebral levels using a robust template-based approach. *Int. J. Biomed. Imaging*, *2014*, 719520.

van Middendorp, J. J., Goss, B., Urquhart, S., Atresh, S., Williams, R. P., & Schuetz, M. (2011). Diagnosis and prognosis of traumatic spinal cord injury. *Global Spine J*, *1*(1), 1–8.

Weber 2nd, K. A., Chen, Y., Wang, X., Kahnt, T., & Parrish, T. B. (2016a). Functional magnetic resonance imaging of the cervical spinalcord during thermal stimulation across consecutive runs. *Neuroimage*, *143*, 267–279.

Weber 2nd, K. A., Chen, Y., Wang, X., Kahnt, T., & Parrish, T. B. (2016b). Lateralization of cervical spinal cord activity during anisometric upper extremity motor task with functional magneticresonance imaging. *Neuroimage*, *125*, 233–243.

West, J., Aalto, A., Tisell, A., Leinhard, O. D., Landtblom, A.-M., Smedby, Ö., & Lundberg, P. (2014). Normal appearing and diffusely abnormal white matter in patients with multiple sclerosis assessed with quantitative {MR}. *PLoS One*, *9*(4), e95161.

Wheeler-Kingshott, C. A., Stroman, P. W., Schwab, J. M., Bacon, M., Bosma, R., Brooks, J., … Tracey, I. (2014). The current state-of-the-art of spinal cord imaging: applications. *Neuroimage*, *84*, 1082–1093.

Wilm, B. J., Svensson, J., Henning, A., Pruessmann, K. P., Boesiger, P., & Kollias, S. S. (2007). Reduced field-of-view MRI using outer volume suppressionfor spinal cord diffusion imaging. *Magn. Reson. Med.*, *57*(3), 625–630.

Xu, J., Shimony, J. S., Klawiter, E. C., Snyder, A. Z., Trinkaus, K., Naismith, R. T., … Song, S.-K. (2013). Improved in vivo diffusion tensor imaging of human cervicalspinal cord. *Neuroimage*, *67*, 64–76.

Yiannakas, M. C., Mustafa, A., De Leener, B., Cohen-Adad, J., Kearney, H., Miller, D. H., & Wheeler-Kingshott, C. (2015). Fully automated segmentation of the cervical spinal cord usingPropSeg: application to multiple sclerosis. In *Proceedings of the 23th Annual Meeting of ISMRM, Toronto,Canada* (p. 4354).

Yiannakas, M. C., Mustafa, A. M., De Leener, B., Kearney, H., Tur, C., Altmann, D. R., … Gandini Wheeler-Kingshott, C. A. M. (2016). Fully automated segmentation of the cervical cord from T1-

weighted MRI using PropSeg: Application to multiple sclerosis. *NeuroImage: Clinical, 10*. https://doi.org/10.1016/j.nicl.2015.11.001

Zhang, J., Jones, M., DeBoy, C. A., Reich, D. S., Farrell, J. A. D., Hoffman, P. N., … Calabresi, P. A. (2009). Diffusion tensor magnetic resonance imaging of Wallerian degeneration in rat spinal cord after dorsal root axotomy. *J. Neurosci., 29*(10), 3160–3171.

4.10 Appendix

The data used for validation were acquired at two sites (UNF-Montreal and CRMBM-Marseille) on a 3T system (TIM Trio, Siemens Healthcare). Acquisition parameters are: slab-selective fast spin echo, TR = 1500 ms, TE = 119 ms, flip angle = 140°, bandwidth = 723 Hz/voxel, voxel size = 1x1x1 mm^3, acquisition time = 6 min. Coverage: brainstem → T5. Note that subjects used for validation were different than subjects used to construct the template and GM model.

4.10.1 Validation of spinal cord segmentation (sct_propseg)

Table 4.3: Results of validation for sct_propseg. Metric (with pass/fail threshold indicated in brackets) is: **dice_segmentation** (>0.9): Dice coefficient between manual cord segmentation and automatic cord segmentation. Note that the Dice coefficients are overall larger than in the previous studies (De Leener et al., 2015a, 2014) (0.97 vs. 0.9), which is explained by the difference in coverage between the two studies (C1-T5 here vs. C1-T12). Since PropSeg is based on a propagation of a 3d mesh, it is subject to propagation errors which accumulate over a large distance. Moreover, given that the cord diameter decreases at the caudal levels, the Dice coefficient is more sensitive to discrepancies caused by binarization (i.e., inclusion/exclusion of cord voxel in manual and automatic segmentation), as pointed out in (Chang, Zhuang, Valentino, & Chu, 2009).

```
Spinal Cord Toolbox (version dev-9af778d77ef6527478a1ad3f8f2179f6e277235c)
Running:
/Users/benjamindeleener/code/spinalcordtoolbox/scripts/isct_test_function.py -f
sct_propseg -d /Volumes/data_shared/sct_testing/article_sct/ -p "-i t2/t2.nii.gz -c
t2"
OS: osx (Darwin-15.0.0-x86_64-i386-64bit), Hostname: bendeleener, CPU
available/used: 8/8, RAM: 16.00 gigabytes. Testing... (started on: 2016-05-30
16:59:28)
        subject  dice_segmentation  duration [s]  status
0           ALT           0.974909     59.192263        0
1            AM           0.979136     25.009005        0
2            ED           0.974385     30.344065        0
3      errsm_03           0.978930     30.219893        0
4      errsm_04           0.980217     33.304414        0
5      errsm_05           0.984458     28.966360        0
```

```
6        errsm_09        0.985376    31.513813        0
7        errsm_10        0.985270    30.059773        0
8        errsm_11        0.963750    33.417223        0
9        errsm_12        0.978226    28.130072        0
10       errsm_13        0.982187    34.205332        0
11       errsm_14        0.970628    29.322435        0
12       errsm_16        0.975682    33.403359        0
13       errsm_24        0.984579    31.423410        0
14       errsm_25        0.972632    33.938798        0
15       errsm_31        0.979778    31.034228        0
16       errsm_35        0.978907    26.739745        0
17       errsm_36        0.948414    34.814216        0
18       errsm_37        0.967442    26.488759        0
19       errsm_44        0.973496    31.830878        0
20             GB        0.972811    52.091329        0
21             HB        0.937498    24.502725        0
22             JW        0.981558    56.317613        0
23             MT        0.970099    37.002365        0
24             PA        0.958671    23.217906        0
25    pain_pilot_1       0.981062    33.690780        0
26    pain_pilot_2       0.979456    31.673408        0
27    pain_pilot_3       0.981869    27.859988        0
28    pain_pilot_4       0.970748    31.189391        0
29    pain_pilot_7       0.970450    31.905474        0
30        sct_001        0.981768    31.928909        0
31        sct_002        0.974058    23.013328        0
32           T045        0.951027    34.562992        0
33           T047        0.983665    10.713219        0
34             VC        0.972095    19.746288        0
           Mean         0.973864    31.793536
            STD          0.010873     9.033228
Passed: 35/35
Total duration: 168s
Status legend: 0: Passed, 1: Crashed, 99: Failed, 200: File(s) missing
```

4.10.2 Validation of spinal cord straightening (sct_straighten_spinalcord)

Table 4.4: Results of validation for sct_straighten_spinalcord. Metrics (with pass/fail threshold indicated in brackets) are: **dice** (>0.9): Dice coefficient between original cord segmentation and cord segmentation following application of warping fields: curved-to-straight then straight-to-curved; **dist_max** (<2mm): maximum distance error between straightened cord centerline and straight line; **mse** (<1mm): Root mean square error between straightened cord centerline and straight line.

```
Spinal Cord Toolbox (version dev-9af778d77ef6527478a1ad3f8f2179f6e277235c)
Running:
/Users/benjamindeleener/code/spinalcordtoolbox/scripts/isct_test_function.py -f
sct_straighten_spinalcord -d /Volumes/data_shared/sct_testing/article_sct/ -p "-i
t2/t2.nii.gz -s t2/t2_seg_manual.nii.gz"
OS: osx (Darwin-15.0.0-x86_64-i386-64bit), Hostname: bendeleener, CPU
available/used: 8/8, RAM: 16.00 gigabytes. Testing... (started on: 2016-05-30
17:21:25)
        subject     dice  dist_max    duration     rmse  status
0           ALT  0.964091  1.210000  138.035741  0.770000       0
1            AM  0.964272  1.240000  129.986078  0.750000       0
2            ED  0.940310  1.220000  136.400379  0.570000       0
```

```
3        errsm_03  0.974188  1.360000  169.131326  0.800000           0
4        errsm_04  0.973933  1.350000  157.414294  0.770000           0
5        errsm_05  0.963595  1.490000  148.234811  0.760000           0
6        errsm_09  0.942894  1.240000  161.720111  0.640000           0
7        errsm_10  0.970445  1.360000  178.990922  0.860000           0
8        errsm_11  0.965220  1.560000  162.602842  0.760000           0
9        errsm_12  0.971098  1.250000  154.384525  0.770000           0
10       errsm_13  0.973564  1.360000  179.241509  0.780000           0
11       errsm_14  0.967366  1.170000  145.726869  0.760000           0
12       errsm_16  0.969258  1.300000  167.700308  0.790000           0
13       errsm_24  0.976938  1.320000  162.213312  0.800000           0
14       errsm_25  0.977069  1.160000  160.847801  0.830000           0
15       errsm_31  0.965974  1.410000  180.545414  0.800000           0
16       errsm_35  0.940472  1.110000  154.124630  0.610000           0
17       errsm_36  0.954251  1.460000  175.945490  0.790000           0
18       errsm_37  0.975308  1.390000  147.528859  0.740000           0
19       errsm_44  0.957694  1.630000  160.090363  0.810000           0
20             GB  0.968203  1.300000  122.859090  0.830000           0
21             HB  0.977198  1.370000  135.946164  0.790000           0
22             JW  0.976327  1.280000  126.539476  0.680000           0
23             MT  0.958034  1.240000  121.892832  0.750000           0
24             PA  0.965978  1.360000  104.423937  0.760000           0
25   pain_pilot_1  0.962826  1.200000  166.212215  0.690000           0
26   pain_pilot_2  0.970687  1.410000  177.270257  0.760000           0
27   pain_pilot_3  0.967363  1.280000  147.872101  0.870000           0
28   pain_pilot_4  0.966756  1.460000  165.254728  0.790000           0
29   pain_pilot_7  0.969397  1.420000  154.295965  0.770000           0
30        sct_001  0.974191  1.200000  163.630688  0.740000           0
31        sct_002  0.970683  1.360000  141.603322  0.790000           0
32           T045  0.967967  1.340000   99.864195  0.690000           0
33           T047  0.978023  1.260000   47.066873  0.780000           0
34             VC  0.970585  1.290000   90.282064  0.800000           0
            Mean  0.966633  1.324571  146.739414  0.761429
             STD  0.009748  0.113716   28.525739  0.063392
Passed: 35/35
Total duration: 768s
```

4.10.3 Validation of template registration (sct_register_to_template)

Table 4.5: Results of validation for sct_register_to_template. Metrics (with pass/fail threshold indicated in brackets) are: **dice_anat2template** (>0.9): Dice coefficient between template cord segmentation and subject cord segmentation following application of warping field anat-to-template; **dice_template2anat** (>0.9): Dice coefficient between subject cord segmentation and template cord segmentation following application of warping field template-to-anat.

```
Spinal Cord Toolbox (version dev-9af778d77ef6527478a1ad3f8f2179f6e277235c)
Running:
/Users/benjamindeleener/code/spinalcordtoolbox/scripts/isct_test_function.py -f
sct_register_to_template -d /Users/benjamindeleener/data/sct_article/article_sct -p
"-i t2/t2.nii.gz -s t2/t2_seg_manual.nii.gz -l t2/labels.nii.gz"
OS: osx (Darwin-15.0.0-x86_64-i386-64bit), Hostname: bendeleener, CPU
available/used: 8/8, RAM: 16.00 gigabytes. Testing... (started on: 2016-05-30
22:24:00)
         subject  dice_anat2template  dice_template2anat  duration [s]  status
0            ALT            0.936628            0.953276  1351.117136         0
1             AM            0.936680            0.944771  1178.249453         0
2             ED            0.928370            0.930995  1346.815756         0
```

```
3        errsm_03         0.938017         0.956620   1280.668386        0
4        errsm_04         0.938522         0.957343   1405.813964        0
5        errsm_05         0.940862         0.960945   1252.367538        0
6        errsm_09         0.935940         0.955477   1395.179839        0
7        errsm_10         0.943405         0.958073   1269.222949        0
8        errsm_11         0.938392         0.943425   1416.074127        0
9        errsm_12         0.938000         0.957287   1245.334603        0
10       errsm_13         0.936076         0.957255   1423.625025        0
11       errsm_14         0.941128         0.954045   1233.543628        0
12       errsm_16         0.934081         0.960331   1392.906353        0
13       errsm_24         0.940717         0.952959   1271.990924        0
14       errsm_25         0.937754         0.960685   1388.556740        0
15       errsm_31         0.939569         0.952918   1282.267960        0
16       errsm_35         0.938398         0.933919   1249.511212        0
17       errsm_36         0.932594         0.943117   1239.583563        0
18       errsm_37         0.931451         0.947375   1237.050915        0
19       errsm_44         0.931822         0.945038   1238.792484        0
20             GB         0.933848         0.949117   1195.073648        0
21             HB         0.939995         0.959203   1165.580928        0
22             JW         0.936659         0.955126   1194.341909        0
23             MT         0.935811         0.947558   1158.239632        0
24             PA         0.928328         0.946324   1179.257488        0
25    pain_pilot_1        0.941512         0.946667   1230.404822        0
26    pain_pilot_2        0.938875         0.948232   1248.543263        0
27    pain_pilot_3        0.941085         0.954422   1228.497101        0
28    pain_pilot_4        0.937990         0.952063   1237.206240        0
29    pain_pilot_7        0.938323         0.952721   1230.258578        0
30        sct_001         0.935758         0.951419   1234.360480        0
31        sct_002         0.935993         0.948645   1217.444211        0
32           T045         0.935448         0.960071    447.979074        0
33           T047         0.938260         0.957898    246.682566        0
34             VC         0.935728         0.954079    437.265764        0
             Mean         0.936915         0.951697   1192.851665
              STD         0.003478         0.007098    265.488879
Passed: 35/35
Total duration: 5773s
```

4.10.4 Validation of vertebral labeling (sct_label_vertebrae)

Table 4.6: Results of validation for sct_label_vertebrae. Metrics (with pass/fail threshold indicated in brackets) are: **diff_man** (<3): Number of labels mismatch between results and gold-standard (i.e., manual labeling of vertebral body center); **max_dist** (<4mm): Maximum Frobenius label distance between results and gold-standard; **rmse** (<2mm): Root mean square error of pairwise labels between results and gold-standard. One subject did not pass the test (errsm_31) because of a lack of contrast between intervertebral discs and vertebral bodies. The number of identified vertebral levels is indicated in the column n_vert.

```
Spinal Cord Toolbox (version dev-63ac386913fc2e047d7961cb1dd68b2f5cbbdc0b)
Running: /Users/jcohen/code/spinalcordtoolbox/scripts/isct_test_function.py -f
sct_label_vertebrae -d /Volumes/data_raid/data_shared/sct_testing/article_sct/ -p "-
i t2/t2.nii.gz -s t2/t2_seg_manual.nii.gz -o t2_seg_labeled.nii.gz"
OS: osx (Darwin-14.4.0-x86_64-i386-64bit), Hostname: django, CPU available/used:
8/8, RAM: 16.00 gigabytes. Testing... (started on: 2016-05-31 10:29:14)
        subject  diff_man  duration [s]  max_dist      rmse    n_vert  status
0           ALT         0    252.061417  3.000000  1.138550        11       0
```

```
 1           AM     0   234.702592  3.316625  1.465656       11      0
 2           ED     0   222.393800  2.000000  0.962250       11      0
 3      errsm_03    0   247.364099  2.828427  1.170628       11      0
 4      errsm_04    0   274.102957  3.162278  1.290994       11      0
 5      errsm_05    0   240.327429  3.464102  1.539601       11      0
 6      errsm_09    0   258.832062  2.828427  1.201850       11      0
 7      errsm_10    0   271.705949  3.316625  1.360828       11      0
 8      errsm_11    0   265.095368  3.741657  1.374369       11      0
 9      errsm_12    0   245.545835  3.741657  1.742710       11      0
10      errsm_13    0   283.595454  2.449489  1.071517       11      0
11      errsm_14    0   227.338844  3.000000  1.232282       11      0
12      errsm_16    0   272.626050  3.316625  1.401058       11      0
13      errsm_24    0   259.355719  2.449490  1.122167       11      0
14      errsm_25    0   260.235856  3.000000  1.347151       11      0
15      errsm_31    0   274.250930  6.403124  2.177324      nan     99
16      errsm_35    0   254.338023  2.236068  1.036375       11      0
17      errsm_36    0   250.107030  3.316625  1.305260       11      0
18      errsm_37    0   242.177974  3.316625  1.088662       11      0
19      errsm_44    0   251.942417  3.605551  1.440165       11      0
20           GB     0   211.370936  2.449490  1.054093       11      0
21           HB     0   191.212892  2.449490  1.088662       11      0
22           JW     0   219.932286  2.449490  0.981307       11      0
23           MT     0   192.001864  2.449490  1.071517       11      0
24           PA     0   191.563530  2.449490  0.942809       11      0
25  pain_pilot_1   0   251.741721  3.162278  1.217161       11      0
26  pain_pilot_2   0   289.184444  2.449490  1.186342       11      0
27  pain_pilot_3   0   211.744835  3.000000  1.401058       11      0
28  pain_pilot_4   0   286.991825  3.000000  1.290994       11      0
29  pain_pilot_7   0   215.993892  3.000000  1.201850       11      0
30      sct_001    0   280.821177  3.316625  1.261980       11      0
31      sct_002    0   207.100989  2.449490  1.088662       11      0
32         T045    0   135.264882  3.000000  1.154701       11      0
33         T047    0    70.504924  2.449490  1.122167       11      0
34           VC     0   117.523521  2.236068  1.000000       11      0
          Mean     0   233.172958  2.994408  1.243791
           STD     0    48.345331  0.750945  0.240435
Passed: 34/35
Total duration: 1130s
Status legend: 0: Passed, 1: Crashed, 99: Failed, 200: File(s) missing
```

4.10.5 Details and validation of gray matter segmentation

Methods: The method of Asman et al. (Asman et al., 2014) was implemented and new features were added, including (i) the possibility to add prior information about the vertebral level in order to gain accuracy on the target shape of the gray matter, (ii) the possibility to segment images from any contrast by adding linear normalization between median intensity values of white/gray matter based on the spinal cord internal structure pre-registration (combining our multi-atlas-based model and vertebral level information), and (iii) the possibility to output probabilistic segmentations of white/gray matter. The dictionary model was built from T_2*-weighted images of 37 healthy adult subjects (TIM Trio, Siemens Healthcare, axial orientation, TR = 540 ms, TE =[5.41, 12.56, 19.16] ms, flip angle = 35°, bandwidth = 200 Hz/voxel, resolution = 0.5×0.5×5mm^3, coverage from C1 to

T2 vertebral levels). Following gray matter segmentation, SCT users can choose to improve the template-based registration as illustrated in Figure 4.2 (purple color).

Validation: 10 subjects (different than the ones used to generate the model) were scanned at 3T with the same acquisition parameters. Processing included the following steps: semi-automatic cord segmentation, registration to template (to obtain vertebral level) and automatic gray matter segmentation using multi-atlas framework. Manual segmentations of the spinal cord gray and white matter were performed pixel-by-pixel using *fslview* using standardized procedure (Yiannakas et al., 2012). The automatic probabilistic multi-atlas based segmentations were thresholded at 0.5 and compared with manual segmentations using 2D Dice coefficient on white and gray matter, along with Hausdorff distance and maximum median distance on skeletonized segmentations.

Figure 4.8 shows examples of fully automatic gray matter segmentation results compared to manual segmentations for T_2*-w and MT images. Validation metrics are given hereafter, as mean ± STD across ten subjects. Dice coefficient for the gray matter was 0.70 ± 0.06 for T_2* and 0.66 ± 0.06 for MT. Dice coefficient for the white matter was 0.90 ± 0.02 for T_2* and 0.89 ± 0.02 for MT. Hausdorff distance was 1.20 ± 0.18 mm for T_2* and 1.64 ± 0.11 mm for MT. Median distance was 0.34 ± 0.06 mm for T_2* and 0.61 ± 0.05 mm for MT.
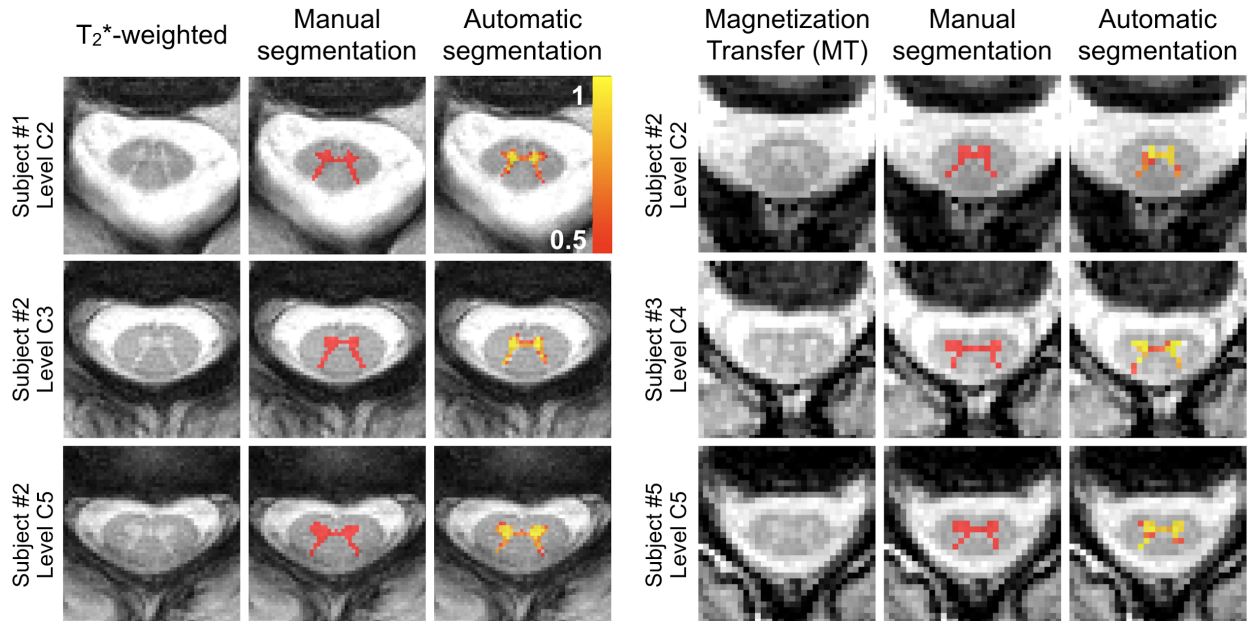
Figure 4.8: Automatic GM segmentation results for T2*-w (top) and MT (bottom) images. The probabilistic automatic segmentations (right column) were thresholded at 0.5 and compared to

manual segmentations (middle column). Numerical results are displayed for each slice as well as averaged across ten healthy subjects.

Thanks to the normalization feature, gray matter segmentation also works on images with different contrast. As a proof-of-concept, diffusion-weighted images were acquired in 10 additional subjects. Acquisition parameters were: Siemens TIM Trio, 4ch neck coil, 2DRF monopolar diffusion-weighted sequence (Finsterbusch, 2009), TR=820ms, TE=88ms, matrix=208×42, resolution=0.8×0.8×5 mm^3, 4 slices positioned orthogonal to the cord and centered in the middle of the vertebral body (gap was adjusted per subject), b-value = 800 s/mm^2, 24 directions, cardiac gated. Preprocessing consisted in motion correction as implemented in SCT. The mean diffusion-weighted data, which exhibits inverted contrast compared to the T_2*-weighted data (white matter bright, gray matter dark), was used for segmenting the gray matter. Following segmentation, the warping field was updated, diffusion tensor were calculated, then FA from all subjects was warped to the MNI-Poly-AMU template. Figure 4.9 (top panel) shows mean FA across subjects, with an overlay of five spinal tracts. Figure 4.9 (bottom panel) shows the mean ± STD values for FA, averaged across 10 subjects. Values are consistent with the literature (Samson et al., 2016). Further validation is required to assess the specific benefits of accounting for the gray matter for template-based analysis. It is likely that in the healthy adult population which is well represented by the MNI-Poly-AMU atlas, there is a moderate benefit of using gray matter segmentation to improve template registration. However, it is anticipated that in pathological cases (e.g., where the shape of the gray matter does not follow the typical trends), using subject-specific shape of the gray matter might improve the accuracy of template registration.

	Level C2	Level C3	Level C4	Level C5	Average across levels
DTI - FA					
Registered WM tracts					
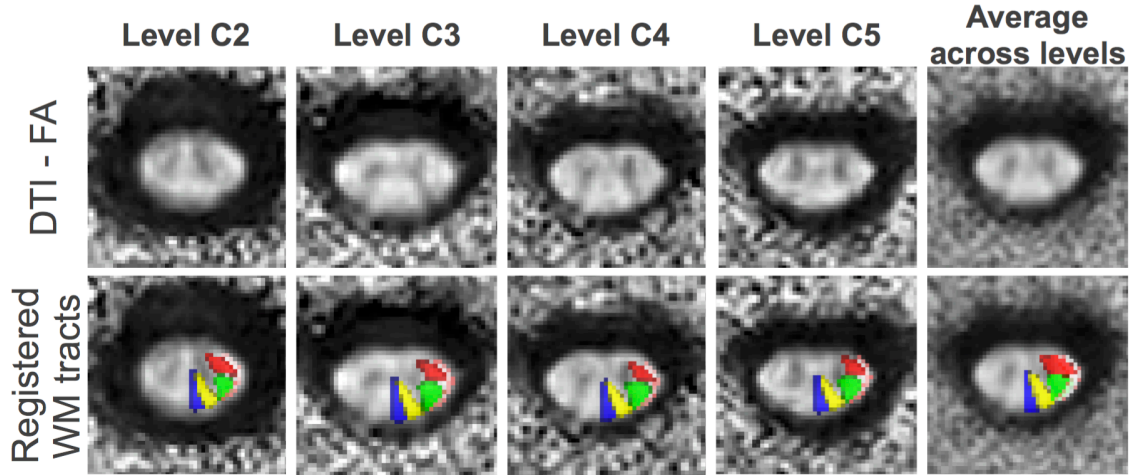
White matter tract	Extracted FA values on 10 healthy subjects				
	Level C2	Level C3	Level C4	Level C5	Average across levels
🔵 Fasciculus gracilis	0.78 ± 0.08	0.73 ± 0.06	0.79 ± 0.07	0.73 ± 0.10	0.75 ± 0.05
🟡 Fasciculus cuneatus	0.83 ± 0.09	0.80 ± 0.07	0.83 ± 0.07	0.76 ± 0.10	0.82 ± 0.05
🟢 Lateral corticospinal tracts	0.77 ± 0.11	0.74 ± 0.11	0.75 ± 0.10	0.67 ± 0.10	0.73 ± 0.08
🌸 Spinocerebellar tracts	0.72 ± 0.28	0.78 ± 0.17	0.79 ± 0.20	0.71 ± 0.14	0.74 ± 0.19
🔴 Spinal lemniscus	0.73 ± 0.18	0.74 ± 0.08	0.78 ± 0.09	0.76 ± 0.10	0.73 ± 0.07

Figure 4.9: Top panel shows FA maps registered to the MNI-Poly-AMU template (including gray matter segmentation and registration), and averaged across ten healthy subjects. Five white matter tracts are overlaid: gracilis (blue), cuneatus (yellow), corticospinal (green), spinocerebellar (pink), and lemniscus (red). Bottom panel reports FA within specific spinal tracts (mean ± STD across ten subjects).

4.10.6 Details and validation of SliceReg

Algorithm: Translations along x and y are estimated slice-by-slice using the convergence framework implemented in ITK (www.itk.org). The cost function includes a regularization term expressed as a polynomial function along z (assumed to be the spinal cord axis). Image metric (cross-correlation, mutual information and mean squares), shrink factor (data subsampling), smoothing and degree of polynomial function used for regularization can be specified. The

software outputs the registered image, forward and backward warping fields as well as a *csv* file with *x* and *y* translations per slice.

Validation: To evaluate the performance of *SliceReg* in a large variety of sequences and acquisition setups, data were acquired in 25 subjects in five different centers: Unité de Neuroimagerie Fonctionnelle (Montreal, n=6), A.A. Martinos Center for Biomedical Imaging (Boston, n=5), FMRIB (Oxford, n=4), Toronto Western Hospital (Toronto, n=5) and Pitié-Salpêtrière Hospital (Paris, n=5). Sequences used were: diffusion-weighted EPI (n=7), spin echo EPI (n=10), gradient echo EPI (n=6) and magnetization transfer gradient echo FLASH (n=2) with variable amount of noise (different coils were used), spatial resolution (0.8 to 1.2mm in-plane) and coverage (varied between 4 to 7 vertebral levels). For each sequence, two volumes showing non-rigid deformations were selected as candidates for co-registration. *SliceReg* (3rd order polynomial) was compared against ANTs (Avants et al., 2011) and FSL FLIRT (Jenkinson, Bannister, Brady, & Smith, 2002), the two latter being constrained to two degrees of freedom (in-plane translations). Mean square metric was used for all methods. Following within-pair registrations, the spinal cord was segmented automatically using *PropSeg* (De Leener et al., 2014) and the estimated transformations were applied to the segmentations using nearest neighbor interpolation. Overlap between the two registered segmentations was assessed using Dice coefficients.

Results: Figure 4.10 compares the performance of *SliceReg*, ANTs 2D and FLIRT 2D for co-registration of two volumes (within modality). Average Dice (N=25 subjects) was respectively 0.87±0.06, 0.83±0.10 and 0.81±0.10 for *SliceReg*, ANTs and FLIRT. Student's t-test (paired for dataset) showed significant difference between *SliceReg* and ANTs (p=0.004) and between *SliceReg* and FLIRT (p=0.00007). Average computation times were 0.92ms, 0.65ms and 0.63ms for *SliceReg*, ANTs and FLIRT, respectively. Despite the ~40% increase of computation time compared to volume-based methods (because one transformation per slice is estimated as opposed to a single one), the average processing time is below 1s, making it suitable for motion correction pipelines.
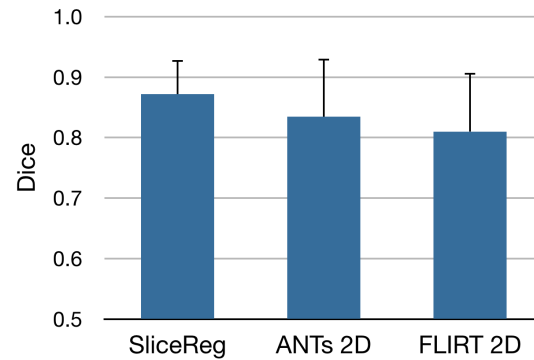
Figure 4.10: Results of registration accuracy for SliceReg, ANTs 2D and FLIRT 2D methods (N=25 subjects). Student's t-test shows significantly higher Dice for SliceReg in comparison with ANTs (p=0.004) and FLIRT (p=0.00007).

4.10.7 Validation of motion correction

Motion correction for diffusion-weighted MRI data was compared against FSL (mcflirt) and the ACID Toolbox (Mohammadi, Möller, Kugel, Müller, & Deppe, 2010) in 10 healthy subjects. Acquisition parameters are listed in section 4.10.5 *Details and validation of gray matter segmentation*. Following motion correction, diffusion tensors were computed and FA was estimated using 'map' method in the spinal cord white matter across slices C2 to C5. Then, mean and standard deviation were computed across subjects. For details the reader is referred to the validation script[19]. Results are presented in Table 4.7. `sct_dmri_moco` led to the highest mean FA across subjects, suggesting that motion correction reduced blurriness in voxels at the periphery of the cord, which are more prone to lower FA due to partial volume with CSF (where FA is close to zero). `sct_dmri_moco` also led to the smallest standard-deviation across subjects. This comparison should be interpreted with care, as more advanced approaches could have been with either of the software tested. For example, mcflirt could be replaced with 2D slice-by-slice FLIRT, although this would have required a dedicated script.

---

[19] https://www.dropbox.com/s/5rpynlkjddfa24q/validation_sct_dmri_moco.sh

Table 4.7: FA averaged across 10 subjects in the white matter from C2 to C5. Comparison of motion correction.

	Mean	SD
No motion correction	0.669	0.073
FSL mcflirt	0.633	0.083
ACID toolbox	0.680	0.078
sct_dmri_moco	0.703	0.056

4.10.8 Validation of metric quantification (sct_extract_metric)

We evaluated the effect of spatial resolution on the accuracy and precision of metric quantification. The same simulation framework has been used as that one from Lévy et al., (Lévy et al., 2015), which investigated the effect of noise, across-tract variability and extraction method on the accuracy and precision. In brief, a synthetic phantom with known values within each tract was created from the WM atlas of the MNI-Poly-AMU template. The phantom consisted of 101 slices covering C7 to T1 vertebral levels at a resolution of 0.5 mm isotropic. Each tract was assigned a random value between 35 and 45. A fixed value of '35' was set in the gray matter, and of '5' in the CSF. After assigning a value for each tract, for the gray matter and for the CSF, all labels were summed to yield a single 3D volume. Gaussian noise was then added to match an SNR of 10 in the white matter. The absolute error between the true value and the estimated metric was calculated for the following methods: binary (bin), weighted-average (wa), maximum likelihood (ml), and maximum a posteriori (map). In order to remove the bias associated with the choice of the value for a given tract, the experiment was repeated 200 times, each time with a new randomly-generated phantom according to the bootstrapping method. The mean and STD of absolute errors across bootstrap experiments were calculated. In order to investigate the effect of spatial resolution, the bootstrapping experiment was repeated after downsampling the phantom at the following resolutions: 0.8x0.8x5mm, 1x1x5mm and 1.5x1.5x5mm. The validation script and data are accessible[20].

Figure 4.11 shows results of the metric extraction for each resolution and each method. The key aspects of these results are that: (i) methods *ml* and *map* perform best at all tested resolutions, (ii) assuming an SNR of 10, to obtain less than 1% and 2% of quantification error the voxel fraction should be at least 240 and 30, respectively (these numbers were upper-rounded from the graph for

---

[20] https://www.dropbox.com/sh/kxphik6zfk27cse/AACn4odVbi9p809udSpuJbHva?dl=0

the method *map*), (iii) the method *ml* provides high accuracy with at high voxel fraction (e.g., fasciculus cuneatus at 0.8mm in-plane over 20 slices), however it diverges dramatically when voxel fraction decreases after a certain point, due to instabilities caused by noise (e.g., voxel fraction <5). This motivates the use of the *map* method.
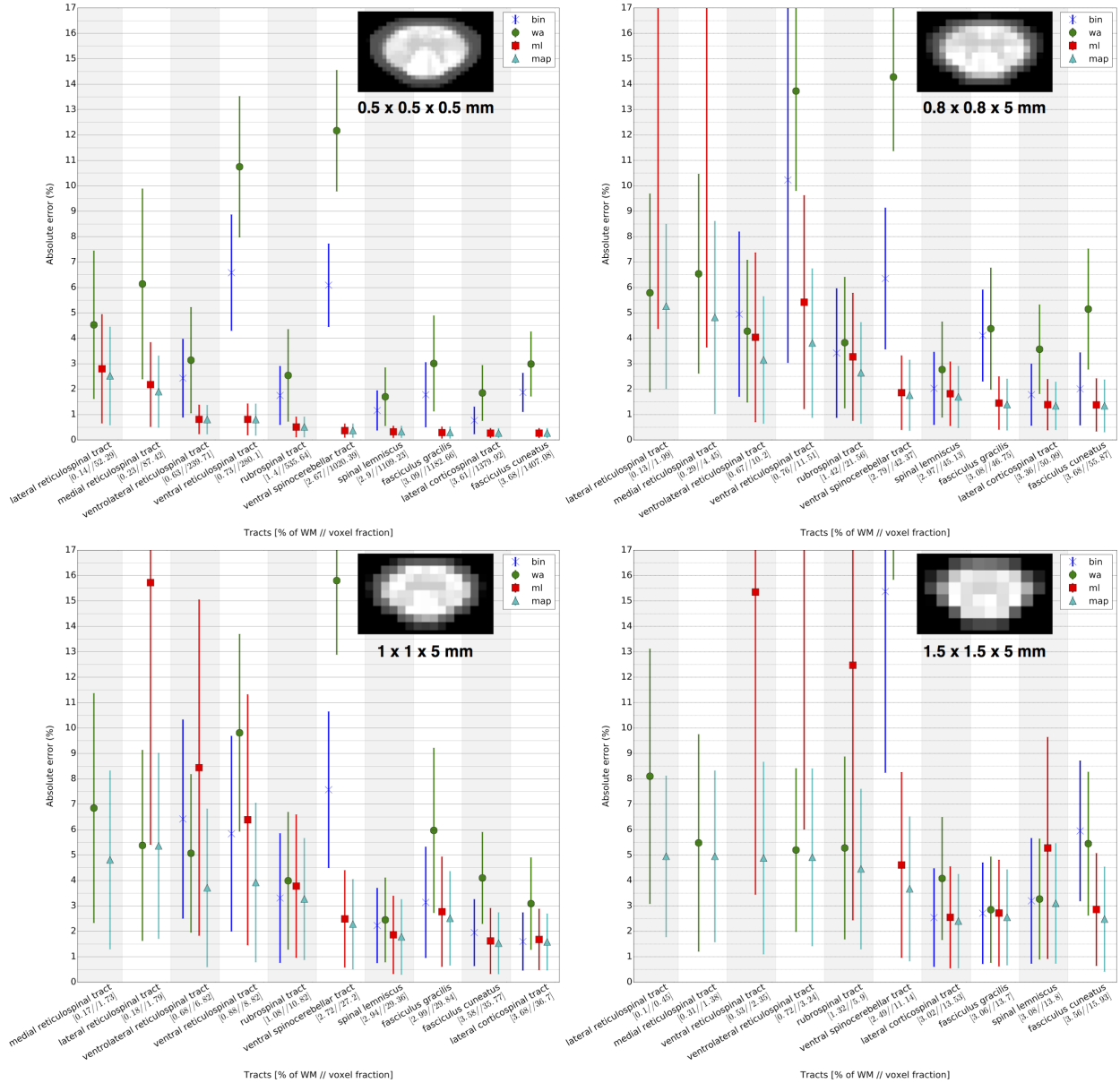
Figure 4.11: Simulation results comparing the accuracy and precision of metric extraction methods at various resolutions. Metric extraction methods are: averaging within binary mask (bin), weighted-averaging within probabilistic mask (wa), maximum likelihood estimation (ml) and maximum a posteriori estimation (map) (Lévy et al., 2015). The abscissa shows different left tracts,

ordered by their volume fraction occupied within the white matter. The volume fraction of a given tract (expressed here in percentage) represents the number of voxels of this tract divided by the number of voxels in the white matter (each voxel being represented by its partial volume information). An image of a randomly-generated synthetic phantom is shown at each resolution. The ordinates show the mean and STD of the absolute error (in percentage of the true value). Note that for very low volume fractions, the bin method is not represented because the tract is too small to pass the 0.5 threshold.

CHAPTER 5   ARTICLE 3: TOPOLOGICALLY PRESERVING STRAIGHTENING OF SPINAL CORD MRI

This manuscript presents the development and validation of a novel algorithm for straightening spinal cord MRI images while preserving the topology of the spinal cord. This algorithm allows the accurate and robust registration of MRI images of the spinal cord, by using NURBS-based interpolation of spinal cord segmentation and the analytical resolution of straightening equations. This method has been validation on a population of healthy subjects and patients with spinal cord compression. Coupled with Chapter 4, this manuscript is an essential contribution to this project as it proposes answers to its second objective.

My contribution (90%) on this article included the design and development of the method, its implementation and validation and the design and redaction of the manuscript. This manuscript has been published in Journal of Magnetic Resonance Imaging in January 2017, Volume 46, Issue 4, pp 1209–19.

Title: Topologically preserving straightening of spinal cord MRI

Authors:

Benjamin De Leener[1], Gabriel Mangeat[1], Sara Dupont[1], Allan R. Martin[2], Virginie Callot[3,4], Nikola Stikov[1,5], Michael G. Fehlings[2], Julien Cohen-Adad[1,6]

Affiliations:

[1] NeuroPoly Lab, Institute of Biomedical Engineering, Polytechnique Montreal, Montreal, QC, Canada

[2] Division of Neurosurgery, Department of Surgery, University of Toronto, Toronto, ON, Canada

[3] Aix-Marseille Université, CNRS, CRMBM UMR 7339, Marseille, France

[4] AP-HM, Hopital de la Timone, Pôle d'imagerie médicale, CEMEREM, Marseille, France

[5] Montreal Heart Institute, Montreal, QC, Canada

[6] Functional Neuroimaging Unit, CRIUGM, Université de Montréal, Montreal, QC, Canada

5.1 Abstract

Purpose: To propose a robust and accurate method for straightening MR images of the spinal cord, based on spinal cord segmentation, that preserves spinal cord topology and that works for any MRI contrast, in a context of spinal cord template-based analysis.

Materials and Methods: The spinal cord curvature is computed using an iterative Non-Uniform Rational B-Spline (NURBS) approximation. Forward and inverse deformation fields for straightening are computed by solving analytically the straightening equations for each image voxel. Computational speed-up was accomplished by solving all voxel equation systems as one single system. Straightening accuracy (mean and maximum distance from straight line), computational time and robustness to spinal cord length was evaluated using the proposed and the standard straightening method (label-based spline deformation) on 3T T2- and T1-weighted images from 57 healthy subjects and 33 patients with spinal cord compression due to degenerative cervical myelopathy (DCM).

Results: The proposed algorithm was more accurate, more robust, and faster than the standard method (mean distance = 0.80 vs 0.83 mm, maximum distance = 1.49 vs 1.78 mm, time = 71 vs 174 sec for the healthy population and mean distance = 0.65 vs 0.68 mm, maximum distance = 1.28 vs 1.55 mm, time = 32 vs 60 sec for the DCM population).

Conclusion: A novel image straightening method that enables template-based analysis of quantitative spinal cord MRI data has been introduced. This algorithm works for any MRI contrast and has been validated on healthy and patient populations. The presented method is implemented in the Spinal Cord Toolbox, an open-source software for processing spinal cord MRI data.

Keywords: Spinal cord, straightening, deformation field, NURBS, SCT, MR image analysis

5.2 Introduction

Magnetic resonance imaging (MRI) has been increasingly used for providing valuable quantitative information about spinal cord morphometry (Fradet et al., 2014; Papinutto et al., 2015), and microstructural data that reflects the degree of tissue injury and prognosis in neurodegenerative diseases (Bastianello et al., 2000; Cohen-Adad, El Mendili, et al., 2013; Nakamura et al., 2008) and traumatic injuries (Cohen-Adad, El Mendili, et al., 2011; Ellingson et al., 2008). In parallel to the development of new acquisition methods for improving the quality of spinal cord MRI data (Cohen-Adad & Wheeler-Kingshott, 2014b; P W Stroman et al., 2014), new image processing tools are being proposed for segmentation and morphometric analyses (Asman et al., 2014; Cohen-Adad et al., 2014; De Leener et al., 2015; De Leener et al., 2014; El Mendili, Chen, Tiret, Pélégrini-Issac, et al., 2015; Horsfield et al., 2010; Losseff, Webb, O'riordan, et al., 1996; Papinutto et al., 2015; Stroman et al., 2008; Ullmann et al., 2014; Yiannakas et al., 2012a) to only cite a few (more can be found in (De Leener, Taso, et al., 2016)). Generic MRI templates and atlases of the spinal cord have been developed as well (El Mendili, Chen, Tiret, Villard, et al., 2015; Fonov et al., 2014; Stroman et al., 2008; Taso et al., 2015; Valsasina et al., 2012), facilitating multi-center studies of large groups of subjects and patients (Castellano et al., 2016; Grabher et al., 2016; Talbott et al., 2016; Taso et al., 2016; Yiannakas et al., 2016) and morphological analysis such as voxel-based morphometry (Valsasina et al., 2012). Because the majority of spinal cord templates show a straight spinal cord, a key element for template-based analyses is the need to straighten images during pre-processing. Straightening MR images of the spinal cord is also particularly useful for generating new templates or register new data on existing templates.

Several groups have developed algorithms for straightening 1.5T and 3T MR images of the spinal cord. Stroman et al. have proposed a re-interpolation approach that reslices voxels transverse to a manually defined reference line (Stroman et al., 2008). While producing satisfactory results, this approach requires manual delineation of the anterior edge of the spinal cord and only outputs the straightened image without a deformation field, i.e., it precludes from integrating this transformation into a template-registration pipeline, as commonly done in the brain for minimizing the number interpolations at each step of the pipeline. Vrtovec et al. have proposed a semi-automatic straightening method of the spine for computed tomography and MRI images based on polynomial approximation (Vrtovec, Likar, & Pernus, 2005). However, their method does not

preserve the topology of the anatomical structures. More recently, other groups proposed similar 3D cubic reinterpolation approaches based on the semi- and fully-automatic delineation of the cord centerline for generating a template of the spinal cord (El Mendili, Chen, Tiret, Villard, et al., 2015; Valsasina et al., 2012). Meanwhile, Fonov et al. proposed a landmark-based straightening approach for generating the MNI-Poly-AMU template (Fonov et al., 2014). The latter approach uses the cord segmentation for calculating the position automatically of landmarks in each slice as a cross pattern and computing a thin-plates transformation that fits landmarks into straight space. While this method provides forward and inverse transformations, it is highly dependent on the landmarks position and thin-plates fitting parameters, and hence it is sensitive to the size of the field of view (FOV).

The purpose of this study is to propose an analytical solution for straightening the spinal cord in MRI images, that preserves the spinal cord topology and works for any MRI contrast and fields of view.

5.3 Materials and methods

Straightening a 3D image of the spinal cord is the process of re-interpolating the image by following the spinal cord curvature, while preserving the topology of the spinal cord and its adjacent structures. Therefore, the goal of the straightening process is to generate a forward and an inverse deformation field between the curved and straight space of the spinal cord. The curved space represents the original image of the spinal cord while the straight space represents the image of the straightened spinal cord. The following paragraphs present the analytical solution to image straightening, based on the NURBS approximation of a curve.

5.3.1 Theory

5.3.1.1 Non-Uniform Rational B-Splines (NURBS)

NURBS are a generalization of b-splines (Piegl & Tiller, 2012). A pth-degree NURBS is defined using the following formulation:

$$C(u) = \frac{\sum_{i=0}^{n} N_{i,p}(u) w_i P_i}{\sum_{i=0}^{n} N_{i,p}(u) w_i} = \sum_{i=0}^{n} R_{i,p}(u) P_i \qquad a \leq u \leq b$$

where P_i are the control points, w_i are the weights associated with each control point and $N_{i,p}(u)$ are the pth-degree B-spline basis functions defined on the nonperiodic and non-uniform knot vector

$$U = \left\{ \underbrace{a, ..., a}_{p+1}, u_{p+1}, ..., u_{m-p-1}, \underbrace{b, ..., b}_{p+1} \right\}.$$ a and b are the limits of the curve parametric domain and

are set, in this study, to 0 and 1, respectively.

Several NURBS properties are particularly suited for curve fitting in images:

- **Derivatives**: All derivatives of $R_{i,p}(u)$ exist, therefore curve derivatives $C'(u)$ exist;

- **Local support and local approximation**: modifying the location of a specific control point or weight only affects the corresponding portion of the curve;

- **Parametrization and boundaries**: NURBS are defined with $u \in [0,1]$ and $C(0) = P_0$ and $C(1) = P_n$, ensuring high control of curve resolution and stability on edges. Points are equally distributed along the approximated curve;

- **Affine invariance**: any affine transformation applied to control points is directly applied on the curve. NURBS curves are also invariant to perspective projections.

Global NURBS approximation can be performed by iteratively computing the number and position of control points required to fit point data with a specified accuracy. Given a specified number n of control points P_i, assuming $p \geq 1$ and $n \geq p$, and a set of point data $Q_0, ..., Q_m$ with $m > n$, we seek a pth-degree NURBS curve $C(u) = \sum_{i=0}^{n} R_{i,p}(u)P_i$ that satisfies the following criteria:

- First and last points are fixed: $Q_0 = C(0)$ and $Q_m = C(1)$

- The remaining error $\sum_{k=1}^{m-1} |Q_k - C(\bar{u}_k)|^2$ is minimum, where $\bar{u}_k$ are the precomputed parametric values and represent the position of point data along the curve.

According to Piegl et al., the solution can be found by solving a linear equation system with $n - 1$ equations and $n - 1$ unknowns using a least square fitting approach (Piegl & Tiller, 2012). By assuming

$$S_k = Q_k - R_{0,p}(\bar{u}_k)Q_0 - R_{n,p}(\bar{u}_k)Q_m \qquad k = 1, ..., m - 1,$$

the n control points P_i satisfying a least squares approximation of Q_k can be computed by solving the following system:

$$P = (R^T R)^{-1} S$$

where S is the vector of $n-1$ points, defined by

$$S = \begin{bmatrix} R_{1,p}(\bar{u}_1)S_1 + \cdots + R_{1,p}(\bar{u}_{m-1})S_{m-1} \\ \vdots \\ R_{n-1,p}(\bar{u}_1)S_1 + \cdots + R_{n-1,p}(\bar{u}_{m-1})S_{m-1} \end{bmatrix},$$

R is the $(m-1) \times (n-1)$ matrix of scalars

$$R = \begin{bmatrix} R_{1,p}(\bar{u}_1) & \cdots & R_{n-1,p}(\bar{u}_1) \\ \vdots & \ddots & \vdots \\ R_{1,p}(\bar{u}_{m-1}) & \cdots & R_{n-1,p}(\bar{u}_{m-1}) \end{bmatrix},$$

and

$$P = \begin{bmatrix} P_1 \\ \vdots \\ P_{n-1} \end{bmatrix}.$$

As demonstrated by De Boor, an appropriate choice of knot vectorization u_k ensures that the matrix $(R^T R)$ is positive definite and well-conditioned, therefore invertible (De Boor, 1978). The weights w_i are computed based on points density as the average distance between adjacent points. A density-based weighting of the curve approximation allows us to compute the fitting with an equally distributed accuracy, even for curves with non-equally distributed points.

The number of control points of the global NURBS approximation is determined by minimizing the distance between the curve and the data:

$$n = \arg\min_n \sum_{k=1}^{m-1} |Q_k - C^n(\bar{u}_k)|^2$$

where C^n is the global approximation of Q_k with n control points. Preliminary experiments suggested 3rd-degree NURBS curves were appropriate for spinal cord image straightening.

5.3.1.2 Topologically-preserving image straightening

In order to preserve the topology of the spinal cord, the straightening process must satisfy three constraints:

1. *The length of the spinal cord must be the same in the curved and straight spaces.* As a straight line covers more space in the z-direction than a curved line, the straight image must be larger in the inferior-superior direction than the curved image.

2. *The points along the curve and straight spinal cord must be equally distributed.* The distances between each corresponding points in the curved and the straight spaces must be preserved.

3. *The size of structures in planes perpendicular to the spinal cord centerline must be unchanged.* Each plane perpendicular to the spinal cord, when re-interpolated in the straight space, must preserve the size of adjacent structures. For example, spinal cord cross-sectional areas must remain the same in curved and straight space.

Let's consider a curved centerline $C_c(u)$ and a straight centerline $C_s(u)$ as introduced in the previous section. Let's also consider a curved image $I_c \in R^{N \times 1}$ and a straight image $I_s \in R^{M \times 1}$ where N and M are the number of voxels in the curved and straight images, respectively. The input of the straightening algorithm is a binary segmentation mask of the spinal cord. The center of mass of the segmentation for each axial slice is calculated and the centerline $C_c(u)$ is extracted using iterative NURBS approximation as described above. The straight image space is generated along with the straight centerline and its size in the inferior-superior direction is equal to the length of the curved centerline, therefore ensuring the first topology constraint. NURBS approximation ensures points are equally distributed along curves, therefore ensuring the second topology constraint.

Each voxel I_c^i (respectively I_s^i) of the curved image is represented by its coordinates (x_{ci}, y_{ci}, z_{ci}) (respectively (x_{sj}, y_{sj}, z_{sj})). The variable i and j will be used to iterate over all voxels. All coordinates are in physical space (i.e., scanner space) in order to avoid issues related to differences in image sizes, spacing and orientations.

The plane $P_c(u_i)$ (respectively $P_s(u_i)$) perpendicular to the curve is built using the first derivative $C'_c(u_i)$ (respectively $C'_s(u_i)$) of the curve as its normal (first axis of the referential frame). The second axis is computed in the sagittal plane of the image and perpendicular to the first axis. The third axes of the plane's reference frame is defined as the axis orthogonal to both the first and second axes, ensuring each plane referential system is defined by three mutually orthogonal axes. Finally, the origin of the system is defined by the coordinates of the point $C_c(u_i)$. Therefore, the

curve point $C_c(u_i)$ and the plane $P_c(u_i)$, perpendicular to the curve $C_c(u)$ and intersecting the curve on $C_c(u_i)$, compose a coordinate system that follows the curve with $0 \leq u \leq 1$. These considerations are illustrated in Figure 5.1.

Let's consider the transformation from the curved image to the straight image. For each voxel I_c^i, the following computations are performed:

A. Find the nearest point $C_c(u_i)$ in centerline C_c. In order to minimize the computation time for high-dimensional space, we used the kd-tree approach as implemented in (Maneewongvatana & Mount, 1999). We assume the plane $P_c(u_i)$, corresponding to the centerline point $C_c(u_i)$, is the nearest plane from the voxel I_c^i. The signed distance between I_c^i and the plane $P_c(u_i)$ is calculated using the following parametric equation:

$$d_i = \frac{ax_{ci} + by_{ci} + cz_{ci} + d}{\sqrt{a^2 + b^2 + c^2}}$$

where (a, b, c, d) are the equation parameters of the plane $P_c(u_i)$.

B. Calculate the coordinates of the projection of I_c^i in the plane $P_c(u_i)$, using the following equation:

$$I_{cp}^i = I_c^i - \left(I_c^i \cdot C_c(u_i) \right) * C'_c(u_i)$$

where $C'_c(u_i)$ is the first derivative of the curve and the normal to the plane $P_c(u_i)$.

C. Compute the coordinates of the projected point I_{cp}^i in the coordinate system of the plane $P_c(u_i)$, using the transformation from the physical coordinate system to the plane coordinate system. Then, calculate the corresponding slice and voxel coordinates in the straight space. As points along the curved and straight centerline are equally distributed, the correspondence between curve points is immediate.

D. Compute the deformation fields that straighten the image (curve → straight) and curve the straightened image (straight to curve). The deformation vectors for each voxels in both directions are calculated as the difference between the coordinates of the voxels that were paired in steps A to C. The distance d_i calculated in A for each voxel is used as a threshold to determine whether the transformation should be included at this location in the warping field. This thresholding reduces the errors at the rostro-caudal limits of the spinal cord and

avoids image deformities in regions with large curvature. The same distance is also used to correct the positions of voxels in curved and straight space, relative to their corresponding planes, so that interpolation errors are minimized.
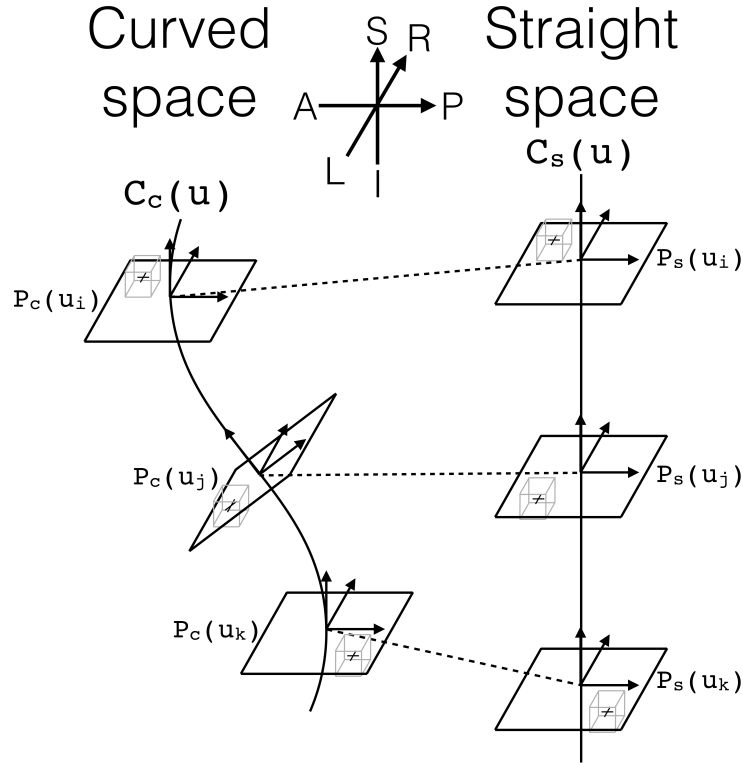
Figure 5.1: Schematic representation of straightening. Spinal cord centerlines in curved and straight space are defined by $C_c(u)$ and $C_s(u)$. Each voxel in one space finds its corresponding voxel in the other space by matching planes perpendicular to the centerline curves. Deformation fields for straightening and curving are interpolated from voxel-by-voxel displacements. Note that the AP direction is preserved in all perpendicular plane-referential frames.

Each one of these four computations steps can be expressed as a matrix-based system to solve only once for all voxels. Therefore, computation times can be reduced drastically by using parallelized algebra computation.

The same procedure described above is applied for computing the deformation field from the straight image to the curved image, with some additional simplifications. Since the proposed straightening approach focuses on the spinal cord and not on distant structures outside the spine, the straight image size can be reduced in the R-L and A-P direction (i.e., ~ 50 mm around the spinal cord) in order to reduce computation time. Moreover, planes perpendicular to the straight curve are

much simpler to compute than the curved ones, as they are all parallel to each other and only the origin of planes coordinate system changes along the curve.

The proposed method is integrated into the Spinal Cord Toolbox, an open-source software for processing spinal cord MRI data, and outputs diffeomorphic forward and inverse deformation fields that can be used in neuroimaging processing pipelines such as AFNI (Cox, 1996), Minc Tools, FSL (Jenkinson, Beckmann, Behrens, Woolrich, & Smith, 2012b; Woolrich et al., 2009), SPM (Friston et al., 1994; Penny, Friston, Ashburner, Kiebel, & Nichols, 2011) and NiPype (Gorgolewski et al., 2011).

5.3.2 Validation

50 healthy subjects (mean age: 27±7 y.o., 31/19 men/women) were recruited and scanned in Montreal (n=33) and Marseille (n=17) on 3T systems (TIM Trio for Montreal and Verio for Marseille, Siemens Healthcare) using the standard 12-channel head, 4-channel neck and 24-channel spine coils. Local Institutional Review Board approval and written informed consent were obtained prior to imaging in both institutions. A T_2-weighted (T_2w) sequence covering the full spinal cord and brainstem was acquired. This large coverage was achieved by acquiring two FOVs per contrast (1: head and cervical spine (T2 vertebral level); 2: cervical, thoracic and lumbar cord (~ L2 vertebral level), stitched together using off-line software tools provided by the manufacturer's MRI console after correcting for image B1 bias field (proprietary algorithm). Acquisition parameters were: slab-selective fast spin echo (SPACE sequence), TR = 1500 ms, TE = 119 ms, flip angle = 140°, bandwidth = 723 Hz/voxel, voxel size = 1x1x1 mm^3. The acquisition time for each volume was 6 min.

To demonstrate the ability of the proposed algorithm to straighten the spinal cord in MRI images with various contrasts, one T_1-weighted (T_1w) image was acquired on a healthy subject, using the same channel coils and coverage as above, and with the following acquisition parameters: multi-echo MPRAGE sequence (van der Kouwe, Benner, Salat, & Fischl, 2008), TR = 2260 ms, TE = [2.09, 3.95, 5.81] ms (averaged), flip angle = 7°, bandwidth = 651 Hz/voxel, voxel size = 1x1x1 mm^3. Note that the proposed straightening algorithm is using only a binary segmentation/centerline of the spinal cord and therefore has been designed to perform equally well on any MRI contrasts, provided that the spinal cord segmentation/centerline are accurate.

33 patients with degenerative cervical myelopathy (DCM) were recruited and scanned at the Toronto Western Hospital on a 3T system (GE Signa Excite HDxt). Patients were diagnosed with degenerative cervical myelopathy (Nouri, Tetreault, Singh, Karadimas, & Fehlings, 2015) by a spine surgeon (MGF) based on one or more symptoms (upper extremity fine motor dysfunction, numbness, weakness, gait dysfunction, imbalance, or bladder dysfunction) plus one or more signs on examination (hyperreflexia, focal weakness, sensory dysfunction, gait ataxia, Romberg sign) and evidence of spinal cord compression on MRI (indentation, flattening, torsion, or circumferential compression) related to degenerative changes (disc degeneration, spondylosis, osteophytes, ligamentous flavour hypertrophy). These patients were selected to evaluate the accuracy of the proposed straightening algorithm on data with abnormal spinal cord shape and curvature. T_2-weighted imaging was performed with a fast spin echo (FIESTA-C sequence) covering C1 to T4 vertebral levels. Acquisition parameters were: TR = 5.368 ms, TE = 2.668 ms, flip angle = 35°, bandwidth = 41.67 Hz/voxel, voxel size = 0.8x0.8x0.8 mm^3, for a total acquisition time of 6 min. In order to demonstrate the ability of the proposed method for straightening the spinal cord on images with various acquisition parameters and scanner, 7 additional healthy subjects were acquired using the same acquisition protocols and added to the healthy population.

The spinal cord in all subjects (N=57) and DCM patients (N=33) data was automatically segmented using SCT tools (De Leener et al., 2015; De Leener et al., 2014). Segmentations were manually corrected by a neurosurgery resident with 6 years of experience in spine surgery (ARM) when necessary (5% in healthy subjects and 96% in DCM patients). All images were automatically straightened with the proposed approach, as well as with the landmark-based method currently implemented in SCT (De Leener, Lévy, et al., 2016; Fonov et al., 2014).

Two validation metrics were used to evaluate the accuracy of the proposed straightening method, both based on the segmentation of the spinal cord. Following straightening, the warping field from curved space to straight space was applied (with tri-linear interpolation) on the segmentation binary image and the center of mass of each axial slice was calculated. The first validation metric is the *mean distance* between centers of mass of the straightened segmentation and a straight line, centered in the FOV of the straight space. The second validation metric is the *maximum distance* between the centers of mass of straightened segmentation and a straight line. Validation metrics are computed as follows:

$$mean\ distance\ error = \sqrt{\frac{1}{k}\sum_{i=1}^{k}\left(\left(x_c^i - x_s\right)^2 + \left(y_c^i - y_s\right)^2\right)}$$

$$maximum\ distance\ error = \max_{i\in[1,k]}\left\{\sqrt{\left(x_c^i - x_s\right)^2 + \left(y_c^i - y_s\right)^2}\right\}$$

where $\left(x_c^i, y_c^i\right)$ are the coordinates of the ith point along spinal cord centerline, k is the number of points along centerline and (x_s, y_s) are the coordinates of the straight line, located at the center of the straight space. The *mean distance* represents the global accuracy while the *maximum distance* captures local errors. Both metrics increase with straightening errors and are equal to zero in case of perfect straightening. Statistical tests (paired student t-tests) for comparing validation results between the proposed approach and the landmark-based approach were done using *numpy* Python library.

An important aspect of spinal cord straightening on MR images is the ability to straighten images with various fields of view (FOV). In order to evaluate the sensitivity of FOV size to the accuracy of the proposed straightening method, a large dataset of images with various FOV was generated by cropping each of the 50 volumes from the first healthy population with 20 random sizes in the inferior-superior direction. This large dataset, composed of 1000 volumes of the spinal cord and their segmentation, was automatically straightened and the two evaluation metrics described above were calculated and compared as a function of the spinal cord length. Note that here the term "spinal cord length" does not refer to the actual length of the spinal cord, but to its apparent length within the superior-inferior coverage of the MRI volume. The apparent spinal cord length was calculated by following the spinal cord centerline through the volume while computing its length for each image slice, therefore taking the spinal cord curvature into account. The computational time required for straightening an image depending on its size was also evaluated. Computations were all done on a Mac Pro Quad-Core 3.7 GHz with 16 Go RAM.

In order to demonstrate the importance of preserving the size of structures in planes perpendicular to the spinal cord, spinal cord CSA was computed from binary segmentations on the first healthy population (N=50) by calculating the area defined by voxels: (i) on axial slices, (ii) on axial slices with curvature correction (area corrected by the cosine of the angle between the spinal cord centerline and the inferior-superior direction) (Tench et al., 2005), and (iii) on straightened images.

Paired Student T-tests were performed to test whether differences between CSA measurements performed with these three methods were observed at a $\alpha = 0.05$ level.

5.4 Results

5.4.1 Accuracy and computational time

All images from 57 healthy subjects and 33 DCM patients (mean age: 58.6 ± 10.5 y.o., 18/15 men/women) were straightened using the landmark-based approach and the proposed analytical approach. Figure 5.2 shows distributions of global and local accuracy as well as computational time for both healthy subjects and patients (see Supplementary Material for detailed numeric results). Significant differences were found between the proposed approach and the landmark-based approach for the mean distance error (mean = 0.80 vs 0.83 mm, p-value = 1.65×10^{-3}), the maximum distance error (mean = 1.49 vs 1.78 mm, p-value = 3.15×10^{-4}) and the computational time (mean = 71 vs 174 sec, p-value = 5.05×10^{-29}) for the healthy population, and for the maximum distance error (mean = 1.28 vs 1.55 mm, p-value = 1.36×10^{-3}) and the computational time (mean = 32 vs 60 sec, p-value = 6.77×10^{-29}) in the DCM population. No significant differences were found for the mean distance error in the DCM population (mean = 0.65 vs 0.68, p-value = 0.18).
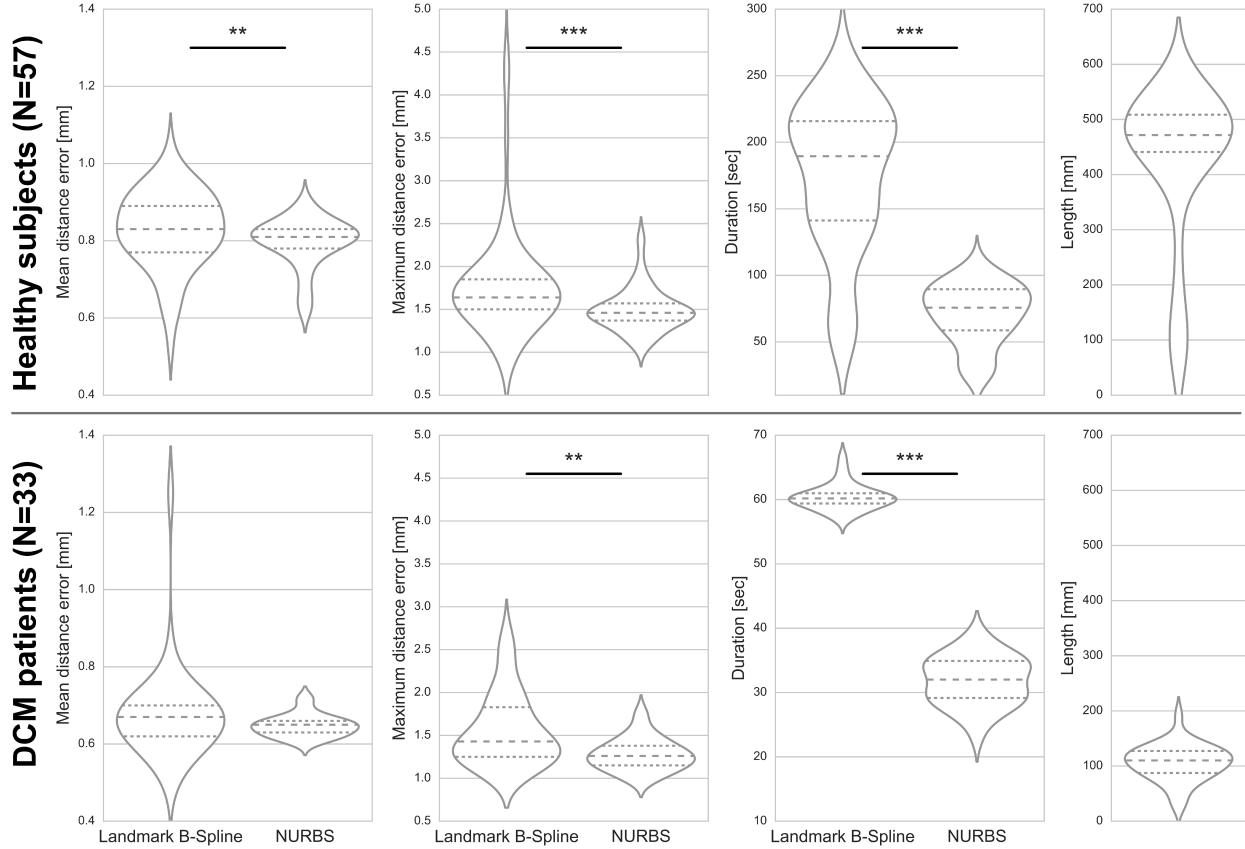
Figure 5.2: Distribution of validation results of straightening (violin plots with median and percentile as dotted lines) on 57 healthy subjects and 33 DCM patients using the landmark-based approach (left plot in each panel) and the proposed approach (right plot). Three validation metrics were calculated: mean distance error (first column from the left), maximum distance error (second column) and computation duration (third column). The length of the spinal cord in healthy subjects and patients is shown on the right column. Asterisks above plots show statistically-significant differences between approaches (*: $p < 0.05$, **: $p < 0.01$, ***: $p < 0.001$).

Examples of straightening are shown in Figure 5.3, demonstrating the robustness of the proposed straightening method even with large variability in spinal cord curvature and image field of view, as well as the preservation of the topology of the spinal cord and its adjacent structures. As a proof-of-concept, a T_1w image was successfully straightened and results were: mean distance error = 0.8 mm, maximum distance error = 1.46 mm and computational time = 115 sec.
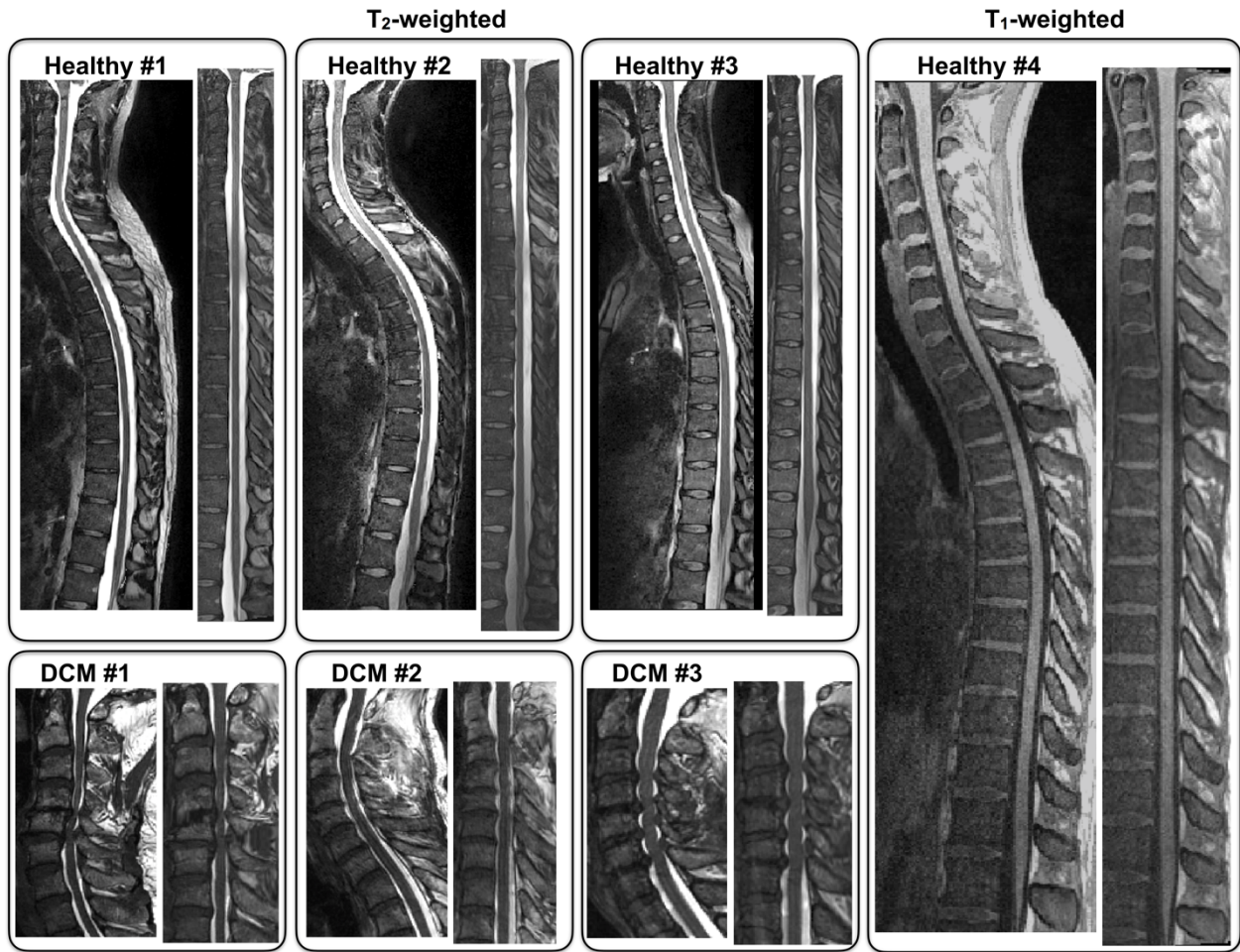
Figure 5.3: Examples of straightening with the proposed method on 4 healthy subjects (3 T_2w and 1 T_1w) and 3 DCM patients. Note the variability in spinal cord curvatures and image fields of view. Note also that original images of curved spinal cord were flattened in the left-right direction for visualization purposes.

5.4.2 Sensitivity to spinal cord length

Figure 5.4 shows the accuracy of straightening and the computational time as a function of spinal cord length. Overall, the proposed approach is more accurate than the landmark-based method for a large spectrum of spinal cord length (from 40 mm to 550 mm). Robustness was also improved, especially for images of the full spinal cord (~500 mm), as demonstrated by the decrease of outliers in the maximum distance error when using the proposed approach. Computational time was less than half with the proposed method. Note the slightly larger mean distance error for cords smaller than 40 mm (except for one subject that shows large errors with the landmark-based approach),

which is likely due to the relative importance of discretization errors compared to image field of view. More particularly, the accuracy of NURBS approximation is directly related to the number of points in the fitted curve. As the number of points is equal to the number of axial slices in the image, the accuracy of the proposed straightening decrease slightly with small FOVs, while remaining acceptable (< 1mm).
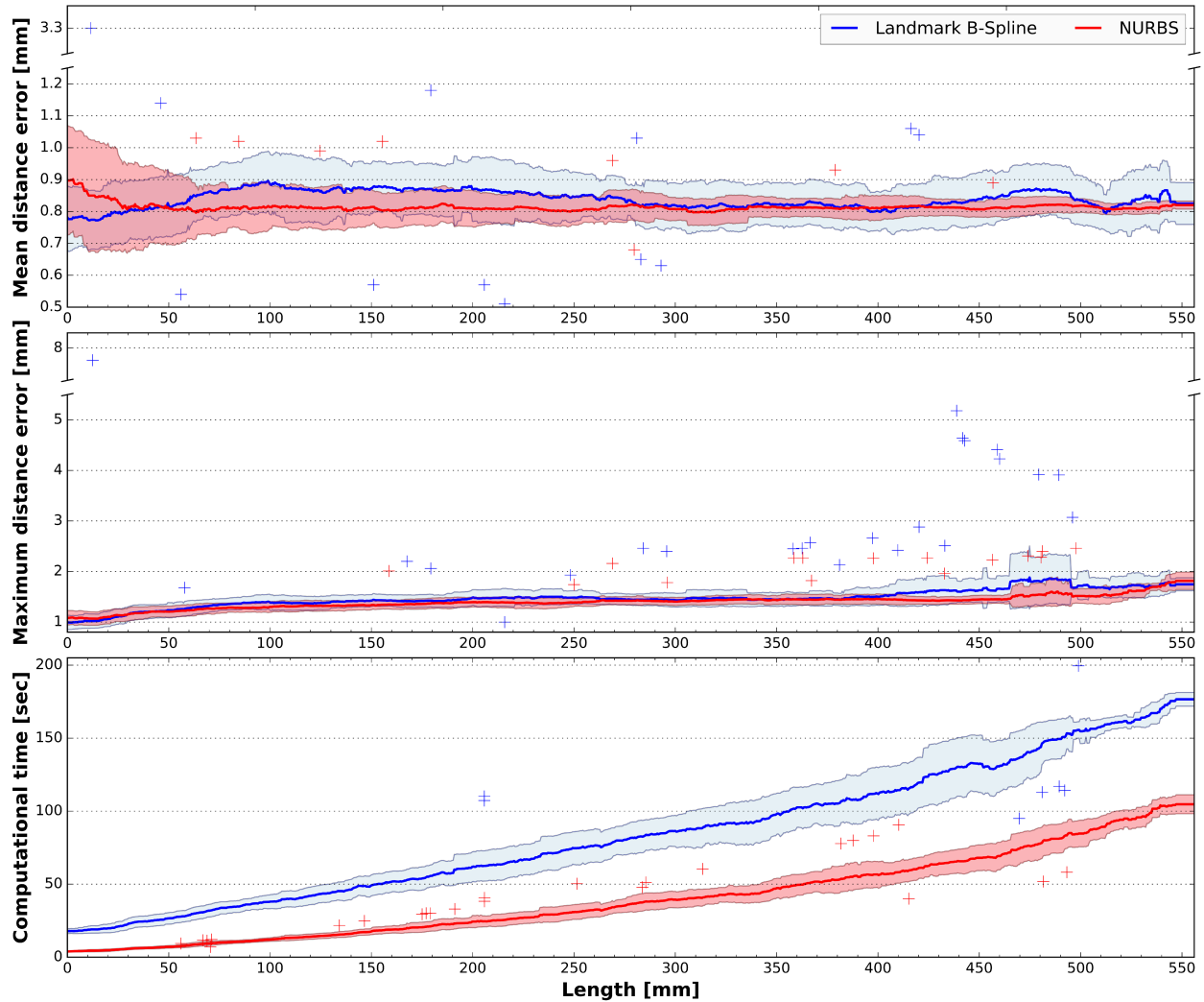
Figure 5.4: Results of straightening as a function of spinal cord length. Mean distance error (top panel), maximum distance error (middle panel) and computational time are lower with the proposed approach (red) than with the landmark-based approach (blue). Outsiders (plus signs) are defined by being outside the "mean +- 2 * std" zone of values.

5.4.3 Cross-sectional area measurements

Figure 5.5a shows the results of CSA calculated: (i) on axial slices in the straight space, using the proposed approach (yellow), (ii) on axial slices with spinal cord curvature correction (red), and (iii) on axial slices without curvature correction (blue). Figure 5.5b shows differences between CSA computed in straight versus curved with correction (red) and CSA computed in straight versus curved without correction (blue). For each axial slice, when the difference was significant (paired Student's t-test, $p<0.05$), an asterisk was represented under the curves. Results show significant differences between the straightening approach and axial measurements without curvature correction, particularly when spinal cord curvature is high ($> 10°$). As expected, much fewer significant differences between the straightening approach and the axial measurements with curvature correction were detected.
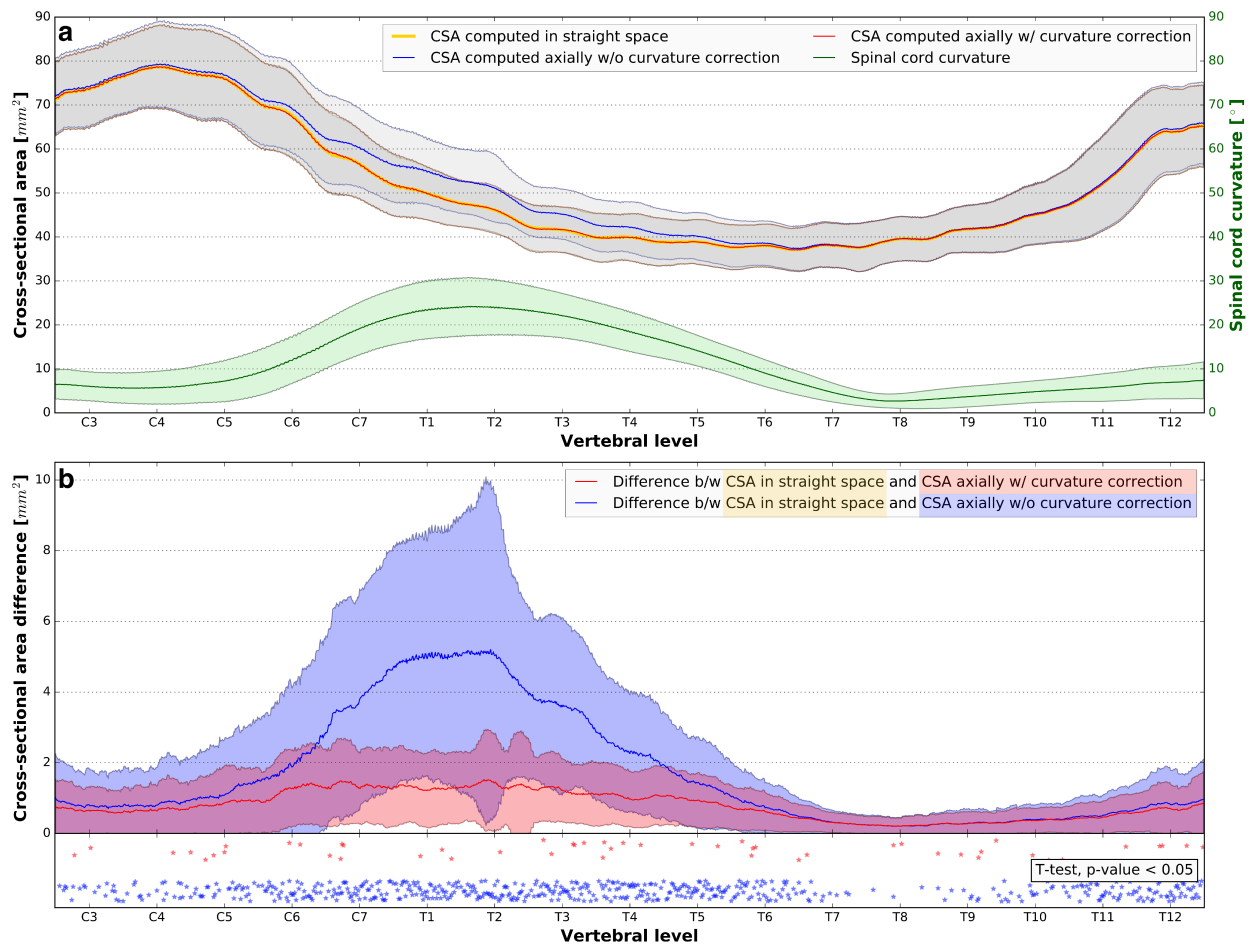
Figure 5.5: Comparison between three different methods of cross-sectional area (CSA) measurement on 50 healthy subjects. The upper panel (a) presents CSA along the spinal cord

measured (i) with the proposed straightening approach (yellow line), (ii) by calculating the area on axial slices and correcting for curvature and (iii) without correcting for curvature. The green line shows the spinal cord curvature along the spinal cord. The lower panel (b) presents the CSA differences between the straight approach and the axial CSA with curvature correction (red area) and between the straight approach and the axial CSA without curvature correction (blue area). Blue and red stars show levels at which CSA differences are significant (paired t-test, p-value<0.05).

5.5 Discussion

In this manuscript, we presented an analytical solution for straightening MR images of the spinal cord that preserves the spinal cord topology (length and area) and its internal and adjacent structures. The proposed method is based on NURBS approximation of spinal cord segmentation/centerline and a per-voxel analytical computation of straightening deformation fields. From our findings, we observed that the analytical computation of image straightening, combined with NURBS approximation of the spinal cord centerline based on spinal cord segmentation, presents superior accuracy, increased robustness to FOV size and decreased computational time when compared to the current standard straightening method (landmark-based b-spline deformation), in both healthy subjects and patients with spine deformities (DCM). Moreover, our method produces forward (curve to straight) and inverse (straight to curve) deformation fields, that can be used in template-based analysis pipelines, unlike existing straightening approaches (El Mendili, Chen, Tiret, Villard, et al., 2015; Horsfield et al., 2010; Stroman et al., 2008). By enabling template-based analysis on patients with spine deformities, spinal cord straightening techniques such as the one we proposed allow the development of new quantitative biomarkers that correlate with clinical features of degenerative diseases, and lead to more sensitive diagnosis of spinal cord injury and better prediction of disease outcomes (Wheeler-Kingshott et al., 2014). Additionally, by calculating CSAs in the curved and straight space, and by taking spine curvature into account, we emphasized the importance of accounting for the cord-to-slice angle when calculating CSAs. Notably, for diagnosis or prognosis purposes, measurement errors without correcting for spinal cord curvature could be larger than the disease-related atrophy.

The key feature of the proposed straightening algorithm is its capacity to work on any MRI contrast (T_1w, T_2w, T_2*w, etc.), as it is using only the spinal cord segmentation/centerline to compute the straightening deformation field. However, the accuracy of straightening inherently relies on the

quality of the spinal cord segmentation and could produce errors in case of segmentation failure (e.g., segmentation exiting the spine). Small and local segmentation errors (e.g., leakage of segmentation by 3-4 voxels across the subarachnoidal space due to lack of contrast on T_1w images) should not strongly affect the quality of the straightening, although this needs to be further evaluated on a case-by-case basis. Another drawback of the NURBS approximation is the minimal number of points required for solving the approximation equation system. Indeed, the $(n-1)\times(n-1)$ equation system has a unique solution at the condition of $n \geq p$, meaning that the number of points must be larger than the degree of the sought curve (i.e., $n \geq 3$). Another key feature of the proposed method is its robustness to the field of view (FOV) in MR images. Indeed, the accuracy of existing straightening methods developed using curve models with fixed polynomial (Vrtovec, Ourselin, Gomes, Likar, & Pernus, 2007) or spline (Fonov et al., 2014) complexity is dependent on the apparent spinal cord length, and is not applicable to arbitrary FOVs. The proposed algorithm is based on an adaptive NURBS approximation of the spinal cord centerline and has demonstrated good robustness towards apparent spinal cord length.

One limitation of the proposed algorithm is the possibility of non-unique solutions for voxels far from the spinal cord (> 10 cm). Indeed, the first step of our straightening method is to find planes perpendicular to the spinal cord that contain each voxel of the input image. Since the NURBS curve representing the centerline is discretized, a voxel far from the curve may not belong to any perpendicular plane. This problem is minimized by the voxel-plane distance correction used at the final step of straightening. However, a voxel could belong to more than one perpendicular plane, leading to multiple straightening solutions and discontinuities in the corresponding region. Though, this issue would appear only in extra-spinal voxels, which aren't important for most spinal cord-related applications, the focus of this manuscript. Spinal cord internal structures such as the white/gray matter and spinal pathways would not be altered much by the straightening process, because of their close proximity with the spinal cord centerline, therefore ensuring the validity of disease monitoring using template-based analysis. Future works will evaluate more deeply the effect of straightening on spinal cord internal structures. Another limitation of the proposed method is the definition of the referential frame of the planes perpendicular to the spinal cord. Indeed, one axis of the plane-referential frame is defined as the anterior-posterior direction. Therefore, our straightening algorithm does not take the potential torsion or axial rotation of the spinal cord in the

coronal plane into account. Future works will include this feature in their straightening implementation.

This study had several limitations. First, although we quantified the accuracy of spinal cord straightening on both healthy and patient cohorts, we only compared CSA measurements using spinal cord segmentation, with and without spinal cord curvature correction, and we did not quantify the accuracy of CSA measurements. Such validation would require ground truth measures of CSA, which is, to the best of our knowledge, currently not available in the literature and would be the focus of future work. Another limitation of this study is the small number of applications of the proposed algorithm. While we only presented a method for straightening spinal cord MRI images, this method could be applied to other anatomical structures, such as blood vessels, provided that further technological advancements, such as spatial regularization, were added to the current implementation of the algorithm.

In conclusion, image straightening is a key step for accurate measure of CSA and for a template-based analysis pipeline dedicated to spinal cord MRI data. In this manuscript, we introduced a new image straightening method that preserves the topology of the spinal cord. This approach is based on an iterative NURBS approximation of spinal cord segmentation and analytical generation of straightening deformation fields. The accuracy and robustness of the proposed method was assessed in healthy subjects and DCM patients, demonstrating better straightening results than the current state-of-the-art. The sensitivity of the method to spinal cord length was also investigated, showing good robustness for any superior-inferior coverage. Finally, different methods for computing CSA were compared, reinforcing the importance of accounting for spinal cord curvature. Future work will include spinal cord axial rotation in the straightening process. The proposed straightening method is available in SCT (De Leener, Lévy, et al., 2016) (v3.0 and higher), an open-source (MIT license) software for processing spinal cord MRI data: http://sourceforge.net/projects/spinalcordtoolbox/.

5.6 Acknowledgements

5.7 References

Asman, A. J., Bryan, F. W., Smith, S. A., Reich, D. S., & Landman, B. A. (2014). Groupwise multi-atlas segmentation of the spinal cord's internal structure. *Med. Image Anal.*, *18*(3), 460–471.

Bastianello, S., Paolillo, A., Giugni, E., Giuliani, S., Evangelisti, G., Luccichenti, G., … Fieschi, C. (2000). MRI of spinal cord in MS. *J. Neurovirol.*, *6 Suppl 2*, S130–3.

Castellano, A., Papinutto, N., Cadioli, M., Brugnara, G., Iadanza, A., Scigliuolo, G., … Salsano, E. (2016). Quantitative MRI of the spinal cord and brain inadrenomyeloneuropathy: in vivo assessment of structuralchanges. *Brain*, *139*(Pt 6), 1735–1746.

Cohen-Adad, J., De Leener, B., Benhamou, M., Cadotte, D., Fleet, D., Cadotte, A., … Others. (2014). Spinal Cord Toolbox: an open-source framework for processingspinal cord MRI data. In *Proceedings of the 20th Annual Meeting of OHBM, Hamburg,Germany* (Vol. 3633, p. 3633).

Cohen-Adad, J., El Mendili, M.-M., Lehéricy, S., Pradat, P.-F., Blancho, S., Rossignol, S., & Benali, H. (2011). Demyelination and degeneration in the injured human spinalcord detected with diffusion and magnetization transfer MRI. *Neuroimage*, *55*(3), 1024–1033.

Cohen-Adad, J., El Mendili, M.-M., Morizot-Koutlidis, R., Lehéricy, S., Meininger, V., Blancho, S., … Pradat, P.-F. (2013). Involvement of spinal sensory pathway in ALS andspecificity of cord atrophy to lower motor neurondegeneration. *Amyotroph. Lateral Scler. Frontotemporal Degener.*, *14*(1), 30–38.

Cohen-Adad, J., & Wheeler-Kingshott, C. (2014). *Quantitative MRI of the Spinal Cord*. Academic Press.

Cox, R. W. (1996). AFNI: software for analysis and visualization of functionalmagnetic resonance neuroimages. *Comput. Biomed. Res.*, *29*(3), 162–173.

De Boor, C. (1978). A practical guide to splines. Number 27 in Applied MathematicalSciences. Springer, New York.

De Leener, B., Cohen-Adad, J., & Kadoury, S. (2015). Automatic Segmentation of the Spinal Cord and Spinal Canal Coupled with Vertebral Labeling. *IEEE Transactions on Medical Imaging*, *34*(8). https://doi.org/10.1109/TMI.2015.2437192

De Leener, B., Kadoury, S., & Cohen-Adad, J. (2014). Robust, accurate and fast automatic segmentation of thespinal cord. *Neuroimage*, *98*, 528–536.

De Leener, B., Lévy, S., Dupont, S. M., Fonov, V. S., Stikov, N., Louis Collins, D., … Cohen-Adad, J. (2016). SCT: Spinal Cord Toolbox, an open-source software for processing spinal cord MRI data. *NeuroImage*. https://doi.org/10.1016/j.neuroimage.2016.10.009

De Leener, B., Taso, M., Cohen-Adad, J., & Callot, V. (2016). Segmentation of the human spinal cord. *Magnetic Resonance Materials in Physics, Biology and Medicine*, *29*(2). https://doi.org/10.1007/s10334-015-0507-2

El Mendili, M.-M., Chen, R., Tiret, B., Pélégrini-Issac, M., Cohen-Adad, J., Lehéricy, S., … Benali, H. (2015). Validation of a semiautomated spinal cord segmentationmethod. *J. Magn. Reson. Imaging*, *41*(2), 454–459.

El Mendili, M.-M., Chen, R., Tiret, B., Villard, N., Trunet, S., Pélégrini-Issac, M., … Benali, H. (2015). Fast and accurate semi-automated segmentation method of spinal cord {MR} images at {3T} applied to the construction of a cervical spinal cord template. *PLoS One*, *10*(3), e0122224.

Ellingson, B. M., Ulmer, J. L., & Schmit, B. D. (2008). Morphology and morphometry of human chronic spinal cord injuryusing diffusion tensor imaging and fuzzy logic. *Ann. Biomed. Eng.*, *36*(2), 224–236.

Fonov, V. S., Le Troter, A., Taso, M., De Leener, B., Lévêque, G., Benhamou, M., … Cohen-Adad, J. (2014). Framework for integrated MRI average of the spinal cordwhite and gray matter: the MNI-Poly-AMU template. *Neuroimage*, *102 Pt 2*, 817–827.

Fradet, L., Arnoux, P.-J., Ranjeva, J.-P., Petit, Y., & Callot, V. (2014). Morphometrics of the entire human spinal cord and spinalcanal measured from in vivo high-resolution anatomicalmagnetic resonance imaging. *Spine*, *39*(4), E262–9.

Friston, K. J., Holmes, A. P., Worsley, K. J., Poline, J.-P., Frith, C. D., & Frackowiak, R. S. J. (1994). Statistical parametric maps in functional imaging: A generallinear approach. *Hum. Brain Mapp.*, *2*(4), 189–210.

Gorgolewski, K., Burns, C. D., Madison, C., Clark, D., Halchenko, Y. O., Waskom, M. L., & Ghosh, S. S. (2011). Nipype: a flexible, lightweight and extensible neuroimagingdata processing framework in python. *Front. Neuroinform.*, *5*, 13.

Grabher, P., Mohammadi, S., Trachsler, A., Friedl, S., David, G., Sutter, R., … Freund, P. (2016). Voxel-based analysis of grey and white matter degeneration incervical spondylotic myelopathy. *Sci. Rep.*, *6*, 24636.

Horsfield, M. A., Sala, S., Neema, M., Absinta, M., Bakshi, A., Sormani, M. P., … Filippi, M. (2010). Rapid semi-automatic segmentation of the spinal cord frommagnetic resonance images: application in multiple sclerosis. *Neuroimage*, *50*(2), 446–455.

Jenkinson, M., Beckmann, C. F., Behrens, T. E. J., Woolrich, M. W., & Smith, S. M. (2012). FSL. *Neuroimage*, *62*(2), 782–790.

Losseff, N. A., Webb, S. L., O'riordan, J. I., Page, R., Wang, L., & others. (1996). Spinal cord atrophy and disability in multiple sclerosis. *Brain*.

Maneewongvatana, S., & Mount, D. M. (1999). It's okay to be skinny, if your friends are fat. In *Center for Geometric Computing 4th Annual Workshop onComputational Geometry* (Vol. 2, pp. 1–8). cs.umd.edu.

Nakamura, M., Miyazawa, I., Fujihara, K., Nakashima, I., Misu, T., Watanabe, S., … Itoyama, Y. (2008). Preferential spinal central gray matter involvement inneuromyelitis optica. An MRI study. *J. Neurol.*, *255*(2), 163–170.

Nouri, A., Tetreault, L., Singh, A., Karadimas, S. K., & Fehlings, M. G. (2015). Degenerative Cervical Myelopathy: Epidemiology, Genetics, andPathogenesis. *Spine*, *40*(12), E675–93.

Papinutto, N., Schlaeger, R., Panara, V., Zhu, A. H., Caverzasi, E., Stern, W. A., … G. (2015). Age, gender and normalization covariates for spinal cord graymatter and total cross-sectional areas at cervical andthoracic levels: A 2D phase sensitive inversion recoveryimaging study. *PLoS One*, *10*(3), e0118576.

Penny, W. D., Friston, K. J., Ashburner, J. T., Kiebel, S. J., & Nichols, T. E. (2011). *Statistical Parametric Mapping: The Analysis of Functional BrainImages*. Academic Press.

Piegl, L., & Tiller, W. (2012). *The NURBS Book.* Springer Science & Business Media.

Stroman, P. W., Figley, C. R., & Cahill, C. M. (2008). Spatial normalization, bulk motion correction andcoregistration for functional magnetic resonance imaging ofthe human cervical spinal cord and brainstem. *Magn. Reson. Imaging*, *26*(6), 809–814.

Stroman, P. W., Wheeler-Kingshott, C., Bacon, M., Schwab, J. M., Bosma, R., Brooks, J., … Tracey, I. (2014). The current state-of-the-art of spinal cord imaging: methods. *Neuroimage*, *84*, 1070–1081.

Talbott, J. F., Narvid, J., Chazen, J. L., Chin, C. T., & Shah, V. (2016). An Imaging-Based Approach to Spinal Cord Infection. *Semin. Ultrasound CT MR*, *37*(5), 411–430.

Taso, M., Girard, O. M., Duhamel, G., Le Troter, A., & others. (2016). Tract-specific and age-related variations of the spinal cordmicrostructure: a multi-parametric MRI study using diffusiontensor imaging (DTI) and inhomogeneous …. *NMR Biomed.*

Taso, M., Le Troter, A., Sdika, M., Cohen-Adad, J., Arnoux, P.-J., Guye, M., … Callot, V. (2015). A reliable spatially normalized template of the human spinal cord--Applications to automated white matter/gray matter segmentation and tensor-based morphometry ({TBM}) mapping of gray matter alterations occurring with age. *Neuroimage*, *117*, 20–28.

Tench, C. R., Morgan, P. S., & Constantinescu, C. S. (2005). Measurement of cervical spinal cord cross-sectional area byMRI using edge detection and partial volume correction. *J. Magn. Reson. Imaging*, *21*(3), 197–203.

Ullmann, E., Pelletier Paquette, J. F., Thong, W. E., & Cohen-Adad, J. (2014). Automatic labeling of vertebral levels using a robust template-based approach. *Int. J. Biomed. Imaging*, *2014*, 719520.

Valsasina, P., Horsfield, M. A., Rocca, M. A., Absinta, M., Comi, G., & Filippi, M. (2012). Spatial normalization and regional assessment of cordatrophy: voxel-based analysis of cervical cord 3DT1-weighted images. *AJNR Am. J. Neuroradiol.*, *33*(11), 2195–2200.

van der Kouwe, A. J. W., Benner, T., Salat, D. H., & Fischl, B. (2008). Brain morphometry with multiecho MPRAGE. *Neuroimage*, *40*(2), 559–569.

Vrtovec, T., Likar, B., & Pernus, F. (2005). Automated curved planar reformation of 3D spine images. *Phys. Med. Biol.*, *50*(19), 4527–4540.

Vrtovec, T., Ourselin, S., Gomes, L., Likar, B., & Pernus, F. (2007). Automated generation of curved planar reformations from MRimages of the spine. *Phys. Med. Biol.*, *52*(10), 2865–2878.

Wheeler-Kingshott, C. A., Stroman, P. W., Schwab, J. M., Bacon, M., Bosma, R., Brooks, J., … Tracey, I. (2014). The current state-of-the-art of spinal cord imaging: applications. *Neuroimage*, *84*, 1082–1093.

Woolrich, M. W., Jbabdi, S., Patenaude, B., Chappell, M., Makni, S., Behrens, T., … Smith, S. M. (2009). Bayesian analysis of neuroimaging data in FSL. *Neuroimage*, *45*(1 Suppl), S173–86.

Yiannakas, M. C., Kearney, H., Samson, R. S., Chard, D. T., Ciccarelli, O., Miller, D. H., & Wheeler-Kingshott, C. A. M. (2012). Feasibility of grey matter and white matter segmentation ofthe upper cervical cord in vivo: a pilot study withapplication to magnetisation transfer measurements. *Neuroimage*, *63*(3), 1054–1059.

Yiannakas, M. C., Mustafa, A. M., De Leener, B., Kearney, H., Tur, C., Altmann, D. R., … Gandini Wheeler-Kingshott, C. A. M. (2016). Fully automated segmentation of the cervical cord fromT1-weighted MRI using PropSeg: Application to multiplesclerosis. *Neuroimage Clin*, *10*, 71–77.

CHAPTER 6   ARTICLE 4: PAM50: UNBIASED MULTIMODAL TEMPLATE OF THE BRAINSTEM AND SPINAL CORD ALIGNED WITH THE ICBM152 SPACE

This article presents a framework for generating MRI template of the spinal cord, and introduces the PAM50. The PAM50 is an unbiased and symmetrical template of the brainstem and full spinal cord that is available for T1-, T2- and T2*-weighted contrasts, that includes probabilistic atlases of the white and gray matter, and that is anatomically compatible with the ICBM152 brain template. The introduction of this framework and spinal cord template is the main contribution of this project and directly answers to its first objective.

My contribution (90%) on this study included the design and development of the framework for the template processing and generating, its implementation and validation, and the design and redaction of the manuscript. This manuscript has been submitted to Neuroimage in July 2017.

Title: PAM50: unbiased multimodal template of the Brainstem and spinal cord aligned with the ICBM152 space

Authors:

Benjamin De Leener[1], Vladimir S. Fonov[2], D. Louis Collins[2], Virginie Callot[3,4], Nikola Stikov[1,5], and Julien Cohen-Adad[1,6]

Affiliations:

[1] NeuroPoly Lab, Institute of Biomedical Engineering, Polytechnique Montreal, Montreal, QC, Canada

[2] Montreal Neurological Institute, McGill University, Montreal, QC, Canada

[3] Aix-Marseille Université, CNRS, CRMBM UMR 7339, Marseille, France

[4] AP-HM, Hopital de la Timone, Pôle d'imagerie médicale, CEMEREM, Marseille, France

[5] Montreal Heart Institute, Montreal, QC, Canada

[6] Functional Neuroimaging Unit, CRIUGM, Université de Montréal, Montreal, QC, Canada

6.1 Abstract

Template-based analysis of multi-parametric MRI data of the spinal cord sets the foundation for standardization and reproducibility, thereby helping the discovery of new biomarkers of spinal-related diseases. While MRI templates of the spinal cord have been recently introduced, none of them cover the entire spinal cord. In this study, we introduced an unbiased multimodal MRI template of the spinal cord and the brainstem, called PAM50, which is anatomically compatible with the ICBM152 brain template and uses the same coordinate system. The PAM50 template is based on 50 healthy subjects, covers the full spinal cord (C1 to L2 vertebral levels) and the brainstem, is available for T1-, T2- and T2*-weighted MRI contrasts and includes a probabilistic atlas of the gray matter and white matter tracts. Template creation accuracy was assessed by computing the mean and maximum distance error between each individual spinal cord centerline and the PAM50 centerline, after registration to the template. Results showed high accuracy for both T1- (mean=0.37+/-0.06 mm; max=1.39+/-0.58 mm) and T2-weighted (mean=0.11+/-0.03 mm; max=0.71+/-0.27 mm) contrasts. Additionally, the preservation of the spinal cord topology during the template creation process was verified by comparing the cross-sectional area (CSA) profile, averaged over all subjects, and the CSA profile of the PAM50 template. The fusion of the PAM50 and ICBM152 templates will facilitate group and multi-center studies of combined brain and spinal cord MRI, and enable the use of existing atlases of the brainstem compatible with the ICBM space.

Keywords

Spinal cord, MRI, template, atlas, ICBM

6.2 Introduction

The spinal cord is a tubular structure that is part of the central nervous system and is embedded into the vertebral bodies, inside the spinal canal. The spinal cord is notably responsible for transmitting information back and forth from the brain to the peripheral nervous system. The spinal cord can be affected by several pathologies, including traumatic injuries, neurodegenerative diseases (e.g., multiple sclerosis), vascular diseases and tumors, often with dramatic clinical consequences for the patients (Rocca, Preziosa, & Filippi, 2015). Over the past few years, improvements of the acquisition and processing techniques dedicated to the spinal cord have enabled researchers to acquire data with higher quality (higher SNR, less artifacts) and to process them following more standardized guidelines (Cohen-Adad & Wheeler-Kingshott, 2014b; Stroman et al., 2014).

Particularly, template-based analysis of multi-parametric MRI data of the spinal cord sets the foundation for standardization and reproducibility. Particularly, it allows researchers to process their data with minimum bias, perform multi-center studies, with the goal of improving patient diagnosis and prognosis and helping the discovery of new biomarkers of spinal-related diseases. For example, several research groups are developing biomarkers that are sensitive to white matter damage and neuronal function in the spinal cord (Cohen-Adad, 2017; Martin et al., 2016; Stroman et al., 2014; Wheeler-Kingshott et al., 2014). However, the lack of common template and reference space for the spinal cord makes it difficult to process quantitative MRI data and to compare results between subjects, groups of subjects and centers.

Several research groups have proposed MRI templates of the spinal cord that are tailored towards specific applications. Stroman et al. (Stroman et al., 2008) created a template based on 1x1x2 mm^3 T2-weighted (T2w) fast-spin echo images from eight healthy subjects, for use in functional MRI studies. The authors later extended this template to 10 subjects and introduced a normalization approach based on the distance from the pontomedullary junction (PMJ) to obtain an improved representation of the spinal levels (Stroman et al., 2012). The same group later used a similar approach to generate a T2w template of the brainstem and cervical spinal cord from 356 subjects (Bosma & Stroman, 2014) and used it in pain studies (Khan & Stroman, 2015; Stroman et al., 2016). Another group built a template out of 15 T1-weighted cervical cord images (Eippert et al., 2009), although one limitation was that the template was created by arbitrarily selecting one subject

that served as a target for registering all the other subjects. Meanwhile, Valsasina et al. (Valsasina et al., 2012) proposed a normalization procedure based on a semi-automated segmentation approach to generate a T1-weighted template of the cervical spinal cord. The template was generated by unfolding images from 19 healthy subjects and averaged to create an initial straight template of the spinal cord. Then the template was refined by rescaling all images on this initial average. The authors used this template to apply voxel-based analysis to a healthy population in the context of spinal cord atrophy. Recently, El Mendili et al. introduced a template of the cervical spinal cord, based on a similar approach but normalized with the spinal cord length instead and using a semi-automated segmentation method (El Mendili, Chen, Tiret, Villard, et al., 2015). Meanwhile, Taso et al. (Taso et al., 2015) constructed an axial T2*-weighted template of the spinal cord from 40 healthy subjects (AMU40), covering the cervical cord, along with probabilistic atlases of white and gray matter. The template was constructed using affine co-registration of all images, based on manual segmentation, by alternatively selecting one subject as a reference. The 40 templates were then registered on a virtual elliptical external reference built from anatomical measurements to provide an unbiased template. This template was used for tensor-based morphometry mapping of age-specific populations, demonstrating anterior gray matter atrophy in elderly volunteers (> 50 y.o.), when compared to a young population (< 40 y.o.). Later, the same authors established a normative database, based on 48 healthy subjects, of cross-sectional area (CSA), diffusion tensor imaging (DTI) and inhomogeneous magnetization transfer (ihMT) metrics in specific white and gray matter subregions.

To address the issue of subject selection bias during template generation and to obtain a sharp-edged looking template, Fonov et al. used template-generation pipelines similar to that used for creating the MNI template (Fonov, Evans, McKinstry, Almli, & Collins, 2009) and introduced the MNI-Poly-AMU, an unbiased template based on T2w data from 16 subjects, covering C1 to T6 vertebral levels that also includes probabilistic atlases of the white and gray matter. The MNI-Poly-AMU template was made available via the *Spinal Cord Toolbox* (SCT), a comprehensive and open-source software for analyze multiparametric MRI data of the spinal cord (De Leener, Lévy, et al., 2017). One limitation of the MNI-Poly-AMU is that it only covers C2 to T6 vertebral levels and is only available for T2-weighted contrast.

Despite these past investigations on spinal cord templates, outstanding limitations remain: none of these templates cover the entire spinal cord, none offers multiple contrasts (T1w and T2w) and

none are compatible with an existing brain template, preventing the study of the brain-cord axis within a single referential system.

The main objective of this study was to propose a new MRI template of the spinal cord that is: (i) left-right symmetric and unbiased with respect to subject selection, (ii) covering the full spinal cord and brainstem, (iii) available for commonly used MRI contrasts (T1-w, T2-w and T2*-w), (iv) merged with probabilistic maps atlases of the spinal cord white and gray matter and (v) anatomically compatible and using the same coordinate system as the ICBM152 "MNI" brain space (Fonov, Evans, et al., 2011; Fonov et al., 2009). An additional objective of this study is to make the template generation procedure accessible via open-source software, so that spinal cord MRI templates from different populations (variable ages, pathologies, etc.) or species could easily be created.

6.3 Materials and Methods

6.3.1 Data acquisition

50 subjects (mean age: 27+/-6.5 y.o., 29/21 men/women) were recruited and scanned in Montreal (n=34) and in Marseille (n=16) between April 2013 and October 2015 on Siemens 3T MRI systems (TIM Trio and Verio, Siemens Healthcare) using the standard 12-channel head, 4-channel neck, and 24-channel spine receive coils. Local Institutional Review Board approval and written informed consent from volunteers were obtained prior to imaging in both institutions. 3D T1-weighted (T1w) and 3D T2-weighted (T2w) volumes were acquired for each subject, covering the full spinal cord, brainstem and brain. This large coverage was achieved by acquiring two FOVs per contrast, one including the head and cervical spine and the other including part of the cervical, thoracic and lumbar cord. The two volumes were stitched together using offline software tools provided by the manufacturer's MRI console after correcting for B1 bias field (proprietary algorithm). T1w/T2w acquisition parameters were: MPRAGE sequence, TR=2260/1500 ms, TE = 2.09/119 ms, TI = 1200 ms (only for the T1w), flip angle = 7/140°, bandwidth 651/723 Hz/voxel, voxel size = 1x1x1 mm3. Total acquisition time was 22 minutes.

6.3.2 Template generation

The PAM50 (for Polytechnique Montreal, Aix-Marseille Université and Montreal Neurological Institute) template was created in three steps (Figure 6.2, A-C) using the T1w and T2w images from the 50 healthy subjects: (i) the spinal cord centerline and the anterior edge of the brainstem, as well as the intervertebral disks positions were semi-automatically extracted on all images using PropSeg (*sct_propseg*) (De Leener et al., 2014) and vertebral labeling tools (*sct_label_vertebrae*) (Ullmann et al., 2014) from SCT (De Leener, Lévy, et al., 2017), (ii) the spinal cord (but not the brainstem) was straightened and vertebral levels were aligned using a Non-Uniform Rational Bezier Spline (NURBS) based nonlinear transformation (De Leener, Mangeat, et al., 2017) and (iii) unbiased left-right symmetric template was constructed using a hierarchical group-wise image-registration method (Fonov et al., 2014). This procedure was used to build the T1w template while the T2w template was generated by applying the individual T1w deformation fields to all T2w images, after T1w and T2w images from each subject were straightened and their vertebral levels aligned using the same centerline-based nonlinear deformation as for T1w images (De Leener, Mangeat, et al., 2017). Additionally, the AMU15 T2*w template (Taso et al., 2014) was merged with the PAM50 template, as described in (Fonov et al., 2014), thereby providing probabilistic atlases of the white and gray matter. The white matter atlas from (Lévy et al., 2015) was also included into the PAM50, providing probabilistic delineation of white matter tracts. An additional atlas of gray matter subregions was built, similarly to the white matter atlas in (Lévy et al., 2015). Finally, the PAM50 spinal cord and brainstem template was registered with the ICBM152 brain template to provide a common referential system for brain-cord studies (Figure 6.2, D).

6.3.2.1 Image pre-processing

Several pre-processing steps were applied on the MR images before template generation (Figure 6.2, A). Following volumes stitching, the spinal cord was automatically segmented using PropSeg (De Leener et al., 2014). Manual corrections were made on all images to accurately segment the conus medullaris and extracting the spinal canal centerline below. The anterior edge of the brainstem was also manually delineated by an expert, as depicted in Figure 6.2. Then, the position of intervertebral disks, pontomedullary groove and pontomedullary junction were semi-automatically identified using a template-matching detection algorithm (Ullmann et al., 2014) and manually corrected. Finally, a slice-based intensity normalization procedure was applied to all

images to homogenize image intensity inside the spinal cord and throughout the entire dataset. The normalization procedure consisted in the extraction of the average intensity profile along the spinal cord centerline with a kernel adapting to the spinal cord area. The intensity of the image was then normalized to the average intensity of the whole dataset.

6.3.2.2 Image straightening and vertebral alignment

Based on spinal cord segmentation, all T1w and T2w images were straightened and vertebral levels were aligned. The straightening procedure was performed using a NURBS-based analytical deformation algorithm that preserves the topology of the spinal cord (De Leener, Mangeat, et al., 2017). Vertebral level alignment was included in the straightening procedure, using a vertebral-based referential system defined in (De Leener, Cohen-Adad, & Kadoury, 2015b) and described as the following.

The spinal cord centerline $C(u)$ can be represented by a pth-degree NURBS, as described in (De Leener et al., 2015b), with u being a uniform parameter with limits set to 0 to 1. Such a representation allows for fast computation of curve derivatives and deformation fields based on curve perpendicular planes. Intervertebral disks, represented by their position in space $D_n = \{x_d, y_d, z_d\}$, can be projected on the centerline $C(u)$ as $\widehat{D}_n = C(u_i)$ where $u_i = argmin_u ||C(u) - D_n||_2$. The first axis (inferior-superior direction) units of the referential system are defined by the position of intervertebral disks $\widehat{D}_n$ along the centerline and by the Euclidean distance between each disk, normalized by the curved distance between adjacent disks. The second and third axes are defined as the left-right and anterior-posterior direction, respectively, and depend on the axial rotation of the spinal cord. Units are in millimeters.

Vertebral alignment of all images was performed by finding the correspondence for each point along the spinal cord centerlines using the vertebrae-based referential system described in (De Leener et al., 2015b), and by integrating this alignment into the straightening nonlinear transformation. The vertebral referential system of the PAM50 template is a straight centerline with vertebral levels length averaged from the 50 subjects below the tip of the C2 vertebrae. Over the brainstem region, the referential system is defined by the pontomedullary groove and pontomedullary junction, and by the average length and curvature of the brainstem over the 50 subjects. Note that the straightening procedure outputs images that are cropped between the lowest

and highest points of the NURBS-based centerline, therefore covering the full spinal cord and brainstem. The PAM50 template aims at covering the brainstem and the full spinal cord, down to the conus medullaris.

6.3.2.3 Hierarchical group-wise image registration

Unbiased left-right symmetric spinal cord and brainstem T1w and T2w templates were generated using the hierarchical group-wise image registration method described in (Fonov et al., 2014). The method is based on the nonlinear registration engine of Automatic Nonlinear Image Matching and Anatomical Labeling (ANIMAL) (Collins, Holmes, Peters, & Evans, 1995) and uses normalized straight images of the spinal cord and brainstem. Overall, this template generation algorithm is performed by iteratively computing the average of all images and nonlinearly registering the images on this average. This procedure is repeated several times with finer grid size and blurring kernels: 4 iterations at 4 mm resolution, 4 iterations at 2 mm, 4 iterations at 1 mm and 4 iterations at 0.5 mm. Left-right symmetry was achieved by flipping all initial images in the left-right direction and integrating them as input into the iterative template generation procedure. While the original images have a 1 mm^3 isotropic resolution, the iterative nonlinear averaging process allows to increase resolution of the final template and to keep high-contrasted structures. Therefore, the final resolution of the template was set to $0.5 \times 0.5 \times 0.5$ mm^3 for a size of $201 \times 201 \times 1200$ voxels. Finally, a slice-based intensity normalization procedure was applied on the final template to homogenize the image intensity inside the spinal cord and thus correct for the intensity bias related to inhomogeneous transmit and receive B1 fields.

6.3.2.4 T2*w template and spinal cord atlases

The AMU15 T2*-weighted (T2*w) 2D probabilistic atlas (Taso et al., 2014) was merged with the PAM50 template using a nonlinear transformation, as described in (Fonov et al., 2014). As the spinal cord gray matter appears brighter than the white matter in T2*w images, the AMU15 template provides information about the spinal cord internal structure. Probabilistic maps of the white and gray matter (Taso et al., 2014) and a probabilistic atlas of the white matter pathways (Lévy et al., 2015) were also registered to the PAM50 following the procedure described in (Lévy et al., 2015), while being extended to the whole spinal cord (C1 to L1).

Additionally, the PAM50 template integrates an atlas of the gray matter subregions, including delineation of left and right ventral horns, dorsal horns and intermediate zones (Figure 6.1). The gray matter atlas was built similarly to (Lévy et al., 2015), by nonlinearly registering the atlas from (Nieuwenhuys, Voogd, & van Huijzen, 2008) to specific slices (one per vertebral level) of the gray matter probabilistic map from AMU15, and interpolating to the entire spinal cord.
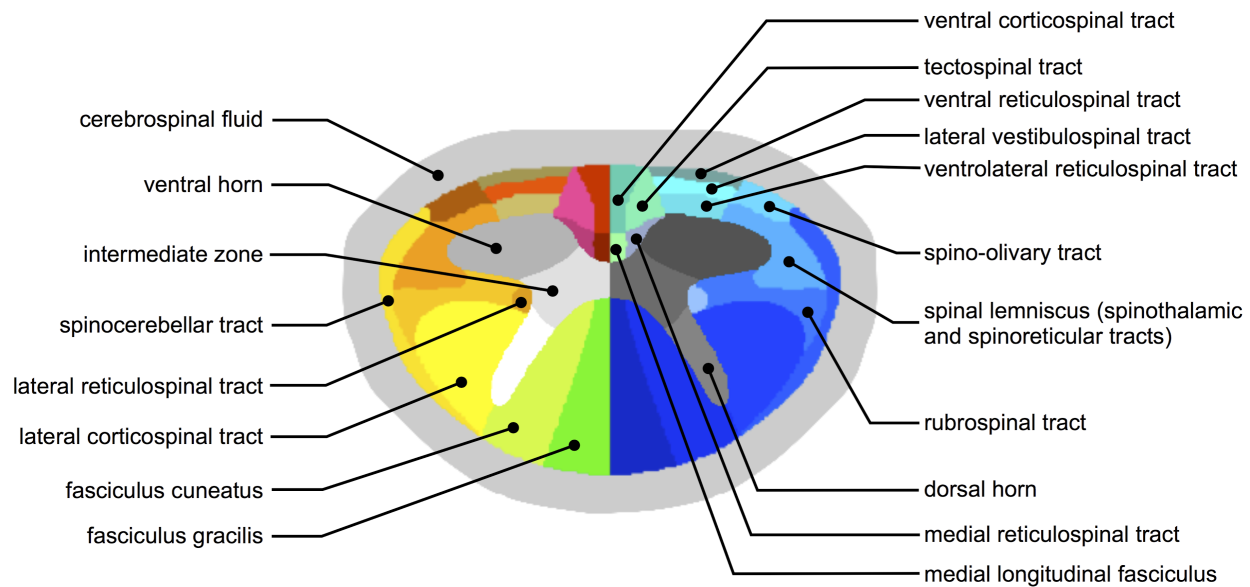
Figure 6.1: Atlas of the white matter pathways from (Lévy et al., 2015) coupled with the newly proposed gray matter subregions, derived from the (Nieuwenhuys et al., 2008) atlas.

6.3.2.5 Fusion of brain, brainstem and spinal cord

The fusion of the PAM50 and the ICBM152 templates was performed by registering the brainstem of both templates into a common space. First, for each subject, the relative curvature of the brainstem, with respect to the pontomedullary junction, registered to the relative curvature of the brainstem on the ICBM152 brain template. Second, an image-based iterative nonlinear transformation (ANTs) (Tustison & Avants, 2013) was performed to accurately co-register both templates, based on the T1w contrast, using the following parameters: BSplineSyN 3D transformation, cross-correlation evaluation metric, three registration steps (smoothing sigmas=4x2x1mm, shrinkage factor=4x2x1 and iterations=20x10x5). To ensure appropriate continuity on edges of images, a mask covering the brainstem region in both images was used in the registration process, with no displacement constraints at the edge of the generated deformation field. The physical space of the final PAM50 is the same as the ICBM152 template, thereby

providing a common physical coordinates system for simultaneous brain, brainstem and spinal cord studies.
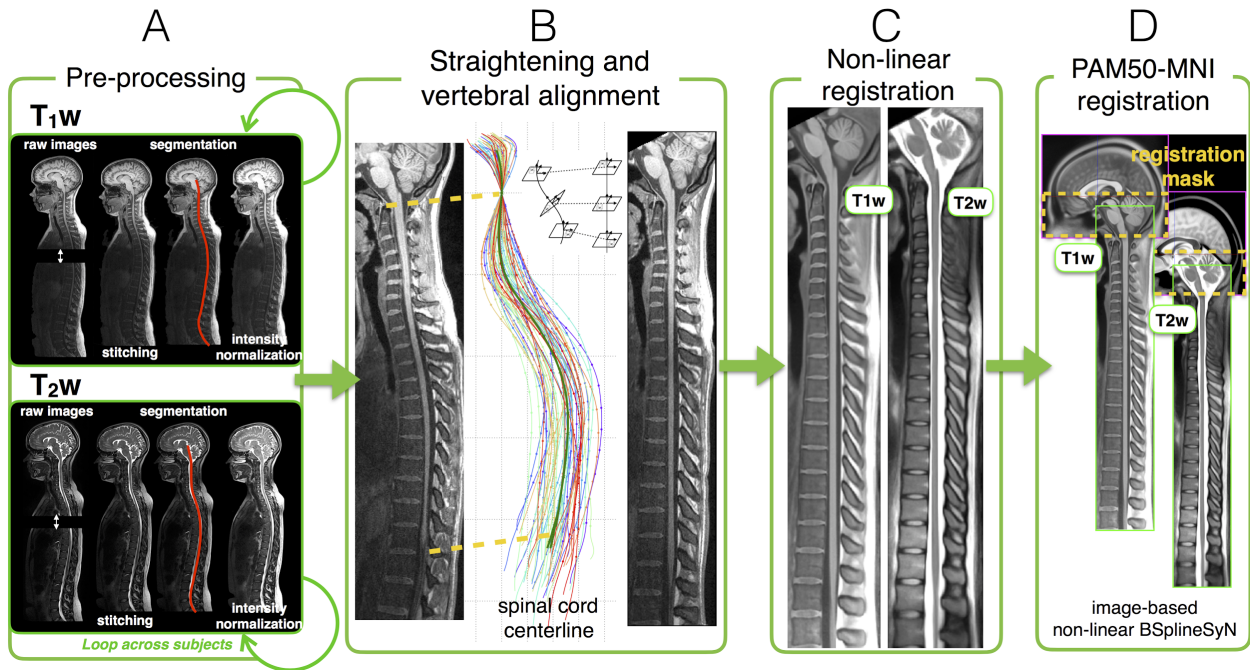
Figure 6.2: Schematic representation of the template generation pipeline. (A) Pre-processing of T1w and T2w data consisted of stitching the images, semi-automatically extracting the spinal canal centerline and brainstem anterior edge and normalizing the image intensity. (B) After pre-processing, the spinal cord of each subject was straightened, and vertebral levels were aligned using a NURBS-based nonlinear transformation. (C) Then, nonlinear iterative deformations were computed in order to co-register all T1w and T2w images into the common PAM50 space; the template image intensity was normalized inside the spinal cord. (D) Lastly, the PAM50 spinal cord template and the ICBM152 MNI brain template were registered using a nonlinear BSplineSyN-based deformation using a mask over the brainstem.

6.3.3 Validation

6.3.3.1 Registration accuracy

Two metrics were used to assess the accuracy of the image registration process used to produce the average template. The straightening and registration of each subject was validated, after registration to the template, by computing the mean and maximum distance error of the straightened spinal

canal centerline and brainstem anterior edge line. Both spinal canal and brainstem lines will be called *centerline* in the following sections for easier use. The *mean centerline error* and *maximum centerline error* were computed between the centers of mass of the centerline of each subject's images and the template centerline. These validation metrics are defined as follows:

$$mean\ distance\ error = \sqrt{\frac{1}{k}\sum_{i=1}^{k}\left(\left(x_A^i - x_B^i\right)^2 + \left(y_A^i - y_B^i\right)^2 + \left(z_A^i - z_B^i\right)^2\right)}$$

$$maximum\ distance\ error = \max_{i\in[1,k]}\left\{\sqrt{\left(x_A^i - x_B^i\right)^2 + \left(y_A^i - y_B^i\right)^2 + \left(z_A^i - z_B^i\right)^2}\right\}$$

where $\left(x_A^i, y_A^i, z_A^i\right)$ and $\left(x_B^i, y_B^i, z_B^i\right)$ are the coordinates of the ith point along the spinal cord centerline in an image A and B, and k is the number of slices in the images, assuming both images share a common space and have the same number of slices. The mean distance represents the global accuracy of the registration, while the maximum distance captures local errors. The accuracy of the registration between the PAM50 and the ICBM152 templates (brainstem region) was assessed visually.

6.3.3.2 CSA preservation

The nonlinear deformations that are applied to the images in order to generate the unbiased average template must preserve the topology of the spinal cord and its adjacent structures. To demonstrate the preservation of the spinal cord dimensions, the cross-sectional area (CSA) of the spinal cord was computed on T1w images for each subject, and its average was compared with the cord CSA extracted from the PAM50 template.

6.3.3.3 Association between vertebral and spinal levels

Vertebral levels based coordinate systems have been largely used in the literature, for example for extracting MS-related spinal cord atrophy information at C2-C3 vertebral level (Losseff, Webb, O'Riordan, et al., 1996; Yiannakas et al., 2015). However, many studies would gain from a spinal segment based coordinate system. Indeed, spinal segments represent the innervation of spinal nerves and are more related to neuroanatomy than vertebral levels. While neuroanatomy textbooks (Mai & Paxinos, 2011) suggests the use of vertebral body rostral to the spinal segment that needs to be predicted, Cadotte et al. have demonstrated this approach to be imprecise (Cadotte et al.,

2015). Based on 20 healthy subjects, the authors have proposed a Gaussian distribution based approach to predict the position of spinal roots along the spinal cord, based on the distance of vertebral bodies from the PMJ. To validate the feasibility of this approach, we calculated the distance between the PMJ and the cervical and lumbar enlargements of the spinal cord, for all 50 subjects from our population, and compared it to the distance between the PMJ and the nearest intervertebral disks, namely C4-C5 for the cervical enlargement and T11-T12 for the lumbar enlargement. As spinal enlargements are known to be related to the neuroanatomy of the spinal cord, a positive correlation between spinal enlargements and closest intervertebral disks would allow to compute a direct probabilistic prediction system for the spinal segments, based on the location of vertebral bodies and intervertebral disks relative to the PMJ.

6.4 Results

6.4.1 PAM50: spinal cord and brainstem template, aligned with ICBM152

Figure 6.3 shows a sagittal view of the PAM50 template fused with the ICBM152 "MNI" brain template. This figure also illustrates the T1w and T2w MRI contrasts, as well as the probabilistic white and gray matter atlases. Figure 6.4 shows axial views of the PAM50 template for T1w, T2w and T2*w MRI contrasts, along with information about the internal structure of the spinal cord.
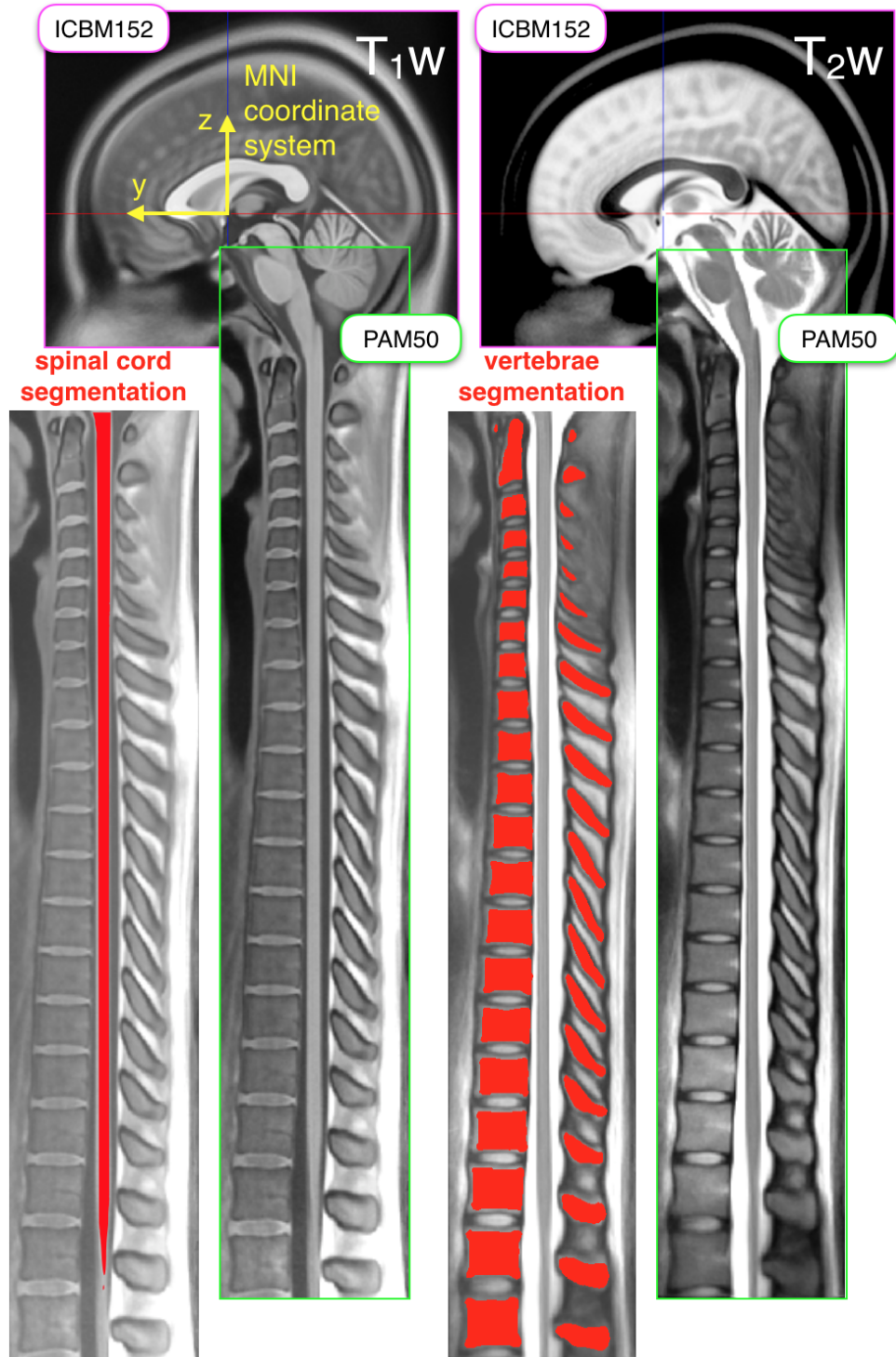
Figure 6.3: Sagittal views of the PAM50 template (T1w and T2w), which covers the brainstem and the full spinal cord (down to T12-L1, where the cauda equina starts), along with segmentation of the spinal cord and vertebrae. The PAM50 spinal cord template is registered with the ICBM152

"MNI" brain template at the level of the brainstem, so that both templates use the same referential coordinate system.
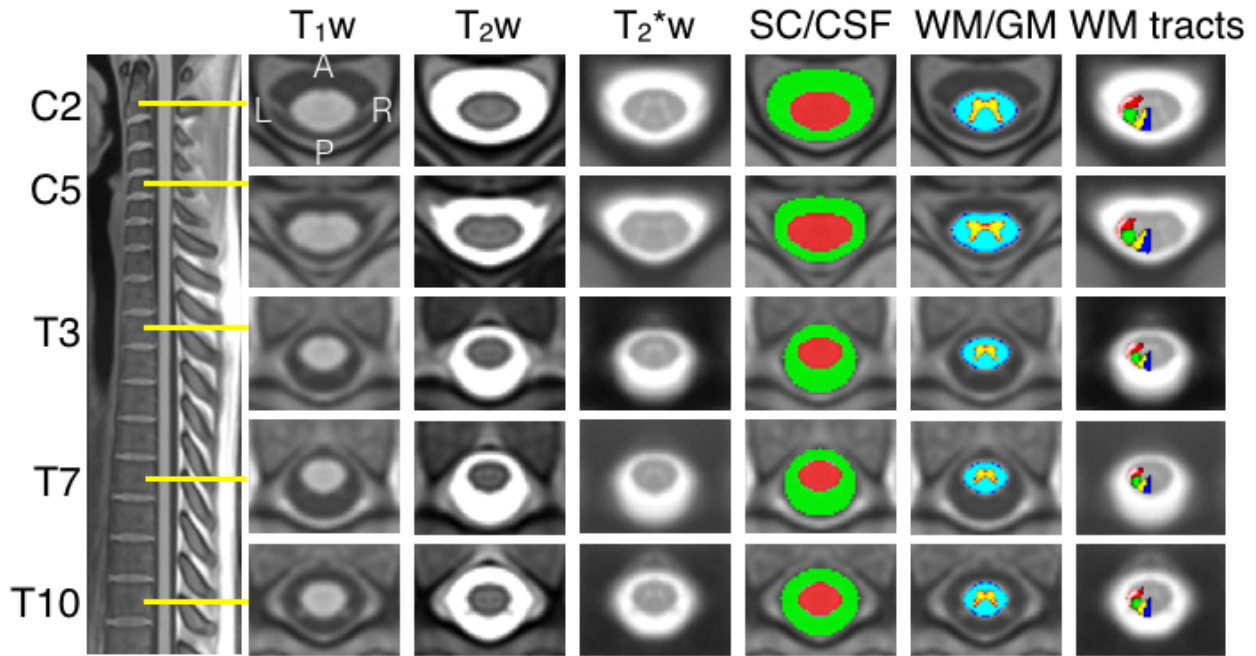
Figure 6.4: Axial view of the T1w, T2w and T2*w contrasts of the PAM50 spinal cord template, with spinal cord (red) and cerebrospinal fluid (green) segmentation, probabilistic maps of the white (light blue) and the gray (red-yellow) matter and probabilistic maps of the white matter pathways (red: spinal lemniscus, pink: spinocerebellar tract, green: cortico-spinal tract, yellow: cuneatus, blue: gracilis).

6.4.2 Registration accuracy

Figure 6.5 shows the mean and maximum distance errors associated with the registration between the centerline of each subject and the PAM50 template. The mean (std) distance error was 0.37 (0.06) mm for T1w and 0.11 (0.03) mm for T2w, and the maximum distance error was 1.39 (0.58) mm for T1w and 0.71 (0.27) mm for T2w images. The lower, but still subpixellar, accuracy for T1w images could be explained by lower contrast between the spinal cord and CSF, when compared to T2w images. These differences in SC/CSF contrast would induce small variability in the spinal cord segmentation, which would lead to lower accuracy when comparing centerlines. Visual evaluation of straightening and registration was satisfactory.
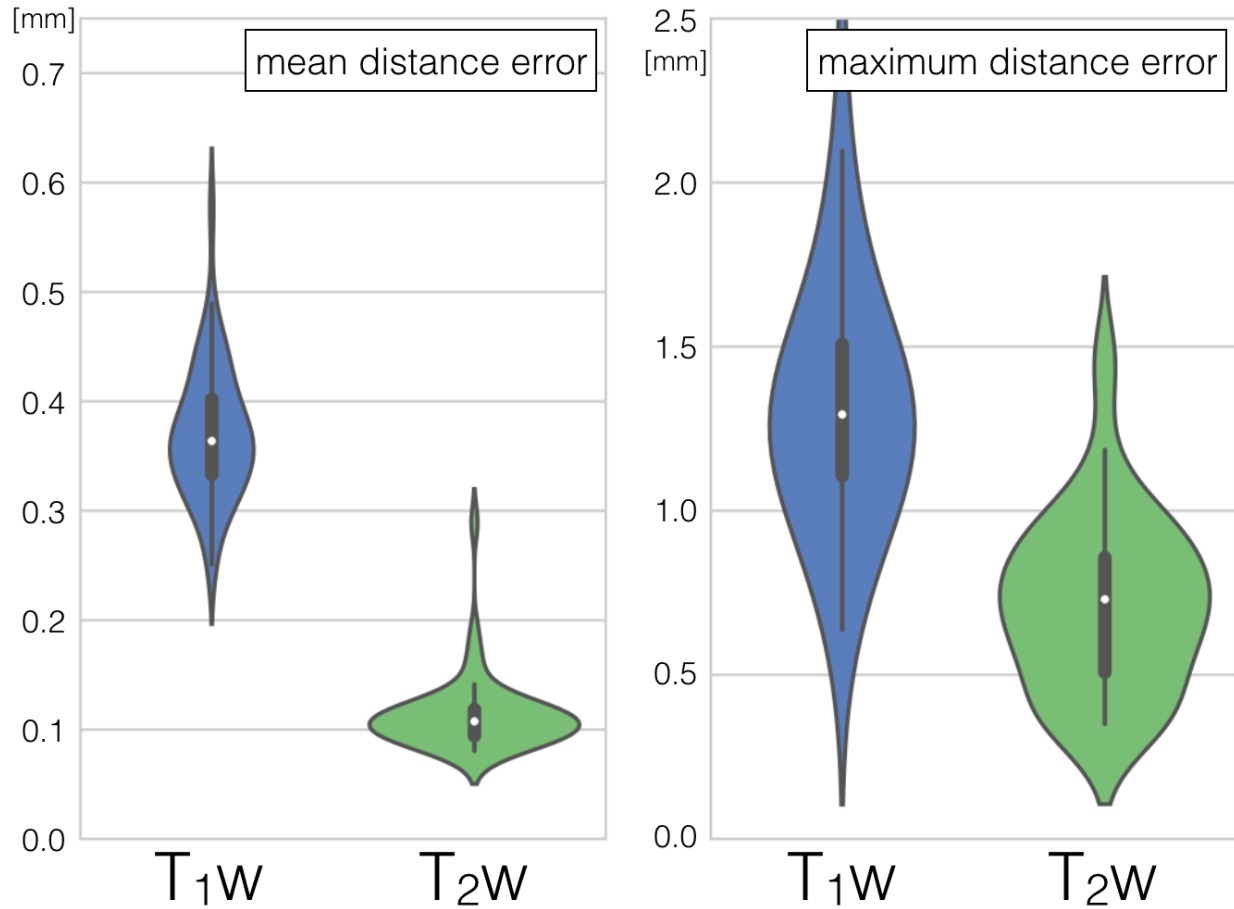
Figure 6.5: Accuracy of the registration process performed on each individual image to generate the PAM50 template, as represented by a kernel density estimation of the distribution (violin plots) of the mean and maximum distance error on spinal cord centerlines along with median values (white dots), quartiles (black boxes) and real distribution when removing outliers (black whiskers).

6.4.3 CSA preservation

FiguresFigure 6.6Figure 6.7 illustrate the spinal cord morphometrics of the population used in this study. Figure 6.6 shows the spinal cord CSA as a function of vertebral level. The top panel shows individual CSAs, highlighting the fairly large inter-subject variability, especially visible at the lumbar enlargement position (black bracket). This variability could partially be attributed to the fact that the CSA is displayed relative to the vertebral level (as opposed to the spinal level) while spinal cord enlargements are more specific to spinal levels. The bottom panel shows the averaged CSA in the native space and the CSA of the generated PAM50 template, exhibiting a fairly good

agreement, and hence suggesting that the straightening and registration processes preserved the overall volume of the spinal cord.
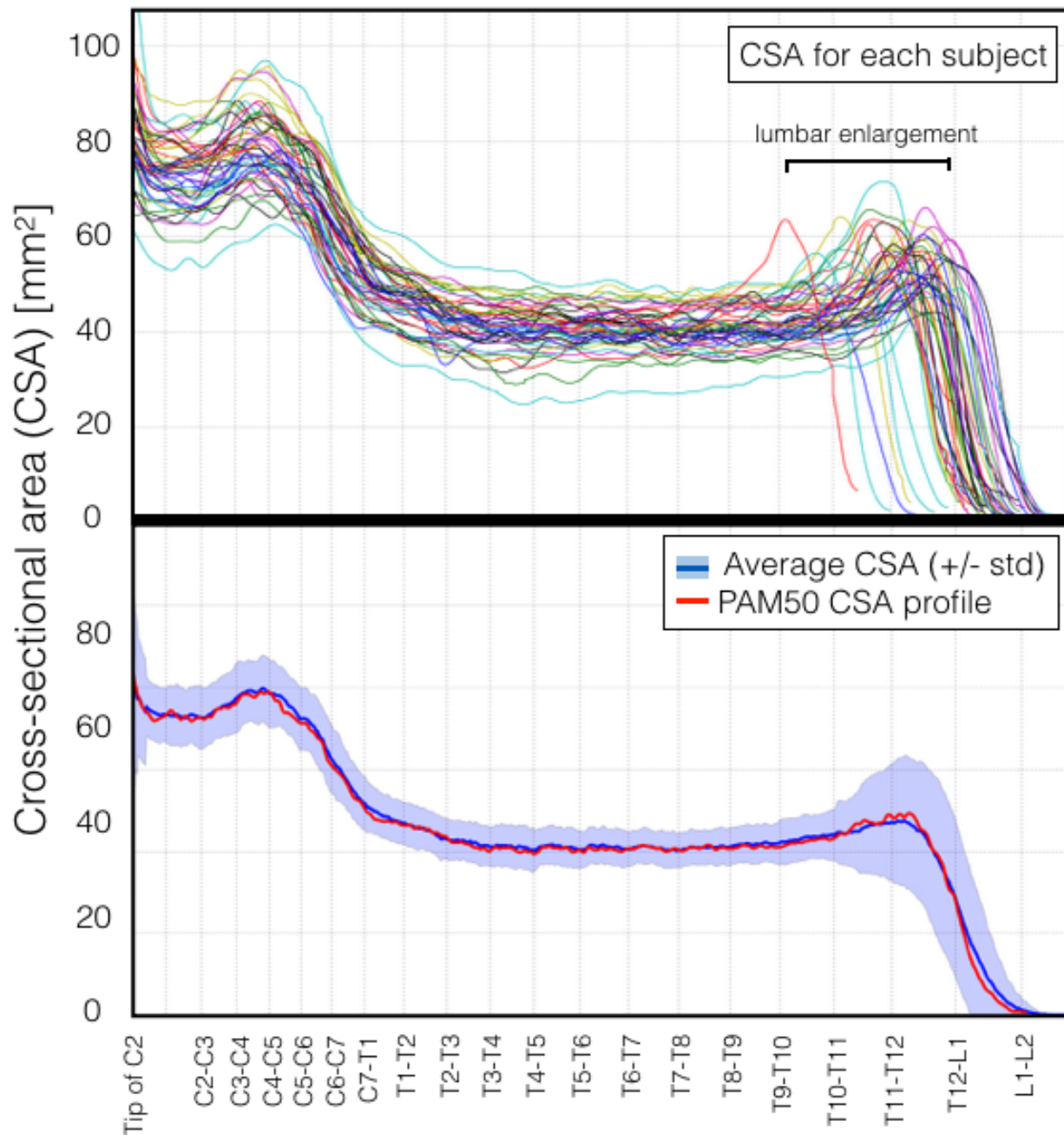
Figure 6.6: (top) Cross-sectional area of the spinal cord for each subject in the dataset as a function of vertebral level. (bottom) In blue, the cross-sectional area of the spinal cord averaged over the 50 subjects. In red, cross-sectional area of the PAM50 template, suggesting that the CSA was preserved between the native subject's space and the transformation to the PAM50 space.

Figure 6.7 shows the position of the intervertebral disks and spinal cord enlargements, relative to the position of the PMJ along the spinal cord. These relative positions are displayed as the mean and standard deviation across the 50 subjects.

Table 6.1 presents the numerical results of the distances (mean +/- std) between the PMJ and the intervertebral disks, as well as the averaged CSA (mean +/- std) of the spinal cord at the location of intervertebral disks. Table 6.1 also presents the same information (distances and CSA) for the cervical and lumbar enlargements.
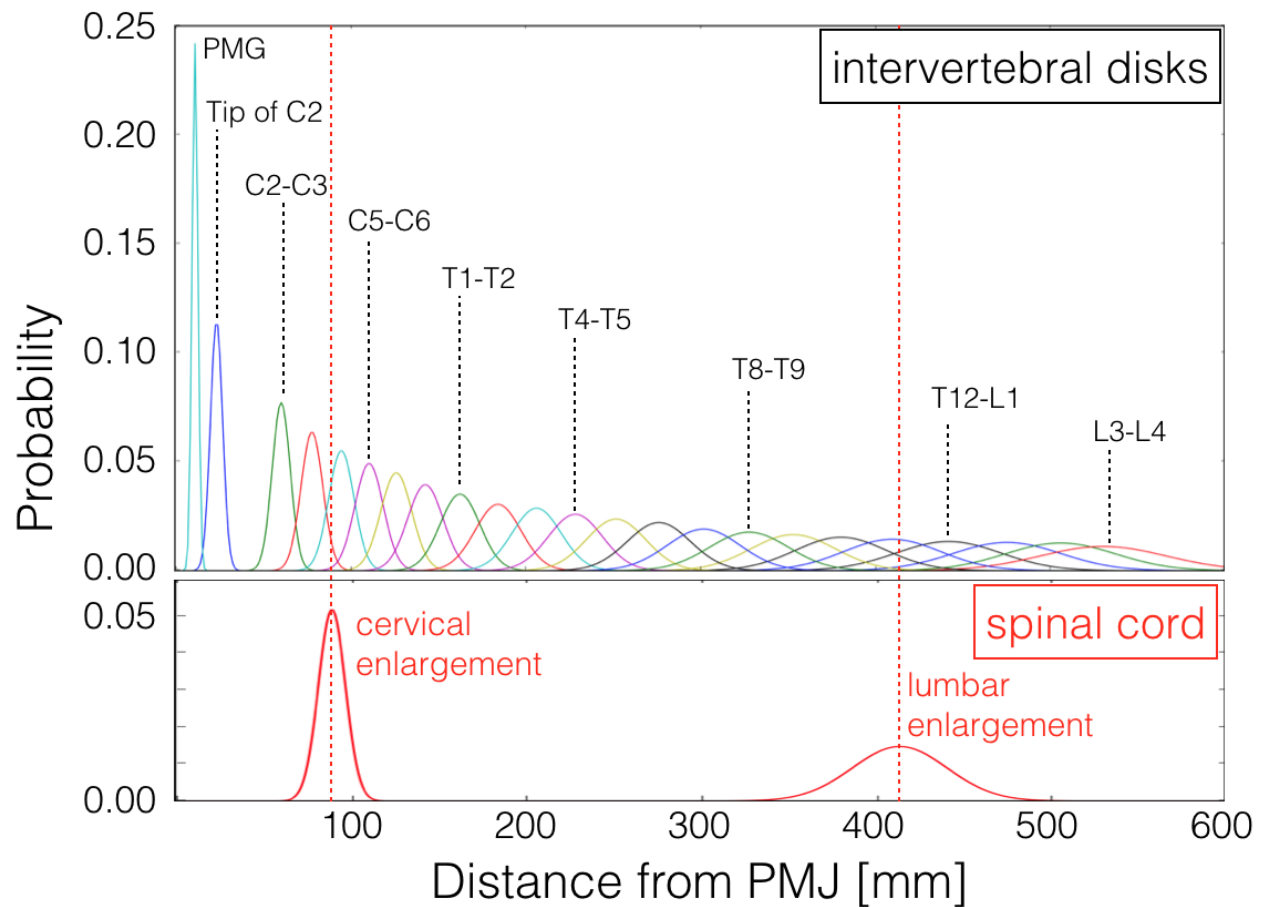
Figure 6.7: (top) Gaussian distribution of position of the Pontomedullary groove (PMG) and the intervertebral disks along the spinal cord depending on the distance (along the spinal cord axis), in millimeters, with respect to the Pontomedullary junction (PMJ), based on positions calculated from the 50 healthy subjects. (bottom) Gaussian distribution of position of the cervical and lumbar enlargements depending on the distance with the PMJ, in millimeters.

Table 6.1: Distance (mean +/- std) in millimeters from PMJ for each intervertebral disk and the spinal enlargements, as well as the CSA (mean +/- std) in mm^2 at the same positions.

	Distance from PMJ [mm] (mean +/- std)	CSA [mm^2] (mean +/- std)
Pontomedullary groove (PMG)	11.44 +/- 1.65	
Tip of C2	23.75 +/- 3.48	79.22 +/- 13.84
C1-C2	42.66 +/- 4.22	73.25 +/- 6.76
C2-C3	60.76 +/- 5.17	72.69 +/- 7.62
C3-C4	78.33 +/- 6.27	77.46 +/- 8.45
C4-C5	95.13 +/- 7.24	78.53 +/- 8.39
C5-C6	110.99 +/- 8.11	72.26 +/- 7.80
C6-C7	126.54 +/- 8.88	62.53 +/- 8.35
C7-T1	143.16 +/- 10.11	51.76 +/- 6.45
T1-T2	162.97 +/- 11.36	46.74 +/- 5.11
T2-T3	184.72 +/- 13.11	43.00 +/- 4.97
T3-T4	206.78 +/- 13.92	41.00 +/- 4.81
T4-T5	228.98 +/- 15.43	40.28 +/- 5.22
T5-T6	252.22 +/- 16.88	40.41 +/- 4.61
T6-T7	276.71 +/- 18.09	40.51 +/- 4.27
T7-T8	302.34 +/- 20.96	40.29 +/- 4.27
T8-T9	328.29 +/- 22.63	41.05 +/- 4.66
T9-T10	353.54 +/- 24.18	42.15 +/- 5.50
T10-T11	380.83 +/- 26.07	43.92 +/- 6.28
T11-T12	410.15 +/- 27.77	47.08 +/- 14.29
T12-L1	442.37 +/- 29.88	28.51 +/- 19.29
L1-L2	475.75 +/- 30.86	1.23 +/- 2.96
L2-L3	506.34 +/- 31.50	0.0 +/- 0.0
L3-L4	530.84 +/- 36.02	0.0 +/- 0.0

| Cervical enlargement | 89.70 +/- 5.74 | 80.63 +/- 8.10 |
| Lumbar enlargement | 414.66 +/- 17.55 | 56.53 +/- 6.29 |

The relation between spinal cord enlargements and intervertebral disks has been explored by comparing the relative position (distance from PMJ) of the cervical and lumbar enlargements and the relative position and their closest intervertebral disk, respectively C4-C5 and T11-T12. Figure 6.8 shows individual plots as well as Pearson's correlation coefficient results between the cervical enlargement and the C4-C5 intervertebral disk positions (r=0.18; p-value=0.20), and between the lumbar enlargement and T11-T12 intervertebral disk positions (r=0.12; p-value=0.40). Results show no significant relationship between the position of spinal enlargements and nearest intervertebral disks, thereby preventing the use of intervertebral disks to predict the position of spinal roots along the spinal cord.
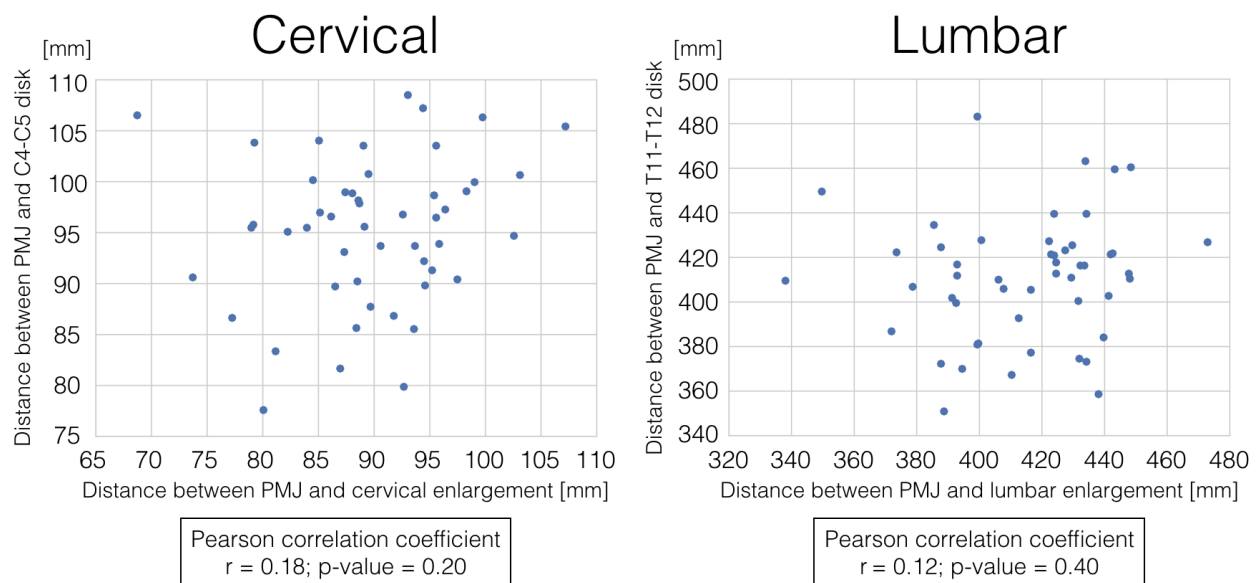
Figure 6.8: Relation between the cervical (left) and lumbar (right) enlargements position (from the PMJ) and the closest intervertebral disk position, respectively C4-C5 and T11-T12. Pearson's correlation coefficient (with associated p-values) are displayed at the bottom of each plot.

6.5 Discussion

This manuscript presented a method for generating the PAM50 template, a subject-unbiased and symmetrical average template of the brainstem and full spinal cord, available for T1w, T2w and T2*w MRI contrasts and including probabilistic atlases of the spinal cord white and gray matter. A notable feature is that the PAM50 template is aligned with the ICBM152 brain template, thereby introducing a common referential coordinate system, which represents the next step towards standardization and can notably facilitate studies featuring simultaneous brain, brainstem and spinal cord acquisitions. The following discussion addresses key features of the PAM50, its current limitations, how researchers can use our open-source code to produce other spinal cord templates, and lists a few example applications.

6.5.1 Subject-unbiased template

While previous studies have proposed methods for generating spinal cord MRI templates, some of them (Eippert et al., 2009; El Mendili, Chen, Tiret, Villard, et al., 2015; Valsasina et al., 2012) relied on the selection of a single subject as reference, thereby inducing a selection bias into the template creation process. The proposed framework addresses the subject-bias issue in two ways. First, an initial template space is created by averaging the spinal cord centerline and the intervertebral disks position over the whole population. While the brainstem curvature and length are matched with those from the ICBM152 brain template, the spinal cord centerline is straightened in the PAM50 space. All subjects are registered to the initial unbiased template space that serves as the initial iteration of the template generation process. Second, the template generation is performed using the iterative nonlinear averaging based on the ANIMAL framework (Collins et al., 1995; Fonov et al., 2009).

To demonstrate the preservation of the average spinal cord topology in the unbiased PAM50 template, we have averaged the CSA profile of each individual subject and compared it to the CSA profile of the PAM50 template (Figure 6.6). Additionally, we demonstrated the sub-millimeter accuracy of the registration procedure by computing the average and maximum distance of the spinal cord centerline of each subject to the centerline of the PAM50 (see Figure 6.5). For future use of the PAM50, registering new subjects to the PAM50 template using SCT involves the exact same procedure, thereby warranting similarly high accuracy.

6.5.2 Vertebral versus spinal level

In the current study, the PAM50 template has been normalized using vertebral levels. This choice has been driven by the radiological workflow, which commonly relies on vertebral levels as a reference for analyze spine data. While a reference based on spinal levels would be of interest, notably for functional MRI studies, it is more difficult to robustly identify these levels. First, it requires very high resolution (typically sub-millimeter) and appropriate contrast to identify nerve rootlets (e.g. heavily T2-weighted), and secondly, the fanning of the nerve rootlets makes it difficult to identify an exact location of spinal levels, especially when going caudally along the cord as the fanning increases (Cadotte et al., 2015). In the present study, we further explored the relationship between vertebral and spinal levels, assuming the latter are closely associated with the location of both cord enlargements. Results showed a poor association, with r=0.18 for the cervical enlargement and r=0.12 for the lumbar enlargement. However, a simple transformation of the image based on the position of the spinal cord enlargements relative to a reference point into the brain (e.g., PMJ) may enable an accurate estimation of the spinal segments position, as suggested by studies of CSA profiles over spinal segments (Frostell et al., 2016; Kameyama et al., 1996), while adjusting for patients' positioning into the scanner (Cadotte et al., 2015). This will be explored in future studies.

6.5.3 Population specific template

It is important to note that the PAM50 template was based on 50 healthy individuals (male/female: 29/21), with age ranging from 21 to 56 y.o. with an average of 27 +/- 6.5 and a median of 24 y.o. Therefore, the PAM50 template represents a population of young adults with a narrow range of age, which needs to be considered when applying it to other populations, such as pediatric and elderly populations, as it has been shown that the morphology of the spinal cord changes with age (Fradet et al., 2014; Kato, Yukawa, Suda, Yamagata, & Ueta, 2012). The same considerations apply to pathological populations. This limitation is, however, mitigated by the segmentation-based nonlinear registration procedure used to map a new subject on the PAM50 template, as implemented in SCT (De Leener, Lévy, et al., 2017), which deforms the cord so that its edges match that from the PAM50 template. Moreover, it is possible to account for the internal gray matter during the registration procedure (Dupont et al., 2017; Taso et al., 2015) as a way to further improve the quality of the registration in healthy and pathological cords.

6.5.4 Open-source scripts for generating spinal cord templates

The proposed framework for spinal cord template creation is freely available (https://github.com/neuropoly/template), and has been heavily simplified and documented so that only a few manual inputs are required from users. This will enable other researchers to create templates specific for their needs, e.g., for pediatric or diseased populations.

6.5.5 Applications for template-based analysis

Several groups have used the MNI-Poly-AMU template (Fonov et al., 2014) for studying spinal cord microstructure (Duval et al., 2017; Duval et al., 2015; Ljungberg et al., 2016; Massire et al., 2016), spinal cord function using resting-state fMRI (Eippert et al., 2017; Kong et al., 2014), pain (Weber 2nd et al., 2016a) and spinal cord laterality (Weber 2nd et al., 2016b) in healthy populations. Moreover, multiple studies have explored spinal cord pathologies using the MNI-Poly-AMU template, including adrenomyeloneuropathy (Castellano et al., 2016), spinal cord infections (Talbott et al., 2016), Acute Flaccid Myelitis (McCoy et al., 2017), Cervical Spondylotic Myelopathy (David, Freund, & Mohammadi, 2017; Grabher et al., 2016) and Degenerative Cervical Myelopathy (Martin et al., 2017; Martin et al., 2017b). These past studies suggest the potential for applications of the new PAM50 template, which is based on a larger population, includes more contrasts and covers the brainstem and the full spinal cord. Moreover, having the PAM50 now aligned with the ICBM152 MNI brain template provides a next step towards standardization and might facilitate studies featuring simultaneous acquisitions of the brain and spinal cord. One example of applications would be the integrated study of global atrophy in neurodegenerative diseases such as Multiple Sclerosis.

6.6 Conclusion

This study introduced the PAM50, a new MRI template of the brainstem and spinal cord. The PAM50 is available in T1w, T2w and T2*w MRI contrasts and includes atlases of the spinal cord internal structures such as gray/white matter regions and white matter pathways. The PAM50 template is also aligned with the ICBM152 brain template, providing a common coordinate system (the "MNI" reference) which could standardize spinal cord studies and facilitate studies involving simultaneous brain and spinal cord acquisitions. All scripts used to generate the PAM50 are made freely available, enabling other researchers to generate population-specific cord templates.

6.7 Acknowledgements

6.8 References

Abdel-Aziz, K., Solanky, B. S., Yiannakas, M. C., Altmann, D. R., Wheeler-Kingshott, C. A. M., Thompson, A. J., & Ciccarelli, O. (2014). Age related changes in metabolite concentrations in the normalspinal cord. *PLoS One*, *9*(10), e105774.

Agosta, F., Laganà, M., Valsasina, P., Sala, S., Dall'Occhio, L., Sormani, M. P., … Filippi, M. (2007). Evidence for cervical cord tissue disorganisation with agingby diffusion tensor MRI. *Neuroimage*, *36*(3), 728–735.

Altman, J., & Bayer, S. A. (2001). An overview of spinal cord organization. In *Development of the Human Spinal Cord: An Interpretation Based onExperimental Studies in Animals* (pp. 1–87). New York: Oxford University Press.

Archip, N., Erard, P.-J., Egmont-Petersen, M., Haefliger, J.-M., & Germond, J.-F. (2002). A Knowledge-Based Approach to Automatic Detection of the Spinal Cord in CT Images. *IEEE Transactions on Medical Imaging*, *21*(12), 1504–16. https://doi.org/10.1109/TMI.2002.806578

Asman, A. J., Bryan, F. W., Smith, S. A., Reich, D. S., & Landman, B. A. (2014). Groupwise multi-atlas segmentation of the spinal cord's internal structure. *Med. Image Anal.*, *18*(3), 460–471.

Aspert, N., Santa Cruz, D., & Ebrahimi, T. (2002). MESH: measuring errors between surfaces using the Hausdorffdistance. In *ICME (1)* (pp. 705–708). stage.nitrc.org.

Bakshi, R., Dandamudi, V. S. R., Neema, M., De, C., & Bermel, R. A. (2005). Measurement of brain and spinal cord atrophy by magneticresonance imaging as a tool to monitor multiple sclerosis. *J. Neuroimaging*, *15*(4 Suppl), 30S–45S.

Bastianello, S., Paolillo, A., Giugni, E., Giuliani, S., Evangelisti, G., Luccichenti, G., … Fieschi, C. (2000). MRI of spinal cord in MS. *J. Neurovirol.*, *6 Suppl 2*, S130–3.

Behrens, T., Rohr, K., & Stiehl, H. S. (2003). Robust segmentation of tubular structures in 3-D medicalimages by parametric object detection and tracking. *IEEE Trans. Syst. Man Cybern. B Cybern.*, *33*(4), 554–561.

Bergo, F. P. G., Franca, M. C., Chevis, C. F., & Cendes, F. (2012). {SpineSeg}: A segmentation and measurement tool for evaluation of spinal cord atrophy. In *Proceedings of the 7th Iberian Conference on Information Systems and Technologies, {CISTI}* (pp. 1–4). Madrid.

Bergo, F. P. G., França, M. C., Chevis, C. F., & Cendes, F. (2012). {SpineSeg}: A segmentation and measurement tool for evaluation of spinal cord atrophy. In *7th Iberian Conference on Information Systems and Technologies ({CISTI} 2012)* (pp. 1–4).

Boykov, Y., Veksler, O., & Zabih, R. (2001). Fast approximate energy minimization via graph cuts. *IEEE Trans. Pattern Anal. Mach. Intell.*, *23*(11), 1222–1239.

Brooks, B. R. (1994). El Escorial World Federation of Neurology criteria for thediagnosis of amyotrophic lateral sclerosis. Subcommittee onMotor Neuron Diseases/Amyotrophic Lateral Sclerosis of theWorld Federation of Neurology Research Group on NeuromuscularDiseases and the El Escorial ``Clinical limits of amyotrophiclateral sclerosis'' workshop contributors. *J. Neurol. Sci.*, *124 Suppl*, 96–107.

Brooks, B. R. (1996). Natural history of ALS: symptoms, strength, pulmonaryfunction, and disability. *Neurology*, *47*(4 Suppl 2), S71–81–2.

Brownell, B., Oppenheimer, D. R., & Hughes, J. T. (1970). The central nervous system in motor neurone disease. *J. Neurol. Neurosurg. Psychiatry*, *33*(3), 338–357.

Buades, A., Coll, B., & Morel, J. (2005). A Review of Image Denoising Algorithms, with a New One. *Multiscale Model. Simul.*, *4*(2), 490–530.

Cadotte, D. W., Cadotte, A., Cohen-Adad, J., Fleet, D., Livne, M., Wilson, J. R., … Fehlings, M. G. (2015). Characterizing the location of spinal and vertebral levels in the human cervical spinal cord. *AJNR Am. J. Neuroradiol.*, *36*(4), 803–810.

Cadotte, D. W., & Fehlings, M. G. (2014). Traumatic Spinal Cord Injury: Acute Spinal Cord Injury andPrognosis. In J. Cohen-Adad & C. Wheeler-Kingshott (Eds.), *Quantitative MRI of the Spinal Cord* (pp. 39–48). Elsevier.

Carbonell-Caballero, J., Manjón, J. V, Mart'\i-Bonmat'\i, L., Olalla, J. R., Casanova, B., la Iglesia-Vayá, M., … Robles, M. (2006). Accurate quantification methods to evaluate cervical cordatrophy in multiple sclerosis patients. *MAGMA*, *19*(5), 237–246.

Chen, M., Carass, A., Oh, J., Nair, G., Pham, D. L., Reich, D. S., & Prince, J. L. (2013). Automatic magnetic resonance spinal cord segmentation with topology constraints for variable fields of view. *Neuroimage*, *83*, 1051–1062.

Ciccarelli, O., Wheeler-Kingshott, C. A., McLean, M. A., Cercignani, M., Wimpey, K., Miller, D. H., & Thompson, A. J. (2007). Spinal cord spectroscopy and diffusion-based tractography toassess acute disability in multiple sclerosis. *Brain*, *130*(Pt 8), 2220–2231.

Cohen-Adad, J., Descoteaux, M., Rossignol, S., Hoge, R. D., Deriche, R., & Benali, H. (2008). Detection of multiple pathways in the spinal cord using q-ballimaging. *Neuroimage*, *42*(2), 739–749.

Cohen-Adad, J., El Mendili, M.-M., Lehéricy, S., Pradat, P.-F., Blancho, S., Rossignol, S., & Benali, H. (2011). Demyelination and degeneration in the injured human spinal cord detected with diffusion and magnetization transfer MRI. *NeuroImage*, *55*(3), 1024–33. https://doi.org/10.1016/j.neuroimage.2010.11.089

Cohen-Adad, J., El Mendili, M.-M., Morizot-Koutlidis, R., Lehéricy, S., Meininger, V., Blancho, S., … Pradat, P.-F. (2013). Involvement of spinal sensory pathway in ALS andspecificity of cord atrophy to lower motor neurondegeneration. *Amyotroph. Lateral Scler. Frontotemporal Degener.*, *14*(1), 30–38.

Cohen-Adad, J., Leblond, H., Delivet-Mongrain, H., Martinez, M., Benali, H., & Rossignol, S. (2011). Wallerian degeneration after spinal cord lesions in catsdetected with diffusion tensor imaging. *Neuroimage*, *57*(3), 1068–1076.

Cohen-Adad, J., Zhao, W., Keil, B., Ratai, E.-M., Triantafyllou, C., Lawson, R., … Atassi, N. (2013). {7-T} {MRI} of the spinal cord can detect lateral corticospinal tract abnormality in amyotrophic lateral sclerosis. *Muscle Nerve*, *47*(5), 760–762.

Coulon, O., Hickman, S. J., Parker, G. J., Barker, G. J., Miller, D. H., & Arridge, S. R. (2002). Quantification of spinal cord atrophy from magnetic resonance images via a B-spline active surface model. *Magnetic Resonance in Medicine : Official Journal of the Society of Magnetic Resonance in Medicine / Society of Magnetic Resonance in Medicine*, *47*(6), 1176–85. https://doi.org/10.1002/mrm.10162

Cruz-Sánchez, F. F., Moral, A., Tolosa, E., de Belleroche, J., & Rossi, M. L. (1998). Evaluation of neuronal loss, astrocytosis and abnormalities of cytoskeletal components of large motor neurons in the human anterior horn in aging. *J. Neural Transm.*, *105*(6–7), 689–701.

De Leener, B., Cohen-Adad, J., & Kadoury, S. (2015). Automatic Segmentation of the Spinal Cord and Spinal Canal Coupled with Vertebral Labeling. *IEEE Transactions on Medical Imaging*, *34*(8). https://doi.org/10.1109/TMI.2015.2437192

De Leener, B., Kadoury, S., & Cohen-Adad, J. (2014). Robust, accurate and fast automatic segmentation of the spinal cord. *NeuroImage*, *98*. https://doi.org/10.1016/j.neuroimage.2014.04.051

De Leener, B., Roux, A., Taso, M., Callot, V., & Cohen-Adad, J. (2015). Spinal cord gray and white matter segmentation using atlasdeformation. In *Proceedings of the 23th Annual Meeting of ISMRM, Toronto,Canada, Toronto* (Vol. 4424, p. 4424). Toronto.

Despotović, I., Goossens, B., & Philips, W. (2015). MRI segmentation of the human brain: challenges, methods,and applications. *Comput. Math. Methods Med.*, *2015*, 450341.

Dubuc, B. (2015). The brain from top to bottom.

El Mendili, M.-M., Chen, R., Tiret, B., Pélégrini-Issac, M., Cohen-Adad, J., Lehéricy, S., … Benali, H. (2015). Validation of a semiautomated spinal cord segmentationmethod. *J. Magn. Reson. Imaging*, *41*(2), 454–459.

El Mendili, M.-M., Chen, R., Tiret, B., Villard, N., Trunet, S., Pélégrini-Issac, M., … Benali, H. (2015). Fast and accurate semi-automated segmentation method of spinal cord {MR} images at {3T} applied to the construction of a cervical spinal cord template. *PLoS One*, *10*(3), e0122224.

Ellingson, B. M., Ulmer, J. L., & Schmit, B. D. (2007). Gray and white matter delineation in the human spinal cordusing diffusion tensor imaging and fuzzy logic. *Acad. Radiol.*, *14*(7), 847–858.

Ellingson, B. M., Ulmer, J. L., & Schmit, B. D. (2008). Morphology and morphometry of human chronic spinal cord injuryusing diffusion tensor imaging and fuzzy logic. *Ann. Biomed. Eng.*, *36*(2), 224–236.

Fonov, V. S., Le Troter, A., Taso, M., De Leener, B., Lévêque, G., Benhamou, M., … Cohen-Adad, J. (2014). Framework for integrated MRI average of the spinal cordwhite and gray matter: the MNI-Poly-AMU template. *Neuroimage*, *102 Pt 2*, 817–827.

Fradet, L., Arnoux, P.-J., Ranjeva, J.-P., Petit, Y., & Callot, V. (2014). Morphometrics of the entire human spinal cord and spinalcanal measured from in vivo high-resolution anatomicalmagnetic resonance imaging. *Spine*, *39*(4), E262–9.

Freund, P., Wheeler-Kingshott, C., Jackson, J., Miller, D., Thompson, A., & Ciccarelli, O. (2010). Recovery after spinal cord relapse in multiple sclerosis is predicted by radial diffusivity. *Mult. Scler.*, *16*(10), 1193–1202.

Fujimoto, K., Polimeni, J. R., van der Kouwe, A. J. W., Reuter, M., Kober, T., Benner, T., … Wald, L. L. (2014). Quantitative comparison of cortical surface reconstructionsfrom MP2RAGE and multi-echo MPRAGE data at 3 and 7 T. *Neuroimage*, *90*, 60–73.

Good, C. D., Johnsrude, I. S., Ashburner, J., Henson, R. N., Friston, K. J., & Frackowiak, R. S. (2001). A voxel-based morphometric study of ageing in 465 normal adulthuman brains. *Neuroimage*, *14*(1 Pt 1), 21–36.

Grady, L. (2006). Random walks for image segmentation. *IEEE Trans. Pattern Anal. Mach. Intell.*, *28*(11), 1768–1783.

Gullapalli, J., Krejza, J., & Schwartz, E. D. (2006). In vivo DTI evaluation of white matter tracts in rat spinalcord. *J. Magn. Reson. Imaging*, *24*(1), 231–234.

Held, P., Dorenbeck, U., Seitz, J., Fründ, R., & Albrich, H. (2003). MRI of the abnormal cervical spinal cord using 2D spoiledgradient echo multiecho sequence (MEDIC) with magnetizationtransfer saturation pulse. A T2* weighted feasibility study. *J. Neuroradiol.*, *30*(2), 83–90.

Held, P., Seitz, J., Fründ, R., Nitz, W., Lenhart, M., & Geissler, A. (2001). Comparison of two-dimensional gradient echo, turbo spin echoand two-dimensional turbo gradient spin echo sequences inMRI of the cervical spinal cord anatomy. *Eur. J. Radiol.*, *38*(1), 64–71.

Hickman, S. J., Hadjiprocopis, A., Coulon, O., Miller, D. H., & Barker, G. J. (2004). Cervical spinal cord {MTR} histogram analysis in multiple sclerosis using a {3D} acquisition and a B-spline active surface segmentation technique. *Magn. Reson. Imaging*, *22*(6), 891–895.

Horsfield, M. A., Sala, S., Neema, M., Absinta, M., Bakshi, A., Sormani, M. P., … Filippi, M. (2010). Rapid semi-automatic segmentation of the spinal cord frommagnetic resonance images: application in multiple sclerosis. *Neuroimage*, *50*(2), 446–455.

Ingle, G. T., Stevenson, V. L., Miller, D. H., & Thompson, A. J. (2003). Primary progressive multiple sclerosis: a 5-year clinical andMR study. *Brain*, *126*(Pt 11), 2528–2536.

Kalkers, N. F., Barkhof, F., Bergers, E., van Schijndel, R., & Polman, C. H. (2002). The effect of the neuroprotective agent riluzole on {MRI} parameters in primary progressive multiple sclerosis: a pilot study. *Mult. Scler.*, *8*(6), 532–533.

Kameyama, T., Hashizume, Y., & Sobue, G. (1996). Morphologic features of the normal human cadaveric spinalcord. *Spine*, *21*(11), 1285–1290.

Kawahara, J., McIntosh, C., Tam, R., & Hamarneh, G. (2013). Augmenting Auto-context with Global Geometric Features forSpinal Cord Segmentation. In *Machine Learning in Medical Imaging* (pp. 211–218). Nagoya, Japan: Springer, Cham.

Kawahara, J., McIntosh, C., Tam, R., & Hamarneh, G. (2013). Globally optimal spinal cord segmentation using a minimal path in high dimensions. In *2013 {IEEE} 10th International Symposium on Biomedical Imaging* (pp. 848–851). IEEE Computer Society.

Kayal, N. (2013). *An investigation of grow cut algorithm for segmentation of MRIspinal cord images in normals and patients with SCI*. Temple University Graduate School, Ann Arbor.

Kearney, H., Yiannakas, M. C., Abdel-Aziz, K., Wheeler-Kingshott, C. A. M., Altmann, D. R., Ciccarelli, O., & Miller, D. H. (2014). Improved MRI quantification of spinal cord atrophy inmultiple sclerosis. *J. Magn. Reson. Imaging*, *39*(3), 617–623.

Kidd, D., Thorpe, J. W., Thompson, A. J., Kendall, B. E., Moseley, I. F., MacManus, D. G., … Miller, D. H. (1993). Spinal cord MRI using multi-array coils and fast spin echo.II. Findings in multiple sclerosis. *Neurology*, *43*(12), 2632–2637.

Klawiter, E. C., Schmidt, R. E., Trinkaus, K., Liang, H.-F., Budde, M. D., Naismith, R. T., … Benzinger, T. L. (2011). Radial diffusivity predicts demyelination in ex vivo multiple sclerosis spinal cords. *Neuroimage*, *55*(4), 1454–1460.

Klein, J. P., Arora, A., Neema, M., Healy, B. C., Tauhid, S., Goldberg-Zimring, D., … Bakshi, R. (2011). A {3T} {MR} imaging investigation of the topography of whole spinal cord atrophy in multiple sclerosis. *AJNR Am. J. Neuroradiol.*, *32*(6), 1138–1142.

Koh, J., Kim, T., Chaudhary, V., & Dhillon, G. (2010). Automatic segmentation of the spinal cord and the dural sac in lumbar {MR} images using gradient vector flow field. In *2010 Annual International Conference of the {IEEE} Engineering in Medicine and Biology* (pp. 3117–3120). Buenos Aires: IEEE.

Koh, J., Scott, P. D., Chaudhary, V., & Dhillon, G. (2011). An automatic segmentation method of the spinal canal from clinical {MR} images based on an attention model and an active contour model. In *2011 {IEEE} International Symposium on Biomedical Imaging: From Nano to Macro* (pp. 1467–1471). ieeexplore.ieee.org.

Kurtzke, J. F. (1983). Rating neurologic impairment in multiple sclerosis: an expandeddisability status scale (EDSS). *Neurology*, *33*(11), 1444–1452.

Law, M. W. K., Garvin, G. J., Tummala, S., Tay, K., Leung, A. E., & Li, S. (2013). Gradient competition anisotropy for centerline extraction andsegmentation of spinal cords. *Inf. Process. Med. Imaging*, *23*, 49–61.

Lévy, S., Benhamou, M., Naaman, C., Rainville, P., Callot, V., & Cohen-Adad, J. (2015). White matter atlas of the human spinal cord with estimation ofpartial volume effect. *Neuroimage*, *119*(0), 262–271.

Lin, X., Blumhardt, L. D., & Constantinescu, C. S. (2003). The relationship of brain and cervical cord volume todisability in clinical subtypes of multiple sclerosis: athree-dimensional MRI study. *Acta Neurol. Scand.*, *108*(6), 401–406.

Lindberg, P. G., Feydy, A., & Maier, M. A. (2010). White matter organization in cervical spinal cord relates differently to age and control of grip force in healthy subjects. *J. Neurosci.*, *30*(11), 4102–4109.

Liu, C., Edwards, S., Gong, Q., Roberts, N., & Blumhardt, L. D. (1999). Three dimensional MRI estimates of brain and spinal cordatrophy in multiple sclerosis. *J. Neurol. Neurosurg. Psychiatry*, *66*(3), 323–330.

Liu, Y., Wang, J., Daams, M., Weiler, F., Hahn, H. K., Duan, Y., … Barkhof, F. (2015). Differential patterns of spinal cord and brain atrophy inNMO and MS. *Neurology*, *84*(14), 1465–1472.

Losseff, N. A., Webb, S. L., O'Riordan, J. I., Page, R., Wang, L., Barker, G. J., … Thompson, A. J. (1996). Spinal cord atrophy and disability in multiple sclerosis. Anew reproducible and sensitive MRI method with potential tomonitor disease progression. *Brain*, *119 (Pt 3)*(3), 701–708.

Lucas, B. C., Bogovic, J. A., Carass, A., Bazin, P.-L., Prince, J. L., Pham, D. L., & Landman, B. A. (2010). The Java Image Science Toolkit ({JIST}) for rapid prototyping and publishing of neuroimaging software. *Neuroinformatics*, *8*(1), 5–17.

Lundell, H., Barthelemy, D., Skimminge, A., Dyrby, T. B., Biering-Sørensen, F., & Nielsen, J. B. (2011). Independent spinal cord atrophy measures correlate to motorand sensory deficits in individuals with spinal cord injury. *Spinal Cord*, *49*(1), 70–75.

MacMillan, E. L., Mädler, B., Fichtner, N., Dvorak, M. F., Li, D. K. B., Curt, A., & MacKay, A. L. (2011). Myelin water and T(2) relaxation measurements in the healthycervical spinal cord at 3.0T: repeatability and changes withage. *Neuroimage*, *54*(2), 1083–1090.

Marques, J. P., Kober, T., Krueger, G., der Zwaag, W., de Moortele, P.-F. cois, & Gruetter, R. (2010). MP2RAGE, a self bias-field corrected sequence for improvedsegmentation and T1-mapping at high field. *Neuroimage*, *49*(2), 1271–1281.

McDonald, W. I., Compston, A., Edan, G., Goodkin, D., Hartung, H. P., Lublin, F. D., … Wolinsky, J. S. (2001). Recommended diagnostic criteria for multiple sclerosis:guidelines from the International Panel on the diagnosis ofmultiple sclerosis. *Ann. Neurol.*, *50*(1), 121–127.

McIntosh, C., & Hamarneh, G. (2006). Spinal crawlers: deformable organisms for spinal cord segmentation and analysis. *Medical Image Computing and Computer-Assisted Intervention :*

MICCAI ... International Conference on Medical Image Computing and Computer-Assisted Intervention, *9*(Pt 1), 808–15. Retrieved from http://www.ncbi.nlm.nih.gov/pubmed/17354965

McIntosh, C., Hamarneh, G., Toom, M., & Tam, R. C. (2011). Spinal Cord Segmentation for Volume Estimation in Healthy and Multiple Sclerosis Subjects Using Crawlers and Minimal Paths. In *2011 {IEEE} First International Conference on Healthcare Informatics, Imaging and Systems Biology* (pp. 25–31). ieeexplore.ieee.org.

Miyanji, F., Furlan, J. C., Aarabi, B., Arnold, P. M., & Fehlings, M. G. (2007). Acute cervical traumatic spinal cord injury: MR imagingfindings correlated with neurologic outcome–prospective studywith 100 consecutive patients. *Radiology*, *243*(3), 820–827.

Mukherjee, D. P., Cheng, I., Ray, N., Mushahwar, V., Lebel, M., & Basu, A. (2010). Automatic segmentation of spinal cord MRI using symmetricboundary tracing. *IEEE Trans. Inf. Technol. Biomed.*, *14*(5), 1275–1278.

Nakamura, M., Miyazawa, I., Fujihara, K., Nakashima, I., Misu, T., Watanabe, S., … Itoyama, Y. (2008). Preferential spinal central gray matter involvement inneuromyelitis optica. An MRI study. *J. Neurol.*, *255*(2), 163–170.

Narayana, P. A., Grill, R. J., Chacko, T., & Vang, R. (2004). Endogenous recovery of injured spinal cord: longitudinal in vivo magnetic resonance imaging. *J. Neurosci. Res.*, *78*(5), 749–759.

Onu, M., Gervai, P., Cohen-Adad, J., Lawrence, J., Kornelsen, J., Tomanek, B., & Sboto-Frankenstein, U. N. (2010). Human cervical spinal cord funiculi: investigation withmagnetic resonance diffusion tensor imaging. *J. Magn. Reson. Imaging*, *31*(4), 829–837.

Papinutto, N., Schlaeger, R., Panara, V., Zhu, A. H., Caverzasi, E., Stern, W. A., … G. (2015). Age, gender and normalization covariates for spinal cord graymatter and total cross-sectional areas at cervical andthoracic levels: A 2D phase sensitive inversion recoveryimaging study. *PLoS One*, *10*(3), e0118576.

Peters, A. M., Brookes, M. J., Hoogenraad, F. G., Gowland, P. A., Francis, S. T., Morris, P. G., & Bowtell, R. (2007). T2* measurements in human brain at 1.5, 3 and 7 T. *Magn. Reson. Imaging*, *25*(6), 748–753.

Pezold, S., Amann, M., Weier, K., Fundana, K., Radue, E. W., Sprenger, T., & Cattin, P. C. (2014). A semi-automatic method for the quantification of spinal cordatrophy. In *Computational Methods and Clinical Applications for SpineImaging* (pp. 143–155). Springer International Publishing.

Pezold, S., Fundana, K., Amann, M., Andelova, M., Pfister, A., Sprenger, T., & Cattin, P. C. (2015). Automatic Segmentation of the Spinal Cord Using Continuous MaxFlow with Cross-sectional Similarity Prior and TubularityFeatures. In J. Yao, B. Glocker, T. Klinder, & S. Li (Eds.), *Recent Advances in Computational Methods and ClinicalApplications for Spine Imaging* (Vol. 20, pp. 107–118). Springer International Publishing.

Qian, W., Chan, Q., Mak, H., Zhang, Z., Anthony, M.-P., Yau, K. K.-W., … Kim, M. (2011). Quantitative assessment of the cervical spinal cord damage inneuromyelitis optica using diffusion tensor imaging at 3 Tesla. *J. Magn. Reson. Imaging*, *33*(6), 1312–1320.

Rossignol, S., Martinez, M., Escalona, M., Kundu, A., Delivet-Mongrain, H., Alluin, O., & Gossard, J.-P. (2015). The ``beneficial'' effects of locomotor training after varioustypes of spinal lesions in cats and rats. *Prog. Brain Res.*, *218*, 173–198.

Samson, R. S., Ciccarelli, O., & others. (2013). Tissue-and column-specific measurements from multi-parameter mapping of the human cervical spinal cord at 3 {T}. *NMR Biomed.*, *26*, 1823–1830.

Schlaeger, R., Papinutto, N., Panara, V., Bevan, C., Lobach, I. V, Bucci, M., … Henry, R. G. (2014). Spinal cord gray matter atrophy correlates with multiple sclerosis disability. *Ann. Neurol.*, *76*(4), 568–580.

Sdika, M., Callot, V., Hebert, M., Duhamel, G., & Cozzone, P. J. (2010). Segmentation of the structure of the mouse spinal cord on DTIimages. In *Proceedings of the 19th scientific meeting, internationalsociety for magnetic resonance in medicine, ISMRM, Stockholm* (Vol. 5092, p. 5092). Stockholm.

Shefner, J. M., Watson, M. L., Simionescu, L., Caress, J. B., Burns, T. M., Maragakis, N. J., … Rutkove, S. B. (2011). Multipoint incremental motor unit number estimation as an outcome measure in {ALS}. *Neurology*, *77*(3), 235–241.

Sigmund, E. E., Suero, G. A., Hu, C., McGorty, K., Sodickson, D. K., Wiggins, G. C., & Helpern, J. A. (2012). High-resolution human cervical spinal cord imaging at 7 {T}. *NMR Biomed.*, *25*(7), 891–899.

Sled, J. G., Zijdenbos, A. P., & Evans, A. C. (1998). A nonparametric method for automatic correction of intensitynonuniformity in MRI data. *IEEE Trans. Med. Imaging*, *17*(1), 87–97.

Smith, S. A., Edden, R. A. E., Farrell, J. A. D., Barker, P. B., & Van Zijl, P. C. M. (2008). Measurement of {T1} and {T2} in the cervical spinal cord at 3 tesla. *Magn. Reson. Med.*, *60*(1), 213–219.

Smith, S. A., Jones, C. K., Gifford, A., Belegu, V., Chodkowski, B., Farrell, J. A. D., … van Zijl, P. C. M. (2010). Reproducibility of tract-specific magnetization transfer and diffusion tensor imaging in the cervical spinal cord at 3 tesla. *NMR Biomed.*, *23*(2), 207–217.

Sonkova, P., Evangelou, I. E., Gallo, A., Cantor, F. K., Ohayon, J., McFarland, H. F., & Bagnato, F. (2008). Semi-automatic segmentation and modeling of the cervical spinalcord for volume quantification in multiple sclerosis patientsfrom magnetic resonance images. In J. M. Reinhardt & J. P. W. Pluim (Eds.), *Medical Imaging* (Vol. 6914, p. 69144I–69144I–10). International Society for Optics and Photonics.

Stevenson, V. L., Leary, S. M., Losseff, N. A., Parker, G. J., Barker, G. J., Husmani, Y., … Thompson, A. J. (1998). Spinal cord atrophy and disability in {MS}: a longitudinal study. *Neurology*, *51*(1), 234–238.

Stroman, P. W. (2009). Spinal fMRI investigation of human spinal cord function overa range of innocuous thermal sensory stimuli and study-relatedemotional influences. *Magn. Reson. Imaging*, *27*(10), 1333–1346.

Stroman, P. W., Figley, C. R., & Cahill, C. M. (2008). Spatial normalization, bulk motion correction andcoregistration for functional magnetic resonance imaging ofthe human cervical spinal cord and brainstem. *Magn. Reson. Imaging*, *26*(6), 809–814.

Stroman, P. W., Tomanek, B., Krause, V., Frankenstein, U. N., & Malisza, K. L. (2002). Mapping of neuronal function in the healthy and injured humanspinal cord with spinal fMRI. *Neuroimage*, *17*(4), 1854–1860.

Stroman, P. W., Wheeler-Kingshott, C., Bacon, M., Schwab, J. M., Bosma, R., Brooks, J., … Tracey, I. (2014). The current state-of-the-art of spinal cord imaging: methods. *Neuroimage*, *84*, 1070–1081.

Tang, L., Wen, Y., Zhou, Z., von Deneen, K. M., Huang, D., & Ma, L. (2013). Reduced field-of-view DTI segmentation of cervical spinetissue. *Magn. Reson. Imaging*, *31*(9), 1507–1514.

Taso, M., Girard, O., Duhamel, G., Le Troter, A., Feiweier, T., Guye, M., … Callot, V. (2015). Regional and age-related variations of the healthy spinal cordstructure assessed by multimodal MRI. In *Proceedings of the 23th annual meeting of ISMRM, Toronto,Canada* (Vol. 681, p. 681). Toronto, Canada.

Taso, M., Le Troter, A., Sdika, M., Cohen-Adad, J., Arnoux, P.-J., Guye, M., … Callot, V. (2015). A reliable spatially normalized template of the human spinal cord--Applications to automated white matter/gray matter segmentation and tensor-based morphometry ({TBM}) mapping of gray matter alterations occurring with age. *Neuroimage*, *117*, 20–28.

Taso, M., Le Troter, A., Sdika, M., Ranjeva, J.-P., Guye, M., Bernard, M., & Callot, V. (2014). Construction of an in vivo human spinal cord atlas based onhigh-resolution MR images at cervical and thoracic levels:preliminary results. *MAGMA*, *27*(3), 257–267.

Tator, C. H., & Fehlings, M. G. (1991). Review of the secondary injury theory of acute spinal cordtrauma with emphasis on vascular mechanisms. *J. Neurosurg.*, *75*(1), 15–26.

Tench, C. R., Morgan, P. S., & Constantinescu, C. S. (2005). Measurement of cervical spinal cord cross-sectional area byMRI using edge detection and partial volume correction. *J. Magn. Reson. Imaging*, *21*(3), 197–203.

Udupa, J. K., & Samarasekera, S. (1996). Fuzzy Connectedness and Object Definition: Theory, Algorithms,and Applications in Image Segmentation. *Graphical Models and Image Processing*, *58*(3), 246–261.

Ullmann, E., Pelletier Paquette, J. F., Thong, W. E., & Cohen-Adad, J. (2014). Automatic labeling of vertebral levels using a robust template-based approach. *Int. J. Biomed. Imaging*, *2014*, 719520.

Valsasina, P., Horsfield, M. A., Rocca, M. A., Absinta, M., Comi, G., & Filippi, M. (2012). Spatial normalization and regional assessment of cordatrophy: voxel-based analysis of cervical cord 3DT1-weighted images. *AJNR Am. J. Neuroradiol.*, *33*(11), 2195–2200.

Van Uitert, R., Bitter, I., & Butman, J. A. (2005). Semi-automatic spinal cord segmentation and quantification. *Int. Congr. Ser.*, *1281*(0), 224–229.

Varma, G., Duhamel, G., de Bazelaire, C., & Alsop, D. C. (2015). Magnetization transfer from inhomogeneously broadened lines: Apotential marker for myelin. *Magn. Reson. Med.*, *73*(2), 614–622.

Wang, Y., Wu, A., Chen, X., Zhang, L., Lin, Y., Sun, S., … Lu, Z. (2014). Comparison of clinical characteristics between neuromyelitisoptica spectrum disorders with and without spinal cord atrophy. *BMC Neurol.*, *14*, 246.

Warfield, S. K., Zou, K. H., & Wells, W. M. (2004). Simultaneous truth and performance level estimation ({STAPLE)}: an algorithm for the validation of image segmentation. *IEEE Trans. Med. Imaging*, *23*(7), 903–921.

Weiler, F., Daams, M., Lukas, C., Barkhof, F., & Hahn, H. K. (2015). Highly accurate volumetry of the spinal cord. In *SPIE Medical Imaging* (Vol. 9413, pp. 941302–941302–6). Orlando, Florida: International Society for Optics and Photonics.

Wheeler-Kingshott, C. A., Stroman, P. W., Schwab, J. M., Bacon, M., Bosma, R., Brooks, J., … Tracey, I. (2014). The current state-of-the-art of spinal cord imaging: applications. *Neuroimage*, *84*, 1082–1093.

Wingerchuk, D. M., Hogancamp, W. F., O'Brien, P. C., & Weinshenker, B. G. (1999). The clinical course of neuromyelitis optica (Devic's syndrome). *Neurology*, *53*(5), 1107–1114.

Xu, J., Shimony, J. S., Klawiter, E. C., Snyder, A. Z., Trinkaus, K., Naismith, R. T., … Song, S.-K. (2013). Improved in vivo diffusion tensor imaging of human cervicalspinal cord. *Neuroimage*, *67*, 64–76.

Yen, C., Su, H.-R., Lai, S.-H., Liu, K.-C., & Lee, R.-R. (2013). 3D Spinal Cord and Nerves Segmentation from STIR-MRI. In *Proceedings of the International Computer Symposium ICS 2012* (pp. 383–392). Hualien, Taiwan.

Yiannakas, M. C., Kearney, H., Samson, R. S., Chard, D. T., Ciccarelli, O., Miller, D. H., & Wheeler-Kingshott, C. A. M. (2012). Feasibility of grey matter and white matter segmentation ofthe upper cervical cord in vivo: a pilot study withapplication to magnetisation transfer measurements. *Neuroimage*, *63*(3), 1054–1059.

Yiannakas, M. C., Mustafa, A. M., De Leener, B., Kearney, H., Tur, C., Altmann, D. R., … Gandini Wheeler-Kingshott, C. A. M. (2016). Fully automated segmentation of the cervical cord from T1-weighted MRI using PropSeg: Application to multiple sclerosis. *NeuroImage: Clinical*, *10*. https://doi.org/10.1016/j.nicl.2015.11.001

Zackowski, K. M., Smith, S. A., Reich, D. S., Gordon-Lipkin, E., Chodkowski, B. A., Sambandan, D. R., … Calabresi, P. A. (2009). Sensorimotor dysfunction in multiple sclerosis and column-specific magnetization transfer-imaging abnormalities in the spinal cord. *Brain*, *132*(Pt 5), 1200–1209.

Zhang, Y., Brady, M., & Smith, S. (2001). Segmentation of brain MR images through a hidden Markovrandom field model and the expectation-maximization algorithm. *IEEE Trans. Med. Imaging*, *20*(1), 45–57.

Zivadinov, R., Banas, A. C., Yella, V., Abdelrahman, N., Weinstock-Guttman, B., & Dwyer, M. G. (2008). Comparison of three different methods for measurement ofcervical cord atrophy in multiple sclerosis. *AJNR Am. J. Neuroradiol.*, *29*(2), 319–325.

CHAPTER 7   TRANSLATING SPINAL CORD MRI PROCESSING TOOLS TO CLINICAL APPLICATIONS

This chapter introduces complementary results to the main developments of this project. First, a reproducibility and repeatability study of CSA measures performed with SCT on a MS population is presented, as part of an oral presentation to an international conference (ISMRM 2017). Second, a novel MRI biomarker of spinal cord white matter injury, based on the ratio between the white and gray matter intensity in T2*-weighted images, is introduced, as part of a collaboration with A. R. Martin, from University of Toronto. Finally, developments on shape morphometrics of the spinal cord are introduced, also as part of a collaboration with A. R. Martin.

7.1 Validation of CSA measurements on a MS population

This study has been submitted to the 25th Annual Meeting of the International Society for Magnetic Resonance in Medicine (ISMRM) as the abstract titled "*Repeatability and reproducibility of spinal cord atrophy measurements in a multiple sclerosis population using the Spinal Cord Toolbox*" (De Leener, Granberg, et al., 2017). I contributed to 80% of the design of the study, 100% of the analysis of data and 100% of the redaction process of the conference abstract and presentation.

Spinal cord atrophy is a major determinant of physical disability in MS and other diseases with neurodegeneration and the spinal cord CSA, calculated over the C1-C2 vertebral levels, is a good biomarker for spinal cord atrophy in multiple sclerosis (MS) (Rocca et al., 2011). However, measuring spinal cord CSA with high reproducibility and repeatability may be hindered by the high variability in image quality across MRI systems. As presented in Chapter 4, SCT enables semi- and fully-automatic measurements of spinal cord CSA by using automatic spinal cord detection and segmentation (De Leener et al., 2014). The main objective of this study is to assess the repeatability and reproducibility of semi-automatic cervical spinal cord cross-sectional area (CSA) measurements using SCT (De Leener, Lévy, et al., 2017) on patients with MS, scanned twice on three clinical MRI scanners on the same day.

7.1.1 Materials and Methods

Study participants: 9 patients with MS (6 females; age 38±13 years) were recruited for the study. Patients were diagnosed according to the latest diagnostic MS criteria (Polman et al., 2011), and

represented all subtypes: 6 relapsing-remitting MS, 2 secondary progressive and 1 primary progressive MS (Lublin et al., 2014) . Their disease duration was 7.3 ± 5.2 years and their median Expanded Disability Status Scale score was 2.0 (range 1.0-5.5). The study was approved by the regional ethics review board and written informed consent was obtained from all participants.

Image acquisition: Each subject was scanned twice with repositioning in three clinical MRI scanners (Siemens Aera and Avanto 1.5T and Trio 3.0T) on the same day with a 3D T1-weighted sequence (magnetization-prepared rapid gradient-echo) covering the brain and upper cervical spinal cord. Imaging parameters were: axial acquisition, 160 slices, 1.5 mm slice thickness, 1.0x1.0 mm in-plane resolution. Aera/Avanto/Trio parameters: flip angle 15/15/9°; echo time 3.02/3.55/3.39 ms; repetition time 1900 ms for all; inversion time 1100/1100/900 ms; bandwidth 160/130/250 Hz/voxel.

Image processing: All images were analyzed using SCT v3.0 using the following processes (Figure 7.1): (i) automatic spinal cord segmentation, (ii) semi-automatic vertebral labeling and (iii) cross-sectional area (CSA) measurements averaged over the C1-C2 vertebral levels. Additionally, manual segmentation and manual vertebral labeling were performed by a trained expert.
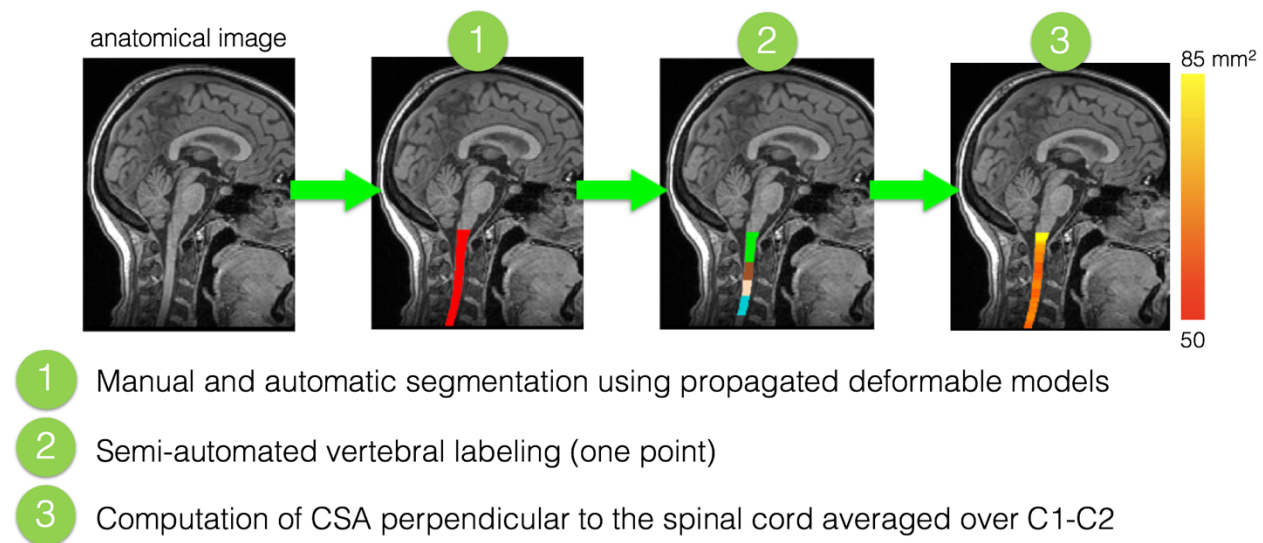
Figure 7.1: Image processing steps applied to all images required to extract CSA along the spinal cord, including segmentation, vertebral labeling and CSA calculation over C1-C2 vertebral level.

Statistical analysis: The coefficient of repeatability (same scanner), the coefficient of reproducibility (across scanners) and the intra-class correlation coefficients (ICC) were computed

as recommended by the Quantitative Imaging Biomarkers Alliance (FMRI Biomarker Committee, 2013) . The repeatability and reproducibility coefficients are defined as the value under which the difference between any two CSA measurements on the same patient should fall within 95% confidence. ICC is defined as the proportion of total variation in CSA measurements explained by between-patient differences rather than variation for the same patients. Additionally, the Minimal Detectable Change, defined as the minimal difference between two measures that would reflect a "true" difference (i.e., not completely due to measurement errors), was calculated for reproducibility measurements.

7.1.2 Results

CSA measurements extracted with manual and automatic spinal cord segmentations are presented in Figure 7.2, along with Dice coefficients between manual and automatic segmentations. These results show the fairly good correspondence between the measurements performed with different scanners. One can also appreciate the high correlation between CSA measures performed automatically when compared to measures performed manually.

Figure 7.3 and Figure 7.4 present statistical results performed on CSA measurements. Particularly, Figure 7.3 show the higher repeatability of CSA measurements performed automatically while ICCs are similar when comparing manual and automatic measurements. These results suggest that CSA measures are relatively repeatable across MRI scanners but that the variability within measures can be explained at ~55% by between-patient differences. Reproducibility coefficients on Figure 7.4 demonstrate the CSA measurements performed on images acquired with 1.5T MRI scanners have high reproducibility than those performed on the 3T scanner. The Minimal Detectable Change results suggest that the minimal change in CSA that could be measured in a longitudinal study, for example by studying the spinal cord atrophy in MS over time, is less than 0.52 mm^2 with automatic pipelines.
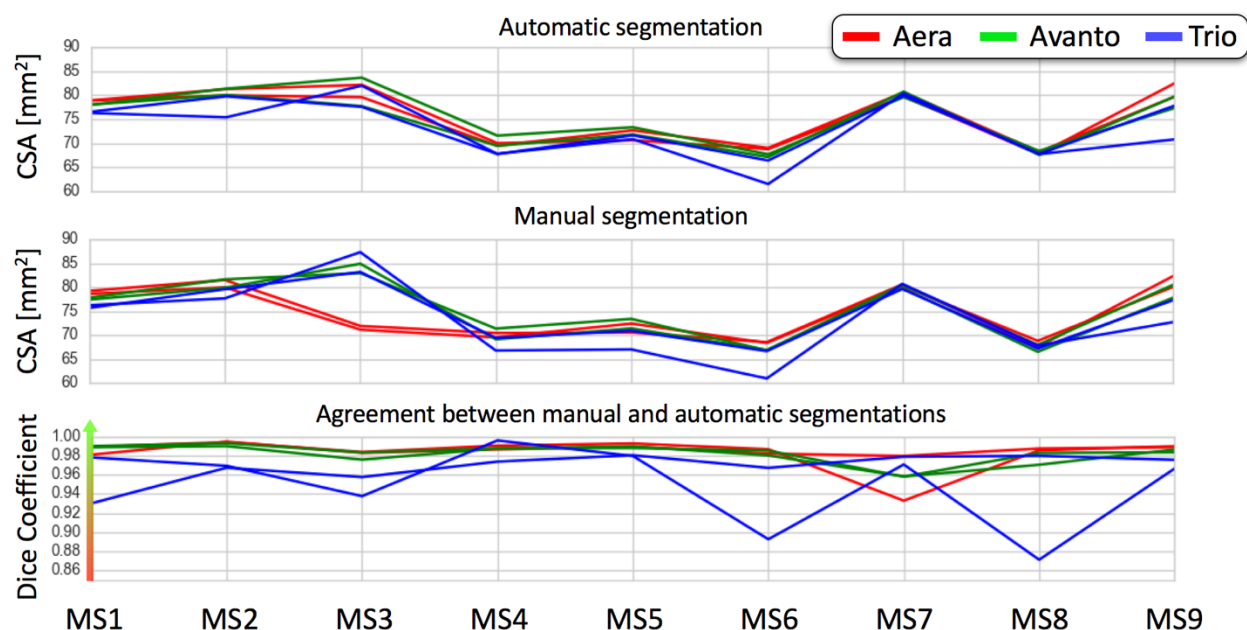
Figure 7.2: (top panels) CSA measurements for the 9 MS patients for the three MRI scanners. (bottom panel) Dice coefficient between manual and automatic segmentations computed using SCT.
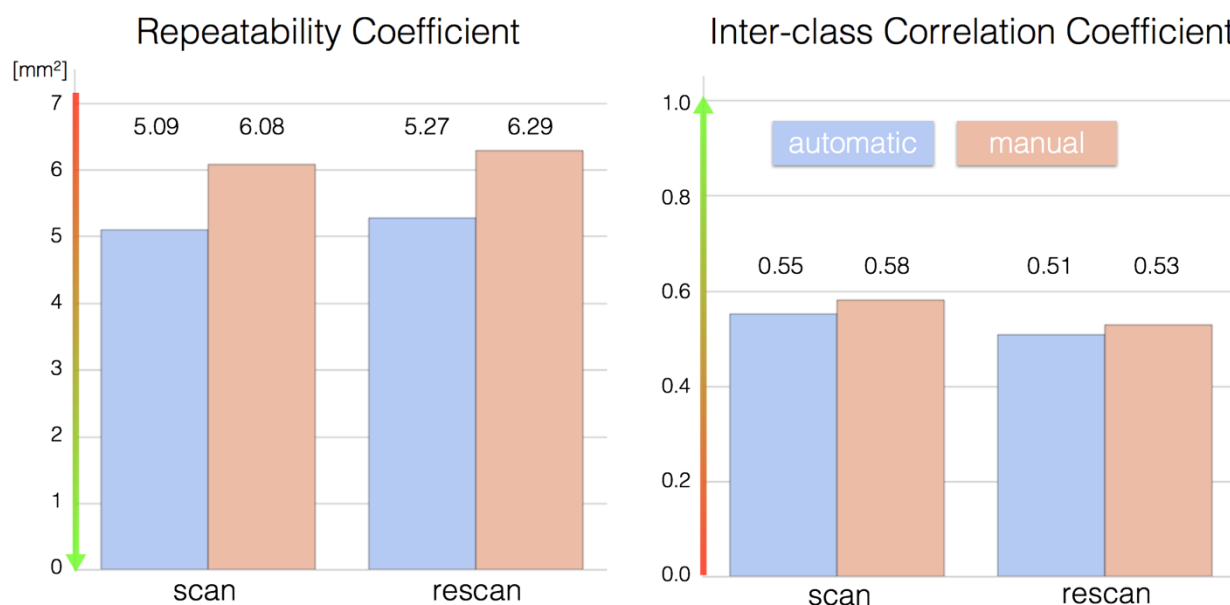
Figure 7.3: Repeatability of automatic (blue) and manual (red) CSA measurements.
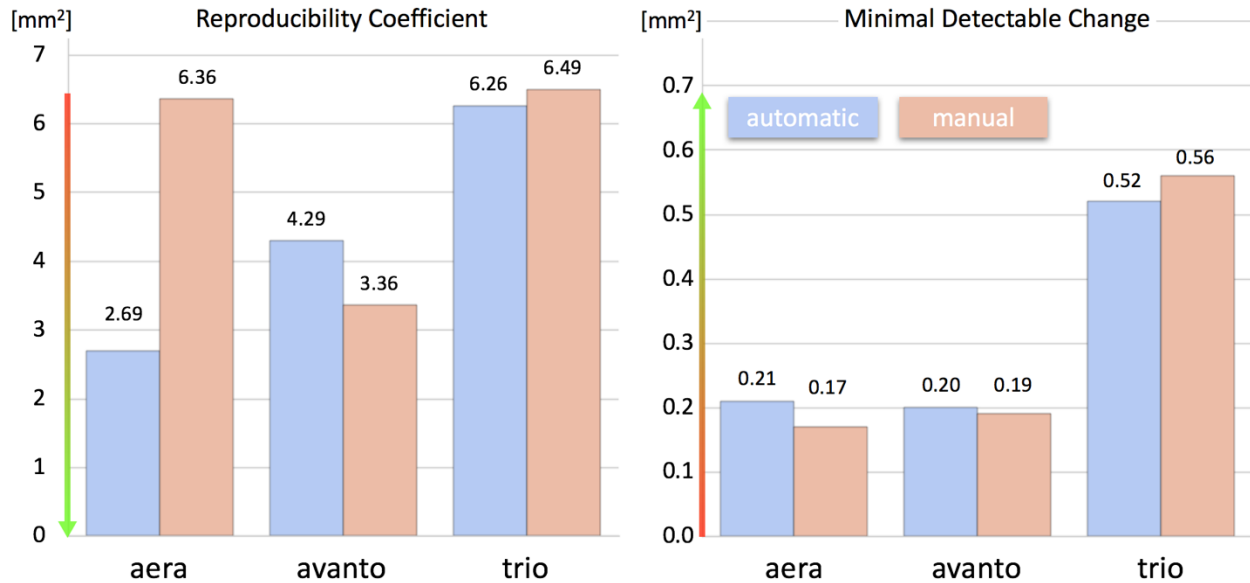
Figure 7.4: Reproducibility of automatic (blue) and manual (red) CSA measurements.

7.1.3 Discussion and conclusions

In concordance with (Yiannakas et al., 2015), we showed the high repeatability and reproducibility of CSA measurements using SCT on a MS population. Surprisingly, CSA measurements are overall more repeatable and reproducible when performed on 1.5T scanners than on 3T scanners, as suggested by Figure 7.3 and Figure 7.4. These findings may be explained by the larger fields-of-view acquired on 1.5T scanners and by different acquisition parameters. The most important finding of this study is the very small Minimal Detectable Change on all scanners, suggesting the ability of SCT to detect subtle changes in spinal cord morphology over time within subjects.

This study demonstrates the ability of semi-automated processing in SCT to quantify the spinal cord atrophy with high reproducibility and repeatability, opening the door to multi-center longitudinal studies of neurodegenerative diseases affecting the spinal cord. Future work will investigate automatic vertebral labeling in order to develop a fully automatic spinal cord CSA measurement pipeline.

7.2 Novel MRI biomarker of spinal cord white matter injury

The use of multiparametric MRI (mpMRI) and quantitative MRI (qMRI) in spinal cord studies has increased over the last few years. Spinal cord mpMRI and qMRI has the potential to provide in vivo measures of the tissue properties, including microstructure and integrity and could lead to improved clinical diagnosis, objective monitoring for disease progression and prediction of clinical outcomes. However, bringing mpMRI and qMRI to clinical setups is technically challenging due to artifacts, limited SNR and the lack of standardized protocols. In collaboration with A. R. Martin and M. G. Fehlings from University of Toronto, we assessed the clinical feasibility of using mpMRI and qMRI to quantify cervical spinal cord tissue injury and we proposed a new biomarker of spinal cord white matter injury. These studies are part of two papers published in peer-reviewed journals:

- Martin, A. R., **De Leener, B.**, Cohen-Adad, J., Cadotte, D. W., Kalsi-Ryan, S., Lange, S. F., … Fehlings, M. G. (2017). Clinically feasible microstructural MRI to quantify cervical spinal cord tissue injury using DTI, MT, and T2∗-weighted imaging: Assessment of normative data and reliability. *American Journal of Neuroradiology*, *38*(6). http://doi.org/10.3174/ajnr.A5163

- Martin, A. R., **De Leener, B.**, Cohen-Adad, J., Cadotte, D. W., Kalsi-Ryan, S., Lange, S. F., … Fehlings, M. G. (2017). A novel MRI biomarker of spinal cord white matter injury: T2∗-weighted white matter to gray matter signal intensity ratio. *American Journal of Neuroradiology*, *38*(6). http://doi.org/10.3174/ajnr.A5162

My contribution to these two papers was approximately 30% and included the design of the study, the implementation of technologies for data processing and the analysis of results.

7.2.1 Clinical feasibility of spinal cord white matter injury metrics

MR images were acquired from 40 healthy subjects on a 3T clinical MRI scanner (Signa Excite HDxt, GE Healthcare, Milwaukee, Wisconsin) in less than 35 minutes, including T2WI, DTI, MT and T2*WI imaging. Details on acquisition can be found in (Martin et al., 2017b). Four measures of SC tissue injury were extracted from various regions of the spinal cord from all subjects: CSA, DTI, MTR and T2*WI WM/GM. Additionally, 18 patients with DCM were included for analysis

of test-retest reliability of measurements. The test-retest procedure included removing the subject from the scanner and repositioning before scanning.

The following processing protocol was performed on all images. First, the spinal cord was automatically segmented using SCT on all MRI contrasts. Segmentation errors were corrected by providing seed points or manual editing when necessary. Second, all images were nonlinearly registered to the MNI-Poly-AMU template and DTI, MTR were directly extracted from WM and GM, and from specific WM tracts, using the maximum-a-posteriori method and the WM atlas from SCT. CSA were extracted from T2WI. The ratio of the T2*WI intensity within the white matter and gray matter was calculated for all slices. The four metrics were averaged over rostral (C1-C3), middle (C4-C5) or maximally compressed (MCL, for DCM patients), and caudal (C6-C7) levels.

Normative values of FA, MTR and T2*WI WM/GM ratio were extracted and presented in Figure 7.5a. Test-retest coefficients are presented on Figure 7.5b for the same three metrics. T2*WI WM/GM ratio demonstrated the lowest inter-subject and test-retest variability, which encourages its use in clinical studies, as this metric calculated on subjects with pathologies will show abnormal results.
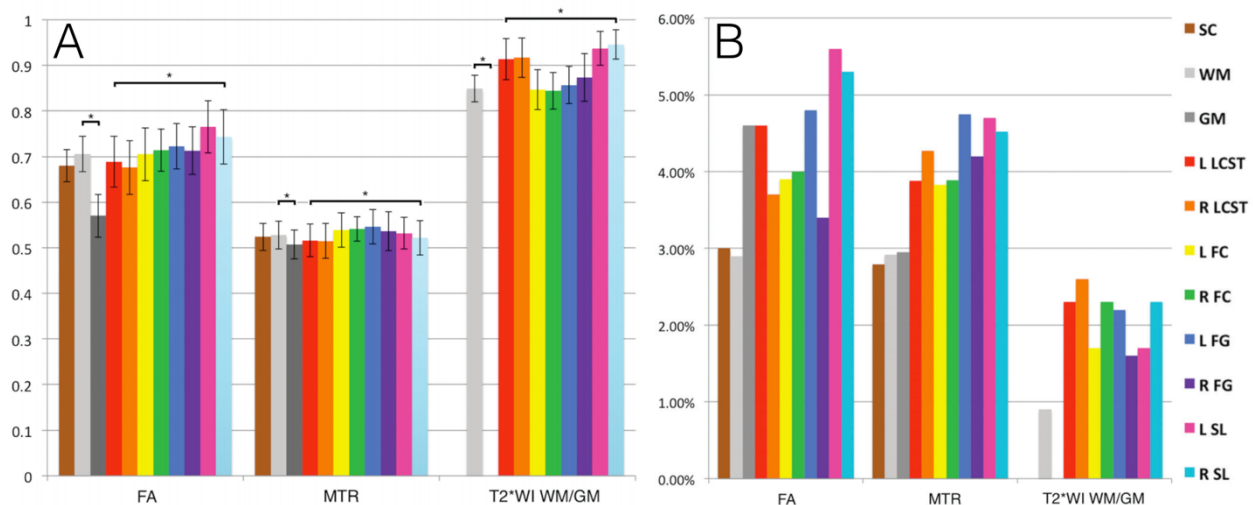
Figure 7.5: (A) Normative values of FA, MTR and T2*WI WM/GM extracted from SC, GM, WM, and specific WM tracts. Asterisks denotes significant differences between groups (p<0.05). (B) Test-retest coefficient of variation of FA, MTR and T2*WI WM/GM. (L indicates left; R, right; FC, fasciculus cuneatus; FG, fasciculus gracilis; SL, spinal lemniscus; LCST, lateral corticospinal tract). Adapted from (Martin et al., 2017b).

7.2.2 New biomarker of spinal cord white matter injury

Encouraged by the results presented in Section 7.2.1, a novel biomarker of spinal cord white matter injury was proposed: the T2*-weighted white matter to gray matter signal intensity ratio.

Forty-eight patients with DCM and 40 healthy subjects were scanned on a 3T MRI scanner with the same protocol as described in Section 7.2.1. MR metrics (CSA, FA, MTR and T2*WI WM/GM and the T2WI signal change) were extracted using the template and probabilistic atlases from SCT (De Leener, Lévy, et al., 2017) at the maximally compressed level of the spinal cord and at rostral and caudal uncompressed levels (Figure 7.6).
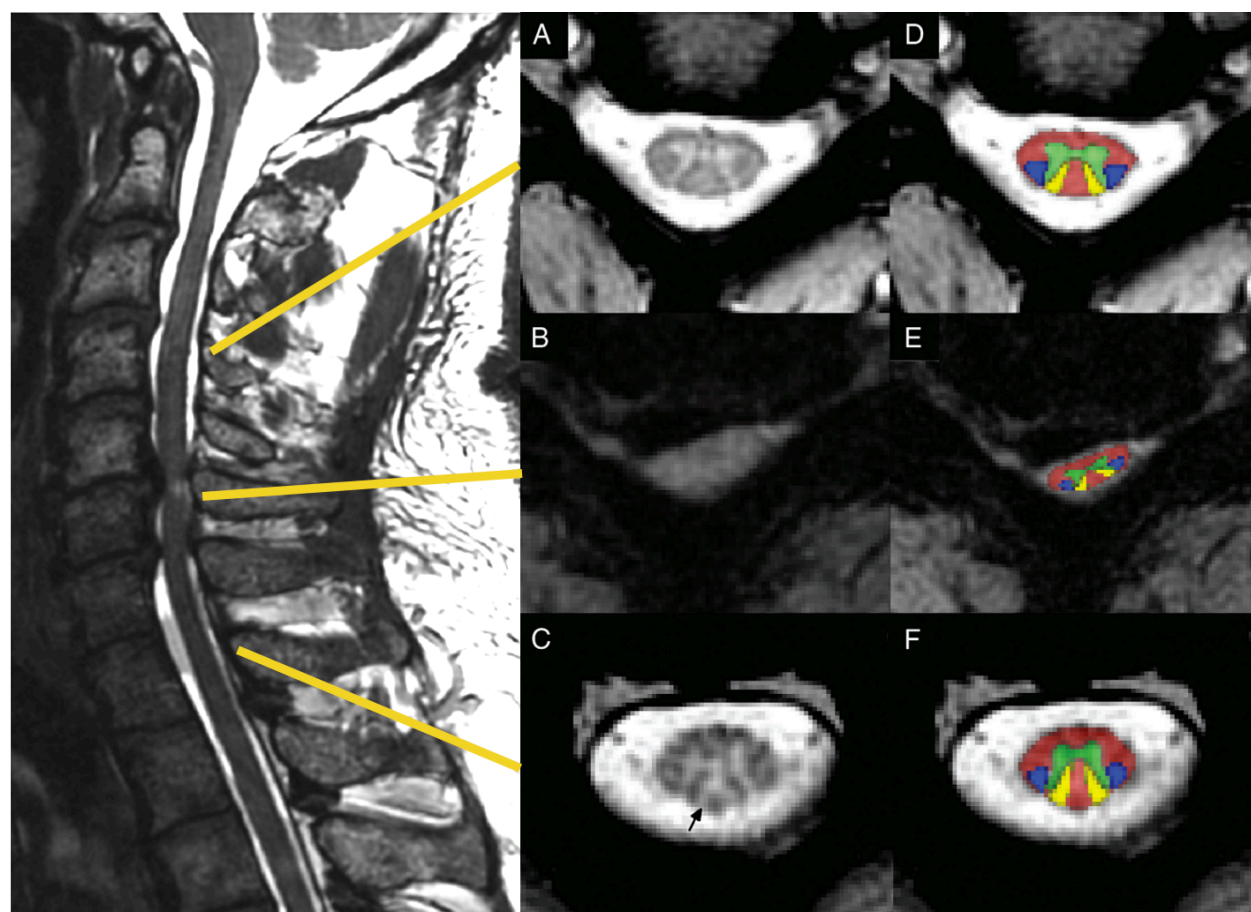
Figure 7.6: (left) Example of T2WI of a DCM patient with severe impairment due to spinal cord compression at C5-C6 vertebral levels with focal hyperintensity. (right) Example of T2*WI of a DCM patient demonstrating loss of GM/WM contrast and Wallerian degeneration. C and F panels show a focal hyperintensity (arrow) within the dorsal columns. Adapted from (Martin et al., 2017a).

These metrics were used to develop a diagnostic tool for DCM. The diagnostic accuracy was assessed with the area under the curve (AUC) and logistic regression, and results are presented in Table 7.1. The T2*WI WM/GM demonstrated a high diagnostic potential, with AUC = 0.775 at rostral levels and 0.721 at caudal levels. When combining all the metrics at all levels in a multivariate logistic regression model, the AUC reached 0.954, retaining rostral T2*WI WM/GM, MCL FA, MCL CSA and T2WI signal change. The T2*WI WM/GM biomarker has also demonstrated significant correlations with clinical features of DCM (mJOA, UE motor and UE sensory scores). More results can be found in (Martin et al., 2017a).

Table 7.1: Summary of MRI metrics extracted from healthy subjects and patients with DCM. Adapted from (Martin et al., 2017a).

Region	Metrics	Healthy subjects (N=40)	Subjects with DCM (N=58)	P value	Diagnostic Accuracy (AUC)
Rostral (C1-C3)	CSA	78.5 ± 8.0	70.9 ± 10.4	9×10^{-5}	0.772
	FA	0.725 ± 0.036	0.687 ± 3.4	2×10^{-4}	0.692
	MTR	52.7 ± 2.4	51.2 ± 3.4	0.01	0.648
	T2*w WM/GM	0.848 ± 0.031	0.884 ± 0.034	8×10^{-7}	0.775
MCL	CSA	76.2 ± 10.4	50.8 ± 18.1	1×10^{-13}	0.890
	FA	0.652 ± 0.048	0.553 ± 0.094	2×10^{-9}	0.813
	MTR	49.9 ± 2.9	47.6 ± 3.8	0.001	0.698
	T2*w WM/GM	0.850 ± 0.022	0.899 ± 0.038	1×10^{-11}	0.860
Caudal (C6-C7)	CSA	63.7 ± 9.1	60.1 ± 10.9	0.08	0.585
	FA	0.599 ± 0.050	0.552 ± 0.060	2×10^{-4}	0.724
	MTR	46.2 ± 3.8	46.4 ± 5.1	0.85	0.515
	T2*w WM/GM	0.862 ± 0.047	0.903 ± 0.053	1×10^{-4}	0.721

This study demonstrated the ability of a new biomarker (T2*WI WM/GM) to assess the integrity of spinal cord white matter. This new biomarker would be easily integrated into a clinical setup, as imaging protocols are standard and already used in clinics, and as its extraction is performed using robust and automated spinal cord image analysis tools. Moreover, the results showed that the combination of T2*WI WM/GM biomarker with other microstructure MR metrics enables a strong diagnostic accuracy (AUC=0.954). Such spinal cord tissue characterization metrics have the potential to provide more sensitive diagnostics of spinal cord injury, improve the monitoring the progression of diseases and recovering, and improve the prediction of outcomes in DCM and spinal pathologies.

7.3 Shape morphometrics of the spinal cord

Such promising results on DCM diagnosis accuracy led us to explore the power of the proposed metrics to detect early apparition of spinal cord compression due to disks, ligaments or vertebrae degeneration. Indeed, the prevalence of asymptomatic degenerative cervical spinal cord compression in the population is estimated between 8 and 20%. However, very little research has been made on this disease, as it does not present a clear pathologic entity. Being capable of distinguishing patients with Asymptomatic Spinal Cord Compression (ASCC) from the healthy population would facilitate the definition of the disease and its progression in terms of research.

Forty neurologically-intact subjects were recruited and underwent T2-weighted imaging (T2WI), DTI, magnetization transfer (MT), and T2*WI at 3T (GE Signa Excite HDxt) covering C1-C7. Acquisition parameters are described in (Martin et al., 2017a). All images were processed automatically using SCT. CSA of the spinal cord was extracted from T2-weighted images, and FA, MTR, and T2*WI WM/GM metrics were extracted from the WM. All metrics were averaged over spinal cord levels (rostral, MCL and caudal). Additionally, shape metrics (Figure 7.7) were computed at each section of the T2*-weighted segmentation mask, including *flattening*, which was measured with compression ratio (CR) = AP/transverse diameter, *indentation*, which was measured using solidity (= the percentage of area representing SC within the convex hull that subtends the SC), and *torsion*, which was measured with relative rotation, by calculating the angle between transverse and horizontal axis, relative to adjacent slices.

All subjects were independently examined by two raters for indentation, flattening, torsion, or circumferential compression of the spinal cord from extrinsic tissues (disc, ligament, or bone). Twenty of forty subjects were diagnosed with ASCC. Relative to these ratings, the diagnostic accuracy of the automated shape analysis, performed with SCT, achieved AUC=99.8% for flattening, 99.3% for indentation, and 98.4% for torsion. Significant differences were found with five MRI metrics (rostral, MCL, and caudal T2*WI WM/GM, rostral MTR, and MCL FA), with T2*WI WM/GM and MTR results suggesting that demyelination is the predominant pathophysiological mechanism in this preclinical state. These results highlight the importance of an objective definition for spinal cord compression and the potential of multivariate analysis of multiparametric MRI and automated spinal cord shape analysis to provide this definition.
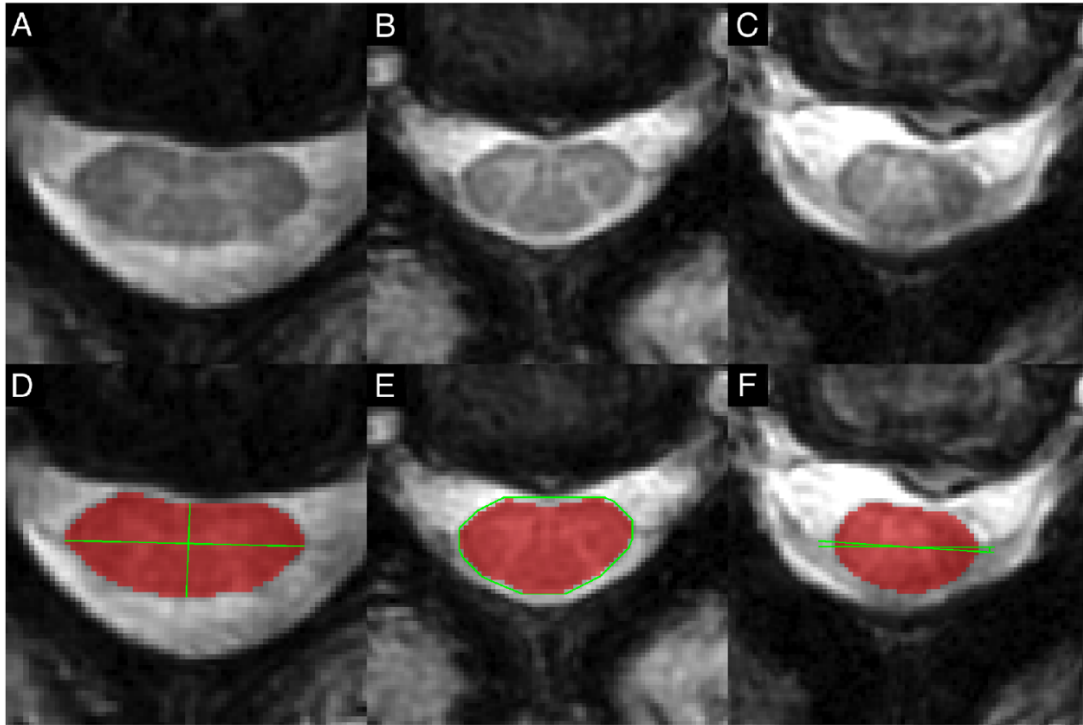
Figure 7.7: Example of asymptomatic spinal cord compression and extraction of shape metrics. A, B and C show T2*-weighted images of the spinal cord with flattening (A), indentation (B) and torsion (C). D, E and F show the computation of these metrics, based on the Principal Component Analysis (PCA) of the spinal cord segmentation mask. Adapted from (Martin et al., 2017a).

CHAPTER 8   GENERAL DISCUSSION

This manuscript presented an unbiased symmetrical MRI template of the spinal cord and new image processing tools dedicated to spinal cord MRI. The proposed template, PAM50, presented in 0, is based on 50 healthy subjects, is available for T1-, T2- and T2*-weighted MRI contrasts, covers the brainstem and the full spinal cord, and is merged with probabilistic atlases of the white matter pathways and gray matter subregions. The PAM50 template is integrated into SCT, a comprehensive and open-source software for processing spinal cord MRI data, which is presented in Chapter 4. More particularly, SCT include segmentation algorithms for the spinal cord and the white and gray matter, and methods for the extraction of MRI metrics within specific regions of the spinal cord and at specific vertebral levels. Additionally, specific registration tools dedicated to spinal cord MR images were developed, as described in Chapter 5, allowing registration of large groups of subjects with high accuracy. While this chapter does not aim at repeating the discussion points covered in Chapter 4, Chapter 5 and 0, the following paragraphs will discuss specific details and implications of the proposed developments, including tools for processing spinal cord MRI data, perspectives on methods for registering spinal cord images, the limitations of the PAM50 template and its atlases, their potential for clinical developments. The discussion will end on the importance of open science in neuroimaging.

8.1 Spinal cord imaging tools

One of the main contribution of the present dissertation is the development of advanced tools for the analysis of spinal cord MRI data, including a generic template of the spinal cord and a comprehensive suite for extracting information from the spinal cord internal structure. A particular attention has been paid to the modularity (easy integration of new templates and algorithms) and cross-platform compatibility of the proposed tools. Indeed, many tools developed for brain imaging, such as statistical analysis from FSL or SPM, are still useful for spinal cord data. Therefore, the input and output files of the proposed tools have been standardized to be compatible with most neuroimaging software, including image files (Nifti), transformation files (affine transformation are deformation fields are compatible with ITK/ANTs) and binary masks.

The Chapter 5 presented the development of an image processing method dedicated to spinal cord MRI images, that enables robust and accurate straightening of spinal cord images, but also the co-

registration of multiple spinal cord MR images, while considering vertebral levels position (0). As it only relies on the spinal cord segmentation, which can be extracted automatically or not, the proposed method provides an analytical solution for spinal cord diffeomorphic registration without any assumption on the spinal cord state. Therefore, this method has the potential to become the state-of-the-art in terms of image registration for spinal cord MRI data.

While SCT, coupled with the PAM50 template, provides a powerful tool for template-based analysis of spinal cord MRI data, many improvements can still be made in the processing of spinal cord MRI images. Particularly, automating the detection of the spinal cord, the vertebral levels and specific reference point such as the pontomedullary junction is a strong challenge, due to the large variability in MR image contrast and field of view. Supervised machine learning techniques coupled with large database of annotated spinal cord MRI data have the potential to tackle these tasks. Improvements on spinal cord segmentation and registration also need to be made, particularly on pathological cases, as large cord deformation, such as atrophy, indentation, torsion, can reduce the accuracy and robustness of the developed tools.

8.2 Template and atlases of the spinal cord

The PAM50 template provides a spatial reference for quantifying multiparametric/quantitative MRI data within specific pathways of the spinal cord white matter or subregions of the gray matter. As described in Chapter 4, the registration pipeline applied to a subject's images takes into account the spinal cord curvature, shape, and internal structure (gray matter). While the exact location of white matter tracts and gray matter subregions can vary across levels and across subjects, the registration process uses regularized deformation that would preserve the overall disposition of white and gray matter regions, based on the atlases merged with the PAM50 template. Moreover, the quantification algorithm that extracts MRI metrics from individual spinal cord tracts used the probabilistic information on the location of all tracts at the same time, thereby ensuring a robust estimation of metrics, even in the presence of noise in the images.

The PAM50 template provides a referential coordinate system based on the vertebral levels. This choice has been driven by the radiological workflow, which commonly relies on vertebral levels as reference. Many studies would gain from a coordinate system based on spinal levels, as spinal segments are more appropriate to study spinal cord functions (e.g., fMRI studies). Unfortunately,

the spinal roots are not easily visible on standard structural MR images and high resolution acquisition would be necessary, however not currently practical for clinical practice. In 0, I briefly studied the relationship between vertebral levels and the spinal cord enlargements (that are related to spinal segments). While no relation between spinal cord enlargements and vertebral levels were found, I strongly believe that spinal roots can be normalized across a population with a template based on the position of spinal cord enlargement relative to a fixed point in the brain (e.g., the pontomedullary junction), as also suggested by recent meta-analysis on spinal cord anatomy (Frostell et al., 2016). This will be the subject of future work.

The PAM50 template has been built with images from 50 young Caucasian healthy subjects and is fairly representative of the general world population. While the registration procedure may take into account some variability across subjects, there is a need for population specific template (e.g., age, race), as suggested recently in the brain by (Rao et al., 2017). Disease-specific template that allows the temporal exploration of disease characteristics, such as atrophy (Fonov, Coupe, Eskildsen, & Collins, 2011), would also be beneficial for the community.

8.3 Translation to a clinical setup and clinical impact

The proposed developments and methods have been tailored towards research, mainly for exploratory studies of individual or groups of subjects and patients. However, SCT and the PAM50 brainstem and spinal cord template have a strong potential for clinical applications, such as improving the diagnosis and prognosis of diseases affecting the spinal cord, and improve the monitoring of disease progression. More particularly, the full spinal cord template and atlases of the spinal cord internal structure enables the extraction of multiparametric and quantitative MRI data from specific subregions of the white and the gray matter of the spinal cord. In collaboration with A. R. Martin and M. G. Fehlings from University of Toronto, strong efforts have been made in the application of the proposed template-based analysis in the context of degenerative cervical myelopathy, leading to the development of a new biomarker of spinal cord white matter injury, the T2*-WI WM/GM ratio, and of new shape-based morphometrics that have the potential of early diagnosis of spinal cord compression. Similar developments can be performed for other neurodegenerative diseases and can lead to the generalization of multiparametric MRI of the spinal cord as biomarker of spinal cord injury.

More broadly, the use of template-based analysis and advances image processing tools in a clinical context enables the *in vivo* extraction of valuable information about the spinal cord, including the study of spinal cord microstructure (Duval et al., 2017; Duval et al., 2015; Ljungberg, 2016; Massire et al., 2016) and white matter integrity (David et al., 2017; Grabher et al., 2016; Martin et al., 2017a). Such analyses have the potential to discover new biomarkers for disease diagnosis, but also at improving our understanding of disease underlying mechanisms. Proper validation of these techniques on large populations of patients must still be accomplished, for example with *ex vivo* histology of microstructural measurements. Functional MRI of the spinal cord is also a topic of interest in the spinal cord imaging literature that benefits directly from comprehensive MRI template/atlas-based analysis (Bosma & Stroman, 2014; Stroman et al., 2012). While vertebral-based templates have been used for pain (Weber 2nd et al., 2016a) and laterality (Weber 2nd et al., 2016b) analyses, as well as resting-state fMRI (Eippert et al., 2017; Kong et al., 2014), templates based on spinal segments would be more appropriate for analysis of spinal cord functions. Finally, many neurodegenerative diseases such as MS and DCM affect the overall structure of the spinal cord, while affecting its internal microstructure. Template-based methods as proposed in this dissertation have the potential to improve the global understanding of these diseases, by combining structural measurements with atlas-based microstructural metric extraction.

8.4 Open science in neuroimaging

The promises of neuroimaging partly rely on the development of reliable, resilient and, ideally, easy-to-use software. While research in neuroscience is still in its infancy, the neuroimaging community needs more than ever to build efficient strategies for providing computing technologies that will enable tomorrow's discoveries. Open science has the potential to provide such strategies, by facilitating the share of data, software, experiment details and results. Indeed, Open science already includes resources and frameworks for sharing data and imaging protocols (e.g., OSF (https://osf.io/), opening publications (e.g., F1000Research, https://f1000research.com/) and open-sourcing software (e.g., GitHub, https://github.com/). Additionally, collaboration initiatives such as Brainhack (Craddock et al., 2016) facilitate the dissemination of ideas and tools and offer unique opportunities to build open collaborations between researchers.

However, open science is not without challenges and releasing open-source software such as SCT (https://github.com/neuropoly/spinalcordtoolbox) comes with responsibilities to the entire

neuroimaging community. Indeed, ensuring the robustness of image processing methods towards the variety of MRI contrasts is only one example of difficulties that neuroimaging software are facing, due to the evolving nature of neuroimaging. Producing tools that allow results to be reproduced by others, through extensive documentation and easy-to-use software, should be the focus of neuroimaging developers.

All the algorithms, tools and methods presented in this dissertation have been developed while promoting and advocating open science. Many efforts have been made to ensure the continuity of the proposed developments, and I recommend to all students and researchers to follow the open science path as I did. Many of my successes resulted from my decision to embrace open science.

CHAPTER 9   CONCLUSION AND RECOMMENDATIONS

The spinal cord MRI community was missing one of the greatest advances of neuroimaging: a generic template of the full spinal cord. The objective of this project was to demonstrate how to create a spinal cord MRI template with minimum bias, that would be available in multiple MRI contrasts, that would be merged with atlases of the spinal cord internal structure, and that would enable simultaneous template-based analysis of the brain, the brainstem and the spinal cord.

The proposed template, the PAM50, is based on the nonlinear average of 50 healthy subjects and is available in T1-, T2- and T2*-weighted contrasts. It covers the brainstem and the full spinal cord, and is registered with the ICBM152 "MNI" brain template, so that both template share the same referential coordinate system. The PAM50 template also includes probabilistic maps of the white matter tracts and gray matter subregions, and is integrated into SCT.

SCT is a comprehensive and open-source software for processing multi-parametric MRI data of the spinal cord that has been developed during this project. Additionally to the PAM50 template, SCT includes automated algorithms for the segmentation of the full spinal cord and spinal cord gray matter, co-registration tools dedicated to multimodal images of the spinal cord and methods for the robust extraction of MRI metrics within white matter tracts and at specific vertebral levels. Moreover, SCT provides basic image processing tools adapted for spinal cord imaging, such as denoising along the spinal cord axis and robust motion correction for time series acquisition.

While the proposed vertebral level based template represents an important contribution to the field of spinal cord MRI analysis, many improvements are still to be made. First, the spinal cord fMRI community would benefit from a template that relies on the position of spinal segments instead of vertebral bodies. Such template would improve group studies on the function of the full spinal cord and studies should be performed on large groups of subjects with high resolution acquisition, in order to explore the different possibilities of conveniently normalizing MRI images of the spinal cord with respect to the spinal segments. Additional image processing tools dedicated to spinal cord MRI data must be further developed for large-scale implementation of SCT and the PAM50 template into clinics. For example, the accuracy of the registration framework highly depends on the quality of spinal cord segmentation. Therefore, robust automated methods for detection and segmentation of the spinal cord and its internal structure should be the focus of future work, as it would enable the inclusion of automated spinal cord analysis framework into clinical setup.

BIBLIOGRAPHY

Abdel-Aziz, K., Solanky, B. S., Yiannakas, M. C., Altmann, D. R., Wheeler-Kingshott, C. A. M., Thompson, A. J., & Ciccarelli, O. (2014). Age related changes in metabolite concentrations in the normalspinal cord. *PLoS One*, *9*(10), e105774.

Adams, R. D., & Salam-Adams, M. (1991). Chronic nontraumatic diseases of the spinal cord. *Neurol. Clin.*, *9*(3), 605–623.

Agosta, F., Laganà, M., Valsasina, P., Sala, S., Dall'Occhio, L., Sormani, M. P., … Filippi, M. (2007). Evidence for cervical cord tissue disorganisation with agingby diffusion tensor MRI. *Neuroimage*, *36*(3), 728–735.

Agosta, F., Pagani, E., Caputo, D., & Filippi, M. (2007). Associations between cervical cord gray matter damage anddisability in patients with multiple sclerosis. *Arch. Neurol.*, *64*(9), 1302–1305.

Altman, J., & Bayer, S. A. (2001). An overview of spinal cord organization. In *Development of the Human Spinal Cord: An Interpretation Based onExperimental Studies in Animals* (pp. 1–87). New York: Oxford University Press.

Archip, N., Erard, P.-J., Egmont-Petersen, M., Haefliger, J.-M., & Germond, J.-F. (2002). A Knowledge-Based Approach to Automatic Detection of the Spinal Cord in CT Images. *IEEE Transactions on Medical Imaging*, *21*(12), 1504–16. https://doi.org/10.1109/TMI.2002.806578

Asman, A. J., Bryan, F. W., Smith, S. A., Reich, D. S., & Landman, B. A. (2014). Groupwise multi-atlas segmentation of the spinal cord's internal structure. *Med. Image Anal.*, *18*(3), 460–471.

Aspert, N., Santa Cruz, D., & Ebrahimi, T. (2002). MESH: measuring errors between surfaces using the Hausdorffdistance. In *ICME (1)* (pp. 705–708). stage.nitrc.org.

Avants, B. B., Epstein, C. L., Grossman, M., & Gee, J. C. (2008). Symmetric diffeomorphic image registration withcross-correlation: evaluating automated labeling of elderlyand neurodegenerative brain. *Med. Image Anal.*, *12*(1), 26–41.

Avants, B. B., Tustison, N. J., Song, G., Cook, P. A., Klein, A., & Gee, J. C. (2011). A

reproducible evaluation of {ANTs} similarity metric performance in brain image registration. *Neuroimage*, *54*(3), 2033–2044.

Avants, B. B., Tustison, N. J., Stauffer, M., Song, G., Wu, B., & Gee, J. C. (2014). The Insight ToolKit image registration framework. *Front. Neuroinform.*, *8*, 44.

Avants, B. B., Tustison, N., & Song, G. (2009). Advanced normalization tools (ANTS). *Insight J.*, *2*, 1–35.

Bakshi, R., Dandamudi, V. S. R., Neema, M., De, C., & Bermel, R. A. (2005). Measurement of brain and spinal cord atrophy by magneticresonance imaging as a tool to monitor multiple sclerosis. *J. Neuroimaging*, *15*(4 Suppl), 30S–45S.

Bastianello, S., Paolillo, A., Giugni, E., Giuliani, S., Evangelisti, G., Luccichenti, G., … Fieschi, C. (2000). MRI of spinal cord in MS. *J. Neurovirol.*, *6 Suppl 2*, S130–3.

Behrens, T., Rohr, K., & Stiehl, H. S. (2003). Robust segmentation of tubular structures in 3-D medicalimages by parametric object detection and tracking. *IEEE Trans. Syst. Man Cybern. B Cybern.*, *33*(4), 554–561.

Bergo, F. P. G., Franca, M. C., Chevis, C. F., & Cendes, F. (2012). {SpineSeg}: A segmentation and measurement tool for evaluation of spinal cord atrophy. In *Proceedings of the 7th Iberian Conference on Information Systems and Technologies, {CISTI}* (pp. 1–4). Madrid.

Bergo, F. P. G., França, M. C., Chevis, C. F., & Cendes, F. (2012). {SpineSeg}: A segmentation and measurement tool for evaluation of spinal cord atrophy. In *7th Iberian Conference on Information Systems and Technologies ({CISTI} 2012)* (pp. 1–4).

Bickenbach, J. (2013). *International perspectives on spinal cord injury*.

Blaiotta, C., Jorge Cardoso, M., & Ashburner, J. (2016). Variational inference for medical image segmentation. *Comput. Vis. Image Underst.*, *151*, 14–28.

Bosma, R. L., & Stroman, P. W. (2014). Assessment of data acquisition parameters, and analysistechniques for noise reduction in spinal cord fMRI data. *Magn. Reson. Imaging*, *32*(5), 473–481.

Boykov, Y., Veksler, O., & Zabih, R. (2001). Fast approximate energy minimization via graph cuts. *IEEE Trans. Pattern Anal. Mach. Intell.*, *23*(11), 1222–1239.

Bozzali, M., Rocca, M. A., Iannucci, G., Pereira, C., Comi, G., & Filippi, M. (1999). Magnetization-transfer histogram analysis of the cervical cordin patients with multiple sclerosis. *AJNR Am. J. Neuroradiol.*, *20*(10), 1803–1808.

Bozzo, A., Marcoux, J., Radhakrishna, M., Pelletier, J., & Goulet, B. (2011). The role of magnetic resonance imaging in the management of acute spinal cord injury. *J. Neurotrauma*, *28*(8), 1401–1411.

Bradbury, E. J., & McMahon, S. B. (2006). Spinal cord repair strategies: why do they work? *Nat. Rev. Neurosci.*, *7*(8), 644–653.

Branco, L. M. T., De Albuquerque, M., De Andrade, H. M. T., Bergo, F. P. G., Nucci, A., & França Jr, M. C. (2014). Spinal cord atrophy correlates with disease duration andseverity in amyotrophic lateral sclerosis. *Amyotroph. Lateral Scler. Frontotemporal Degener.*, *15*(1–2), 93–97.

Brex, P. A., Leary, S. M., O'Riordan, J. I., Miszkiel, K. A., Plant, G. T., Thompson, A. J., & Miller, D. H. (2001). Measurement of spinal cord area in clinically isolatedsyndromes suggestive of multiple sclerosis. *J. Neurol. Neurosurg. Psychiatry*, *70*(4), 544–547.

Brodmann, K. (1909). Vergleichende Lokalisationslehre der Groshirnrinde. *Leipzig: Barth*.

Brooks, B. R. (1994). El Escorial World Federation of Neurology criteria for thediagnosis of amyotrophic lateral sclerosis. Subcommittee onMotor Neuron Diseases/Amyotrophic Lateral Sclerosis of theWorld Federation of Neurology Research Group on NeuromuscularDiseases and the El Escorial ``Clinical limits of amyotrophiclateral sclerosis'' workshop contributors. *J. Neurol. Sci.*, *124 Suppl*, 96–107.

Brooks, B. R. (1996). Natural history of ALS: symptoms, strength, pulmonaryfunction, and disability. *Neurology*, *47*(4 Suppl 2), S71–81–2.

Brosch, T., Tang, L. Y. W., Youngjin Yoo, Li, D. K. B., Traboulsee, A., & Tam, R. (2016). Deep 3D Convolutional Encoder Networks With Shortcuts forMultiscale Feature Integration Applied to Multiple SclerosisLesion Segmentation. *IEEE Trans. Med. Imaging*, *35*(5), 1229–1239.

Brownell, B., Oppenheimer, D. R., & Hughes, J. T. (1970). The central nervous system in motor neurone disease. *J. Neurol. Neurosurg. Psychiatry*, *33*(3), 338–357.

Buades, A., Coll, B., & Morel, J. (2005). A Review of Image Denoising Algorithms, with a New One. *Multiscale Model. Simul.*, *4*(2), 490–530.

Cadotte, D. W., Cadotte, A., Cohen-Adad, J., Fleet, D., Livne, M., Wilson, J. R., … Fehlings, M. G. (2015). Characterizing the location of spinal and vertebral levels in the human cervical spinal cord. *AJNR Am. J. Neuroradiol.*, *36*(4), 803–810.

Cadotte, D. W., & Fehlings, M. G. (2014). Traumatic Spinal Cord Injury: Acute Spinal Cord Injury andPrognosis. In J. Cohen-Adad & C. Wheeler-Kingshott (Eds.), *Quantitative MRI of the Spinal Cord* (pp. 39–48). Elsevier.

Cadotte, D. W., Wilson, J. R., Mikulis, D., Stroman, P. W., Brady, S., & Fehlings, M. G. (2011). Conventional MRI as a diagnostic and prognostic tool inspinal cord injury: a systemic review of its application todate and an overview on emerging MRI methods. *Expert Opin. Med. Diagn.*, *5*(2), 121–133.

Cameron Craddock, R., S Margulies, D., Bellec, P., Nolan Nichols, B., Alcauter, S., A Barrios, F., … Xu, T. (2016). Brainhack: a collaborative workshop for the open neurosciencecommunity. *Gigascience*, *5*, 16.

Carbonell-Caballero, J., Manjón, J. V, Mart'\i-Bonmat'\i, L., Olalla, J. R., Casanova, B., la Iglesia-Vayá, M., … Robles, M. (2006). Accurate quantification methods to evaluate cervical cordatrophy in multiple sclerosis patients. *MAGMA*, *19*(5), 237–246.

Castellano, A., Papinutto, N., Cadioli, M., Brugnara, G., Iadanza, A., Scigliuolo, G., … Salsano, E. (2016). Quantitative MRI of the spinal cord and brain inadrenomyeloneuropathy: in vivo assessment of structuralchanges. *Brain*, *139*(Pt 6), 1735–1746.

Caviness, V. S., Meyer, J., Makris, N., & Kennedy, D. N. (1996). MRI-Based Topographic Parcellation of Human Neocortex: An Anatomically Specified Method with Estimate of Reliability. *Journal of Cognitive Neuroscienc*, *8*(6), 566–587. https://doi.org/10.1162/jocn.1996.8.6.566

Chang, H.-H., Zhuang, A. H., Valentino, D. J., & Chu, W.-C. (2009). Performance measure characterization for evaluating neuroimagesegmentation algorithms. *Neuroimage*, *47*(1), 122–135.

Charil, A., Caputo, D., Cavarretta, R., Sormani, M. P., Ferrante, P., & Filippi, M. (2006).

Cervical cord magnetization transfer ratio and clinicalchanges over 18 months in patients with relapsing-remittingmultiple sclerosis: a preliminary study. *Mult. Scler.*, *12*(5), 662–665.

Chen, M., Carass, A., Oh, J., Nair, G., Pham, D. L., Reich, D. S., & Prince, J. L. (2013). Automatic magnetic resonance spinal cord segmentation with topology constraints for variable fields of view. *Neuroimage*, *83*, 1051–1062.

Ciccarelli, O., Wheeler-Kingshott, C. A., McLean, M. A., Cercignani, M., Wimpey, K., Miller, D. H., & Thompson, A. J. (2007). Spinal cord spectroscopy and diffusion-based tractography toassess acute disability in multiple sclerosis. *Brain*, *130*(Pt 8), 2220–2231.

Cohen-Adad, J. (2017). Functional Magnetic Resonance Imaging of the Spinal Cord:Current Status and Future Developments. *Semin. Ultrasound CT MR*, *38*(2), 176–186.

Cohen-Adad, J., De Leener, B., Benhamou, M., Cadotte, D., Fleet, D., Cadotte, A., … Others. (2014). Spinal Cord Toolbox: an open-source framework for processingspinal cord MRI data. In *Proceedings of the 20th Annual Meeting of OHBM, Hamburg,Germany* (Vol. 3633, p. 3633).

Cohen-Adad, J., Descoteaux, M., Rossignol, S., Hoge, R. D., Deriche, R., & Benali, H. (2008). Detection of multiple pathways in the spinal cord using q-ballimaging. *Neuroimage*, *42*(2), 739–749.

Cohen-Adad, J., El Mendili, M.-M., Lehéricy, S., Pradat, P.-F., Blancho, S., Rossignol, S., & Benali, H. (2011a). Demyelination and degeneration in the injured human spinalcord detected with diffusion and magnetization transfer MRI. *Neuroimage*, *55*(3), 1024–1033.

Cohen-Adad, J., El Mendili, M.-M., Lehéricy, S., Pradat, P.-F., Blancho, S., Rossignol, S., & Benali, H. (2011b). Demyelination and degeneration in the injured human spinal cord detected with diffusion and magnetization transfer MRI. *NeuroImage*, *55*(3), 1024–33. https://doi.org/10.1016/j.neuroimage.2010.11.089

Cohen-Adad, J., El Mendili, M.-M., Morizot-Koutlidis, R., Lehéricy, S., Meininger, V., Blancho, S., … Pradat, P.-F. (2013). Involvement of spinal sensory pathway in ALS andspecificity of cord atrophy to lower motor neurondegeneration. *Amyotroph. Lateral Scler. Frontotemporal Degener.*, *14*(1), 30–38.

Cohen-Adad, J., Gauthier, C. J., Brooks, J. C. W., Slessarev, M., Han, J., Fisher, J. A., … Hoge,

R. D. (2010). {BOLD signal responses to controlled hypercapnia in humanspinal cord. *Neuroimage*, *50*(3), 1074–1084.

Cohen-Adad, J., Leblond, H., Delivet-Mongrain, H., Martinez, M., Benali, H., & Rossignol, S. (2011). Wallerian degeneration after spinal cord lesions in catsdetected with diffusion tensor imaging. *Neuroimage*, *57*(3), 1068–1076.

Cohen-Adad, J., Lévy, S., & Avants, B. (2015). Slice-by-slice regularized registration for spinal cord MRI:SliceReg. In *Proceedings of the 23th Annual Meeting of ISMRM, Toronto,Canada* (Vol. (in press), p. 5553). Toronto.

Cohen-Adad, J., Mareyam, A., Keil, B., Polimeni, J. R., & Wald, L. L. (2011). 32-channel RF coil optimized for brain and cervical spinalcord at 3 T. *Magn. Reson. Med.*, *66*(4), 1198–1208.

Cohen-Adad, J., & Wheeler-Kingshott, C. (Eds.). (2014a). *Quantitative MRI of the Spinal Cord*. Elsevier.

Cohen-Adad, J., & Wheeler-Kingshott, C. (2014b). *Quantitative MRI of the Spinal Cord*. Academic Press.

Cohen-Adad, J., Zhao, W., Keil, B., Ratai, E.-M., Triantafyllou, C., Lawson, R., … Atassi, N. (2013). {7-T} {MRI} of the spinal cord can detect lateral corticospinal tract abnormality in amyotrophic lateral sclerosis. *Muscle Nerve*, *47*(5), 760–762.

Collins, D. L., Evans, A. C., Holmes, C., & Peters, T. M. (1995). Automatic 3{D} Segmentation of Neuro-Anatomical Structures from {MRI}. *Information Processing in Medical Imaging*, *3*, 139–152.

Collins, D. L., Holmes, C. J., Peters, T. M., & Evans, A. C. (1995). Automatic 3-D model-based neuroanatomical segmentation. *Hum. Brain Mapp.*, *3*(3), 190–208.

Compston, A., & Coles, A. (2008). Multiple sclerosis. *The Lancet*, *372*(9648), 1502–1517. https://doi.org/10.1016/S0140-6736(08)61620-7

Coulon, O., Hickman, S. J., Parker, G. J., Barker, G. J., Miller, D. H., & Arridge, S. R. (2002). Quantification of spinal cord atrophy from magnetic resonance images via a B-spline active surface model. *Magnetic Resonance in Medicine : Official Journal of the Society of*

Magnetic Resonance in Medicine / Society of Magnetic Resonance in Medicine, *47*(6), 1176–85. https://doi.org/10.1002/mrm.10162

Cox, R. W. (1996). AFNI: software for analysis and visualization of functionalmagnetic resonance neuroimages. *Comput. Biomed. Res.*, *29*(3), 162–173.

Cruz-Sánchez, F. F., Moral, A., Tolosa, E., de Belleroche, J., & Rossi, M. L. (1998). Evaluation of neuronal loss, astrocytosis and abnormalities of cytoskeletal components of large motor neurons in the human anterior horn in aging. *J. Neural Transm.*, *105*(6–7), 689–701.

Datta, E., Papinutto, N., Schlaeger, R., Zhu, A., Carballido-Gamio, J., Henry, R., & G. (2017). Gray matter segmentation of the spinal cord with activecontours in MR images. *Neuroimage*, *147*, 788–799.

David, G., Freund, P., & Mohammadi, S. (2017). The efficiency of retrospective artifact correction methods in improving the statistical power of between-group differences in spinal cord {DTI}. *Neuroimage*.

De Boor, C. (1978). A practical guide to splines. Number 27 in Applied MathematicalSciences. Springer, New York.

De Leener, B., Cohen-Adad, J., & Kadoury, S. (2015a). Automatic Segmentation of the Spinal Cord and Spinal CanalCoupled With Vertebral Labeling. *IEEE Trans. Med. Imaging*, *34*(8), 1705–1718.

De Leener, B., Cohen-Adad, J., & Kadoury, S. (2015b). Automatic Segmentation of the Spinal Cord and Spinal CanalCoupled With Vertebral Labeling. *IEEE Trans. Med. Imaging*, *34*(8), 1705–1718.

De Leener, B., Cohen-Adad, J., & Kadoury, S. (2015). Automatic Segmentation of the Spinal Cord and Spinal Canal Coupled with Vertebral Labeling. *IEEE Transactions on Medical Imaging*, *34*(8). https://doi.org/10.1109/TMI.2015.2437192

De Leener, B., Granberg, T., Fink, K., Stikov, N., & Cohen-Adad, J. (2017). Repeatability and reproducibility of spinal cord atrophymeasurements in a multiple sclerosis population using the SpinalCord Toolbox. In *Proceedings of the 25th Annual Meeting of ISMRM, Honolulu,USA*.

De Leener, B., Kadoury, S., & Cohen-Adad, J. (2014). Robust, accurate and fast automatic segmentation of thespinal cord. *Neuroimage*, *98*, 528–536.

De Leener, B., Kadoury, S., & Cohen-Adad, J. (2014). Robust, accurate and fast automatic segmentation of the spinal cord. *NeuroImage*, *98*. https://doi.org/10.1016/j.neuroimage.2014.04.051

De Leener, B., Lévy, S., Dupont, S. M., Fonov, V. S., Stikov, N., Louis Collins, D., … Cohen-Adad, J. (2016). SCT: Spinal Cord Toolbox, an open-source software for processing spinal cord MRI data. *NeuroImage*. https://doi.org/10.1016/j.neuroimage.2016.10.009

De Leener, B., Lévy, S., Dupont, S. M., Fonov, V. S., Stikov, N., Louis Collins, D., … Cohen-Adad, J. (2017). SCT: Spinal Cord Toolbox, an open-source software forprocessing spinal cord MRI data. *Neuroimage*, *145*(Pt A), 24–43.

De Leener, B., Lévy, S., Dupont, S. M., Fonov, V. S., Stikov, N., Louis Collins, D., … Cohen-Adad, J. (2017). SCT: Spinal Cord Toolbox, an open-source software for processing spinal cord MRI data. *NeuroImage*, *145*. https://doi.org/10.1016/j.neuroimage.2016.10.009

De Leener, B., Mangeat, G., Dupont, S., Martin, A. R., Callot, V., Stikov, N., … Cohen-Adad, J. (2017). Topologically preserving straightening of spinal cord MRI. *J. Magn. Reson. Imaging*.

De Leener, B., Mangeat, G., Dupont, S., Martin, A. R., Callot, V., Stikov, N., … Cohen-Adad, J. (2017). Topologically preserving straightening of spinal cord MRI. *Journal of Magnetic Resonance Imaging*. https://doi.org/10.1002/jmri.25622

De Leener, B., Roux, A., Taso, M., Callot, V., & Cohen-Adad, J. (2015). Spinal cord gray and white matter segmentation using atlasdeformation. In *Proceedings of the 23th Annual Meeting of ISMRM, Toronto,Canada, Toronto* (Vol. 4424, p. 4424). Toronto.

De Leener, B., Taso, M., Cohen-Adad, J., & Callot, V. (2016). Segmentation of the human spinal cord. *Magnetic Resonance Materials in Physics, Biology and Medicine*, *29*(2). https://doi.org/10.1007/s10334-015-0507-2

Despotović, I., Goossens, B., & Philips, W. (2015). MRI segmentation of the human brain: challenges, methods,and applications. *Comput. Math. Methods Med.*, *2015*, 450341.

Destrieux, C., Fischl, B., Dale, A., & Halgren, E. (2010). Automatic parcellation of human cortical gyri and sulci using standard anatomical nomenclature. *NeuroImage*, *53*(1), 1–15. https://doi.org/10.1016/j.neuroimage.2010.06.010

Dowell, N. G., Jenkins, T. M., Ciccarelli, O., Miller, D. H., & Wheeler-Kingshott, C. A. M. (2009). Contiguous-slice zonally oblique multislice (CO-ZOOM)diffusion tensor imaging: examples of in vivo spinal cord andoptic nerve applications. *J. Magn. Reson. Imaging*, *29*(2), 454–460.

Dubuc, B. (2015). The brain from top to bottom.

Dupont, S. M., De Leener, B., Taso, M., LeTroter, A., Nadeau, S., Stikov, N., … Cohen-Adad, J. (2017). Fully-integrated framework for the segmentation andregistration of the spinal cord white and gray matter. *Neuroimage*, *150*, 358–372.

Dupont, S. M., De Leener, B., Taso, M., Stikov, N., Callot, V., & Cohen-Adad, J. (2016). Fully-integrated framework for registration of spinal cord whiteand gray matter. In *Proceedings of the 24th Annual Meeting of ISMRM, Singapore,Singapore*.

Duval, T., Le Vy, S., Stikov, N., Campbell, J., Mezer, A., Witzel, T., … Cohen-Adad, J. (2017). g-Ratio weighted imaging of the human spinal cord in vivo. *Neuroimage*, *145*(Pt A), 11–23.

Duval, T., McNab, J. A., Setsompop, K., Witzel, T., Schneider, T., Huang, S. Y., … Cohen-Adad, J. (2015). In vivo mapping of human spinal cord microstructure at 300mT/m. *Neuroimage*, *118*(0), 494–507.

Eippert, F., Finsterbusch, J., Bingel, U., & Büchel, C. (2009). Direct evidence for spinal cord involvement in placebo analgesia. *Science*, *326*(5951), 404.

Eippert, F., Kong, Y., Winkler, A. M., Andersson, J. L., Finsterbusch, J., Büchel, C., … Tracey, I. (2017). Investigating resting-state functional connectivity in thecervical spinal cord at 3 T. *Neuroimage*, *147*, 589–601.

El Mendili, M.-M., Chen, R., Tiret, B., Pélégrini-Issac, M., Cohen-Adad, J., Lehéricy, S., … Benali, H. (2015). Validation of a semiautomated spinal cord segmentationmethod. *J. Magn. Reson. Imaging*, *41*(2), 454–459.

El Mendili, M.-M., Chen, R., Tiret, B., Villard, N., Trunet, S., Pélégrini-Issac, M., … Benali, H.

(2015). Fast and accurate semi-automated segmentation method of spinal cord {MR} images at {3T} applied to the construction of a cervical spinal cord template. *PLoS One, 10*(3), e0122224.

El Mendili, M.-M., Cohen-Adad, J., Pelegrini-Issac, M., Rossignol, S., Morizot-Koutlidis, R., Marchand-Pauvert, V., … Pradat, P.-F. (2014). Multi-parametric spinal cord MRI as potential progressionmarker in amyotrophic lateral sclerosis. *PLoS One, 9*(4), e95516.

Ellingson, B. M., Ulmer, J. L., & Schmit, B. D. (2007). Gray and white matter delineation in the human spinal cordusing diffusion tensor imaging and fuzzy logic. *Acad. Radiol., 14*(7), 847–858.

Ellingson, B. M., Ulmer, J. L., & Schmit, B. D. (2008). Morphology and morphometry of human chronic spinal cord injuryusing diffusion tensor imaging and fuzzy logic. *Ann. Biomed. Eng., 36*(2), 224–236.

Engl, C., Schmidt, P., Arsic, M., Boucard, C. C., Biberacher, V., Röttinger, M., … Mühlau, M. (2013). Brain size and white matter content of cerebrospinal tractsdetermine the upper cervical cord area: evidence fromstructural brain MRI. *Neuroradiology, 55*(8), 963–970.

Evangelou, N., DeLuca, G. C., Owens, T., & Esiri, M. M. (2005). Pathological study of spinal cord atrophy in multiplesclerosis suggests limited role of local lesions. *Brain, 128*(Pt 1), 29–34.

Evans, A. C. (2007). ANIMAL + INSECT : Improved Cortical. In *Information Processing in Medical Imaging, 16th International Conference, {IPMI'99}, Visegr{á}d, Hungary, June 28 - July 2, 1999, Proceedings* (Vol. 1613, pp. 210–223).

Evans, A. C., Marrett, S., Neelin, P., Collins, L., Worsley, K., Dai, W., … Bub, D. (1992). Anatomical mapping of functional activation in stereotacticcoordinate space. *Neuroimage, 1*(1), 43–53.

Facon, D., Ozanne, A., Fillard, P., Lepeintre, J.-F., Tournoux-Facon, C., & Ducreux, D. (2005). MR diffusion tensor imaging and fiber tracking in spinalcord compression. *AJNR Am. J. Neuroradiol., 26*(6), 1587–1594.

Fawcett, J. W., Curt, A., Steeves, J. D., Coleman, W. P., Tuszynski, M. H., Lammertse, D., … Short, D. (2007). Guidelines for the conduct of clinical trials for spinal cord injury as

developed by the {ICCP} panel: spontaneous recovery after spinal cord injury and statistical power needed for therapeutic clinical trials. *Spinal Cord*, *45*(3), 190–205.

Filippi, M., Bozzali, M., Horsfield, M. A., Rocca, M. A., Sormani, M. P., Iannucci, G., … Comi, G. (2000). A conventional and magnetization transfer MRI study of thecervical cord in patients with MS. *Neurology*, *54*(1), 207–213.

Finsterbusch, J. (2009). High-resolution diffusion tensor imaging with innerfield-of-view EPI. *J. Magn. Reson. Imaging*, *29*(4), 987–993.

Fischl, B. (2012). FreeSurfer. *Neuroimage*, *62*(2), 774–781.

FMRI Biomarker Committee. (2013, June). Indices of Repeatability, Reproducibility, and Agreement.

Fonov, V., Coupe, P., Eskildsen, S., & Collins, D. (2011). Atrophy-specific MRI brain template for Alzheimer's disease andmild cognitive impairment. *Alzheimers. Dement.*, *7*(4), S58.

Fonov, V., Evans, A. C., Botteron, K., Almli, C. R., McKinstry, R. C., Collins, D. L., & Brain Development Cooperative Group. (2011). Unbiased average age-appropriate atlases for pediatric studies. *Neuroimage*, *54*(1), 313–327.

Fonov, V. S., Evans, A. C., McKinstry, R. C., Almli, C. R., & Collins, D. L. (2009). Unbiased nonlinear average age-appropriate brain templates frombirth to adulthood. *Neuroimage*, *47*, S102.

Fonov, V. S., Le Troter, A., Taso, M., De Leener, B., Lévêque, G., Benhamou, M., … Cohen-Adad, J. (2014). Framework for integrated MRI average of the spinal cordwhite and gray matter: the MNI-Poly-AMU template. *Neuroimage*, *102 Pt 2*, 817–827.

Fonov, V. S., Le Troter, A., Taso, M., De Leener, B., Lévêque, G., Benhamou, M., … Cohen-Adad, J. (2014). Framework for integrated MRI average of the spinal cord white and gray matter: The MNI-Poly-AMU template. *NeuroImage*, *102*(P2). https://doi.org/10.1016/j.neuroimage.2014.08.057

Foxley, S., Mollink, J., Ansorge, O., Scott, C., Jbabdi, S., Yates, R., … Miller, K. (2015). Whole post-mortem spinal cord imaging with diffusion-weighted steady state free precession at {7T}. *Proceedings of the 23th Annual Meeting of ISMRM, Toronto, Canada*, 4429.

Fradet, L., Arnoux, P.-J., Ranjeva, J.-P., Petit, Y., & Callot, V. (2014). Morphometrics of the entire human spinal cord and spinalcanal measured from in vivo high-resolution anatomicalmagnetic resonance imaging. *Spine*, *39*(4), E262–9.

Freund, P., Wheeler-Kingshott, C., Jackson, J., Miller, D., Thompson, A., & Ciccarelli, O. (2010). Recovery after spinal cord relapse in multiple sclerosis is predicted by radial diffusivity. *Mult. Scler.*, *16*(10), 1193–1202.

Friston, K. J., Holmes, A. P., Worsley, K. J., Poline, J.-P., Frith, C. D., & Frackowiak, R. S. J. (1994). Statistical parametric maps in functional imaging: A generallinear approach. *Hum. Brain Mapp.*, *2*(4), 189–210.

Frost, M. A., & Goebel, R. (2012). Measuring structural-functional correspondence: spatial variability of specialised brain regions after macro-anatomical alignment. *Neuroimage*, *59*(2), 1369–1381.

Frostell, A., Hakim, R., Thelin, E. P., Mattsson, P., & Svensson, M. (2016). A Review of the Segmental Diameter of the Healthy Human SpinalCord. *Front. Neurol.*, *7*, 238.

Fujimoto, K., Polimeni, J. R., van der Kouwe, A. J. W., Reuter, M., Kober, T., Benner, T., … Wald, L. L. (2014). Quantitative comparison of cortical surface reconstructionsfrom MP2RAGE and multi-echo MPRAGE data at 3 and 7 T. *Neuroimage*, *90*, 60–73.

Good, C. D., Johnsrude, I. S., Ashburner, J., Henson, R. N., Friston, K. J., & Frackowiak, R. S. (2001). A voxel-based morphometric study of ageing in 465 normal adulthuman brains. *Neuroimage*, *14*(1 Pt 1), 21–36.

Gorgolewski, K., Burns, C. D., Madison, C., Clark, D., Halchenko, Y. O., Waskom, M. L., & Ghosh, S. S. (2011). Nipype: a flexible, lightweight and extensible neuroimagingdata processing framework in python. *Front. Neuroinform.*, *5*, 13.

Grabher, P., Mohammadi, S., Trachsler, A., Friedl, S., David, G., Sutter, R., … Freund, P. (2016). Voxel-based analysis of grey and white matter degeneration incervical spondylotic myelopathy. *Sci. Rep.*, *6*, 24636.

Grady, L. (2006). Random walks for image segmentation. *IEEE Trans. Pattern Anal. Mach. Intell.*, *28*(11), 1768–1783.

Grussu, F., Schneider, T., Zhang, H., Alexander, D. C., & Wheeler-Kingshott, C. A. M. (2015). Neurite orientation dispersion and density imaging of the healthy cervical spinal cord in vivo. *Neuroimage, 111*, 590–601.

Gullapalli, J., Krejza, J., & Schwartz, E. D. (2006). In vivo DTI evaluation of white matter tracts in rat spinalcord. *J. Magn. Reson. Imaging, 24*(1), 231–234.

Gupta, H., Schmitter, D., Uhlmann, V., & Unser, M. (2017). General Surface Energy for Spinal Cord and Aorta Segmentation. In *Proceedings of the Fourteenth IEEE International Symposiumon Biomedical Imaging: From Nano to Macro (ISBI`` 17)* (pp. 319–322). bigwww.epfl.ch.

Hagler Jr, D. J., Saygin, A. P., & Sereno, M. I. (2006). Smoothing and cluster thresholding for cortical surface-basedgroup analysis of fMRI data. *Neuroimage, 33*(4), 1093–1103.

Harlow, D. E., Honce, J. M., & Miravalle, A. A. (2015). Remyelination Therapy in Multiple Sclerosis. *Front. Neurol., 6*, 257.

Held, P., Dorenbeck, U., Seitz, J., Fründ, R., & Albrich, H. (2003). MRI of the abnormal cervical spinal cord using 2D spoiledgradient echo multiecho sequence (MEDIC) with magnetizationtransfer saturation pulse. A T2* weighted feasibility study. *J. Neuroradiol., 30*(2), 83–90.

Held, P., Seitz, J., Fründ, R., Nitz, W., Lenhart, M., & Geissler, A. (2001). Comparison of two-dimensional gradient echo, turbo spin echoand two-dimensional turbo gradient spin echo sequences inMRI of the cervical spinal cord anatomy. *Eur. J. Radiol., 38*(1), 64–71.

Hickman, S. J., Hadjiprocopis, A., Coulon, O., Miller, D. H., & Barker, G. J. (2004). Cervical spinal cord {MTR} histogram analysis in multiple sclerosis using a {3D} acquisition and a B-spline active surface segmentation technique. *Magn. Reson. Imaging, 22*(6), 891–895.

Hori, M., Okubo, T., Aoki, S., Kumagai, H., & Araki, T. (2006). Line scan diffusion tensor MRI at low magnetic fieldstrength: feasibility study of cervical spondylotic myelopathyin an early clinical stage. *J. Magn. Reson. Imaging, 23*(2), 183–188.

Horsfield, M. A., Sala, S., Neema, M., Absinta, M., Bakshi, A., Sormani, M. P., … Filippi, M. (2010). Rapid semi-automatic segmentation of the spinal cord frommagnetic resonance images: application in multiple sclerosis. *Neuroimage, 50*(2), 446–455.

Horváth, A., Pezold, S., Weigel, M., Parmar, K., Bieri, O., & Cattin, P. (2016). Variational Segmentation of the White and Gray Matter in theSpinal Cord Using a Shape Prior. In *Computational Methods and Clinical Applications for SpineImaging* (pp. 26–37). Springer, Cham.

Iglesias, C., Sangari, S., El Mendili, M.-M., Benali, H., Marchand-Pauvert, V., & Pradat, P.-F. (2015). Electrophysiological and spinal imaging evidences for sensory dysfunction in amyotrophic lateral sclerosis. *BMJ Open*, *5*(2), e007659.

Ingle, G. T., Stevenson, V. L., Miller, D. H., & Thompson, A. J. (2003). Primary progressive multiple sclerosis: a 5-year clinical andMR study. *Brain*, *126*(Pt 11), 2528–2536.

Iwata, N. K., Kwan, J. Y., Danielian, L. E., Butman, J. A., Tovar-Moll, F., Bayat, E., & Floeter, M. K. (2011). White matter alterations differ in primary lateral sclerosisand amyotrophic lateral sclerosis. *Brain*, *134*(Pt 9), 2642–2655.

Jenkinson, M., Bannister, P., Brady, M., & Smith, S. (2002). Improved optimization for the robust and accurate linear registration and motion correction of brain images. *Neuroimage*, *17*(2), 825–841.

Jenkinson, M., Beckmann, C. F., Behrens, T. E. J., Woolrich, M. W., & Smith, S. M. (2012a). FSL. *Neuroimage*, *62*(2), 782–790.

Jenkinson, M., Beckmann, C. F., Behrens, T. E. J., Woolrich, M. W., & Smith, S. M. (2012b). FSL. *Neuroimage*, *62*(2), 782–790.

Kalkers, N. F., Barkhof, F., Bergers, E., van Schijndel, R., & Polman, C. H. (2002). The effect of the neuroprotective agent riluzole on {MRI} parameters in primary progressive multiple sclerosis: a pilot study. *Mult. Scler.*, *8*(6), 532–533.

Kameyama, T., Hashizume, Y., & Sobue, G. (1996). Morphologic features of the normal human cadaveric spinalcord. *Spine*, *21*(11), 1285–1290.

Kara, B., Celik, A., Karadereler, S., Ulusoy, L., Ganiyusufoglu, K., Onat, L., … Hamzaoglu, A. (2011). The role of DTI in early detection of cervical spondyloticmyelopathy: a preliminary study with 3-T MRI. *Neuroradiology*, *53*(8), 609–616.

Kato, F., Yukawa, Y., Suda, K., Yamagata, M., & Ueta, T. (2012). Normal morphology, age-

related changes and abnormal findingsof the cervical spine. Part II: Magnetic resonance imagingof over 1,200 asymptomatic subjects. *Eur. Spine J.*, *21*(8), 1499–1507.

Kawahara, J., McIntosh, C., Tam, R., & Hamarneh, G. (2013). Augmenting Auto-context with Global Geometric Features forSpinal Cord Segmentation. In *Machine Learning in Medical Imaging* (pp. 211–218). Nagoya, Japan: Springer, Cham.

Kawahara, J., McIntosh, C., Tam, R., & Hamarneh, G. (2013). Globally optimal spinal cord segmentation using a minimal path in high dimensions. In *2013 {IEEE} 10th International Symposium on Biomedical Imaging* (pp. 848–851). IEEE Computer Society.

Kayal, N. (2013). *An investigation of grow cut algorithm for segmentation of MRIspinal cord images in normals and patients with SCI*. Temple University Graduate School, Ann Arbor.

Kearney, H., Miller, D. H., & Ciccarelli, O. (2015). Spinal cord MRI in multiple sclerosis [mdash] diagnostic,prognostic and clinical value. *Nat. Rev. Neurol.*, *11*(6), 327–338.

Kearney, H., Yiannakas, M. C., Abdel-Aziz, K., Wheeler-Kingshott, C. A. M., Altmann, D. R., Ciccarelli, O., & Miller, D. H. (2014). Improved MRI quantification of spinal cord atrophy inmultiple sclerosis. *J. Magn. Reson. Imaging*, *39*(3), 617–623.

Khan, H. S., & Stroman, P. W. (2015). Inter-individual differences in pain processing investigatedby functional magnetic resonance imaging of the brainstem andspinal cord. *Neuroscience*, *307*, 231–241.

Kidd, D., Thorpe, J. W., Thompson, A. J., Kendall, B. E., Moseley, I. F., MacManus, D. G., … Miller, D. H. (1993). Spinal cord MRI using multi-array coils and fast spin echo.II. Findings in multiple sclerosis. *Neurology*, *43*(12), 2632–2637.

Kiebel, S. J., Poline, J. B., Friston, K. J., Holmes, A. P., & Worsley, K. J. (1999). Robust smoothness estimation in statistical parametric mapsusing standardized residuals from the general linear model. *Neuroimage*, *10*(6), 756–766.

Klawiter, E. C., Schmidt, R. E., Trinkaus, K., Liang, H.-F., Budde, M. D., Naismith, R. T., … Benzinger, T. L. (2011). Radial diffusivity predicts demyelination in ex vivo multiple sclerosis spinal cords. *Neuroimage*, *55*(4), 1454–1460.

Klein, A., Andersson, J., Ardekani, B. A., Ashburner, J., Avants, B., Chiang, M.-C., … Parsey,

R. V. (2009). Evaluation of 14 nonlinear deformation algorithms applied tohuman brain MRI registration. *Neuroimage*, *46*(3), 786–802.

Klein, J. P., Arora, A., Neema, M., Healy, B. C., Tauhid, S., Goldberg-Zimring, D., … Bakshi, R. (2011). A {3T} {MR} imaging investigation of the topography of whole spinal cord atrophy in multiple sclerosis. *AJNR Am. J. Neuroradiol.*, *32*(6), 1138–1142.

Koh, J., Kim, T., Chaudhary, V., & Dhillon, G. (2010). Automatic segmentation of the spinal cord and the dural sac in lumbar {MR} images using gradient vector flow field. In *2010 Annual International Conference of the {IEEE} Engineering in Medicine and Biology* (pp. 3117–3120). Buenos Aires: IEEE.

Koh, J., Scott, P. D., Chaudhary, V., & Dhillon, G. (2011). An automatic segmentation method of the spinal canal from clinical {MR} images based on an attention model and an active contour model. In *2011 {IEEE} International Symposium on Biomedical Imaging: From Nano to Macro* (pp. 1467–1471). ieeexplore.ieee.org.

Kong, Y., Eippert, F., Beckmann, C. F., Andersson, J., Finsterbusch, J., Büchel, C., … Brooks, J. C. W. (2014). Intrinsically organized resting state networks in the humanspinal cord. *Proc. Natl. Acad. Sci. U. S. A.*, *111*(50), 18067–18072.

Kong, Y., Jenkinson, M., Andersson, J., Tracey, I., & Brooks, J. C. W. (2012). Assessment of physiological noise modelling methods for functional imaging of the spinal cord. *Neuroimage*, *60*(2), 1538–1549.

Kurtzke, J. F. (1983). Rating neurologic impairment in multiple sclerosis: an expandeddisability status scale (EDSS). *Neurology*, *33*(11), 1444–1452.

Laule, C., Vavasour, I. M., Leung, E., Li, D. K. B., Kozlowski, P., Traboulsee, A. L., … Moore, G. R. W. (2011). Pathological basis of diffusely abnormal white matter: insights from magnetic resonance imaging and histology. *Mult. Scler.*, *17*(2), 144–150.

Law, M. W. K., Garvin, G. J., Tummala, S., Tay, K., Leung, A. E., & Li, S. (2013). Gradient competition anisotropy for centerline extraction andsegmentation of spinal cords. *Inf. Process. Med. Imaging*, *23*, 49–61.

Lévy, S., Benhamou, M., Naaman, C., Rainville, P., Callot, V., & Cohen-Adad, J. (2015). White matter atlas of the human spinal cord with estimation ofpartial volume effect. *Neuroimage*,

119(0), 262–271.

Liao, C.-C., Ting, H.-W., & Xiao, F. (2017). Atlas-Free Cervical Spinal Cord Segmentation on MidsagittalT2-Weighted Magnetic Resonance Images. *J. Healthc. Eng.*, *2017*.

Lin, X., Blumhardt, L. D., & Constantinescu, C. S. (2003). The relationship of brain and cervical cord volume todisability in clinical subtypes of multiple sclerosis: athree-dimensional MRI study. *Acta Neurol. Scand.*, *108*(6), 401–406.

Lindberg, P. G., Feydy, A., & Maier, M. A. (2010). White matter organization in cervical spinal cord relates differently to age and control of grip force in healthy subjects. *J. Neurosci.*, *30*(11), 4102–4109.

Liu, C., Edwards, S., Gong, Q., Roberts, N., & Blumhardt, L. D. (1999). Three dimensional MRI estimates of brain and spinal cordatrophy in multiple sclerosis. *J. Neurol. Neurosurg. Psychiatry*, *66*(3), 323–330.

Liu, Y., Wang, J., Daams, M., Weiler, F., Hahn, H. K., Duan, Y., … Barkhof, F. (2015). Differential patterns of spinal cord and brain atrophy inNMO and MS. *Neurology*, *84*(14), 1465–1472.

Ljungberg, E. (2016). *Characterization of myelin water imaging using a gradient andspin echo sequence in human brain and spinal cord*. University of British Columbia.

Ljungberg, E. A., Kolind, S. H., Tam, R., Freedman, M. S., Li, D. K., & Traboulsee, A. L. (2015). Correcting Cervical Spinal Cord Area for Cord LengthStrengthens Correlation Between Atrophy and Ambulation. In *MULTIPLE SCLEROSIS JOURNAL* (Vol. 21, pp. 789–790). researchgate.net.

Ljungberg, E., Vavasour, I., Tam, R., Yoo, Y., Rauscher, A., Li, D. K. B., … Kolind, S. (2016). Rapid myelin water imaging in human cervical spinal cord. *Magn. Reson. Med.*

Losseff, N. A., Webb, S. L., O'Riordan, J. I., Page, R., Wang, L., Barker, G. J., … Thompson, A. J. (1996). Spinal cord atrophy and disability in multiple sclerosis. Anew reproducible and sensitive MRI method with potential tomonitor disease progression. *Brain*, *119 (Pt 3)*(3), 701–708.

Losseff, N. A., Webb, S. L., O'riordan, J. I., Page, R., Wang, L., & others. (1996). Spinal cord

atrophy and disability in multiple sclerosis. *Brain*.

Lowekamp, B. C., Chen, D. T., Ibáñez, L., & Blezek, D. (2013). The Design of SimpleITK. *Front. Neuroinform.*, *7*, 45.

Lublin, F. D., Reingold, S. C., Cohen, J. A., Cutter, G. R., Sørensen, P. S., Thompson, A. J., … Polman, C. H. (2014). Defining the clinical course of multiple sclerosis: the 2013revisions. *Neurology*, *83*(3), 278–286.

Lucas, B. C., Bogovic, J. A., Carass, A., Bazin, P.-L., Prince, J. L., Pham, D. L., & Landman, B. A. (2010). The Java Image Science Toolkit ({JIST}) for rapid prototyping and publishing of neuroimaging software. *Neuroinformatics*, *8*(1), 5–17.

Luessi, F., Kuhlmann, T., & Zipp, F. (2014). Remyelinating strategies in multiple sclerosis. *Expert Rev. Neurother.*, *14*(11), 1315–1334.

Lundell, H., Barthelemy, D., Skimminge, A., Dyrby, T. B., Biering-Sørensen, F., & Nielsen, J. B. (2011). Independent spinal cord atrophy measures correlate to motorand sensory deficits in individuals with spinal cord injury. *Spinal Cord*, *49*(1), 70–75.

Mac Donald, C. L., Dikranian, K., Bayly, P., Holtzman, D., & Brody, D. (2007). Diffusion tensor imaging reliably detects experimental traumatic axonal injury and indicates approximate time of injury. *J. Neurosci.*, *27*(44), 11869–11876.

MacMillan, E. L., Mädler, B., Fichtner, N., Dvorak, M. F., Li, D. K. B., Curt, A., & MacKay, A. L. (2011). Myelin water and T(2) relaxation measurements in the healthycervical spinal cord at 3.0T: repeatability and changes withage. *Neuroimage*, *54*(2), 1083–1090.

Mai, J. K., & Paxinos, G. (2011). *The human nervous system*. Academic Press.

Mamata, H., Jolesz, F. A., & Maier, S. E. (2005). Apparent diffusion coefficient and fractional anisotropy inspinal cord: age and cervical spondylosis-related changes. *J. Magn. Reson. Imaging*, *22*(1), 38–43.

Maneewongvatana, S., & Mount, D. M. (1999). It's okay to be skinny, if your friends are fat. In *Center for Geometric Computing 4th Annual Workshop onComputational Geometry* (Vol. 2, pp. 1–8). cs.umd.edu.

Mann, R. S., Constantinescu, C. S., & Tench, C. R. (2007). Upper cervical spinal cord cross-

sectional area in relapsingremitting multiple sclerosis: application of a new techniquefor measuring cross-sectional area on magnetic resonanceimages. *J. Magn. Reson. Imaging*, *26*(1), 61–65.

Marques, J. P., Kober, T., Krueger, G., der Zwaag, W., de Moortele, P.-F. cois, & Gruetter, R. (2010). MP2RAGE, a self bias-field corrected sequence for improvedsegmentation and T1-mapping at high field. *Neuroimage*, *49*(2), 1271–1281.

Martin, A. R., Aleksanderek, I., Cohen-Adad, J., Tarmohamed, Z., Tetreault, L., Smith, N., … Fehlings, M. G. (2016). Translating state-of-the-art spinal cord MRI techniques toclinical use: A systematic review of clinical studiesutilizing DTI, MT, MWF, MRS, and fMRI. *Neuroimage Clin*, *10*, 192–238.

Martin, A. R., De Leener, B., Aleksanderek, I., Cohen-Adad, J., Cadotte, D. W., Kalsi-Ryan, S., … Others. (2016). A prospective longitudinal study in degenerative cervical myelopathy using quantitative microstructural {MRI} with tract-specific metrics. In *Proceedings of the 24th Annual Meeting of International Society for Magnetic Resonance in Medicine, Suntec City, Singapore*.

Martin, A. R., De Leener, B., Cohen-Adad, J., Cadotte, D. W., Kalsi-Ryan, S., Lange, S. F., … Fehlings, M. G. (2017a). A Novel MRI Biomarker of Spinal Cord White Matter Injury:T2*-Weighted White Matter to Gray Matter Signal IntensityRatio. *AJNR Am. J. Neuroradiol.*, *38*(6), 1266–1273.

Martin, A. R., De Leener, B., Cohen-Adad, J., Cadotte, D. W., Kalsi-Ryan, S., Lange, S. F., … Fehlings, M. G. (2017a). A novel MRI biomarker of spinal cord white matter injury: T2*-weighted white matter to gray matter signal intensity ratio. *American Journal of Neuroradiology*, *38*(6). https://doi.org/10.3174/ajnr.A5162

Martin, A. R., De Leener, B., Cohen-Adad, J., Cadotte, D. W., Kalsi-Ryan, S., Lange, S. F., … Fehlings, M. G. (2017b). Clinically Feasible Microstructural MRI to Quantify CervicalSpinal Cord Tissue Injury Using DTI, MT, andT2*-Weighted Imaging: Assessment of Normative Data andReliability. *AJNR Am. J. Neuroradiol.*, *38*(6), 1257–1265.

Martin, A. R., De Leener, B., Cohen-Adad, J., Cadotte, D. W., Kalsi-Ryan, S., Lange, S. F., … Fehlings, M. G. (2017b). Clinically feasible microstructural MRI to quantify cervical spinal

cord tissue injury using DTI, MT, and T2∗-weighted imaging: Assessment of normative data and reliability. *American Journal of Neuroradiology*, *38*(6). https://doi.org/10.3174/ajnr.A5163

Massire, A., Taso, M., Besson, P., Guye, M., Ranjeva, J.-P., & Callot, V. (2016). High-resolution multi-parametric quantitative magneticresonance imaging of the human cervical spinal cord at 7T. *Neuroimage*, *143*, 58–69.

McCormick, M., Liu, X., Jomier, J., Marion, C., & Ibanez, L. (2014). ITK: enabling reproducible research and open science. *Front. Neuroinform.*, *8*, 13.

McCoy, D. B., Talbott, J. F., Wilson, M., Mamlouk, M. D., Cohen-Adad, J., Wilson, M., & Narvid, J. (2017). MRI Atlas-Based Measurement of Spinal Cord Injury PredictsOutcome in Acute Flaccid Myelitis. *AJNR Am. J. Neuroradiol.*, *38*(2), 410–417.

McDonald, W. I., Compston, A., Edan, G., Goodkin, D., Hartung, H. P., Lublin, F. D., … Wolinsky, J. S. (2001). Recommended diagnostic criteria for multiple sclerosis:guidelines from the International Panel on the diagnosis ofmultiple sclerosis. *Ann. Neurol.*, *50*(1), 121–127.

McIntosh, C., & Hamarneh, G. (2006). Spinal crawlers: deformable organisms for spinal cord segmentation and analysis. *Medical Image Computing and Computer-Assisted Intervention : MICCAI ... International Conference on Medical Image Computing and Computer-Assisted Intervention*, *9*(Pt 1), 808–15. Retrieved from http://www.ncbi.nlm.nih.gov/pubmed/17354965

McIntosh, C., Hamarneh, G., Toom, M., & Tam, R. C. (2011). Spinal Cord Segmentation for Volume Estimation in Healthy and Multiple Sclerosis Subjects Using Crawlers and Minimal Paths. In *2011 {IEEE} First International Conference on Healthcare Informatics, Imaging and Systems Biology* (pp. 25–31). ieeexplore.ieee.org.

Miller, D. H., Barkhof, F., Frank, J. A., Parker, G. J. M., & Thompson, A. J. (2002). Measurement of atrophy in multiple sclerosis: pathologicalbasis, methodological aspects and clinical relevance. *Brain*, *125*(Pt 8), 1676–1695.

Miyanji, F., Furlan, J. C., Aarabi, B., Arnold, P. M., & Fehlings, M. G. (2007). Acute cervical traumatic spinal cord injury: MR imagingfindings correlated with neurologic outcome–

prospective studywith 100 consecutive patients. *Radiology*, *243*(3), 820–827.

Mohammadi, S., Freund, P., Feiweier, T., Curt, A., & Weiskopf, N. (2013). The impact of post-processing on spinal cord diffusion tensor imaging. *Neuroimage*, *70*, 377–385.

Mohammadi, S., Möller, H. E., Kugel, H., Müller, D. K., & Deppe, M. (2010). Correcting eddy current and motion effects by affine whole-brain registrations: evaluation of three-dimensional distortions and comparison with slicewise correction. *Magn. Reson. Med.*, *64*(4), 1047–1056.

Mori, S., Oishi, K., & Faria, A. V. (2009). White matter atlases based on diffusion tensor imaging. *Curr. Opin. Neurol.*, *22*(4), 362–369.

Mühlau, M., Engl, C., Boucard, C. C., Schmidt, P., Biberacher, V., Görsch, I., … Weindl, A. (2014). Spinal cord atrophy in early Huntington's disease. *Ann Clin Transl Neurol*, *1*(4), 302–306.

Mukherjee, D. P., Cheng, I., Ray, N., Mushahwar, V., Lebel, M., & Basu, A. (2010). Automatic segmentation of spinal cord MRI using symmetricboundary tracing. *IEEE Trans. Inf. Technol. Biomed.*, *14*(5), 1275–1278.

Nair, G., Carew, J. D., Usher, S., Lu, D., Hu, X. P., & Benatar, M. (2010). Diffusion tensor imaging reveals regional differences in thecervical spinal cord in amyotrophic lateral sclerosis. *Neuroimage*, *53*(2), 576–583.

Nakamura, M., Miyazawa, I., Fujihara, K., Nakashima, I., Misu, T., Watanabe, S., … Itoyama, Y. (2008). Preferential spinal central gray matter involvement inneuromyelitis optica. An MRI study. *J. Neurol.*, *255*(2), 163–170.

Narayana, P. A., Grill, R. J., Chacko, T., & Vang, R. (2004). Endogenous recovery of injured spinal cord: longitudinal in vivo magnetic resonance imaging. *J. Neurosci. Res.*, *78*(5), 749–759.

Nieuwenhuys, R., Voogd, J., & van Huijzen, C. (Eds.). (2008). Topography of Spinal Cord, Brain Stem and Cerebellum. In *The Human Central Nervous System: A Synopsis and Atlas* (pp. 177–245). Springer.

Nouri, A., Tetreault, L., Singh, A., Karadimas, S. K., & Fehlings, M. G. (2015). Degenerative

Cervical Myelopathy: Epidemiology, Genetics, andPathogenesis. *Spine*, *40*(12), E675–93.

Oh, J., Zackowski, K., Chen, M., Newsome, S., Saidha, S., Smith, S. A., … Reich, D. S. (2013). Multiparametric MRI correlates of sensorimotor function inthe spinal cord in multiple sclerosis. *Mult. Scler.*, *19*(4), 427–435.

Onu, M., Gervai, P., Cohen-Adad, J., Lawrence, J., Kornelsen, J., Tomanek, B., & Sboto-Frankenstein, U. N. (2010). Human cervical spinal cord funiculi: investigation withmagnetic resonance diffusion tensor imaging. *J. Magn. Reson. Imaging*, *31*(4), 829–837.

Papinutto, N., Bakshi, R., Bischof, A., & others. (2017). Gradient nonlinearity effects on upper cervical spinal cord areameasurement from 3D T1-weighted brain MRI acquisitions. *Magnetic*.

Papinutto, N., Schlaeger, R., Panara, V., Zhu, A. H., Caverzasi, E., Stern, W. A., … G. (2015). Age, gender and normalization covariates for spinal cord graymatter and total cross-sectional areas at cervical andthoracic levels: A 2D phase sensitive inversion recoveryimaging study. *PLoS One*, *10*(3), e0118576.

Penny, W. D., Friston, K. J., Ashburner, J. T., Kiebel, S. J., & Nichols, T. E. (2011). *Statistical Parametric Mapping: The Analysis of Functional BrainImages*. Academic Press.

Peters, A. M., Brookes, M. J., Hoogenraad, F. G., Gowland, P. A., Francis, S. T., Morris, P. G., & Bowtell, R. (2007). T2* measurements in human brain at 1.5, 3 and 7 T. *Magn. Reson. Imaging*, *25*(6), 748–753.

Pezold, S., Amann, M., Weier, K., Fundana, K., Radue, E. W., Sprenger, T., & Cattin, P. C. (2014). A semi-automatic method for the quantification of spinal cordatrophy. In *Computational Methods and Clinical Applications for SpineImaging* (pp. 143–155). Springer International Publishing.

Pezold, S., Fundana, K., Amann, M., Andelova, M., Pfister, A., Sprenger, T., & Cattin, P. C. (2015). Automatic Segmentation of the Spinal Cord Using Continuous MaxFlow with Cross-sectional Similarity Prior and TubularityFeatures. In J. Yao, B. Glocker, T. Klinder, & S. Li (Eds.), *Recent Advances in Computational Methods and ClinicalApplications for Spine Imaging* (Vol. 20, pp. 107–118). Springer International Publishing.

Piegl, L., & Tiller, W. (2012). *The NURBS Book*. Springer Science & Business Media.

Polman, C. H., Reingold, S. C., Banwell, B., Clanet, M., Cohen, J. A., Filippi, M., … Wolinsky, J. S. (2011). Diagnostic criteria for multiple sclerosis: 2010 revisions tothe McDonald criteria. *Ann. Neurol.*, *69*(2), 292–302.

Poon, P. C., Gupta, D., Shoichet, M. S., & Tator, C. H. (2007). Clip Compression Model Is Useful for Thoracic Spinal Cord Injuries: Histologic and Functional Correlates. *Spine*, *32*(25). Retrieved from http://journals.lww.com/spinejournal/Fulltext/2007/12010/Clip_Compression_Model_Is_Useful_for_Thoracic.12.aspx

Prados, F., Ashburner, J., Blaiotta, C., Brosch, T., Carballido-Gamio, J., Cardoso, M. J., … Cohen-Adad, J. (2017). Spinal cord grey matter segmentation challenge. *Neuroimage*, *152*, 312–329.

Prados, F., Cardoso, M. J., Yiannakas, M. C., Hoy, L. R., Tebaldi, E., Kearney, H., … Ourselin, S. (2016). Fully automated grey and white matter spinal cord segmentation. *Sci. Rep.*, *6*, 36151.

Qian, W., Chan, Q., Mak, H., Zhang, Z., Anthony, M.-P., Yau, K. K.-W., … Kim, M. (2011). Quantitative assessment of the cervical spinal cord damage inneuromyelitis optica using diffusion tensor imaging at 3 Tesla. *J. Magn. Reson. Imaging*, *33*(6), 1312–1320.

Rao, N. P., Jeelani, H., Achalia, R., Achalia, G., Jacob, A., Bharath, R. dawn, … K. Yalavarthy, P. (2017). Population differences in brain morphology: Need for population specific brain template. *Psychiatry Research: Neuroimaging*, *265*, 1–8. https://doi.org/10.1016/j.pscychresns.2017.03.018

Ritter, F., Boskamp, T., Homeyer, A., Laue, H., Schwier, M., Link, F., & Peitgen, H.-O. (2011). Medical image analysis. *IEEE Pulse*, *2*(6), 60–70.

Rocca, M. A., Horsfield, M. A., Sala, S., Copetti, M., Valsasina, P., Mesaros, S., … Filippi, M. (2011). A multicenter assessment of cervical cord atrophy among MSclinical phenotypes. *Neurology*, *76*(24), 2096–2102.

Rocca, M. A., Preziosa, P., & Filippi, M. (2015). Spinal cord diseases. In M. Filippi (Ed.), *Oxford Textbook of Neuroimaging* (pp. 323–334). Oxford University Press.

Ronneberger, O., Fischer, P., & Brox, T. (2015). U-Net: Convolutional Networks for Biomedical

ImageSegmentation.

Rossignol, S., Martinez, M., Escalona, M., Kundu, A., Delivet-Mongrain, H., Alluin, O., & Gossard, J.-P. (2015). The ``beneficial'' effects of locomotor training after varioustypes of spinal lesions in cats and rats. *Prog. Brain Res.*, *218*, 173–198.

Rovaris, M., Bozzali, M., Santuccio, G., Ghezzi, A., Caputo, D., Montanari, E., … Filippi, M. (2001). In vivo assessment of the brain and cervical cord pathology ofpatients with primary progressive multiple sclerosis. *Brain*, *124*(Pt 12), 2540–2549.

Rovaris, M., Gallo, A., Riva, R., Ghezzi, A., Bozzali, M., Benedetti, B., … Filippi, M. (2004). An MT MRI study of the cervical cord in clinicallyisolated syndromes suggestive of MS. *Neurology*, *63*(3), 584–585.

Rovaris, M., Judica, E., Ceccarelli, A., Ghezzi, A., Martinelli, V., Comi, G., & Filippi, M. (2008). Absence of diffuse cervical cord tissue damage in early,non-disabling relapsing-remitting MS: a preliminary study. *Mult. Scler.*, *14*(6), 853–856.

Rowland, J. W., Hawryluk, G. W. J., Kwon, B., & Fehlings, M. G. (2008). Current status of acute spinal cord injury pathophysiology and emerging therapies: promise on the horizon. *Neurosurg. Focus*, *25*(5), E2.

Samson, R. S., Ciccarelli, O., & others. (2013). Tissue-and column-specific measurements from multi-parameter mapping of the human cervical spinal cord at 3 {T}. *NMR Biomed.*, *26*, 1823–1830.

Samson, R. S., Lévy, S., Schneider, T., Smith, A. K., Smith, S. A., Cohen-Adad, J., & Gandini Wheeler-Kingshott, C. A. M. (2016). ZOOM or Non-ZOOM? Assessing Spinal Cord Diffusion TensorImaging Protocols for Multi-Centre Studies. *PLoS One*, *11*(5), e0155557.

Schlaeger, R., Papinutto, N., Panara, V., Bevan, C., Lobach, I. V, Bucci, M., … Henry, R. G. (2014). Spinal cord gray matter atrophy correlates with multiple sclerosis disability. *Ann. Neurol.*, *76*(4), 568–580.

Schroeder, W., Martin, K., & Lorensen, B. (2006). *The Visualization Toolkit: An Object-oriented Approach to 3DGraphics* (Vol. 4). Kitware.

Sdika, M., Callot, V., Hebert, M., Duhamel, G., & Cozzone, P. J. (2010). Segmentation of the

structure of the mouse spinal cord on DTIimages. In *Proceedings of the 19th scientific meeting, internationalsociety for magnetic resonance in medicine, ISMRM, Stockholm* (Vol. 5092, p. 5092). Stockholm.

Shefner, J. M., Watson, M. L., Simionescu, L., Caress, J. B., Burns, T. M., Maragakis, N. J., … Rutkove, S. B. (2011). Multipoint incremental motor unit number estimation as an outcome measure in {ALS}. *Neurology*, *77*(3), 235–241.

Sigmund, E. E., Suero, G. A., Hu, C., McGorty, K., Sodickson, D. K., Wiggins, G. C., & Helpern, J. A. (2012). High-resolution human cervical spinal cord imaging at 7 {T}. *NMR Biomed.*, *25*(7), 891–899.

Sled, J. G., Zijdenbos, A. P., & Evans, A. C. (1998). A nonparametric method for automatic correction of intensitynonuniformity in MRI data. *IEEE Trans. Med. Imaging*, *17*(1), 87–97.

Smith, S. A., Edden, R. A. E., Farrell, J. A. D., Barker, P. B., & Van Zijl, P. C. M. (2008). Measurement of {T1} and {T2} in the cervical spinal cord at 3 tesla. *Magn. Reson. Med.*, *60*(1), 213–219.

Smith, S. A., Jones, C. K., Gifford, A., Belegu, V., Chodkowski, B., Farrell, J. A. D., … van Zijl, P. C. M. (2010). Reproducibility of tract-specific magnetization transfer and diffusion tensor imaging in the cervical spinal cord at 3 tesla. *NMR Biomed.*, *23*(2), 207–217.

Smith, S. M., Jenkinson, M., Woolrich, M. W., Beckmann, C. F., Behrens, T. E. J., Johansen-Berg, H., … Matthews, P. M. (2004). Advances in functional and structural MR image analysis andimplementation as FSL. *Neuroimage*, *23 Suppl 1*, S208–19.

Sonkova, P., Evangelou, I. E., Gallo, A., Cantor, F. K., Ohayon, J., McFarland, H. F., & Bagnato, F. (2008). Semi-automatic segmentation and modeling of the cervical spinalcord for volume quantification in multiple sclerosis patientsfrom magnetic resonance images. In J. M. Reinhardt & J. P. W. Pluim (Eds.), *Medical Imaging* (Vol. 6914, p. 69144I–69144I–10). International Society for Optics and Photonics.

Spinal Cord Injury Canada. (2015). Spinal Cord Injury Facts.

Standring, S. (2008). *Gray's Anatomy E-Book: The Anatomical Basis of ClinicalPractice*. Elsevier Health Sciences.

Standring, S. (2008). Spinal cord: internal organization. *Gray's Anatomy, 40th Edition*, 257–274.

Stevenson, V. L., Leary, S. M., Losseff, N. A., Parker, G. J., Barker, G. J., Husmani, Y., … Thompson, A. J. (1998). Spinal cord atrophy and disability in {MS}: a longitudinal study. *Neurology*, *51*(1), 234–238.

Stroman, P. W. (2009). Spinal fMRI investigation of human spinal cord function overa range of innocuous thermal sensory stimuli and study-relatedemotional influences. *Magn. Reson. Imaging*, *27*(10), 1333–1346.

Stroman, P. W., Bosma, R. L., & Tsyben, A. (2012). Somatotopic arrangement of thermal sensory regions in thehealthy human spinal cord determined by means of spinal cordfunctional MRI. *Magn. Reson. Med.*, *68*(3), 923–931.

Stroman, P. W., Figley, C. R., & Cahill, C. M. (2008). Spatial normalization, bulk motion correction andcoregistration for functional magnetic resonance imaging ofthe human cervical spinal cord and brainstem. *Magn. Reson. Imaging*, *26*(6), 809–814.

Stroman, P. W., Khan, H. S., Bosma, R. L., Cotoi, A. I., Leung, R., Cadotte, D. W., & Fehlings, M. G. (2016). Changes in Pain Processing in the Spinal Cord and Brainstemafter Spinal Cord Injury Characterized by Functional MagneticResonance Imaging. *J. Neurotrauma*, *33*(15), 1450–1460.

Stroman, P. W., Tomanek, B., Krause, V., Frankenstein, U. N., & Malisza, K. L. (2002). Mapping of neuronal function in the healthy and injured humanspinal cord with spinal fMRI. *Neuroimage*, *17*(4), 1854–1860.

Stroman, P. W., Wheeler-Kingshott, C., Bacon, M., Schwab, J. M., Bosma, R., Brooks, J., … Tracey, I. (2014). The current state-of-the-art of spinal cord imaging: methods. *Neuroimage*, *84*, 1070–1081.

Summers, P. E., Brooks, J. C. W., & Cohen-Adad, J. (2014). Spinal cord {fMRI}. In *Quantitative {MRI} of the spinal cord*. Elsevier Inc.

Talbott, J. F., Narvid, J., Chazen, J. L., Chin, C. T., & Shah, V. (2016). An Imaging-Based Approach to Spinal Cord Infection. *Semin. Ultrasound CT MR*, *37*(5), 411–430.

Tang, L., Wen, Y., Zhou, Z., von Deneen, K. M., Huang, D., & Ma, L. (2013). Reduced field-of-

view DTI segmentation of cervical spinetissue. *Magn. Reson. Imaging*, *31*(9), 1507–1514.

Tartaglino, L. M., Croul, S. E., Flanders, A. E., Sweeney, J. D., Schwartzman, R. J., Liem, M., & Amer, A. (1996). Idiopathic acute transverse myelitis: MR imaging findings. *Radiology*, *201*(3), 661–669.

Taso, M., Girard, O., Duhamel, G., Le Troter, A., Feiweier, T., Guye, M., … Callot, V. (2015). Regional and age-related variations of the healthy spinal cordstructure assessed by multimodal MRI. In *Proceedings of the 23th annual meeting of ISMRM, Toronto,Canada* (Vol. 681, p. 681). Toronto, Canada.

Taso, M., Girard, O. M., Duhamel, G., Le Troter, A., & others. (2016). Tract-specific and age-related variations of the spinal cordmicrostructure: a multi-parametric MRI study using diffusiontensor imaging (DTI) and inhomogeneous …. *NMR Biomed.*

Taso, M., Le Troter, A., Sdika, M., Cohen-Adad, J., Arnoux, P.-J., Guye, M., … Callot, V. (2015). A reliable spatially normalized template of the human spinal cord--Applications to automated white matter/gray matter segmentation and tensor-based morphometry ({TBM}) mapping of gray matter alterations occurring with age. *Neuroimage*, *117*, 20–28.

Taso, M., Le Troter, A., Sdika, M., Ranjeva, J.-P., Guye, M., Bernard, M., & Callot, V. (2014). Construction of an in vivo human spinal cord atlas based onhigh-resolution MR images at cervical and thoracic levels:preliminary results. *MAGMA*, *27*(3), 257–267.

Tator, C. H., & Fehlings, M. G. (1991). Review of the secondary injury theory of acute spinal cordtrauma with emphasis on vascular mechanisms. *J. Neurosurg.*, *75*(1), 15–26.

Tench, C. R., Morgan, P. S., & Constantinescu, C. S. (2005). Measurement of cervical spinal cord cross-sectional area byMRI using edge detection and partial volume correction. *J. Magn. Reson. Imaging*, *21*(3), 197–203.

Thielen, K. R., & Miller, G. M. (1996). Multiple sclerosis of the spinal cord: magnetic resonanceappearance. *J. Comput. Assist. Tomogr.*, *20*(3), 434–438.

Thompson, A. J., & Baneke, P. (2014). *Atlas of MS 2013*.

Tofts, P. (2003). *Quantitative {MRI} of the Brain: Measuring Changes Caused by Disease*. (Wiley, Ed.).

Tustison, N. J., & Avants, B. B. (2013). Explicit B-spline regularization in diffeomorphic imageregistration. *Front. Neuroinform.*, *7*, 39.

Udupa, J. K., & Samarasekera, S. (1996). Fuzzy Connectedness and Object Definition: Theory, Algorithms,and Applications in Image Segmentation. *Graphical Models and Image Processing*, *58*(3), 246–261.

Ullmann, E., Pelletier Paquette, J. F., Thong, W. E., & Cohen-Adad, J. (2014). Automatic labeling of vertebral levels using a robust template-based approach. *Int. J. Biomed. Imaging*, *2014*, 719520.

Valsasina, P., Horsfield, M. A., Rocca, M. A., Absinta, M., Comi, G., & Filippi, M. (2012). Spatial normalization and regional assessment of cordatrophy: voxel-based analysis of cervical cord 3DT1-weighted images. *AJNR Am. J. Neuroradiol.*, *33*(11), 2195–2200.

Valsasina, P., Rocca, M. A., Agosta, F., Benedetti, B., Horsfield, M. A., Gallo, A., … Filippi, M. (2005). Mean diffusivity and fractional anisotropy histogram analysisof the cervical cord in MS patients. *Neuroimage*, *26*(3), 822–828.

van der Kouwe, A. J. W., Benner, T., Salat, D. H., & Fischl, B. (2008). Brain morphometry with multiecho MPRAGE. *Neuroimage*, *40*(2), 559–569.

van Middendorp, J. J., Goss, B., Urquhart, S., Atresh, S., Williams, R. P., & Schuetz, M. (2011). Diagnosis and prognosis of traumatic spinal cord injury. *Global Spine J*, *1*(1), 1–8.

Van Uitert, R., Bitter, I., & Butman, J. A. (2005). Semi-automatic spinal cord segmentation and quantification. *Int. Congr. Ser.*, *1281*(0), 224–229.

Varma, G., Duhamel, G., de Bazelaire, C., & Alsop, D. C. (2015). Magnetization transfer from inhomogeneously broadened lines: Apotential marker for myelin. *Magn. Reson. Med.*, *73*(2), 614–622.

Vrtovec, T., Likar, B., & Pernus, F. (2005). Automated curved planar reformation of 3D spine images. *Phys. Med. Biol.*, *50*(19), 4527–4540.

Vrtovec, T., Ourselin, S., Gomes, L., Likar, B., & Pernus, F. (2007). Automated generation of curved planar reformations from MRimages of the spine. *Phys. Med. Biol.*, *52*(10), 2865–2878.

Wang, Y., Wu, A., Chen, X., Zhang, L., Lin, Y., Sun, S., … Lu, Z. (2014). Comparison of clinical characteristics between neuromyelitisoptica spectrum disorders with and without spinal cord atrophy. *BMC Neurol.*, *14*, 246.

Warfield, S. K., Zou, K. H., & Wells, W. M. (2004). Simultaneous truth and performance level estimation ({STAPLE)}: an algorithm for the validation of image segmentation. *IEEE Trans. Med. Imaging*, *23*(7), 903–921.

Weber 2nd, K. A., Chen, Y., Wang, X., Kahnt, T., & Parrish, T. B. (2016a). Functional magnetic resonance imaging of the cervical spinalcord during thermal stimulation across consecutive runs. *Neuroimage*, *143*, 267–279.

Weber 2nd, K. A., Chen, Y., Wang, X., Kahnt, T., & Parrish, T. B. (2016b). Lateralization of cervical spinal cord activity during anisometric upper extremity motor task with functional magneticresonance imaging. *Neuroimage*, *125*, 233–243.

Weiler, F., Daams, M., Lukas, C., Barkhof, F., & Hahn, H. K. (2015). Highly accurate volumetry of the spinal cord. In *SPIE Medical Imaging* (Vol. 9413, pp. 941302–941302–6). Orlando, Florida: International Society for Optics and Photonics.

West, J., Aalto, A., Tisell, A., Leinhard, O. D., Landtblom, A.-M., Smedby, Ö., & Lundberg, P. (2014). Normal appearing and diffusely abnormal white matter in patients with multiple sclerosis assessed with quantitative {MR}. *PLoS One*, *9*(4), e95161.

Wheeler-Kingshott, C. A., Stroman, P. W., Schwab, J. M., Bacon, M., Bosma, R., Brooks, J., … Tracey, I. (2014). The current state-of-the-art of spinal cord imaging: applications. *Neuroimage*, *84*, 1082–1093.

Wilm, B. J., Svensson, J., Henning, A., Pruessmann, K. P., Boesiger, P., & Kollias, S. S. (2007). Reduced field-of-view MRI using outer volume suppressionfor spinal cord diffusion imaging. *Magn. Reson. Med.*, *57*(3), 625–630.

Wingerchuk, D. M., Hogancamp, W. F., O'Brien, P. C., & Weinshenker, B. G. (1999). The clinical course of neuromyelitis optica (Devic's syndrome). *Neurology*, *53*(5), 1107–1114.

Woolrich, M. W., Jbabdi, S., Patenaude, B., Chappell, M., Makni, S., Behrens, T., … Smith, S. M. (2009). Bayesian analysis of neuroimaging data in FSL. *Neuroimage*, *45*(1 Suppl), S173–86.

Xu, J., Shimony, J. S., Klawiter, E. C., Snyder, A. Z., Trinkaus, K., Naismith, R. T., … Song, S.-K. (2013). Improved in vivo diffusion tensor imaging of human cervicalspinal cord. *Neuroimage*, *67*, 64–76.

Yanase, M., Matsuyama, Y., Hirose, K., Takagi, H., Yamada, M., Iwata, H., & Ishiguro, N. (2006). Measurement of the cervical spinal cord volume on MRI. *J. Spinal Disord. Tech.*, *19*(2), 125–129.

Yen, C., Su, H.-R., Lai, S.-H., Liu, K.-C., & Lee, R.-R. (2013). 3D Spinal Cord and Nerves Segmentation from STIR-MRI. In *Proceedings of the International Computer Symposium ICS 2012* (pp. 383–392). Hualien, Taiwan.

Yiannakas, M. C., Kearney, H., Samson, R. S., Chard, D. T., Ciccarelli, O., Miller, D. H., & Wheeler-Kingshott, C. A. M. (2012a). Feasibility of grey matter and white matter segmentation ofthe upper cervical cord in vivo: a pilot study withapplication to magnetisation transfer measurements. *Neuroimage*, *63*(3), 1054–1059.

Yiannakas, M. C., Kearney, H., Samson, R. S., Chard, D. T., Ciccarelli, O., Miller, D. H., & Wheeler-Kingshott, C. a M. (2012b). Feasibility of grey matter and white matter segmentation of the upper cervical cord in vivo: A pilot study with application to magnetisation transfer measurements. *NeuroImage*, *63*(3), 1054–9. https://doi.org/10.1016/j.neuroimage.2012.07.048

Yiannakas, M. C., Mustafa, A., De Leener, B., Cohen-Adad, J., Kearney, H., Miller, D. H., & Wheeler-Kingshott, C. (2015). Fully automated segmentation of the cervical spinal cord usingPropSeg: application to multiple sclerosis. In *Proceedings of the 23th Annual Meeting of ISMRM, Toronto,Canada* (p. 4354).

Yiannakas, M. C., Mustafa, A. M., De Leener, B., Kearney, H., Tur, C., Altmann, D. R., … Gandini Wheeler-Kingshott, C. A. M. (2016). Fully automated segmentation of the cervical cord fromT1-weighted MRI using PropSeg: Application to multiplesclerosis. *Neuroimage Clin*, *10*, 71–77.

Yiannakas, M. C., Mustafa, A. M., De Leener, B., Kearney, H., Tur, C., Altmann, D. R., … Gandini Wheeler-Kingshott, C. A. M. (2016). Fully automated segmentation of the cervical cord from T1-weighted MRI using PropSeg: Application to multiple sclerosis. *NeuroImage:*

Clinical, *10*. https://doi.org/10.1016/j.nicl.2015.11.001

Yushkevich, P. A., Piven, J., Hazlett, H. C., Smith, R. G., Ho, S., Gee, J. C., & Gerig, G. (2006). User-guided 3D active contour segmentation of anatomicalstructures: significantly improved efficiency and reliability. *Neuroimage*, *31*(3), 1116–1128.

Zackowski, K. M., Smith, S. A., Reich, D. S., Gordon-Lipkin, E., Chodkowski, B. A., Sambandan, D. R., … Calabresi, P. A. (2009). Sensorimotor dysfunction in multiple sclerosis and column-specific magnetization transfer-imaging abnormalities in the spinal cord. *Brain*, *132*(Pt 5), 1200–1209.

Zhang, J., Jones, M., DeBoy, C. A., Reich, D. S., Farrell, J. A. D., Hoffman, P. N., … Calabresi, P. A. (2009). Diffusion tensor magnetic resonance imaging of Wallerian degeneration in rat spinal cord after dorsal root axotomy. *J. Neurosci.*, *29*(10), 3160–3171.

Zhang, Y., Brady, M., & Smith, S. (2001). Segmentation of brain MR images through a hidden Markovrandom field model and the expectation-maximization algorithm. *IEEE Trans. Med. Imaging*, *20*(1), 45–57.

Zivadinov, R., Banas, A. C., Yella, V., Abdelrahman, N., Weinstock-Guttman, B., & Dwyer, M. G. (2008). Comparison of three different methods for measurement ofcervical cord atrophy in multiple sclerosis. *AJNR Am. J. Neuroradiol.*, *29*(2), 319–325.